



HAL
open science

Enhancing perovskite solar cells through upconversion nanoparticles insertion

Mathilde Schoenauer

► **To cite this version:**

Mathilde Schoenauer. Enhancing perovskite solar cells through upconversion nanoparticles insertion. Materials. Sorbonne Université, 2018. English. NNT : 2018SORUS369 . tel-02865362

HAL Id: tel-02865362

<https://theses.hal.science/tel-02865362>

Submitted on 11 Jun 2020

HAL is a multi-disciplinary open access archive for the deposit and dissemination of scientific research documents, whether they are published or not. The documents may come from teaching and research institutions in France or abroad, or from public or private research centers.

L'archive ouverte pluridisciplinaire **HAL**, est destinée au dépôt et à la diffusion de documents scientifiques de niveau recherche, publiés ou non, émanant des établissements d'enseignement et de recherche français ou étrangers, des laboratoires publics ou privés.

Doctoral School Physique et Chimie des Matériaux (ED 397)

LPEM, ESPCI

Enhancing Perovskite Solar Cells Through Upconversion Nanoparticles Insertion

THESIS

In order to obtain the title of Philosophiæ Doctor of Sorbonne Université

Specialty: Material Sciences

By

Mathilde Schoenauer Sebag

Directed by Zhuoying Chen and Lionel Aigouy

Publically defended on the 28/09/2018 in front of a jury composed by:

Mrs Christel Laberty-Robert
Mrs Emmanuelle Deleporte
Mr Antonio Garcia-Martin
Mr Artem A. Bakulin
Mr Lionel Aigouy
Mrs Zhuoying Chen

President of the jury
Reviewer
Reviewer
Member of the jury
Ph.-D. Supervisor
Ph.-D. Director

LCMP, UPMC
LAC, ENS Cachan
IMN, CSIC
Imperial College London
LPEM, ESPCI
LPEM, ESPCI

Acknowledgments

There are many people my gratitude goes to.

Starting with Zhuoying, who showed strong motivation where I could be lacking of it, and who taught me how to seek for interesting results where all I could see was wasted time! Wherever my professional path takes me, I will try to adopt her determination and her skill to focalize and fix one thing at a time.

Lionel has been during these three years a joyful and nevertheless scientifically solid base on which I was grateful to rely in the hopeless moments. The cocktail I shall drink for the next years, made by Lionel: a powerful mix of slyness and handy skills, being serious and playing down at the same time !

My gratitude goes to our team which also counts Laurent, with whom it was a pleasure to work and chat, Hengyang, with whom we shared synthesis secrets, Hungju (Mr Simulation!), for his holy help and whom I thank for the norwegian dreams drifting across our discussions, as well as Cyrine, Tingting and Gabriel.

This work would be much diminished without the help of Zhelu, whose kindness is one of the most sincere one I have ever seen. An inspiring balance between hard worker and world curious.

I would like to thank the team in Chimie Paris we had the chance to work with, Patrick and Karmel. Tough though interesting doubting mornings are part of a research's life!

Big thank also to Zhipeng Shao for his precious help on perovskite fabrication.

I had the chance to share my office with Silvanna, whose passionnate debates on italian traditions or plays or books brought my thoughts in some fresh nest before diving back in the inextricable science, Huyen and Jonathan.

I am also thanking all the others students in the lab, passed or present: Louiza, Nathalie, Lorenzo, Marie, Anne, Fatimata, Alexis, Eva, Clément, Manon, Marion, Alex, François, Paul, Thomas, Robin and Joujou.

Je voudrais également remercier Marie-Claude, pour les joyeuses et artistiques discussions, ainsi que Sophie. Francis, toujours très disponible et serviable, m'a beaucoup aidé et je lui souhaite le tour du monde qu'il mérite. Je remercie Armel, dont les bonnes ondes ne font qu'à peine finir de s'estomper, Bruno Bresson, pour son aide au MEB et sa bienveillance, et Hervé Aubin et Cheryl Palma-Feuillet pour leur aide également au MEB.

Les observations au TEM n'auraient pas été faisables sans la disponibilité et la gentillesse de Tianzhen, et l'utilisation de l'évaporateur du LPEM m'a été accordée avec élégance par Stéphane Holé. Je tiens également à remercier l'équipe du plateau technique de l'IPGG, Olivier, Guillaume et Guillaume.

Merci à Nicolas Sanson, Thomas, Sandrine et Nicolas Lequeux, qui à 4 m'ont apporté un indispensable éclairage quant à la magie des nanobâtonnets.

Merci également à Kamran, pour ses encouragements et les fenêtres ouvertes sur des étendues désertiques et autres récits, et Yannick de Wilde pour avoir eu confiance en une chimiste.

La vie au labo n'aurait été sans commune comparaison si l'équipe de choc Réré-Wiwi-Dada avait manqué à l'appel. Merci à Rémi, un homme sans pareil, avec qui il est toujours agréable de plonger dans une piscine, à Dada, qui sait offrir les meilleures pauses café que l'univers ait songé à créer, sans parler des résolutions de problèmes physiques, et bien sûr Herr Rischau, mit wem reden heisst fließen, über Wahrheit und Rationalität.

I am profoundly thankful to Ni Zhao and her team to have welcomed me in CUHK, in particular Jason Cao and Yang Zhou who spent extra time with me at the lab to form me. The discussions with Yang were of precious help for the understanding of the complexity of perovskite material and of Chinese culture.

I would also like to thank the team in Madrid Antonio and Maria, as well as the team in Cambridge, Jiangbin and Artem.

Je remercie l'équipe du Laboratoire de Physique Expérimentale de Centrale Supélec composé de Gloria et Franz, et mes collègues doctorants-enseignants Cyrille et Delphine. L'enseignement y a été un grand plaisir.

Il existe des professeurs, disséminés ici et là dans les universités les lycées les collèges les écoles, qui ont conféré une certaine magie à la physique et la chimie, grâce à leur talents de conteurs modernes, ou bien qui ont encouragé ma curiosité. Je leur adresse une pensée : de Mr Sabban à Mr Barbet-Massin, de Ludovic Tortech à Didier Gourier, dont la pédagogie n'a d'égale que la passion pour son domaine, Mr Nasset (1ere), la toute première professeure de Physique-Chimie à Epin dont le nom m'échappe, à Madame Delay (CP), merci à Mr Barboux, et aux coffrets pour chimistes en herbes des années 60 glanés chez Emmaus.

Je voudrais remercier le monsieur de la sécurité dont je ne connais toujours pas le prénom malgré nos longues discussions sur Baden Baden ou l'impunité, et le personnel du ménage, qui travaille discrètement à ce que nos poubelles soient vidées.

Merci au SDF Brice qui dort dans la rue derrière l'ESPCI et qui vend des livres d'histoires et qui en a toujours de bonnes à raconter (des histoires).

Merci à l'école républicaine, bien que l'égalité des chances ait encore du chemin devant elle.

I would like to thank things and immaterial things, which have participated to my comfort and my fulfilment during those years: la route des thés pour les voyages orientaux que ses saveurs parfumées m'ont permis de réaliser tout en restant dans le 5e arrondissement, le mug dont l'imperfection rend le contact réconfortant, la boulangerie Morange de la rue mouffetard pour les pains au chocolat succulents, ainsi que les artistes qui m'inspirent et grâce auxquels une journée pluvieuse à l'ESPCI à taper un manuscrit peut se transformer momentanément et aléatoirement en souk, en salle à la population exigeante, en marathon plein d'adrénaline, en voyage à bord d'un taxi brousse malien, en chevauchée mongole, en pub british, en arène antique : Bambooman, Joni Void, Boston 168, Verdi, Matmos, Ali Farka Touré, Ballaké Cissoko, Leopold Nord, Roman Fluegel, , Liu Fang, Francis Bebey, Oumou Sangaré, Huun Hur Tu, Matthew Herbert, Dakha Brakha, Tosca, Tinariwen...

Merci aux arbres supports de ce manuscrit.

Et ceux qui font, ont fait et feront qui je suis.

Mes partenaires musicaux : Olivier, Guigui, Marc, Tony, Stefan, Tom, Min-Jung. Mention pour celui qui a en partie réveillé tout cela (et pour son inspirante approche), Fred ! Et Théis pour sa savante lanterne. Merci à Alister pour m'avoir passé le pied à l'étrier de la MAO, pour l'olivier qui nous survivra.

L'impro Erard, qui a vu le jour en même temps que ce travail, pour leur énergie et leur malice, pour les moments sur scène, autant ceux où l'on brille que ceux on l'on choie piteusement, et pour ceux à venir : Debbie, Lucille, Momo, Auré, Faysal, Tom, Matthieu, Adibou, Paul R et Paul B, Raph, Geoffrey, Maxime, Simon, Théo, Cécile, Sylvain, Guillaume, Caroline et Clément.

Ma vie théâtrale fut également marquée pendant ces 3 ans par mon passage chez la compagnie des Gens Pensent Pas Moins dont je tiens à saluer les membres inspirés !

La famille a deux noms, et je tiens à saluer tous les cousins pour ces moments où l'on n'a plus à rien prouver : Gohu, Timothée, Jérôme, Banal, Maxime, Benoit, Toux, Nayan, Phosfaure, Deub, Manillas et Yomgui.

Je voudrais aussi remercier mon grand ami petit, Jugurtha, empereur de l'émerveillement et qui représente une base si solide qu'elle en devient piédestal, et Rémi pour sa sage légèreté. I need to thank those who boost my summers and make winter shorter by invading my space and thoughts with exotic memories and languages, Katya, Henry, Dan, Martin, Josh, Sam, Elsa, Paul Seelman, le grand Gaspard, Brandon, Pat le roi, and Miki.

Les camarades chimistes, Brice, Caroline, Thomas, Mathilde, Florian, Marie, Mylord, je les salue et lève mon bécher à leur santé. Je voudrais remercier les amis « non groupés » pour l'enchantement qu'ils me procurent, les histoires qu'ils me racontent, les progrès qu'ils m'aident à faire, pour les conversations, les désaccords et la fourberie dont ils sont capables, merci à vous Capucine, Irène, Sophie, Hugo Partouche, Elliott, Elliot et Clara, Arthur et Zoé, Esther, Robin. Merci à Sylvain, à mes anciens colocs de la grande villa du bonheur, Aurélien, Jade, Victor, Tom et Marion, vous êtes chics et beaux.

Merci à Jean, à Ramon, à Antoine. Je salue les grands-parents qui agitent leurs mouchoirs bariolés là-haut, et celui qui agite ses post-it ici en bas, la famille Sebag et la famille Schoenauer.

Merci à ma sœur, elle dont contempler la détermination suffirait à déplacer une montagne (mais dont la variation d'humeur consisterait en une thèse propre).

Merci à mon père, à ma mère.

Résumé en français

Les énergies renouvelables peuvent à la fois répondre au besoin croissant en énergie tout en répondant à la nécessité de décarboniser l'énergie. La ressource énergétique solaire est quasi infinie (la terre reçoit plus d'énergie solaire en une heure qu'elle en consomme en un an) mais reste pourtant peu exploitée.

Les cellules solaires hybrides à base de perovskite connaissent depuis les années 2000 un essor sans précédent dans le monde de la recherche en technologies solaires. Elles appartiennent à la catégorie des films minces, et nécessitent donc bien moins de matière première que les cellules au silicium, pour le moment largement majoritaires sur le marché.

Cependant, elles n'absorbent pas au-delà de 800 nm, et tout l'infrarouge est donc non converti par ce type de cellules solaires. Ce doctorat a pour but d'augmenter l'absorption dans l'infrarouge et donc le rendement de la cellule solaire. Pour cela, on y place des particules appelées nanoparticules d'upconversion, qui convertissent un rayonnement infrarouge en visible. Il s'agit d'un phénomène d'absorption simultané de deux photons. Cet effet ayant un rendement assez faible, il convient de le booster par l'insertion de nanoparticules métalliques afin de pouvoir bénéficier de l'augmentation de l'intensité du champ électromagnétique dans leur voisinage proche (effet dit plasmonique). En combinant les deux types de particules on parvient à augmenter l'absorption des particules à upconversion, et en les plaçant tous deux dans une cellule solaire, on augmente donc son rendement.

English Summary

Renewable energies represent nowadays one of the keys that can tackle at the same time energy supply needs and a sustainable environmental behavior. Photovoltaic devices convert the energy of sunlight into electricity, and solar energy remains one of the most common renewable energy sources.

In the search for cost-effective solar cells, the recently discovered solution-processable hybrid organic-inorganic perovskites are considered as one of the most important candidates. They belong to the category of thin-film technologies and require much less and as abundant resource than Si. One limiting parameter of such photovoltaic devices is however the absorption of low-energy photons (wavelength over 800 nm, the near-infrared range).

In order to address this specific loss of sub bandgap photons' absorption, this PhD thesis aims to develop plasmonic-enhanced upconversion approaches to extend the spectral sensitivity of organo-metal halide perovskite solar cells to the near-IR spectrum.

Near-infrared-to-visible up-conversion fluorescent materials can be used to widen the part of the spectrum used for electric current generation. Two low-energy photons are added up in order to give a higher energy photon. However, this effect has a rather small efficiency. This effect being quite inefficient, the idea is to combine those particles with metallic nanoparticles, that have the property to enhance electromagnetic field intensity at a certain wavelength (this is called plasmonic effect). By combining both types of particles, we thus enhance the activity of up-conversion materials (higher emission). Once implemented in a perovskite solar cell, this increases its efficiency.

Table of contents

Table of notations	1
Introduction.....	4
Chapter 1. Theoretical background and fundamental principles of solar energy generation, upconversion, plasmonic effect and plasmonic enhanced upconversion	11
I. Perovskite solar cell : presentation and theoretical analysis	11
1. General functioning of a solar cell.....	11
2. Description of theoretical p-n junction model and electrical parametrization of the device....	13
a. Current-potential equation obtained from p-n junction model	13
b. Description of J_{sc}, V_{oc}, FF and PCE	14
c. Equivalent electrical circuit – Non Ideal case	15
d. International reference solar spectrum	15
3. Solar cell efficiency limitations.....	16
a. Shockley Queisser limit.....	16
b. Losses and recombination.....	18
c. Optimizing solar cells – How to reduce losses ?	18
4. Perovskite material as solar converter.....	19
a. The successful story of perovskite solar cells	19
b. Reason behind perovskite’s success	20
c. Current limits of perovskite devices.....	22
II. Upconversion mechanism	23
1. Rare earth optical properties – Advantage of coupled ions	23
2. Processes implied in upconversion	24
3. Expression of Probabilities of different processes	26
a. Spontaneous emission.....	26
b. Stimulated processes.....	26
c. Energy transfer	26
d. Multi phonon relaxation	28
4. Detailing upconversion process and quantum efficiency	28
a. Complete description of upconversion process.....	28
b. Quantum efficiency	29
5. Dependency of luminescence intensity	30
a. To incident power.....	30
b. To particle’s size	32

6.Implementation of UCNPs in solar devices	33
III. Theory of Plasmonic resonance	34
1.Drude model and permittivity.....	35
2.Localized Surface Plasmon Resonance (LSPR).....	35
a.Case of a small sphere – Rayleigh model	36
b. Short introduction to Mie Theory	36
c. Near-field local enhancement.....	38
d. Qualitative adaptation to the case of nanorods	39
3.Implementation in solar devices	40
a.Advantage and drawbacks of plasmonic NP.....	40
b.State-of-the-art and fabrication methods.....	41
IV. Plasmonic enhanced upconversion – Case of a metallic nanosphere and an upconversion particle.....	42
1.Luminescence enhancement outcome	43
a.Excitation enhancement factor	43
b.Emission enhancement factor	44
c.Total enhancement.....	44
d.Modification of transition coefficients	44
2.Variation of the enhancement factor with distance	44
a. Comparing quantum efficiencies in the case of an optical emitter (Electrodynamic Theory)	44
b. Comparing relative luminescence – Case of an upconversion emitter (Electrodynamic Theory)	45
3.State of the art	47
V.Finite Difference Time Domain (FDTD) Simulation principle	47
Chapter 2. Fabrication and characterization of solar cells.....	49
I.Obtaining and comparing data for efficient optimization	49
Before describing the solar cell fabrication and different layers' optimizations, a little notice should be given on how to obtain results and analyze them in order to draw the most useful and reasonable conclusions. We will first expose the measurement methods before critically discuss the best way to analyze the results.....	49
1.I-V curve measurement	49
a.Set-up	49
b. C- program data analyzer	49
2. Extern Quantum Efficiency (EQE).....	50
3. Data acquisition and analysis precautions	50

a.Variability and repeatability of experiments	51
b. Comparing results - Ideal case	52
c.Comparing results – the reality	53
d.Comparing results – what we chose to do	54
II.Solar cell fabrication	54
1.Pre-treatment and general precautions.....	55
2.Electron Transport Layer – TiO ₂	56
a.Sol-gel method	56
0.15 M Titanium diisopropoxide bis(acetylacetonate) in butan-1-ol.....	57
b.Optimization of two recipes ¹Ti and ³Ti	58
3.Perovskite	60
a.HC(NH₂)₂I (FAI) and CH₃NH₂I (MAI) synthesis	61
b.¹ MAPbI₃ and MAPbI_{3-x}Cl_x in DMF (N,N-dimethylformamide)	61
c. Solvent engineering methods - ²MAPbI₃ in DMSO, FA_{0.83}Cs_{0.17}Pb(I_{0.6}Br_{0.4})₃ in DMF	63
4. HTL.....	64
a.Poly TPD and ¹Spiro comparison	64
b. ¹Spiro vs ²Spiro	65
5. Gold	65
Chapter 3. Synthesis, Optical and Structural characterization of nanorods and upconversion nanoparticles.....	67
I.Nanoparticles characterization’s methods	67
a. Absorbance measurements.....	67
b. PhotoLuminescence Quantum Efficiency (PLQE)	68
c. PhotoLuminescence (PL) spectrum	70
d.Excitation power dependence of luminescence intensity	71
e. Transmission and Scanning Electron Microscopy	72
f. X-Ray Diffraction method.....	72
g. Fluorescence lifetime	73
II. Upconversion nanoparticles : characterization and synthesis.....	73
1.NaYF ₄ :1%Er ³⁺ :10%Yb ³⁺ hydrothermal.....	73
a.Syntheses A to C - Sodium citrate ligand	73
b.Synthesis D and E - EDTA ligand	75
c.XRD	76
2. KY ₇ F ₂₂ and KY ₃ F ₁₀ :YF ₃ :5%Er ³⁺ :20%Yb ³⁺ Coprecipitation	76

a.Synthesis	77
b.XRD	78
c. PL Lifetime	79
d. SEM	80
3. KY ₃ F ₁₀ :5%Er ³⁺ :20 %Yb ³⁺ hydrothermal.....	80
a.Synthesis	80
b.TEM	81
c. Infrared vibrational spectra	81
4. NaYF ₄ :30%Gd ³⁺ :2%Er ³⁺ :18Yb ³⁺	82
a.Synthesis 1 – Octadecene ligand – Solvothermal	82
b.Synthesis 2 – oleic acid ligand – Hydrothermal	82
b.TEM	82
5. Ligands’ problematic	83
6. Qualitative comparison	85
a.Ratio of luminescent particles	85
b.The elimination	86
III. Nanorods (NRs) synthesis and characterization	87
1.Synthesis protocols.....	88
a.Seed Mediated Growth	88
b.Growth mechanism	88
c.Optimization of the synthesis – Variation of Silver nitrate volume	89
2. Ligands and solvent problematics	90
Chapter 4. Incorporation of nanoparticles in perovskite solar cells	91
I. Plasmonic NPs and nanostructures, simulation and incorporation in solar devices	91
1.Choice of NRs aspect ratio : comparison between experiment and simulation.....	91
a.Model of absorption for a gold NRs on a glass substrate	91
b.Field distribution around a gold nanorod	93
2.Case of gold nanodisks in array : Radius impact on LSPR.....	94
a.Far-field absorption	94
b.Near-field localization	95
3.Deposition processes – Morphological optimization.....	96
a.NRs alone	96
b.UCNPs and NRs	97
4. Plasmonic enhanced upconversion – Preliminary studies	99

II. UCNPs implementation in perovskite solar cells.....	100
1. Considering the morphology of the device	101
a. Impact of the presence of the UCNPs on perovskite surface coverage	101
b. Study of the impact of the concentration of UCNPs dispersions on their surface distribution on FTO and on perovskite	102
c. Influence of the presence of UCNPs on device's roughness.....	103
2. Electrical characterizations.....	104
a. Influence of concentration and configuration – KY_7F_{22}	104
b. External Quantum Efficiency (EQE) of the device – in collaboration with Zhelu Hu.....	107
c. Comment on others UCNPs	108
d. Plasmonic enhanced upconversion in a solar device – Preliminary study.....	108
3. Optical characterizations.....	109
a. LBIC/fluorescence mapping under NIR excitation	109
b. Under laser irradiation: variation of current with excitation power.....	112
c. In situ luminescence variation with UCNPs concentration	113
Conclusion and perspectives	116
Annexes	117
Annex 1 - Current-voltage equation for the case of an ideal diode.....	117
Annex 2. Upconversion models.....	124
A.Upconversion mechanism: electronic population level time derivative equations [98].....	124
B.Parameters for the UC model developed by Anderson et al.[98].....	126
Annex 3. Drude's model	127
Annex 4. Localized Surface Plasmon Resonance 's condition for a sphere[144].	128
Annex 5. FDTD Equations	131
Annex 6. Statistical analysis - T-table [304].....	134
Annex 7. Tables of values for perovskite solar cell fabrication optimization.....	135
Annex 8. Chemicals providers	136
Annex 9. Gold growth on UCNPs.....	137
Annex 10. Influence of concentration in UCNPs on the morphology of the solar cell.....	138
Annex 11. Doped $KY_3F_{10}:YF_3$, KY_3F_{10} and $NaYF_4$ insertion in perovskite devices	139
A. $KY_3F_{10}:YF_3$ – in collaboration with Zhelu Hu	139
a. IV-Curve	139
b. Concentration and configuration optimization	140
c. EQE	141

B.KY ₃ F ₁₀	141
a.IV-Curve	141
b.Concentration and configuration optimization	142
C.NaYF ₄ hydrothermal (synthesis D)	143
a. IV-Curve	143
D. NRs and KY ₃ F ₁₀	144
Annex 12 – LBIC/fluorescence mapping for KY ₃ F ₁₀ :YF ₃	145
A.Standard Measure.....	145
B.Using another microscope magnification	146
References.....	147

Table of notations
Abbreviations

ETL	Electron Transport Layer
HTL	Hole Transport Layer
FTO	Fluoride Tin Oxide
ITO	Indium Tin Oxide
HOMO	Highest Occupied Molecular Orbital
LUMO	Lowest Unoccupied Molecular Orbital
UCNPs	UpConversion NanoParticles
NP	NanoParticle
ESA	Excited State Absorption
GSA	Ground State Absorption
SPE	Spontaneous Emission
MPR	MultiPhonon Relaxation
STE	Stimulated Emission
CR	Cross Relaxation
APTE	Addition de Photon par Transfert d'Énergie
ET	Energy Transfer
ETU	Energy Transfer Upconversion
SEM	Scanning Electron Microscope
TEM	Transmission Electron Microscope
PL	PhotoLuminescence
PLQE	PhotoLuminescence Quantum Efficiency
FF	Fill Factor
PCE	PhotoConversion Efficiency
Jsc	Short Circuit Current
Voc	Open Circuit Voltage
FDTD	Finite Difference Time Domain
TiO ₂	Titanium Dioxide
DSSC	Dye Sensitized Solar Cell
NP	NanoParticle
NS	Nanosphere
CIGS	Copper Indium Gallium Selenide (or sulfur)
GaAs	Gallium Arsenide
Si	Silicium
CdS	Cadmium Sulfide
CZTSSe	Copper Zinc Tin Sulfide Selenide
CIS	Copper Indium Selenide (or sulfide)
InP	Indium Phosphide
CdTe	Cadmium Telluride
Al ₂ O ₃	Aluminium oxide
MA	MethylAmmonium –CH ₃ NH ₂ –
PML	Perfect Matched Layer

AM	Air Mass
eV	electronVolt
LSPR	Localized Surface Plasmon Resonance
DS	DownShifting
MPPT	Maximum Power Point Tracking
SERS	Surface Enhanced Raman Spectroscopy
IPA	Isopropranol
TTIP	Titanium Isopropoxide
rpm	round per minute
FAI	Formamidinium iodide $\text{HC}(\text{NH}_2)_2\text{I}$
MAI	Methylamonium iodide $\text{CH}_3\text{NH}_2\text{I}$
DMF	N,N-dimethylformamide
DCB	dichlorobenzene
CBZ	chlorobenzene
TBP	4,tert-butylpyridine
Li-TFSI	Lithium bis(trifluoromethanesulfonyl)imide
DMSO	Diméthylsulfoxide
THF	Tetrahydrofuran
AR	Aspect Ratio

Constants

k_b	boltzmann constant
h	Planck constant
c	light's speed
e	charge of an electron

Notations

T	temperature
n	Volumic density of electrons
p	Volumic density of holes
J_x	Current density
\vec{a}	Acceleration
$\vec{\delta}$	Displacement
\vec{E}	Electric Field
\vec{D}	Electric Induction
\vec{H}	Magnetic Field
L_x	Diffusion length of "x"
μ_x	mobility of specie "x"
α	Polarizability
ρ	Charge Density
σ	Conductivity
σ_x	Absorption cross section of "x"

ϵ_x	Permittivity of material "x"
χ	Susceptibility
$\vec{\mu}$	Electric dipole momentum
P	Volumic polarization
ϕ_x	Potential "x"
E_x	Value of the energy of level "x"
E_g	Energy of the bandgap
λ	Wavelength
ω	Pulsation
ω_p	Plasma frequency
R_s	Serie Resistance
R_{SH}	Shunt Resistance
V	Potential
I	Current
H_x	Hamiltonian of interaction "x"
τ_x	Lifetime of "x"
k_x	transition rate of process "x"
g_x	Degeneracy of level "x"
Γ_x	Decay rates for "x"
$u(\omega)$	Spectral Photon Energy Density
A_{if}	Einstein coefficient for transition i --> f
n_x	Population of level "x"
N_x	Volumic concentration of carrier "x"
ρ_p	Pump Constant
P_p	Incident Pump Power
m	conduction electron mass
γ	Constant of a material defining probability of shocks
η	Quantum Efficiency
μ	Permabillity
\bar{x}	Average of value x
Σ	Standard deviation

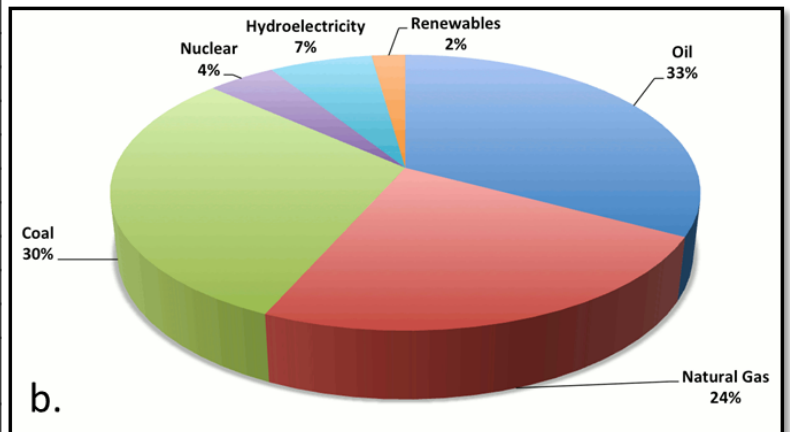
Introduction

Society and renewable energy

In 2016 the 21st COP was held in Paris. This international climate summit had a main objective to define some concrete measures to restrict the increase of the world's temperature under +2°C. One of them is to stop by 2050 our fossil fuel consumption [1]. Following a UN report, the world population will then be around 9.7 billions inhabitants[2]. This increase of population mainly concerns lower social classes whose energy consumption is under the average [5], who will mostly be living in cities by 2050 (world urbanisation rate will then reach 70% [3]). The optimisation of energy consumption and distribution is easier to implement in cities, since network energies benefit from the density of urban zones, where transport is also more optimized and less energy-consuming. However this is not yet the case of the main cities mostly touched by this rural exodus, for which these criteria are not a priority.

It is thus necessary to play on the energy performance as well as on energy saving, one being related to technology and science, the other being more turned towards citizen's habits and political decisions.

Sector	Emissions (g equiv. CO ₂ /kWh)
Nuclear power	4
Hydraulic (run of river)	6
Hydraulic (restrained)	6
Wind Turbine	14
Solar (Si)	30-45
Hydraulic (pumped-up)	137
Fuel	1 119
Diesels	885
Coal 600 MW (desulphurization included)	1 022
Coal 250 MW (desulphurization not included)	1 065
Combustion turbine (gaz)	1 103
Combined cycle Gas	499



a.

Figure 1 (a) Table listing the quantity of produced CO₂ per kWh for different energy production sectors [6, 8] (b) World energy mix in 2014 [15]

Fossil fuel combustion is the main greenhouse gases (GHG) production source, as we can see if we look simultaneously to [Figure 1.a.](#), which gives the weight of CO₂ produced per kWh for different energy production sources, and [b.](#), which shows the world energy mix in 2014. If we want to reduce GHG emission, it's crucial to modify the energy mix toward decarbonized energy sources.

The controversial report of ADEME (Agence de l'Environnement et de la Maitrise de l'Energie, french public organism in charge of environmental public policies) published in june 2016 addresses the possibility of a 100% renewable energy mix in France by 2050.

One of the main issue regarding renewable energies is their intermittence. Demand's fluctuation is around 15% of mean power. They are essentially treated by hydroelectricity (in Pumped

Hydroelectric Energy Storage or PHES, in which energy produced by other power plants might be stored under the form of potential energy). Photovoltaic or wind energies are intermittent energy sources, since their production varies along a day following meteorological parameters. Increasing the renewable energy part of the energy mix would imply a step of rescaling energy storage. Li-ion battery cannot be alone the solution to this problem, since we would need 10 times all the batteries already existing in the world to store 1% of the energy consumed in one year in France [7].

Climate challenges are numerous. Controlling our energy consumption and our GHS emission have become a necessity.

Solar panels and industry

Photovoltaic device, as well as solar thermal and photochemical energy converters, use solar energy to produce another type of energy : electrical power.

There are several different types of commercialized solar panels, which are shown in the organigram presented in Figure 2.

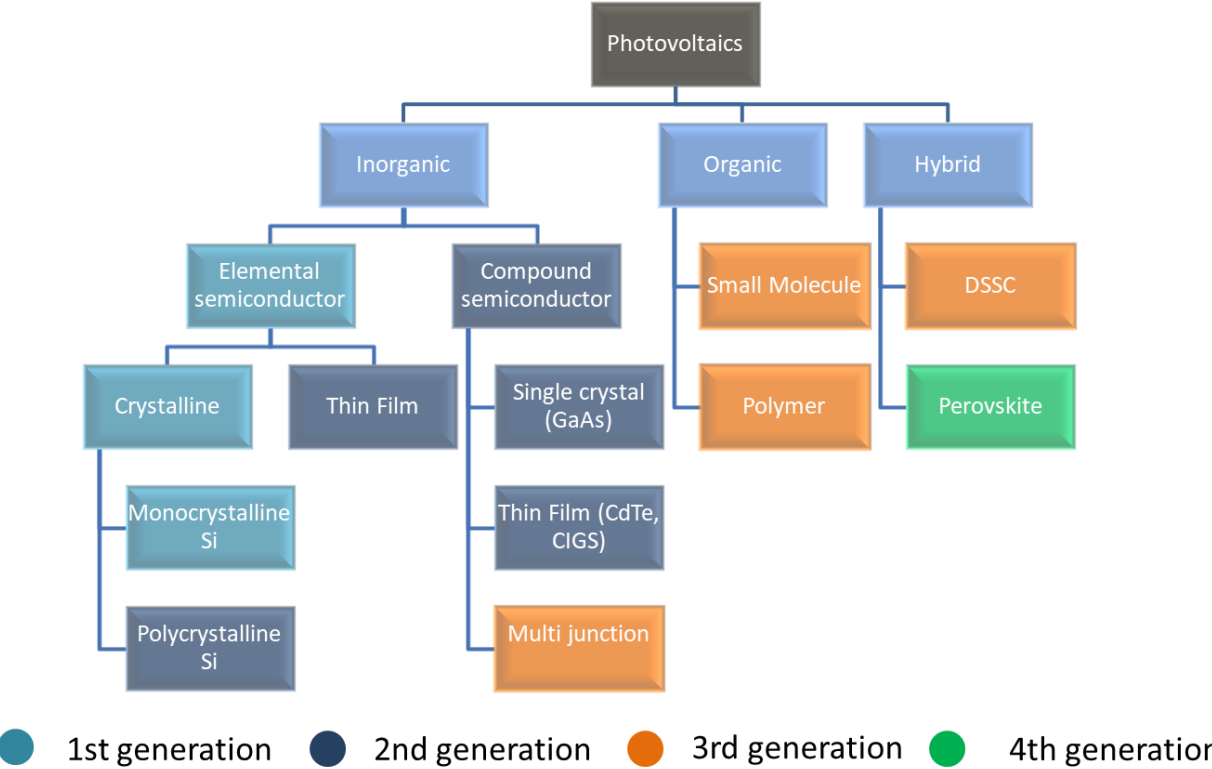


Figure 2 Organigram featuring different solar cell technologies.

Most of commercialized solar panels are silicon-based. There are mainly three types of silicon solar cells: amorphous silicon (not represented on Figure 2), monocrystalline and polycrystalline.

Monocrystalline silicon solar cells have a higher efficiency than polycrystalline ones (25.6% against 20.8% for laboratory results in 2016 [9]), their main drawback compared to thin film technologies is that they require a lot of material. The absorber layer’s thickness is between 160 and 190 μm, against 3μm for the two others. Although silicon is the most abundant element of the earth’s crust after

oxygen, processes to produce highly pure silicon for energy generation require a lot of energy, as we can see on [Figure 1](#). The cost in g(CO₂)/KWh for CdTe (cadmium telluride) or CIGS (copper indium gallium selenide) based technologies is two times smaller than for silicon [8]. However, cadmium toxicity on one hand, and scarcity of indium and telluride on the other hand, represent a major drawback to these two technologies [10]: the economical factor cannot be the only one that comes into consideration.

The different efficiencies of these technologies are compared on [Figure 3](#).

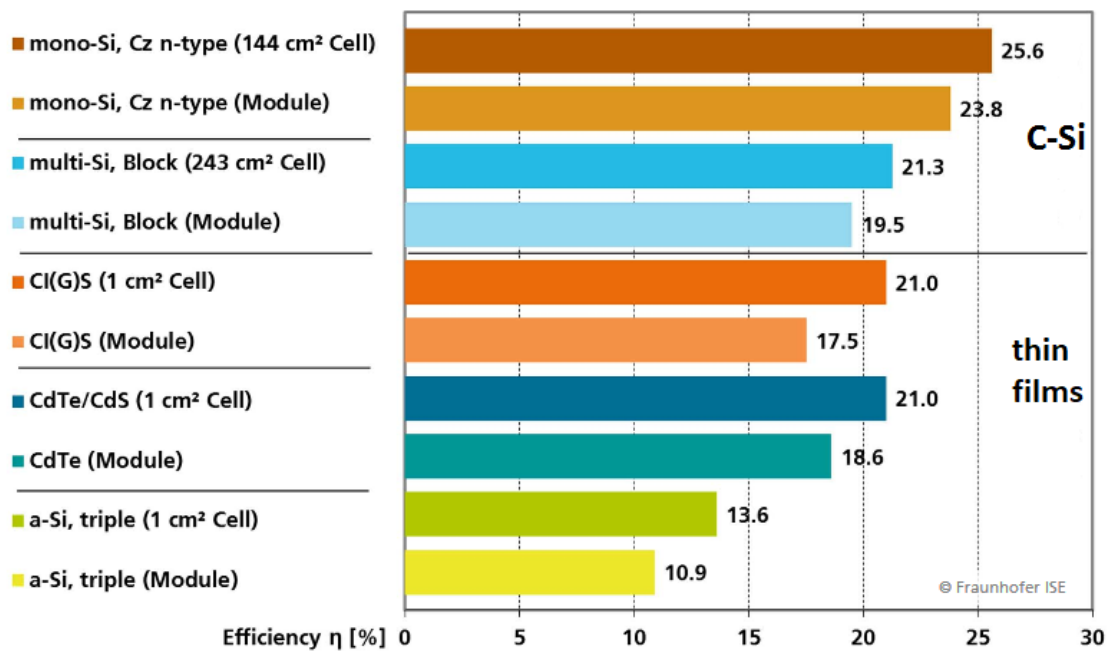


Figure 3. Efficiencies comparison between thin films and crystalline silicon solar cells (c-Si) [9]

In a word, an abundant material, appropriate to thin films technologies, was ready to enter the scientific world.

The birth of perovskite as a solar converter

Perovskite is above all a crystallographic structure of formula ABX₃. It was first designating the mineral CaTiO₃ found in mount Oural by the german mineralogist Gustav Rose described in 1839, and named after a Russian mineralogist, Lew A. Perovski. There exists many different types of perovskite, such as CaTiO₃, MgSiO₃, SrFeO₃, BaTiO₃, LiNbO₃, SrZrO₃, and KMgF₃, each of them possessing different phases, with very specific optical and electrical behavior.

In the world of solar energy, it appears in the late 00's [11]. Efficiencies of perovskite based photovoltaic devices rapidly increased, and their fabrication process are the origins of the fast escalation and fascination it had exerted over the past few years on the research world of solar cells, ([Figure 4](#)).

Organometal halide perovskite solar cells, further called perovskite solar cells, belong to the category of solution processable solar cells, which means all the layers they are composed of can be deposited using the technique of spin-coating (apart from top electrode). This technique is simple and relies on the use of a spin-coater, which is user-friendly, easy to handle and to store, adaptable to large scale

low-cost fabrication (e.g. roll-to-roll print). This is a major difference by comparison with Si, GaAs, CdTe or CIGS, which often require complex high vacuum deposition equipment that are heavy to handle and necessitate constraining manipulation conditions (clean room).

Best Research-Cell Efficiencies

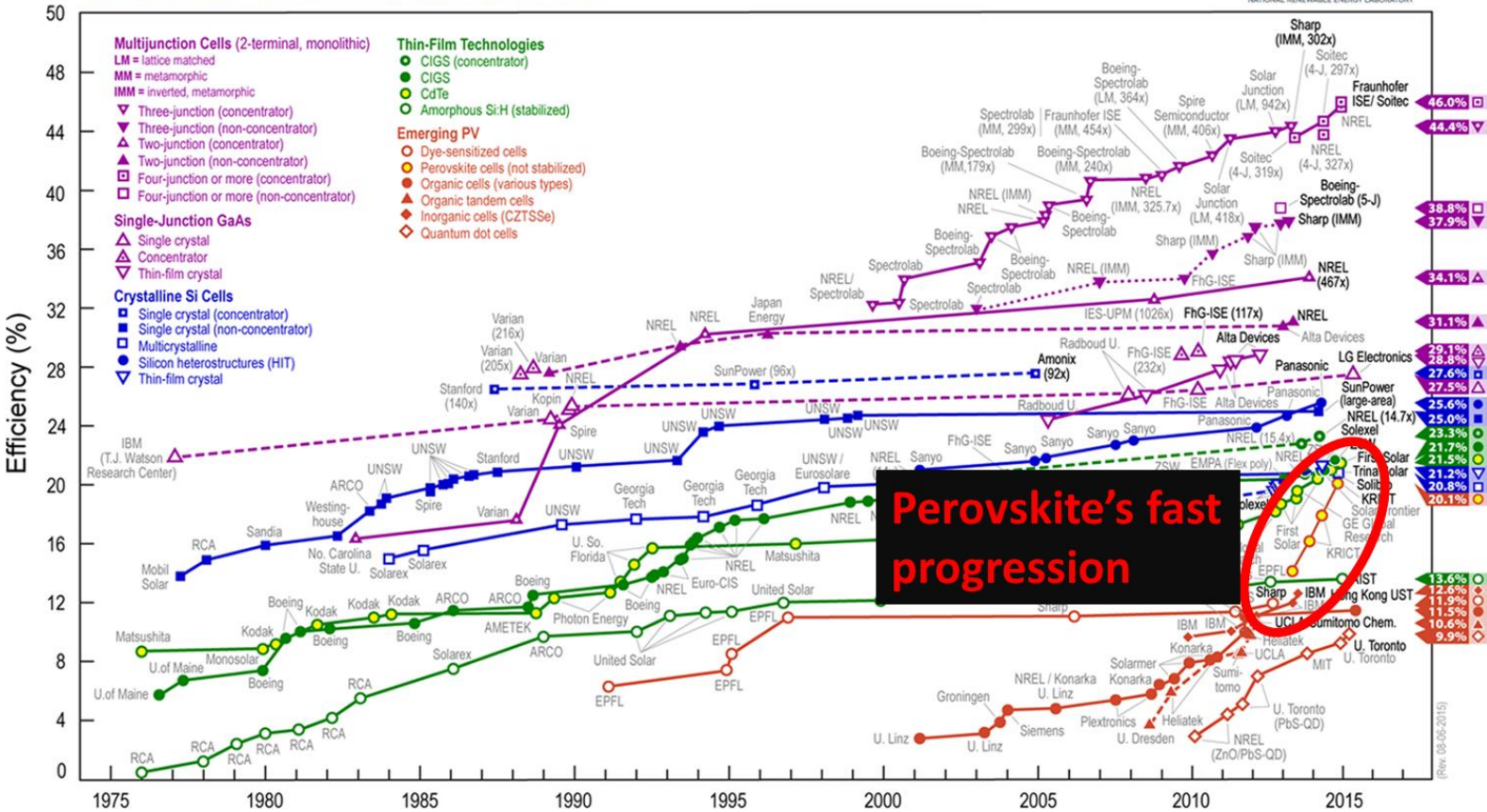


Figure 4. Evolution of maximal efficiencies obtained for different solar cell technologies between 1975 and 2015. We can notice the recent and fast evolution that characterize perovskite technology since it entered the solar energy world [12]

However, there are still some obstacles before perovskite can be widely used in solar panels. Perovskite is an optically active material which belongs to semiconductors. This means that they have a forbidden energy bandgap separating the conduction band from the valence band. Electrons in the valence band can hop to the conduction band after being excited by a photon. This mechanism, which will be later further explained, is the one involved in photocurrent generation, ie charge generation by light absorption. The condition that the absorbed photon's energy has to satisfy is:

$$\lambda < \frac{h \cdot c}{E_g}$$

where E_g is the bandgap energy in eV, h is Planck constant in eV.s, c the light speed in m/s and λ the incident photon wavelength in m^{-1} .

This means that photons whose wavelength does not satisfy this condition cannot be absorbed. The gap being around 1.5 eV indicates that photons whose wavelength is longer than 800 nm cannot be absorbed. Furthermore, photons whose energy is above the bandgap, like UV photons, are absorbed but one part of their energy is lost by thermalization which is a non-radiative relaxation from higher energy levels to lower ones: in a word, the solar spectrum (Figure 5) is not exploited at its maximum capacity.

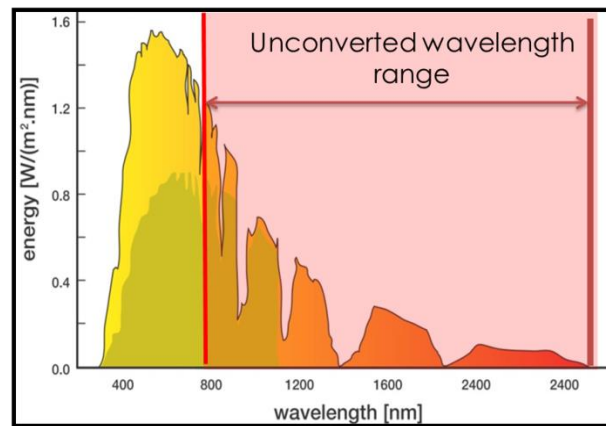


Figure 5. Solar Spectrum AM1.5 (corresponds to the spectrum measured at sea level). [13]

There are several strategies to harvest photons with an energy smaller than the bandgap. Tandem solar cells for instance consist of stacking different absorbers with different bandgaps, as simply described by Figure 6. Each material will let photons with a lower energy go through, and each layer converts the fraction of light that had not been converted by previous layers. This is a way to optimize total absorption.

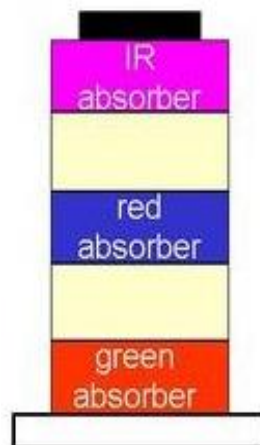


Figure 6. Simple scheme of a tandem solar cell. Light comes from the bottom side of this scheme. [16]

The method we have decided to investigate in this work relies on the use of another optical cleverness called upconversion. The absorption of two photons in the near infra-red (NIR) spectrum results in the emission of a photon of a higher energy. With this method, we can convert a part of NIR to which perovskite solar cells were transparent so far.

This original property of UpConversion NanoParticles (UCNPs) is due to rare earth doping, most of the time erbium and ytterbium Er^{3+} and Yb^{3+} .

This effect is relatively inefficient (around 3% of the incoming photons, which are themselves from a narrow 100 nm-wide band, will be converted). Nevertheless, it can be enhanced thanks to plasmonic effect, which is the enhancement of local electromagnetic field around metallic nanostructures. By combining both types of particles, UCNPs one side with for instance plasmonic gold nanorods (Au NRs) on the other side, one can improve the upconversion absorption and/or emission, and the overall absorption of the solar cell in the NIR, thus aiming a higher photovoltaic efficiency.

In this work, we will describe the theoretical aspects of those phenomena (photocurrent generation, solar cells limitations, upconversion and plasmonic effect followed by plasmonic enhanced upconversion) before discussing the experimental methods we have followed, for solar cell fabrications as well as UCNPs and gold NRs synthesis and characterizations. The third part will address the implementation of UCNPs in perovskite devices, and the electrical and optical modifications that result, as well as the preliminary studies including gold NRs in such devices.

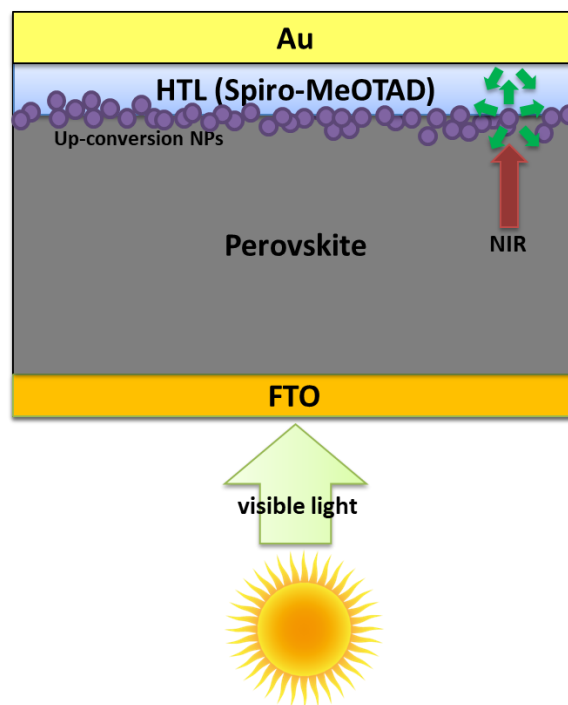


Figure 7. Scheme of a UCNP implemented perovskite solar cell

References

- [1] <https://blogs.mediapart.fr/jacques-treiner/blog/240215/climat-lobjectif-des-2-c-de-rechauffement-appartient-helas-au-passe>
- [2] <http://www.un.org/en/development/desa/news/population/2015-report.html>
- [3] <https://www.monde-diplomatique.fr/2010/04/GOLUB/19008>
- [4] Mix électrique 100% renouvelable ? Analyses et optimisations. ADEME, Artelys, Armines-Persee, Energies demain [5] <http://donnees.banquemondiale.org/indicateur/EG.USE.ELEC.KH.PC>
- [6] <http://www.connaissancedesenergies.org/fiche-pedagogique/cop21-conference-sur-le-climat-de-paris#notes>
- [7] <https://blogs.mediapart.fr/jacques-treiner/blog/060517/un-kwh-aleatoire-ne-remplace-pas-un-kwh-garanti>
- [8] Emissions from photovoltaic life cycles, V. M. Ethenakis, H. C. Kim, E. Alsema, Environ. Sci. Technol. 2008, 42, 2168-2174
- [9] Photovoltaics report – Fraunhofer Institute for Solar Energy Systems
- [10] Implications for CdTe and CIGS technologies production costs of indium and tellurium scarcity, C. Candelise, M. Winksel, R. Gross, Progress in Photovoltaics Research and Application, Sept 2012
- [11] Organometal halide perovskites as visible-light sensitizers for photovoltaic cells, A. Kojima, K. Teshima, Y. Shirai, T. Miyasaka, J. Am. Chem. Soc. 2009, 131, p 6050-6051
- [12] NREL, , “National Center for Photovoltaics,” <http://www.nrel.gov/ncpv/> (22 August 2015).
- [13] Downconversion for solar cells with lanthanide ion couples, thèse de Linda Aarts, Université d’Utrecht, 2009
- [14] Detailed balance limit of the efficiency of tandem solar cells, Alexis De Vos, J. Phys. D: Appl. Phys., 13 (1980) 839-46
- [15] BP Statistical review of the world energy, june 2014
- [16] https://www.iapp.de/iapp/agruppen/osol/?Research:Organic_Solar_Cells:Tandem_Cells

Chapter 1. Theoretical background and fundamental principles of solar energy generation, upconversion, plasmonic effect and plasmonic enhanced upconversion

I. Perovskite solar cell : presentation and theoretical analysis

1. General functioning of a solar cell

A solar cell produces electricity from an incoming radiation. Photons are converted into charges inside the photovoltaic device. Harvested charges create the electrical current that is generated. There are different types of solar cells, that were described in the introduction, and we will now mainly focus on thin films solution processable hybrid organic inorganic halide perovskite solar cells. A typical perovskite solar cell is a stacking of several thin layers, as shown on [Figure 8](#). Most of them are spun using a spin-coater. Here is a list of those layers, in the order of progression of the light:

- Fluoride Tin Oxide (FTO) layer. This is a transparent conductive oxide which is the electrode at which electrons will be collected. Sometimes it can be replaced by ITO (Iodide Tin Oxide). Glass substrates are purchased already coated.
- Electron Transport Layer (ETL). Usually made of compact TiO_2 , but can be replaced by SnO_2 . This layer is a matching layer: its LUMO (Lowest Unoccupied Molecular Orbital) is equal or slightly lower than the one of the absorber in order to attract electrons.
- Perovskite material, the absorber. It's the layer in which photons are absorbed and charges created. The formula is ABX_3 where $\text{A} = \text{CH}_3\text{NH}_3$, called MA (for methylammonium), $\text{HC}(\text{NH}_2)_2$, called FA (for formamidinium), or Cs, $\text{B} = \text{Sn}$, Pb and $\text{X} = \text{I}$, Cl , Br . In this work, we investigated $\text{CH}_3\text{NH}_3\text{PbI}_3$, $\text{CH}_3\text{NH}_3\text{PbI}_{3-x}\text{Cl}_x$ and $\text{FA}_{0.83}\text{Cs}_{0.17}\text{Pb}(\text{I}_{0.6}\text{Br}_{0.4})_3$.
- Hole Transport Layer (HTL). It is also a matching layer, whose HOMO (Highest Occupied Molecular Orbital) is equal or slightly higher than the one of the absorber in order to attract holes. It's usually a polymer, like poly-TPD (Poly(N,N'-bis-4-butylphenyl-N,N'-bisphenyl)benzidine), PTAA (poly (triaryl amine)), P3HT (Poly(3-hexylthiophene-2,5-diyl)) or spiro-OMeTAD (2,2',7,7'-Tetrakis-(N,N-di-4-methoxyphenylamino)-9,9'-spirobiuorene), which have been investigated in this work.
- Gold. It is the top electrode at which holes are collected.

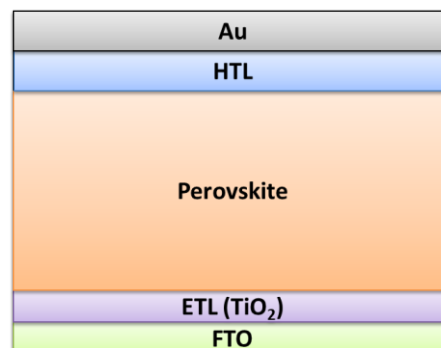


Figure 8. Simple scheme of a perovskite solar cell. Light comes from the bottom of the cell.

Current creation due to incoming radiation absorption follows these steps, which are represented in [Figure 9](#).

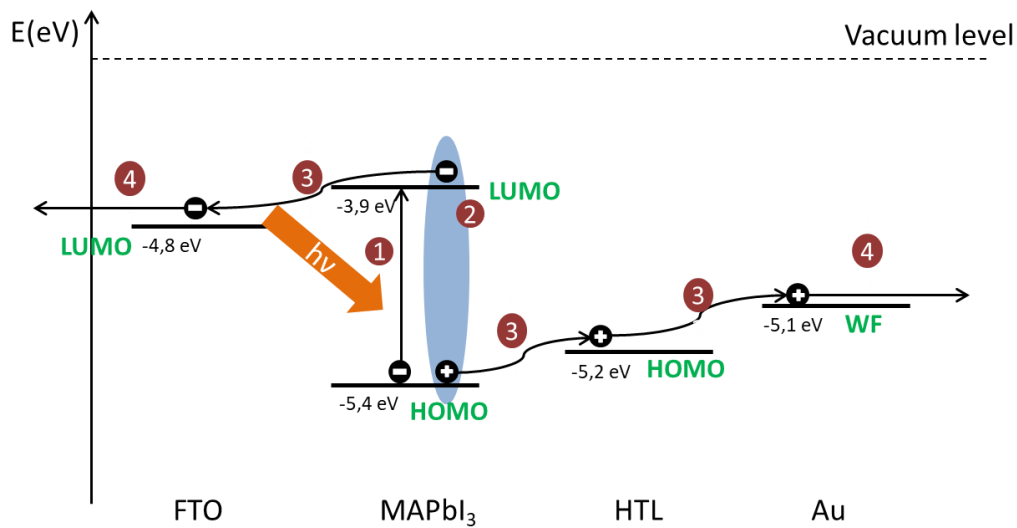


Figure 9. Electronic levels of the different layers in a perovskite solar cell and mechanism of current generation in 4 main steps for a ETL-free MAPbI₃ device (Inspired by Ref [1]). WF stands for working function.

- 1: Hole and electron generations, through the absorption of a photon by perovskite. In silicon solar cells, electron and hole are bound and we rather talk about exciton generation, but in the case of perovskite solar cells, exciton binding energy is only around a couple of milielectronvolts, which is under thermal energy ($kT=25\text{meV}$ at room temperature).
- 2: This implies the direct generation of free charges.[2] The hole is in the absorber's HOMO and the electron in the absorber's LUMO.
- Perovskite has a direct gap, which means that the maximum energy of the valence band occurs at the same wavevector than the minimum of the conduction band, which implies that no extra phonon is required for the excitation of an electron in order to conserve total wave vector. This is not the case for amorphous silicon solar cell which does not have a well-defined E-k relationship.
- 3: Diffusion of charges through perovskite and to the electrodes, electron to FTO and holes to gold. Perovskite is in particular advantageous on that specific point: diffusion lengths are around $1.9\ \mu\text{m}$ for electrons and $1.5\ \mu\text{m}$ for holes, which is 10 times longer than for a-Si.[3]
- 4: Charge extraction: charges are extracted and contribute to current generation.

There are many obstacles to a smooth proceeding of this steps, such as radiative or non radiative charges recombination (instead of diffusing apart from each other, hole and electron recombined, either by emitting a photon or a phonon), Auger recombination (energy of the electron transferred to another electron in the conduction band), or Shockley-Read-Hall recombination: charges are trapped by deep-level traps created by an impurity in the lattice. General losses be further addressed.

The main reason why charges actually diffuse is driven by electronic level matching, as we can see on [Figure 9](#). Once excited on a certain level, an electron is more likely to reach a layer whose LUMO is slightly under the position of the excited level it's in. On the other hand, a hole is more likely to reach a layer whose HOMO is slightly over its current position. These conditions narrow the number of

materials you can use, for a given absorber. Each time a new type of absorber is tried out, the HTL and ETL may have to be changed in order for them to fill out this condition.

2. Description of theoretical p-n junction model and electrical parametrization of the device

a. Current-potential equation obtained from p-n junction model

A solar cell in the dark is often described like an ideal diode, which is itself modeled by a p-n junction. This type of junction consists in a interface between two regions of the same semiconductor with a different doping, p- and n-. A p- or n- doped semiconductor is an intrinsic semiconductor to which have been added atoms with respectively a lower and higher atomic number, which are called respectively acceptors or donors (of electrons).

However, perovskite solar cells with a ETL and HTL behave more like a p-i-n junctions: a p-i-n junction is composed of an intrinsic semiconductor between to n- and p-doped semiconductor. The main advantage of the p-i-n junction is that diffusion length of carriers generated in the *i* region is longer than in doped material [4]. In our case, perovskite material represents the *i* region. (In particular cases, it can also be n- or p- doped depending on its stoichiometry [5][6]). Perovskite contacts on both sides with p- and n- doped semiconductors with different work functions [3], in our case HTL and TiO₂ respectively. [Figure 10](#) displays the schematic band diagram for a p-n and a p-i-n junction.

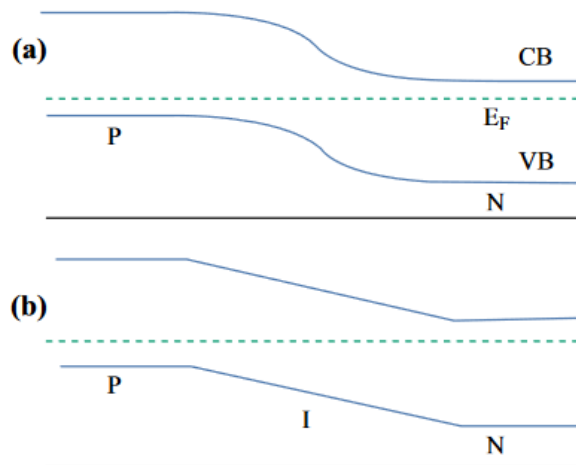


Figure 10. Band diagram comparison between a (a) p-n junction and a (b) p-i-n junction. [7]

For simplicity, we will describe the current-voltage equations under the framework of a p-n junction. The equations generally hold for p-i-n junctions[8]. The model is developed in Annex 1.

A solar cell under illumination is modeled like a solar cell under dark (diode) with a generator in parallel, which generates the photocurrent, as we can see on [Figure 12](#), which represents the intensity-potential typical characteristic of a perovskite solar cell. So the current can be expressed as the subtraction between the dark current, whose expression is given by Equation 2, to the photocurrent generated by light absorption. The equations giving the current density of an ideal diode modeled as a p-n junction as a function of applied bias are thus given by Equation 1 and 2:

$$J = J_{dark}(V) - J_{sc} \quad 1$$

with

$$J_{dark} = J_0(e^{qV/k_bT} - 1)$$

2

Where

- J_0 is a constant in, mA/cm²,
- J_{sc} the short circuit current density, in mA/cm²,
- q the charge of an electron, in C,
- V the applied bias, in V,
- k_b the Boltzman constant, in J/K and
- T the temperature in K.

Measured current is conventionally negative when the mass is connected to the anode (FTO, electron collector), and the bias is hold on the cathode which is the gold electrode. As the bias varies, the current follows the law described above. A typical I-V curve under illumination as shown on [Figure 11](#) is then obtained.

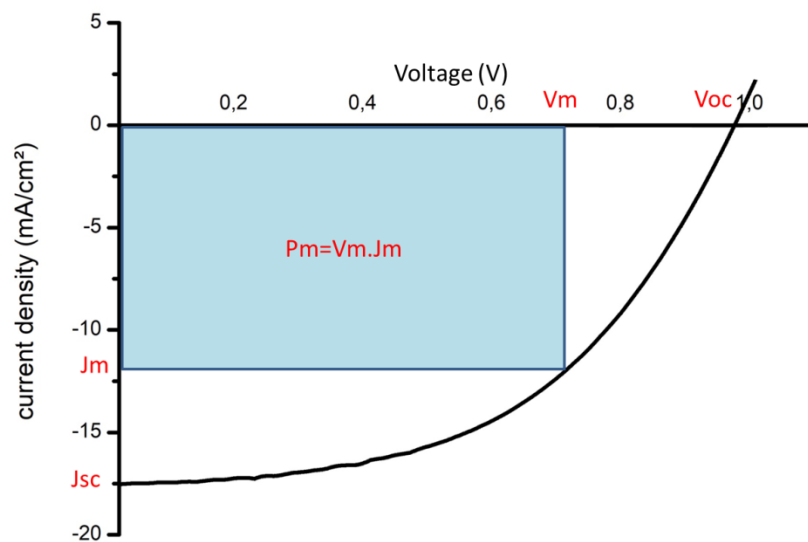


Figure 11: Typical I-V curve obtained in this work for a perovskite solar cell.

b. Description of J_{sc} , V_{oc} , FF and PCE

Four parameters are used to describe the functioning of a solar cell, and they're all represented on [Figure 11](#), which is a typical I-V curve obtained in this work.

- J_{sc} . Short circuit current, in mA/cm². It is the current measured for a voltage equal to zero.
- V_{oc} . Open circuit voltage, in V. It corresponds to the voltage at which the current is equal to zero.
- PCE. Power Conversion Efficiency, in %. It's the maximal value of the product of $J \times V$, also called P_{max} normalized by the incident light intensity.
- FF. Fill factor, in %. It's the ratio $\frac{P_{max}}{J_{sc} \cdot V_{oc}}$. It qualitatively represents how far the curve is for the ideal case in which the series resistance, which can be approximated by the inverse of the slope of $\Delta J / \Delta V$ at $V = V_{oc}$, is equal to zero, and in which the shunt resistance, which can be

approximated by the slope of $\Delta J/\Delta V$ at $V=0$, is equal to infinity. Series and shunt resistances are also used in case we model a real solar cell by an electric circuit, as shown in [Figure 12](#).

Those four parameters' values are compared for different experimental conditions and once rigorous statistics are applied, it allows us to conclude whether one condition relatively increases the cell efficiency or not. Their variations also allow giving some hypothesis on the precise effect of the modification of experimental conditions on the solar cell.

c. Equivalent electrical circuit – Non Ideal case

A solar cell can be modeled like an electrical circuit, as shown in [Figure 12](#).

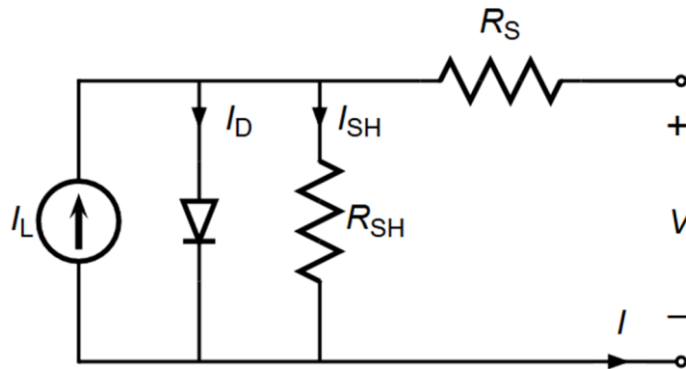


Figure 12 Equivalent electrical circuit of a solar cell [9].

The solar cell is modeled by the combination of a diode in parallel with a generator, that photogenerates current, both in parallel with a shunt resistance R_{SH} and in series with a series resistance R_S . We thus have the total current $I = I_D + I_{SH} - I_L$. The voltage across the diode, V_d is equal to $V + IR_S$ where V is the imposed bias. We also have $I_{SH} = V_d/R_{SH}$, as the Ohm's law says.

Using the diode equation for I_D , and replacing V in Equation 2 by V_d , and using current density instead of current (by dividing by the cell's surface) we obtain below the Equation 3 that gives the real current density obtained taking shunt and series resistances into account. More complex circuits can be used to model a solar cell, but will not be examined in this work.

$$J = J_0 \left(e^{\frac{q(V + JR_S)}{k_b T}} - 1 \right) + \frac{V + JR_S}{R_{SH}} - J_L \quad 3$$

d. International reference solar spectrum

In order for the photovoltaic research community to be able to compare their results, I-V curve have to be measured under standard illumination called AM 1.5G.

AM stands for an air mass, which is used to characterize solar spectrum on the earth's surface, expressed as a ratio relative to the shortest vertical path. Atmosphere is responsible of attenuation of the solar energy intensity, through scattering and absorption, whose influence is proportional to the thickness the solar beam passes through. AM 1.5 corresponds to an intensity at a zenith angle of

48.2°, which is taken as a spectra reference for photovoltaic performance evaluation, and which concerns most of solar installations and industries under temperate latitudes.

The reference solar spectral irradiance AM 1.5 is available on the National Renewable Energy Laboratory. Direct normal terrestrial and extra-terrestrial spectral irradiances taken from this source are plotted Figure 13. We notice the irradiance at 975 nm (max of absorption of the upconversion nanoparticles we use in this work) is around 550 mW.m⁻².nm⁻¹.

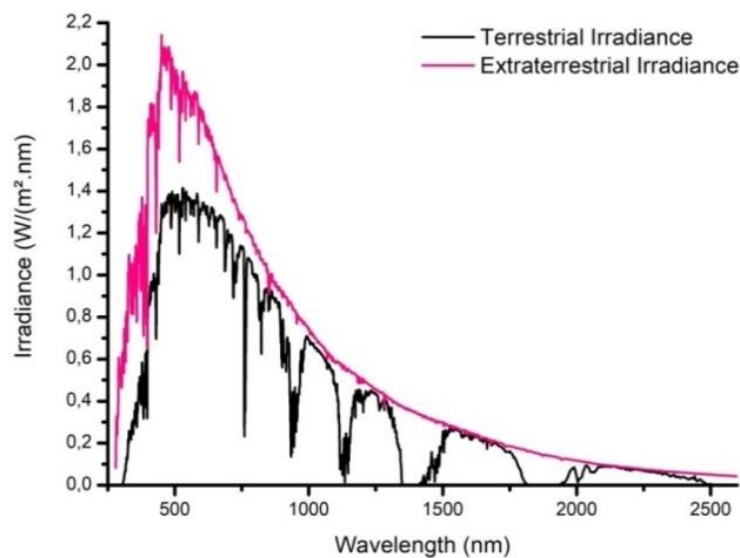


Figure 13. Terrestrial and extra-terrestrial solar Irradiance as a function of wavelength [305]

3.Solar cell efficiency limitations

a.Shockley Queisser limit

Shockley and Queisser established in 1961 a theoretical limit of efficiency of solar cells [10]. They first estimate the ultimate efficiency for any device that includes an absorber. Their hypothesis are the following :

- the efficiency depends on four parameters: the temperature of the sun T_s , the temperature of the cell T_c , the probability that a photon with an energy higher than bandgap produces a hole-pair electron τ_s , and a geometrical factor, f , that takes into account the angle between the solar beam and the solar cell.
- photons with energy higher than the bandgap have the same effect as photons whose energy is equal to the bandgap, and photons with a lower energy won't produce any effect
- each photon whose energy is equal or higher to the bandgap produce one electron-hole pair
- the number of incident photons follow Planck's distribution law, given by Equation 4.

$$B(\lambda) = \frac{2hc^2}{\lambda^5} \frac{1}{\left(e^{\frac{hc}{\lambda k_b T}} - 1\right)} \quad 4$$

Where

- B is the spectral radiance, which is the power per solid angle unit and area normal to propagation unit, in $\text{W}\cdot\text{cm}^{-2}\cdot\text{nm}^{-1}$
- h is Planck constant, in J.s,
- c the speed of light in vacuum, in m/s,
- k_b Boltzmann constant, in J/K,
- λ the wavelength of electromagnetic radiation, in m,
- T the absolute temperature, in K.

With a bandgap of 1.1eV and the sun temperature being 6000°K and the cell's temperature being 0°C, they obtained a maximum efficiency reaching 44%.

In a second time, they took into account real phenomenon such as recombination occurring in solar cells and calculated this time a semi-empirical efficiency limit. An extra hypothesis was that hole-electron pairs are eliminated as rapidly as they are produced.

Four relatively vague processes are taken into account, which have been described in the section I.1.

- generation of hole-electron pairs
- radiative recombination of the pairs
- other non-radiative processes (thermalisation)
- removal of holes from the p-type region and electrons from the n-type region under the form of a current.

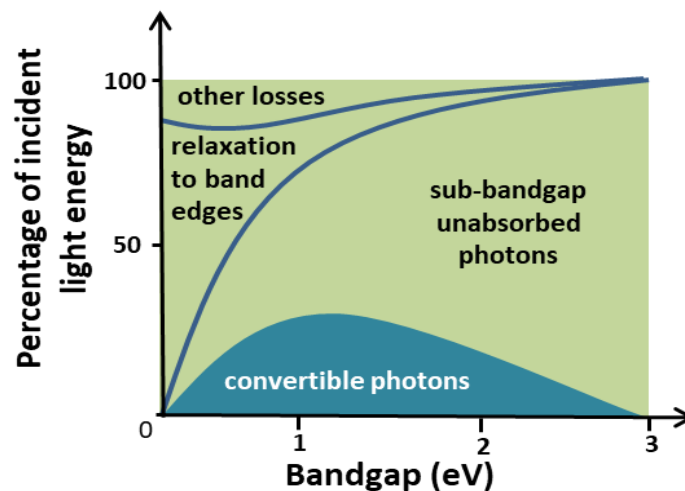


Figure 14 Shockley-Queisser limit scheme: fraction of useful incident light energy in function of semiconductor's bandgap and other phenomenon which prevent higher conversion rates (Inspired by Ref [11]).

The efficiency of the cell was computed as function of bandgap, considering the cell is a blackbody at 300°C, for different values of f (geometrical factor) and t_s . The simplified version of their results is presented in [Figure 14](#).

The maximal percentage of incident light that is actually converted into electricity is relatively small, 33% in the best case for silicon solar cell and it is estimated to be 31.4% for halide perovskite solar cells, both under standard AM 1.5 [12].

b. Losses and recombination

There are several sources of losses:

-For small bandgaps, a big part of incident energy is lost in non-radiative relaxation (a UV-photon might create an electron-hole pair, but most of its energy, in terms of total available electronvolts, will be lost).

-The majority of losses are caused by photons that are not absorbed because their energy is inferior to the bandgap. This is the loss we addressed in this work.

-Recombination is also a source of losses. They can be divided in different categories[4]:

→Radiative recombination, which means spontaneous photon emission through recombination of an electron with a hole;

→Auger recombination, which implies the interaction of a charge carrier with a similar one (electron with electron, hole with hole), resulting in the decay across the band gap in favor of an increase of kinetic energy of the other charge carrier by an amount equal to the band gap. This is a frequent phenomenon in low bandgap materials with high carrier densities, in which interactions between charge carriers are more frequent;

→Relaxation processes, which are due to the imperfections of materials, involve localized trap state and come from impurities or defects in the crystal structure. They are the dominant mechanisms.

Perovskite solar cells are polycrystalline thin films technologies, and the probabilities of recombination are higher than for monocrystalline technologies: dislocations, vacancies, interstitials, extrinsic impurities, mostly concentrated at grain boundaries, are as many possibilities for recombination sites. Impurities are in particular harmful for the device: they introduce new electronic states, and depending on the relative position of those states, they can either act as dopants (for shallow levels close to conduction or valence band), or as traps for either types of carrier (for deep intra bandgap levels). Trapped charges introduce major perturbations in charge carrier flows, electric fields, and overall efficiency of the cells. A maximization of grain sizes and minimization of impurities is thus a constant aim. 12 μm – large $\text{FA}_{0.83}\text{Cs}_{0.17}\text{Pb}(\text{I}_{0.6}\text{Br}_{0.4})_3$ were achieved by our team[13], which is very encouraging for perovskite solar cells based on this material.

c. Optimizing solar cells – How to reduce losses ?

There are several ways to optimize solar cells. The optimal solar cell would combine good light absorption and internal conversion efficiency (at least one photon = one electron-hole pair), and minimal losses due to radiative or non-radiative recombination. This can be obtained by reducing impurities and maximizing grain size (grain boundaries and impurities act as mid-gap states which act as non-radiative recombination centers [14]) and calling on the photon recycling effect (if a photon is produced by recombination, it can be reabsorbed [15]). Thermalisation processes such as charge relaxation to band edges are harder to get rid of for a given material, since they mostly depend on the value of the bandgap. If we consider a given absorber which has already been structurally optimized, we can improve a solar cell by changing the geometry of devices. Optimizing electromagnetic field is the key word.

As a few example, we can cite the use of an anti-reflection coating [16], the use of spherical solar cells [17] or the disposition of solar panels in a V configuration, in order to reuse what has been lost during the first reflection [18]. Some optical spacer such as ZnO or TiO_2 has also been used in order to

localize the maximal intensity of the electromagnetic field intensity inside the absorber layer, for instance in polymer solar cells [19]–[22]. Those optic spacers allow a control of intern interferences by localizing destructive interferences far from active layer.

We can also cite the use of diffraction grids that increase the length of light path inside the active layer [23], or the use of photonic crystals. Photonic crystals are nano-structured materials whose index can be modulated. By tuning the geometrical parameters of the microstructure, light can be trapped in the active layer in a spectral range matching with the absorption of the solar converter.

In this work, we will target spectral losses in perovskite due to its relatively high bandgap.

4. Perovskite material as solar converter

a. The successful story of perovskite solar cells

As said earlier, perovskite material can adopt the generic formula ABX_3 crystallographic structure, shown in Figure 15. In the idealized cubic cell, the A atom sites at body center position $(1/2, 1/2, 1/2)$, B at cube corner position $(0, 0, 0)$ and X at face centered positions $(1/2, 1/2, 0)$, $(1/2, 0, 1/2)$ and $(0, 1/2, 1/2)$. It belongs to the group $Pm3m$ [24]. Orthorhombic and tetragonal phases are the most common non-cubic variants of perovskite.

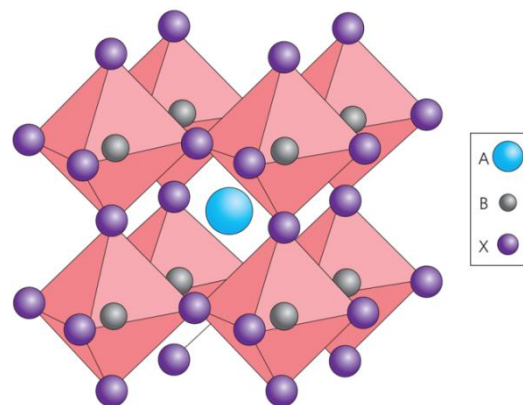


Figure 15 Cristallographic structure of perovskite [45]

Inorganic perovskite materials are naturally present in nature and widely used for different applications due to the diverse range of electronic properties they can adopt: capacitors, piezoelectric, insulator, high melting point, conductor, catalyst, superconductor or colossal magneto resistance, as shown Figure 16. Those properties are mainly resulting from the flexibility of bond angles, due to cation displacements out of the center of the coordination polyhedra, that can lead to tilting of the octahedral [25]–[27].

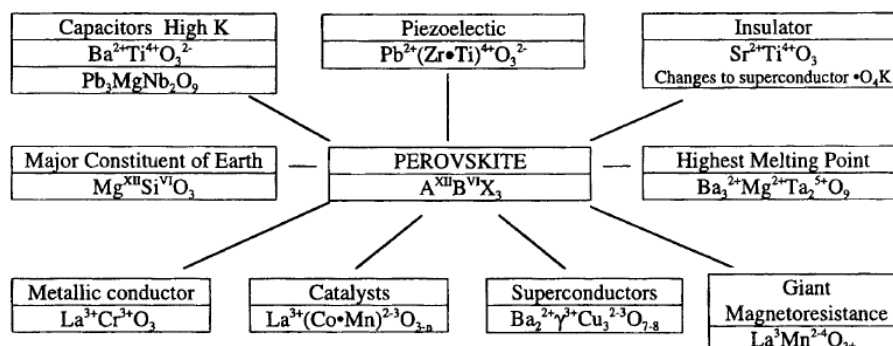


Figure 16. Diagram showing different types of inorganic perovskite materials presenting different properties and applications [24]

The semiconducting properties of perovskite materials have led researchers to use them as light emitters [28][29] or even lasers [30], and as light absorbers. That's how they became widely and quickly used in the world of photovoltaic energies.

Organometal halide perovskites used in photovoltaic technologies feature strong intermolecular hydrogen bonds between the hydrogens atoms of the amino group and the halides, and organic ions are held by weak Van der Waals binding forces (principally in low dimensional perovskites [31]). Any divalent transition metal ions (Cu^{2+} , Ni^{2+} , Co^{2+} , Fe^{2+} , Mn^{2+} , Pd^{2+} , Sn^{2+} , Pb^{2+} , etc) could occupy the B site, but Pb and Sn have been mainly used for their good optoelectronic properties.[32] The A site can be occupied by organic molecules such as methylammonium (MA, CH_3NH_3), formamidinium (FA, $\text{NH}-\text{CH}-\text{NH}_2$) or inorganic Cs or Rb cations, or a mix between those elements. The X site can be occupied by halides, such as Cl^- , I^- , Br^- or a mixture of them. Perovskite solar cells' efficiency climbed from 3.8% in 2009 [33] up to 22.1% in June 2017 [5]. This last result was achieved by tailoring MA, FA (as cations), I and Br ratios and solvent engineering in order to improve electronic properties and decrease concentration of deep-level traps. It featured a 200 nm layer of mesoporous TiO_2 and a 500 nm layer of perovskite and gave a J_{sc} of $25 \text{ mA}\cdot\text{cm}^{-2}$, V_{oc} of 1.1 V, and a FF of 82%, yielding to the maximal PCE so far observed: 22.1%.

Perovskites were also used as absorbers in Dye Sensitized Solar Cells (DSSCs): a PCE over 9% was for instance obtained for a MAPbI_3 DSSC [34]. DSSC are low cost solar cells based on the use of a photo-sensitized anode and an electrolyte.

FA-based perovskite materials are becoming a major avenue of research, because of FA thermal stability and the narrower bandgap of FAPbI_3 compared to the one of MAPbI_3 (and if we look at Shockley Queisser's limit efficiency, it's maximal for relative low bandgaps, around 1.2 eV). However, it exhibits a particular photo-inactive "yellow" phase [35], [36] that was partially solved by using double cation Cs-FA [37], [38] [39], [40]. However, then again, the difference of radius of cations can also result in the presence of a yellow phase at room temperature due to distortions of the lattice [41]. This is why MA-FA achieve so far the best performances: MA being smaller than FA, its addition reduces the effective cationic radius of FA-based perovskites. [41]

In general, optimizing the efficiency goes together with compromises between competing factors. For instance, if the aim is to mix halides or metallic ions (Pb-Sn compounds) in order to increase the bandgap up to 1.7eV, which can be desired for silicon-perovskite tandem solar cell, we find that halide segregation can occur when Br and I are equimolar [42], which increases the number of recombination centers and endangers the long term stability of materials.

A tandem solar cell is a stacking of different absorbers. The order of stacking follows the increasing order of absorbers' bandgaps. In that case, high band-gap materials allow to harvest and convert high energy-photons, whereas silicon with a bandgap of 1.1eV would be in charge of lower energy photons.

b. Reason behind perovskite's success

One of the origins accounting for the high performance of perovskite solar cells lies in its high absorption coefficient, (Figure 17). High absorption implies in particular a reduction of required thickness for an equally efficient charge generation and an improved collection. The absorption is in particular high due to the directness of its bandgap.

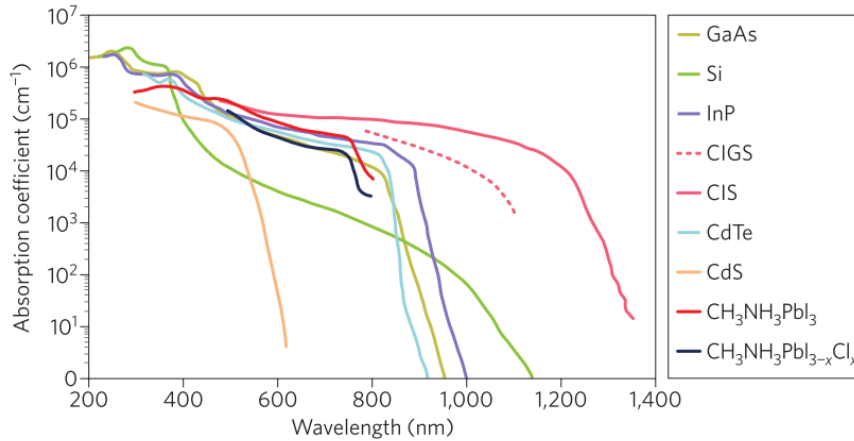


Figure 17. Absorption coefficients for different photovoltaic materials[43]–[45]

Another strength of this material is a relative low loss-in-potential. The loss-in-potential is the difference between the E_g/q and V_{oc} .

The open circuit voltage represents the largest energy difference between any level in the absorber. It is a signature of the density of shallow trap states. The more shallow trap states there are, the smaller will be the potential of extracted charges, since the energy difference between the initial and final state is smaller. If the loss-in-potential is small, it means V_{oc} is close to E_g/q . This is equivalent to saying that the external radiative efficiency, defined as the ratio of recombination events in the radiative emissions, is high [46]. There are fewer non-radiative recombinations such as phonon emission due to relaxation of electrons to shallow trap states. It means if there are recombinations, they're more likely to be radiative.

The loss-in-potential is thus a qualitative measure of non-radiative recombination. Small loss-in-potentials is characteristic of low non-radiative recombination rates. For perovskite, it's closed to 450 meV for the best devices, which is much less than other materials like CdTe, a-Si, CZTSSe (copper zinc tin sulfide selenide), organic photovoltaics, which stagnate between 600 meV, but similar to the one obtained by Si, CIGS, and worse than the one for GaAs (200 meV) [47][45].

This low non-radiative recombination rate require large grain sizes and low grain-boundary activity as well as low density of intragranular defects.[45] We define two types of defects.

Shottky defects, which occur for an equal number of positive and negative vacancies, don't seem to generate defect states having energies within the bandgap. It's rather Frenkel defects, which occur for an equal number of vacancies and interstitials of the same ion, that seem to be effective as non-radiative recombination centers, following Ref [48], such as Pb, I and MA vacancies. Another study [49] gave similar conclusions, precisizing that their formation energies being high, those defects are more likely to form in low concentrations in the case of perovskite, since the material deposition temperature is low compared to most of photovoltaic materials. This explains why high-performance perovskite solar cells with low loss-in-potential can be fabricated following a wide choice of deposition methods and cell structures.

Two other reasons for perovskite's success are the values of photogenerated charge carrier diffusion lengths and carrier lifetime, which are correlated. MAPbI_{3-x}Cl_x features for instance a carrier diffusion length of 1 μ m [50], and decay times of several microseconds have been reported in transient photoluminescence experiments [51], [52]. These values are higher than lifetimes in GaAs (tens of nanoseconds) but lower than in Si (tens of milliseconds) [53].

c. Current limits of perovskite devices

However, when it comes to photovoltaic technology and industry, upscaling, cost per kWh, PCE and long-term stability are four factors on which any candidate has to be competitive.

In the case of perovskite, fabrication process is both an advantage and an inconvenience: spin-coating is a relatively cheap deposition process, but it tends to form non-uniform layers and especially on large surfaces. So work on other deposition methods need to be achieved for up-scaling such as roll-to-roll printing or vapor deposition [41].

We can distinguish extrinsic degradations related to the external factors such as heat, UV light or moisture, from intrinsic degradations.

Environmental conditions such as heat may be related to degradation: On one hand, MA is thermally unstable. On the other hand, spiro-OMeTAD, often used as HTL, crystallizes under thermal stress which allows an interaction between metal electrode and perovskite [48] [49]. By using thermally stable HTL such as polytriarylamine (PTAA), however, encouraging stability results were obtained for mixed cations RbCsMAFA composing the perovskite layer, under nitrogen atmosphere, for 500 hours at 85°C, and the device retained 95% of its initial performance [51].

For devices including an ETL, ultraviolet (UV) light has also been reported to be harmful to the long-term stability, mainly because of TiO₂ degradation that follows the UV absorption of this layer [56]. A way to address this would be using electron contacts with wide bandgaps like BaSnO₃ [57] or SnO₂ [58].

Finally, moisture severely influences stability of organic photovoltaic devices [41][59]. Encapsulation with ethylene-vinyl acetate for a Si-perovskite tandem solar cell [60] showed an improved stability. By adding a downshifting fluoropolymers on top of their device, Bella et al. addressed both of these problematics (UV and moisture) and obtained a stability during 90 days for devices tested on a roof with rain and variable temperatures [61]. Downshifting material also broadens the converted part of solar spectrum by converting high energy photons into smaller energy photons.

Before trying to fight against extrinsic degradation factors, intrinsic degradation factors have first to be addressed.

- Ionic movement quickly leads to slow performance degradation, hysteresis [62] and reversible losses [63][64]. They are attributed to lattice deformation, halide migration within the perovskite as a result of infrared radiation [64]. Ions migration leads to their accumulations at the interfaces which are mostly reversible but can still be an obstacle for long term stability.
- Lithium salt are used as dopant for hole conduction in the spiro-OMeTAD. It has been reported that lithium salts' migration through perovskite layer affect the efficiency of devices [65].

There are indeed various points on which perovskite based photovoltaic devices have to be improved before it can be commercialized and compete with state-of-the-art technologies such as Si or GaAs (which also have their own problems to solve).

When it comes to stability, which is a key point that prevents commercialization so far, both intrinsic and extrinsic degradation must be offset. Experimental protocols (for instance periodical measures instead of continuous maximum power point tracking or MPPT) are also a crucial aspect when it comes to instability's measurement and evaluation. Some outdoor field testings have been translated into accelerated testing procedures that were designed for Si or organic photovoltaic

material and that are now being applied to perovskite solar cells. It's however likely that they should be adapted and revisited, being either too strict or too mild to give a probable estimate.

This work aims improving perovskite solar cells' efficiency by converting infrared photons. By combining the research on different improvable points, perovskite based solar panels could soon be commercialized.

II. Upconversion mechanism

The idea behind photon upconversion is to convert long-wavelength radiations like those from the near infrared (NIR) spectrum into shorter wavelength ones.

Briefly, the absorption of two photons of a lower energy can be followed by the emission of one photon of a higher energy. This photon is simply emitted by the relaxation of an electron on a high energy level that had been reached through successive excitations caused by absorption of lower energy photons.

The existence of the particular optical property exhibited by UpConversion NanoParticles (UCNPs) is a consequence of several parameters including relative positions of the electronic levels of each type of rare-earth ions, which depend themselves on crystal host (that creates the crystal field), and the existence of nonresonance energy transfers [66]. Other parameters such as temperature, ion concentrations or luminescence lifetimes impact the luminescence characteristics.

The use of UCNPs in solar devices is particularly interesting as it allows the conversion of sub-bandgap photons into photons that will be absorbed by the device, thus increasing the performance of the device.

1. Rare earth optical properties – Advantage of coupled ions

Rare earth refers to seventeen chemicals in the periodic table, including the fifteen lanthanides plus yttrium and scandium. They are relatively abundant despite their name. The term "rare" refers to the relative difficulty to separate them from each other and to the fact that they are relatively dispersed [67].

Implemented in fluoride matrixes, rare earth elements exhibit electronic levels which allow upconversion. Rare earths have a partially filled 4f shell, which are shielded by the 5s² and 5p⁶ orbitals from interacting with the ligands. The influence of the host lattice on optical transitions is essential to upconversion process: it's the crystal field that induces a deviation for the symmetry of the orbital configuration, allowing 4f-4f transitions which were forbidden due to Laporte rule because of their symmetry. Upconversion mechanisms as described in the literature involve absorption and non-radiative energy transfers which both rely on those 4f-4f forbidden transitions.

Most of the time, two atoms are required for the upconversion process. One is called the sensitizer, and it's chosen in function of the spectral range to be converted. The other is called the absorber, and it's the atom to which the energy of the sensitizer is twice transferred. Coupled ions upconversion systems such as Er³⁺/Yb³⁺[68]–[72], Pr³⁺/Yb³⁺ [73] Nd³⁺/Yb³⁺ [74] or Tm³⁺/Yb³⁺[75] are widely used. Here are a few criteria the couples have to follow to be good upconversion systems candidates:

- Broad-band absorption and high absorption cross-section in the NIR region for the sensitizer,

- Efficient energy transfer, which either implies high overlapping between the absorption band of the absorber and the emission band of the sensitizer or that the energy transfers are phonon-assisted [66]
- The absorption of the sensitizer at the emission wavelength of the absorber has to be avoided.

These constraints eliminate many possible couples of ions. A degree of liberty can however be found for these requirements to be filled, through the choice of the host matrix, since the crystal field shifts energy levels and the host can be chosen specifically in order to fit those criterion.

Coarsely summarized, upconversion mechanism involves transfer of energy from the sensitizer to the absorber which may be or not in an excited state [76]. In our system, we chose the most common couple $\text{Er}^{3+}/\text{Yb}^{3+}$ in which ytterbium plays the role of the sensitizer which has a relatively narrow absorption around 980nm, which corresponds to the ${}^2\text{F}_{7/2} \rightarrow {}^2\text{F}_{5/2}$ transition, while erbium plays the role of absorber. We also mostly work with potassium fluoride matrixes such as KY_7F_{22} and sodium fluoride matrixes like NaYF_4 . Absorption spectrum of Ytterbium and Erbium is shown on [Figure 18\(b\)](#), and the photoluminescence spectrum on [Figure 18\(a\)](#). We see indeed that the absorption range of Ytterbium does not overlap with the emission.

The absorption of our UCNPs are around 975 nm and the emissions present two peaks, one around 650 nm and the other around 550 nm, corresponding respectively to ${}^4\text{F}_{9/2} \rightarrow {}^4\text{I}_{15/2}$ and ${}^4\text{S}_{3/2} \rightarrow {}^4\text{I}_{15/2}$ (the small peak around 525nm corresponds to ${}^2\text{H}_{11/2} \rightarrow {}^4\text{I}_{15/2}$).

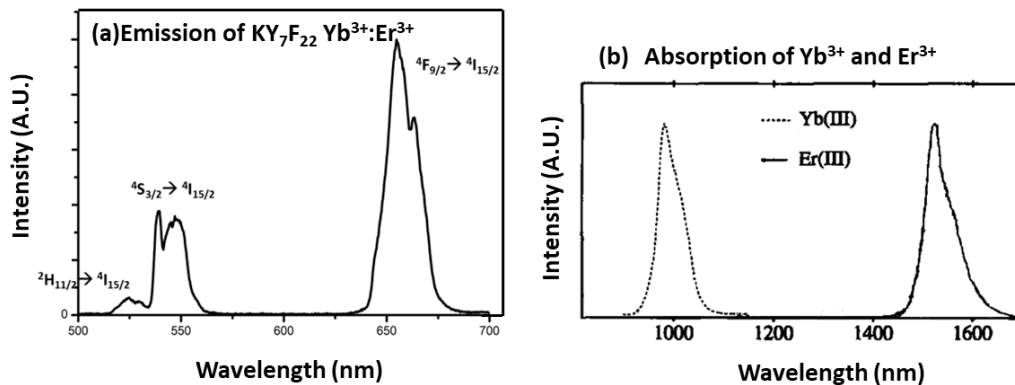


Figure 18. (a) Photoluminescence spectrum obtained for KY_7F_{22} , doped with 5% Er^{3+} and 20% Yb^{3+} under 975 laser excitation. (b) Absorption spectra of Er^{3+} and Yb^{3+} [77].

2. Processes implied in upconversion

There are multiple possible processes implied in upconversion absorption and emission. They are listed below, and most of them are shown in the schematic upconversion mechanism presented by [Figure 21](#). Most of the time, those processes call on the presence of two lanthanide ions, one sensitizer and one absorber.

- GSA (Ground State Absorption) which can be followed by a ETU (Energy Transfer Upconversion) or ESA (Excited State Absorption) [78] [79]. GSA + ETU (formally called APTE for Addition de Photons par Transfert d'Énergie) is the most probable event occurring in Yb/Er system. The simplified scheme of these steps can be found on [Figure 19](#).

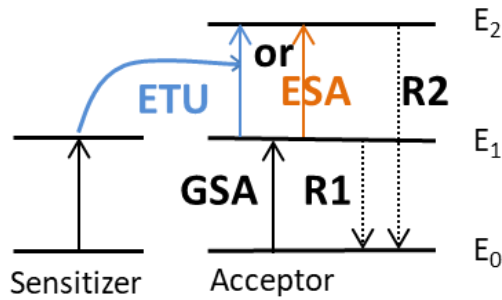


Figure 19. Schematic GSA + ETU process between a sensitizer and an absorber presenting three energy levels E_0 , E_1 and E_2 , which will be successively excited through energy transfer from sensitizer. The dotted lines represent radiative relaxations.

- STE (stimulated emission). It's when the relaxation of an electron to a lower level is provoked by an incoming photon.
- SPE (spontaneous emission). It's when the excited state relaxation is spontaneous. Most of the emissions are spontaneous. There are 4 relaxations that lead to visible emission: from the $^4F_{9/2}$ (emission around 525 nm), $^4S_{3/2}$ (around 550 nm), $^2H_{11/2}$ (around 660 nm) and less intense from $^2H_{9/2}$ (around 410 nm) down to ground level $^4I_{15/2}$ [80]. All the electronic levels are represented [Figure 22](#). Those emissions correspond to the photoluminescence spectrum shown in [Figure 18\(a\)](#), measured on KY_7F_{22} , doped with 5% Er^{3+} and 20% Yb^{3+} under 975 laser illumination.
- MPR (multi-phonon relaxation). Once the excited state is reached, electrons reach lower level by emitting phonons through MPR.
- CR (cross-relaxation). It's the opposite of ETU: the excited state is transferred back down to the sensitizer.

Different upconversion systems in different crystals have different major processes, which have themselves various relative efficiencies. Some of them are schematically drawn on [Figure 20](#) together with their respective quantum efficiencies.

The main reason why most of people use Er^{3+}/Yb^{3+} system is because they have the highest quantum efficiency. However, most of the time, a combination of all those processes exist simultaneously.

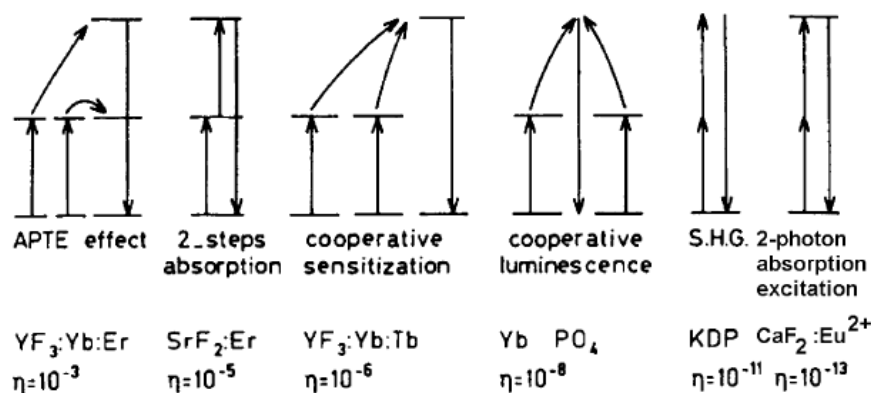


Figure 20. Various two-photon upconversion processes. η represent quantum efficiency in cm^2/W for two photons processes, and more generally in $(cm^2/W)^{n-1}$ for n-photon process and normalized to an incident flux. SHG stands for second harmonic generation.[81]

3.Expression of Probabilities of different processes

We will now give the expressions of SPE, GSA, ESA, STE, and ETU. Theoretical calculations are based on those expressions and give access to theoretical calculation of quantum yield. Another method to obtain it will be exposed in the next part.

a.Spontaneous emission

The probability of spontaneous emission is directly given by Einstein coefficients A_{if} that are based on the theory of photon-atom interaction [82]. It's the inverse of lifetime of the energy level. Einstein coefficients can be calculated using Judd-Ofelt parameters, which are parameters characterizing the strength of the crystal field [83]. This development will not be discussed in this work.

b.Stimulated processes

GSA, ESA and STE are three stimulated processes. The probability of absorption or relaxation W_{if} can be described by [83]

$$W_{if} = \frac{\pi^2 c^3}{\hbar \omega_{if}^3} \frac{g_f}{g_i} u(\omega_{if}) A_{fi} \quad 5$$

Where

- c is the speed of light in m/s,
- \hbar the planck constant divided by 2π , in J.s,
- ω_{if} the angular frequency of transition from level i to level f ($\Delta E = \hbar\omega = hv$ corresponds to the energy difference between level f and level i), in rad.s^{-1} ,
- g_i and g_f are respectively the degeneracies of levels i and f ,
- $u(\omega_{if})$ is the spectral photon energy density, in J/m^2 ,
- A_{fi} is the Einstein coefficient as described above.

c. Energy transfer

Energy transfer is the key point for coupled ions upconverting systems. As shown in [Figure 21](#), there exist different types of energy transfer.

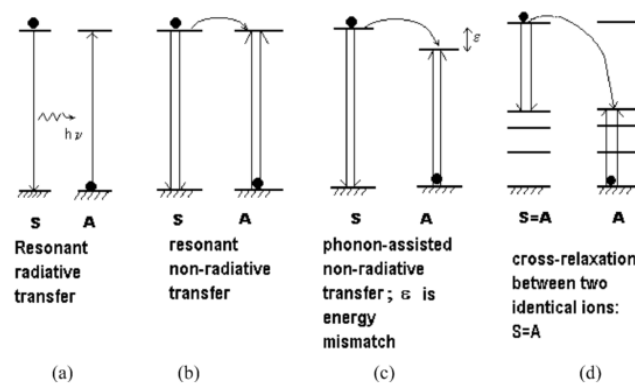


Figure 21. Different energy transfer mechanisms implying a sensitizer S and an absorber A.[81] Energy transfer can be radiative (a), non radiative (b), or multiphonon- assisted (c). Non radiative transfer may also be self-quenched by cross relaxation (d) which is to be avoided for a higher upconversion quantum yield.

The probability per time's unit for a resonant radiative energy transfer as a function of the distance between the sensitizer (S) and absorber (A) R (in m) is found to be [84] :

$$p_{SA,R}(R) = \frac{\sigma_A}{4\pi R^2 \tau_s} \int F_s(\nu) A_A(\nu) d\nu \quad 6$$

Where

- τ_s is sensitizer's excited state's lifetime, in s,
- σ_A the absorption cross section, in m^2 ,
- the integral represents the spectral overlap between A and S (F is the function describing the sensitizer's fluorescence spectrum and A is the function describing the absorber's absorbance spectrum).

In the case of non radiative energy transfer, the excitation jumps from one ion to the other before it's able to emit a photon. Förster, who first addressed this theoretical case using quantum-mechanics, considered dipole-dipole interactions. The probability for such an event $p_{SA,NR,F}$ per time unit is given by Equation 7, that is deduced from Fermi's golden rule [81]

$$p_{SA,NR,F} = \frac{2\pi}{\hbar} |\langle S^*A^0 | H_{SA} | S^0A^* \rangle|^2 \rho_E \quad 7$$

Where

- H_{SA} is the electric dipole-dipole interaction Hamiltonian,
- ρ_E the density of final states, which means the density of states in which sensitizers and absorbers have the same energy, in J,
- \hbar is the Planck constant divided by 2π , in J.s,
- S^* and A^* are the wave function of sensitizer and absorber when excited,
- S^0 and A^0 are the wave function of sensitizer and absorber in a ground state.
- The product S^*A^0 represents the initial state's wave function (in which the sensitizer is excited and the absorber at the ground state) and the product S^0A^* the final state's wave function.

By considering other interactions than dipole-dipole ones, Dexter extended this theory to multipole interactions and deduced that the energy transfer probability per time unit can be written as [85]

$$p_{SA,NR,D} = \frac{1}{\tau_s} \left(\frac{R_0}{R} \right)^s \quad 8$$

Where

- τ_s is sensitizer's excited state's lifetime, in s,
- R the inter-ion distance, in m,
- R_0 the critical transfer distance for which excitation transfer and spontaneous relaxation are equally probable, in m,
- s is an integer which worth 6 for dipole-dipole interaction (Forster's case), 8 for dipole-quadrupole interactions, and 10 for quadrupole-quadrupole interactions.

Probability goes as R^{-2} for the radiative case instead of R^{-6} , R^{-8} , or R^{-10} for the non-radiative case. Many publications [86]–[95] address ET and different expression of this probability can be found. It will not be further developed in this work.

d. Multi phonon relaxation

The probability for multiphonon relaxation W_{MPR} has been empirically found to follow approximately the relation [96], [97]

$$W_{MPR,if} = W_{MPR} e^{-\kappa \Delta E_{if}} \quad 9$$

where W_{MPR} and κ (in eV^{-1}) are material constants which depend on the host material (in particular the energy of a phonon) and ΔE_{if} the energy gap between initial and final states, in eV. The probability of MPR decreases with phonon energy. For low energy phonons, more of them are needed to bridge the same gap.

4. Detailing upconversion process and quantum efficiency

a. Complete description of upconversion process

This calculation is based on a new model developed by Anderson et al. [98] for upconversion in $\beta\text{-NaYF}_4\text{:Yb}^{3+}\text{:Er}^{3+}$ and which is described by interactions between Yb^{3+} and Er^{3+} as pictured in [Figure 22](#). The mechanism is described as follow:

“Green luminescence arises from the ${}^2\text{H}_{11/2}, {}^4\text{S}_{3/2}$ levels via a two photons process with sequential energy transfer wherein the Er^{3+} is excited first from ${}^4\text{I}_{15/2}$ to ${}^4\text{I}_{11/2}$ and, subsequently, from ${}^4\text{I}_{11/2}$ to ${}^4\text{F}_{7/2}$, which relaxes nonradiatively to the thermalized emitting-state manifold, ${}^2\text{H}_{11/2}, {}^4\text{S}_{3/2}$. Red emission arises from ${}^4\text{F}_{9/2}$ after ${}^4\text{S}_{3/2}$ decays nonradiatively to ${}^4\text{F}_{9/2}$ or when ETU promotes Er^{3+} from ${}^4\text{I}_{13/2}$ to ${}^4\text{F}_{9/2}$. The requisite ${}^4\text{I}_{13/2}$ is populated by well-established Er–Er cross relaxation [...] Blue UC emission from ${}^2\text{H}_{9/2}$ has also been observed [99] and attributed to ETU promoting Er^{3+} from ${}^4\text{F}_{9/2}$ up to, or just above, the blue-emitting ${}^2\text{H}_{9/2}$ ”.

It is thus a mix of all the processes mentioned above in II.2. (apart from STE).

We can write the set of equations that rules de population of levels n_x ($x=1-9$) of Erbium and n_y ($y = 1$ or 2) of Ytterbium. The time derivative of a state (\dot{n}_x) is equal to the sum of transition rate constants times the initial state population level. The details of the calculations are available in Annex 2.A. Equations [70-80](#).

All the transition rates were calculated by solving the equations (Annex 2.A) using Euler method and by comparing them to experimentally determined parameters: level populations give access to theoretical luminescence decay curve shapes and relative intensities. So by fitting those curves with curves that were experimentally obtained, the authors were able to obtain an estimation of those parameters. They are given in Annex 2.B.

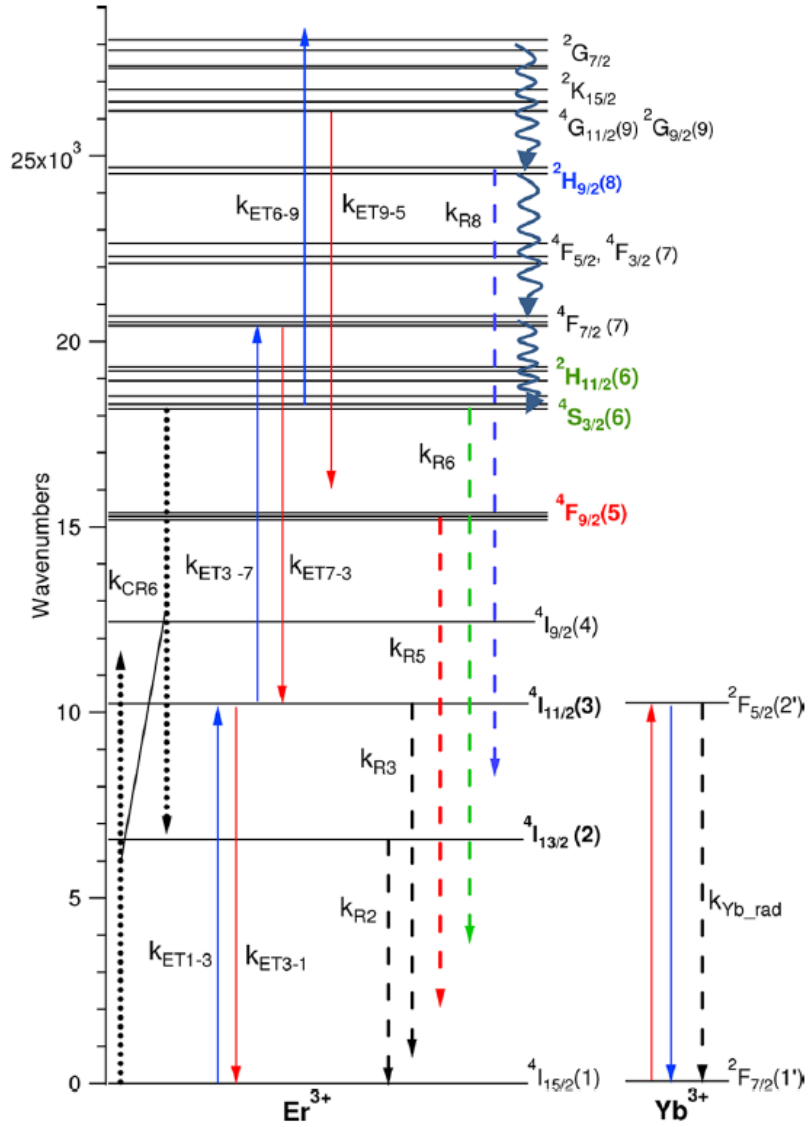


Figure 22. Upconversion mechanism. All the processes mentioned are not represented. Dotted lines correspond to cross relaxations, solid lines to relaxation (in red) or excitation (in blue) following GSA, ESA or ETU, and dashed-lines to radiative relaxations [98]

b. Quantum efficiency

The quantum efficiency or quantum yield (QY) η_i is the ratio of radiated light from level i over incident light. It can also be expressed as the ratio of radiative decay rates that participate to a photon emission detectable in the far field over the sum of radiative and non-radiative decay rates that participate to relaxation from this level [100][98], as expressed below

$$\eta_i = \frac{k_{Ri}}{k_{Ri} + k_{Nri} + \sum_{j \neq i} k_{ETi-j} + k_{CRI-j}} \quad 10$$

In our case, $i=5, 6$ or 8 . We thus have

$$\eta_5 = \frac{k_{R5}}{k_{R5} + k_{NR5} + k_{ET5-8}} \quad 11$$

$$\eta_6 = \frac{k_{R6}}{k_{R6} + k_{NR6} + k_{CR6-1}} \quad 12$$

$$\eta_8 = \frac{k_{R8}}{k_{R8} + k_{NR8}} \quad 13$$

We don't consider emissions from levels 3 and 2 as they are in the NIR.

The total quantum efficiency is the sum of all the quantum efficiencies for each transition:

$$\eta_{tot} = \eta_5 + \eta_6 + \eta_8 \quad 14$$

Using transitions rates found by the theoretical method explained above, a total quantum efficiency around 7%, and around 3 - 4 % for the green emission were found by Anderson et al. [98], which is relatively close to what was experimentally found by Van Veggel [101]. Both results concern Er^{3+} and Yb^{3+} doped $NaYF_4$.

5. Dependency of luminescence intensity

a. To incident power

Let's consider an upconversion luminescence involving the sequential absorption of n photons. The dependency of the pump power P may range from P^0 to P^1 , the two borderline cases being identified as infinitely large or small upconversion rates respectively. The study of the parameter n can be a signature of competitive mechanisms like ESA versus ETU. A consequence of the conservation of energy is that a nonlinear process cannot maintain its nonlinear nature up to infinite excitation energy, and we often observe a "saturation" of upconversion intensity at higher pump powers [102].

In most cases, UC is a two-photons absorption process, resulting from GSA + ETU or ESA, which result in a quadratic dependence of the number of upconverted photons on the excitation power [103].

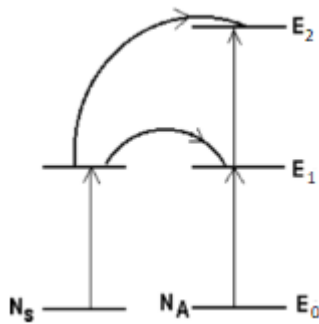


Figure 23. Schematic levels of transitions in a two ions upconversion system.

It can however sometimes also result from 3, 4, or 5-photon absorption process [104], which would in these cases imply other mechanisms with lower probabilities such as cooperative sensitization, cooperative luminescence or second harmonic generation [78].

Let's consider Figure 23. In our case, we will consider that the system is defined by one atom that both plays the role of a sensitizer and of an absorber, and that GSA+ETU is the only mechanism. Let's write time derivative of levels 1 and 2 [103]:

$$\dot{n}_1 = \rho_P \sigma_A n_0 - k_{ET1-1} n_1^2 - k_{R1} n_1 \quad 15$$

$$\dot{n}_2 = k_{ET1-1}n_1^2 - k_{R2}n_2 \quad 16$$

Where ρ_p is the pump constant, directly proportional to the incident pump power P_p , σ_A the absorption cross section of the atom, n_i the population density of level i ($i=0, 1$ or 2), k the transition rate of ETU and A_1 the Einstein coefficient.

If the steady-state is reached (\dot{n}_1 and \dot{n}_2 are equal to zero), this gives us:

$$\rho_p \sigma_A n_0 = k_{ET1-1}n_1^2 + k_{R1}n_1 \quad 17$$

$$k_{ET1-1}n_1^2 = k_{R2}n_2 \quad 18$$

If linear decay (that corresponds to R1 on [Figure 19](#)) is the dominant depletion mechanism of level 1, ETU can be neglected in Equation 17, which gives us $n_2 \propto n_1^2 \propto P_p^2$. On the other hand if upconversion dominates depletion of level 1, we have $n_1 \propto P_p^{1/2}$ so $n_2 \propto P_p$, which is the other limit. The slope of luminescence is between the two borderline cases.

Pollnau et al. [103] generalized these solutions first to 4 steps-excitation (like in $\text{Cs}_3\text{Lu}_2\text{Cl}_9:\text{Er}^{3+}$) and then to any upconversion process implying n -photon excitation. Both won't be detailed here. Their result is summarized in the Table 2 below.

Influence of upconversion	Upconversion mechanism	Predominant decay route	Fraction of absorbed pump power	Power dependence
(1) Small	ETU or ESA	next lower state or ground state	small or large	$N_i \sim P^i$
(2) Large	(A) ETU	(i) next lower state	small or large	$N_i \sim P^{i/n}$
		(ii) ground state	small or large	$N_i \sim P^{1/2}$
	(B) ESA	(i) next lower state	(a) small	$N_i \sim P^1$
			(b) large	$N_i \sim P^i$
		(ii) ground state	small or large	$N_i \sim P^0$ $N_i \sim P^1$

Table 1. Different pump power's dependency for a n -level upconversion system with different dominant mechanisms for different limit cases: small (1) or large (2) upconversion, by ETU (A) or ESA (B), decay predominantly into the next lower-lying state (i) or by luminescence to the ground state (ii), and finally a small (a) or a large (b) fraction of pump absorbed. Luminescence from level i is proportional to the population of level i [103].

Small or large influence of upconversion are described respectively as "small upconversion rates and short intrinsic lifetimes, i.e., luminescence dominates over upconversion as a depletion mechanism of the intermediate excited states" and "large upconversion rates and long intrinsic lifetimes, i.e., upconversion dominates depletion of the intermediate excited states".

To summarize, in most cases, if the measured slope of the logarithm of incident power as a function of the logarithm of the luminescence intensity is x , the upconversion mechanism will imply n photons, where n is the smallest integer greater than x [103].

Let's note that at high power densities, the power dependence reveals a plateau, which is an indication of the saturation of the upconversion process. For instance, in the case of $\text{BaYF}_5:\text{Tm}^{3+}:\text{Yb}^{3+}$, Vetrone et al. demonstrate the existence of this saturation above a power density of $57\text{W}/\text{cm}^2$, that they attributed to the fact that, if we take the notations of the levels of the absorber in [Figure 23](#),

$E_1 \rightarrow E_2$ transition is so efficient that it exceeds the $E_1 \rightarrow E_0$ decay rate [105]. At low power densities, there is an insufficient number of excited sensitizers, so transferred electrons are immediately excited to upper states. Whereas at high power densities, there are enough excited sensitizers to completely populate E_1 , and any “extra” excited sensitizers will not contribute to energy transfers anymore. This behavior can be observed in Figure S3 of Ref[106].

However we cannot compare this saturation value with our power densities which are in $W/cm^2/nm$.

b.To particle’s size

Does the luminescence intensity increases as the UCNPs’ size increase or is the relation more complex?

In the first approximation, we could assume that the more RE ions we have, the more intense the luminescence becomes. So as the particle’s size increase, the PLQE (Photoluminescence Quantum Efficiency) increases, as experimentally observed by Boyer and Van Veggel [101].

In the second approximation, we notice only the ions that are close to the surface will be efficient far-field emitters. Indeed, the emission can occur through energy transfer (the ET range is 7 nm [107]) or through photon emission, and we easily understand that only surface ions can emit photons that will escape the matrix. However, rare-earth ions tend to migrate close to the surface, and the distribution in the volume is not homogeneous: Fischer et al. show for instance that “for a spherical particle with a diameter of 20 nm, 70% of the RE ions are found in a shell volume within a distance of 3.2 nm from the surface”. This length

happens to be “the average migration distance which the [initial] excitation energy can travel”. Ions located further from the surface than this length will not contribute to luminescence emission. This means, in particular, that for 84 nm nanocrystal, for which only 21% of the rare earths ions are located within the 3.2 nm shell, only 21% of rare earth ions will effectively emit and their emission will reach the surface. (The value of this radius depends on excitation energy.)

We see that the proportion of the UCNPs contributing to luminescence depends on the irradiance and on the size of the particle.

The volume to surface ratio also seems to be playing a role in this complex relation between PLQE and size: many surface defects owing to the open inorganic bonds represent relevant quenching pathways [108].

Experimentally, an unpublished work executed by Hengyang Xiang shows a clear increase of PLQE with the size [Figure 24](#).

Boyer et al. also measured a quantum efficiency of 3% for UCNPs over 100 nm diameter, 0.3% for 100 nm, 0.1% for 30nm, and 0.005% for 10 nm, for the same rare earth doping levels (2 mol % Er and

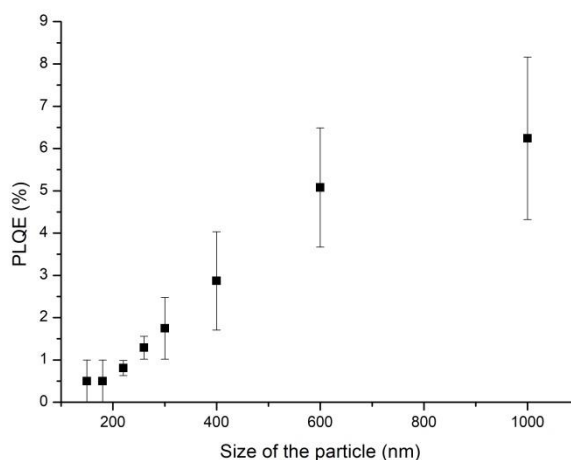


Figure 24. Variation of PLQE with UCNPs’ size for $NaYF_4:Er^{3+}$ (collaboration with Hengyang Xiang). Excitation wavelength: $1.55 \mu m$

20 mol % Yb), and the same NaYF₄ matrix [101]. This result is coherent with another one that studies the relation between UC intensity and UCNPs' height using a confocal laser and atomic force microscope. They found a UC intensity of 50a.u. for a particle's height around 50 nm and around 175 a.u. for a particle's height around 65 nm [109].

6. Implementation of UCNPs in solar devices

Upconverting material for improved solar cells must exhibit certain optical properties:

- high absorption in the NIR,
- high upconversion efficiency at low excitation intensity,
- good optical coupling between the upconverter and the solar absorber
- a spectral absorption at a lower energy than solar absorber bandgap,
- a spectral emission at an energy equal or higher to the solar absorber bandgap.

Various forms of upconversion materials have therefore been applied into solar cells based on different semiconducting materials. They are applied in a position either before or after the illumination reaches the semiconducting absorber (termed below as “front” or “rear” side respectively). For example, a Yb³⁺ and Er³⁺ co-doped vitroc ceramic layer has been placed on the rear side of a GaAs solar cell capable to harvest a sub-bandgap illumination (1.39 eV) and generate a photovoltaic efficiency of 2.5% [110]. Polycrystalline 20% Er³⁺-doped NaYF₄, mixed with white oil transparent to NIR, was adhered to the rear side of a crystalline silicon solar cell exhibiting an external quantum efficiency (EQE, the number of charges created over incident photons) close to 3.4% at 1523 nm (at 6mW)[111]. On solution-processed solar cells, a front side application of upconversion materials is the main configuration used by different works: for example, a Yb³⁺ and Er³⁺ co-doped TiO₂ layer has led to a 2.4% increase of short-circuit current in DSSC [112]. Similarly, Ho³⁺, Yb³⁺ and F⁻ tridoped TiO₂ NPs (NanoParticles) were applied in DSSCs leading to a 37% enhancement of PCE compared to reference device without any upconversion layer [113]. On P3HT:PCBM organic solar cells, an upconversion quantum efficiency of 0.19% was observed under the illumination of a 980 nm laser diode (at 250 mW cm⁻²) when a Yb³⁺ and Er³⁺ co-doped yttrium fluoride upconversion phosphor was placed in the front side of the cell [114]. On MAPbI₃ perovskite solar cells, by a front side configuration He *et al.* applied Yb³⁺ and Er³⁺ co-doped NaYF₄ NPs as a mesoporous scaffold and observed an increase of PCE from 17.8% to 18.1% upon 980 nm laser illumination (at 28 W cm⁻²)[115].

Even if larger UCNPs present bigger PL intensity, inserting big particles whose diameter exceeds the thickness of the layer that covers it can severely damage the device. Good luminescence (like a QY around 6%) with a reasonable size (under 300 nm) is quite a challenge. Adding another particle that would increase the QY of the UCNPs would be necessary, and this idea came to minds long ago. By coupling UCNPs with metallic NPs exhibiting a resonance at the wavelength of absorption and/or emission of the UCNPs, called plasmonic resonance, the overall emission of the UCNPs would be increased without further damaging the device, without mentioning that the presence of metallic NP alone in a solar device increase its efficiency. Plasmonic resonance will be the subject of the next part, before looking in part IV. at the coupling between plasmonic effect and upconversion.

III. Theory of Plasmonic resonance

Plasmonic resonance is a phenomenon that occurs under incident light illumination at the interface between two materials whose permittivities have opposite signs. The conduction electrons' cloud starts oscillating under incident electric field and can resonate at a certain wavelength. Plasmons are quasi-particles which are plasma oscillation quantum.

The first voluntary highlight was conducted by A. Otto in 1968 by bringing a dielectric prism close to a metallic layer [116]. He noticed reflection decreased as the distance between the two objects was smaller than the wavelength.

The scientific story starts however earlier, with Faraday, in 1857, who gave a possible explanation of the modification of light by metallic particles [117], Mie then elaborated his theory (later detailed), and Langmuir and Tonk went on, suggesting the term "plasma" [118]. The story kept moving forward, from Pines and Bohm, who showed the oscillation where due to conduction electrons' excitation [119], [120] to Rutherford [121] and Lang, to Bohm and Gross [122], until in 1956 Pines uses the term "plasmon" to call those elementary excitation quantum [119]. Then, Ritchie, Powel, Swan, Stern and Ferrel contributed to the research on plasmons by showing the existence of those collective surface oscillations [123]–[126].

However, as often in science, the plasmonic effect was exploited long before being known. The first use of metallic nanoparticles exhibiting unexpected optical properties appears to be in ancient Egyptian cosmetics [127]. In the domain of art, the first known piece of art that uses plasmonic effect is the Lycurgus' cup, in the 4th century, that contains gold and silver nanoparticles [128]. The color of the cup changes from opaque green to translucent red when the light source goes from outside to inside the cup, as shown on [Figure 25](#).



Figure 25. Lycurgus' cup. On the left, light comes from outside of the cup, and on the right from the inside. [127]

Some Maya paintings are also colored using metallic nanoparticles [129] as well as stain glass windows of St-Etienne de Bourges' cathedral of Saint Chapel in Paris [130].

Today, plasmonic and nanoparticles are broadly used in several domains, from stain-glass windows, to pigmentation, cosmetics, wave guides [131]–[133], super-lenses [134], biomedical from diagnoses to photothermal treatment for cancer [130], [135], [136], diodes [137], lasers [138], captors [130]–[132], [134][139], nano-antennas [131], [132], [134], [139], different types of characterization and nonlinear effects (surface enhanced Raman spectroscopy (SERS) of dark field microscopy) [130]–[132][140]–[142], to solar cells [143][132]. This last point will be discussed particularly in the upcoming part.

1. Drude model and permittivity

We will now consider Drude's model, which is an adaptation of the kinetic theory of gases. Here, the conduction electrons are considered as a gas. Our aim is to find the condition on electric field's frequency for electronic cloud's resonance. This will be simply called resonance from now on. Let us consider the interface metal/air under a harmonic electromagnetic field $\overline{E}_0(\vec{r}, t) = \overline{E}_0 e^{i\omega t}$.

The equations are developed in Annex 3. They are adapted from Ref [144]. They give us the expression of the permittivity of the metal, defined as

$$\epsilon_{metal} = 1 - \frac{\omega_p^2}{\omega^2 + \gamma^2} + i \frac{\omega_p^2 \gamma}{\omega(\omega^2 + \gamma^2)} \quad 19$$

Where γ is a damping constant, and ω_p is the plasma frequency defined as

$$\omega_p = \sqrt{\frac{ne^2}{\epsilon_0 m}} \quad 20$$

Where

- n is the electron density
- e their charge, in C,
- ϵ_0 permittivity of vacuum, in F/m,
- m their mass, in kg.

The permittivity varies non-linearly as a function of the frequency of the light. Since the polarization is directly proportional to the permittivity, we understand that the electronic procession is also moving. Let's consider the real part of the permittivity in Equation 19, as we are not looking at material's absorption losses (which corresponds to the imaginary part [145]), and that $\omega \gg \gamma$ (verified apart from UV and deep UV [146]). In a set-up as used in Drude's model (air/metal interface for an electromagnetic field oscillating at a frequency ω , and a plasma frequency ω_p defined by the equation above), we can distinguish three regimes:

- $\omega_p > \omega$: $\epsilon < 0$, the incident wave is reflected
- $\omega_p = \omega$: $\epsilon = 0$, plasma is resonant
- $\omega_p < \omega$: $1 > \epsilon > 0$, the incident wave is transmitted

Let's note this equation only takes conduction electrons into account, which is fairly verified for alkali metals, whereas for noble metals, valence electrons can also have an impact on permittivity.

2. Localized Surface Plasmon Resonance (LSPR)

We study the optical response of a spherical metallic nanoparticle. We are looking for the condition on the incoming electric field's wavelength for the electronic cloud to resonate. This phenomenon is called Localized Surface Plasmon Resonance or LSPR.

a. Case of a small sphere – Rayleigh model

We first consider the case of very small particles (<50nm). The model is all detailed in Annex 4 (Rayleigh model). This approach suggests that we consider that for a given time t, the electric field is constant on the nanoparticle, as schematically shown [Figure 26](#). From this model, we deduce the expression of the polarizability of the metal sphere:

$$\alpha = 4\pi r^3 \frac{\epsilon_{metal} - \epsilon_{env}}{2\epsilon_{env} + \epsilon_{metal}} \quad 21$$

Where ϵ_{metal} is the permittivity of the metal of the sphere and ϵ_{env} the permittivity of the environment. Radiative corrections were not taken into account in this equation but for more information, the reader can refer to [147]. They principally appear when we describe polarizability as a tensor.

The resonance occurs when $f(\omega) = (\text{Re}(\epsilon_{metal}(\omega)) + 2\epsilon_{env}(\omega))^2 + \text{Im}(\epsilon_{metal}(\omega))^2$ is minimal.

The expression of the scattering and absorption cross sections for the case of a small sphere are given by [148]

$$\sigma_{sca} = \frac{k^4}{6\pi} (3V)^2 \frac{(\epsilon_r' - 1)^2 + \epsilon_r''^2}{(\epsilon_r' + 2)^2 + \epsilon_r''^2} \quad 22$$

$$\sigma_{abs} = k 3V \frac{3\epsilon_r''}{(\epsilon_r' + 2)^2 + \epsilon_r''^2} \quad 23$$

Where $\epsilon_r = \epsilon_r' + i \epsilon_r'' = \epsilon_{metal} / \epsilon_{env}$.

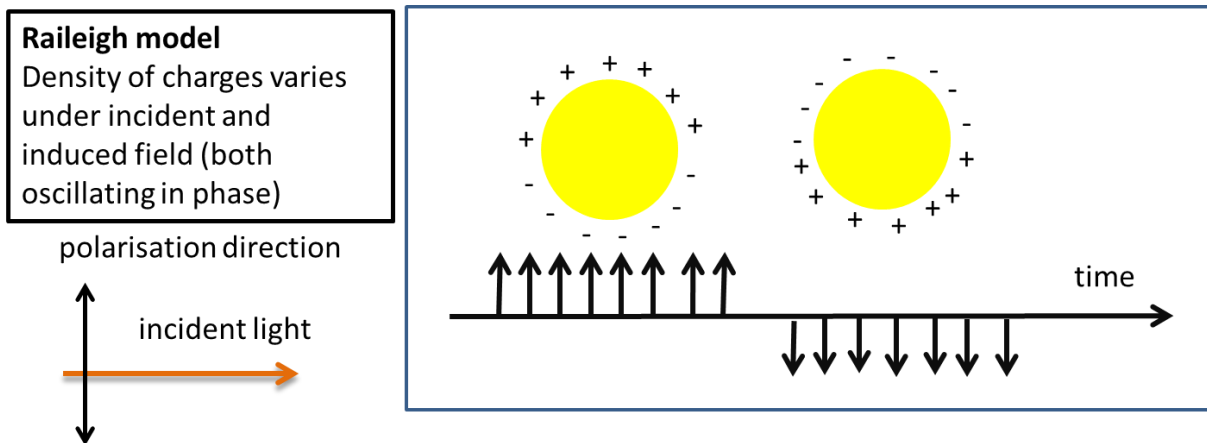


Figure 26. Schematic representation of a metallic nanoparticle under incident light for the Rayleigh model

b. Short introduction to Mie Theory

Rayleigh model is valid for small spheres, for which the position of the resonance does not depend on the particle size. But for particles' size larger than 50 nm, his model is no longer valid because of retardation effects. In 1905, the German physicist Gustav Mie extended Rayleigh's theory of diffusion of light by nanoparticles [149] to bigger particles [150]. By solving Maxwell's equations using polar

coordinates, he expressed scattering σ_{sca} , absorption σ_{abs} , and total extinction σ_{ext} cross sections using harmonic functions described by those four equations:

$$\sigma_{ext} = \frac{2}{x^2} \sum_{n=1}^{\infty} (2n+1) Re(a_n + b_n) \quad 24$$

$$\sigma_{sca} = \frac{2}{x^2} \sum_{n=1}^{\infty} (2n+1)(a_n^2 + b_n^2) \quad 25$$

$$\sigma_{abs} = \sigma_{ext} - \sigma_{sca} \quad 26$$

$$a_n = \frac{m\psi_n(mx)\psi_n'(x) - \psi_n(x)\psi_n'(mx)}{m\psi_n(mx)\xi_n'(x) - m\xi_n(x)\psi_n'(mx)} \quad 27$$

$$b_n = \frac{\psi_n(mx)\psi_n'(x) - m\psi_n(x)\psi_n'(mx)}{\psi_n(mx)\xi_n'(x) - m\xi_n(x)\psi_n'(mx)} \quad 28$$

Where

- m is the ratio of refractive index of the sphere to that of surrounding medium n_m ,
- x is the size parameter given as $2\pi n_m R/\lambda$,
- R being the NP's radius in m ,
- λ the wavelength in m
- ψ_n and ξ_n are the Riccati-Bessel functions and the prime represents the first derivative.

The size of the metallic NP for instance plays a role on the resonating electron's cloud, and thus on the intensity of the induced electric field. The spheres are not just dipoles like in Rayleigh model described previously ([Figure 26](#)). In addition, other modes (multipolar ones) can also exist ([Figure 27](#)). We will not detail them here.

Calculations of those cross sections can be run by computers with different types of codes, like the one developed by Ivan Charamisinau for gold nanoshells [151] or on Mathematica by Sönnichsen [127]. For gold nanorods, Jain et al. [152] used the discrete dipole approximation method [153], which is a space discretization method similar to the Finite Elements one that will be later described.

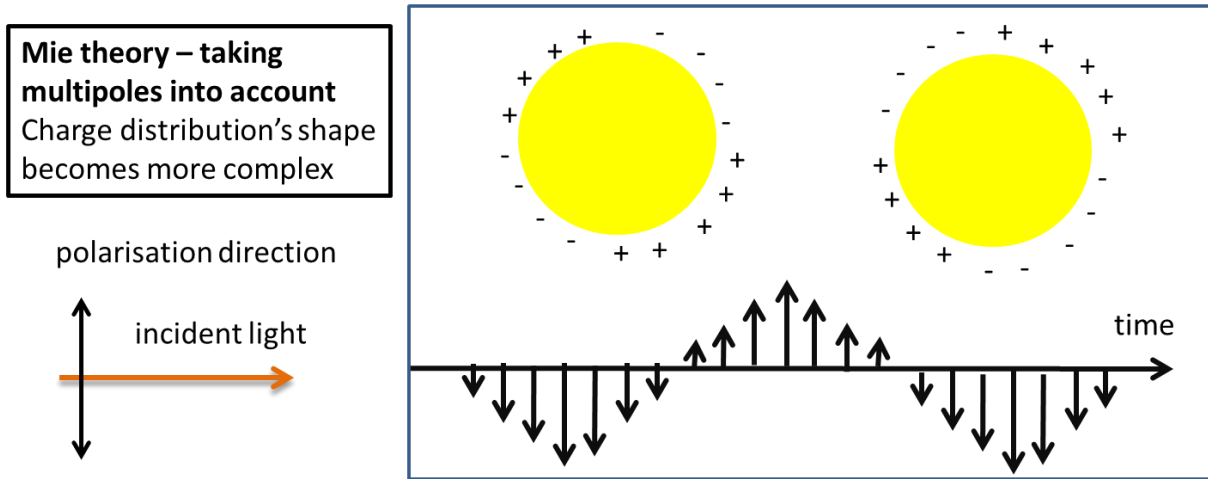


Figure 27 Schematic representation of metallic nanoparticle under incident light for bigger particles in the case of the presence of multipoles [154]

In terms of absorption, the existence of a wavelength at which the resonance occurs is translated by the existence of an absorption peak at this wavelength, as shown [Figure 28](#), which is the absorbance spectra in the visible for gold nanodisks arrays of diameter 150nm. The LSPR is located around 780 nm.

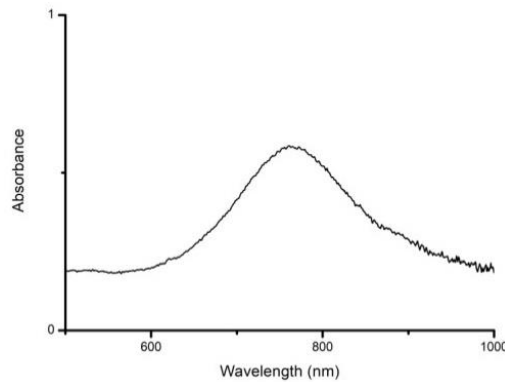


Figure 28. Absorbance spectrum for gold nanodisks array. The diameter of the disks is 150nm.

c. Near-field local enhancement

Another phenomenon related to LSPR, can be observed in the case of a metallic nanoparticle under an electromagnetic field: local field enhancement. This was underlined by Near-Field measurements that we performed at the laboratory. In those experiments, gold nanodisks' near field is imaged using an upconverter as surface scanning tip. We can visualize the near-field being enhanced in the vicinity of a metallic nanoparticle.

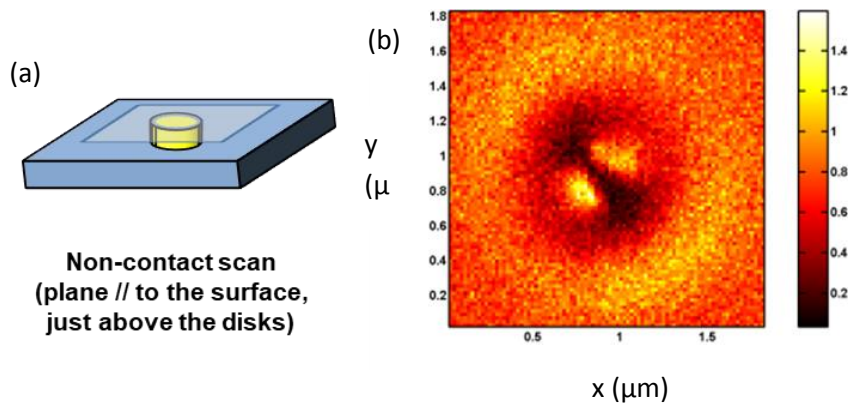


Figure 29. Near-Field experiment in which the enhancement of local electromagnetic field is clearly demonstrated. a. Scheme of the experiment. A near-field scanning is done on a surface parallel to the surface of a 60 nm diameter nanodisk. b. The intensity of the field is stronger in two lobes close to the nanodisk.

d. Qualitative adaptation to the case of nanorods

Nanorods are strongly anisotropic, and it is well known that shape of particles have a significant impact on optical characteristics [148], [155]–[159]. There are two visible dipole modes: the longitudinal and the transversal one, which correspond themselves to two different resonance wavelengths for two different polarization, as pictured [Figure 30](#) (the longitudinal mode is the second smaller bump, the first one corresponding to nanospheres also present in the sample).

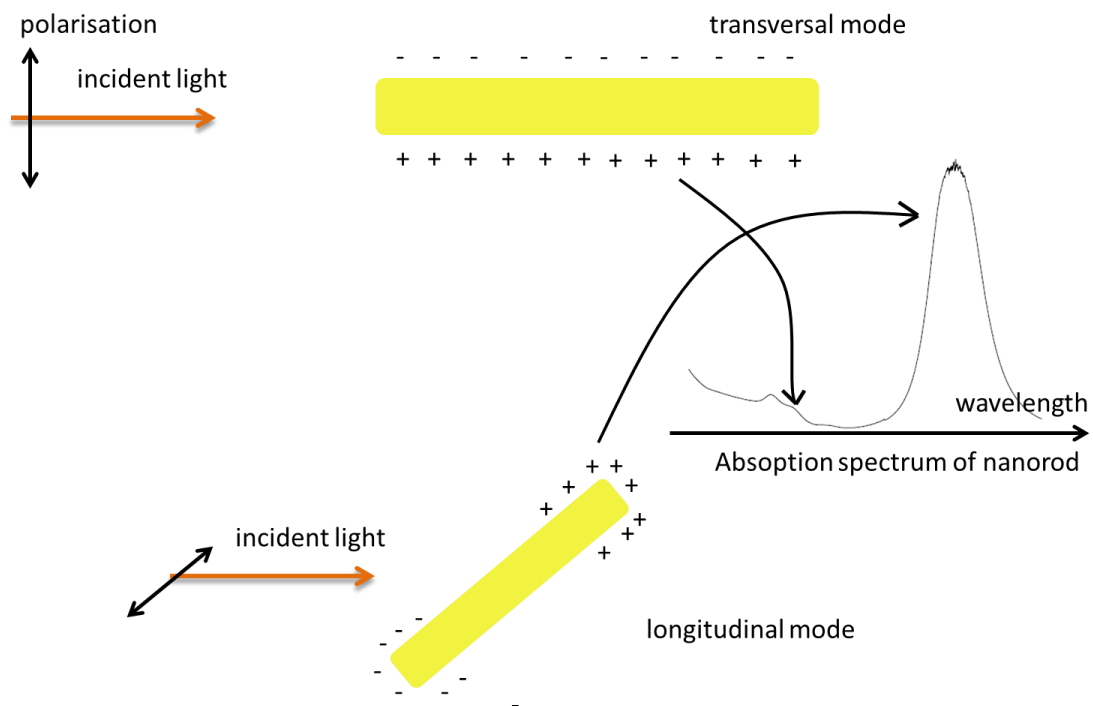


Figure 30. Resonance modes for nanorods.

The longitudinal mode is provoked by electrons oscillating along the axis of the nanorods and happens at a longer wavelength.

The variation of the wavelength at which the absorption is maximal (LSPR) as a function of the nanorod aspect ratio AR (defined as the length of the rod over the diameter) will be later discussed.

3. Implementation in solar devices

a. Advantage and drawbacks of plasmonic NP

The first time surface plasmons were incorporated in photovoltaic devices was in 1980 when Wenpeng Chen used a metallic diffraction grid close to a silicon amorphous diode. An increase of photovoltaic signal was observed [160].

There are several reasons why photovoltaic devices can largely benefit from plasmonic effect. Here we will in particular pay attention to thin-film solar cells.

→ by generating a high intensity electromagnetic field (as shown in near-field imaging [Figure 29](#)) and by localizing it into absorbing layers, efficiencies of the devices can increase (light concentration). NPs act as effective antennas for the incident light. Antennas are particularly useful in materials where the carrier diffusion lengths are small, so where the benefit to generate them close to the junction is big.

→ by scattering incident light, the optical path can be elongated, also increasing devices' efficiencies (light trapping). The direction of scattered light is nearly symmetrical between forward and reverse directions [159][148], but this is no longer the case when the NP is at the interface between two dielectric, and in that case, it will scatter preferentially into the dielectric with the larger permittivity [161].

Some tests were run in 1991 on organic solar cell containing copper phthalocyanine CuPc [162]. Photocurrent was multiplied by 2.7 for copper NP insertions in the same type of solar cell, a publication later published [163]. Recent work studied the incorporation of such particles in perovskite solar cells [164], [165].

The increase of photogenerated current was also explained in 2000 by the schematic image of a bridge for free charge carriers to cross the Schottky contact between ITO and the organic material [163]. The existence of this bridge is due to metallic nanoparticles. Several work prove an increase of photocurrent (up to 80% [166] at LSPR) and efficiency of solar devices [166]–[171].

It was also shown that localized plasmonic resonance increases the probability for excitons to dissociate into free charge carriers by reducing its binding energy [172]. It's in particular the plasmon-exciton coupling that is in charge of this effect: the charge transfer between plasmon and exciton allows the overcome of the initial Colombian potential [173]–[176].

The major drawback of plasmonic NP implementation in solar devices is the absorption of the NPs. This term refers to the loss of photons that decay in the metal particle via nonradiative channels to produce heat [177]–[179]. This absorption is in direct competition with useful absorption in the photovoltaic material. It has been noticed that introducing plasmonic structures absorbing in a spectral region where the absorption of the absorber is already substantially complete can degrade the system [180]. The ratio of parasitic absorption over useful near and far-field scattering in the metal is the key parameter to estimate whether plasmonic NPs will be an advantage for the device. This ratio can however be handled to some extent by modifying the size, morphology, material of the plasmonic structure and the position in the device.

Metallic NPs can also act as charge carrier recombination centers when they are placed in the absorber [177], [181], [182], often leading to a reduction of Voc and Jsc [183]. The chemical and physical compatibility of the solvents associated with respectively the metallic NPs and perovskite (or other absorbing material) can however be a major practical issue raised by the use of NPs in photovoltaic devices (which will be addressed later), as well as the costs of the precious metals used (usually gold and silver).

b.State-of-the-art and fabrication methods

Plasmonic resonance depending on several parameters such as the metal used, shape (nanospheres (alloys, pure or coreshells) [172][176] [184]–[186][187][188], nanorods[189], nano-antennas [190], nanoarrays[191]...), opto-geometrical parameters (surface density, size), wavelength, light polarization, incident angle, and of course the position of particles regarding the absorbing layer (Figure 31), with different advantages and inconvenient it implies.

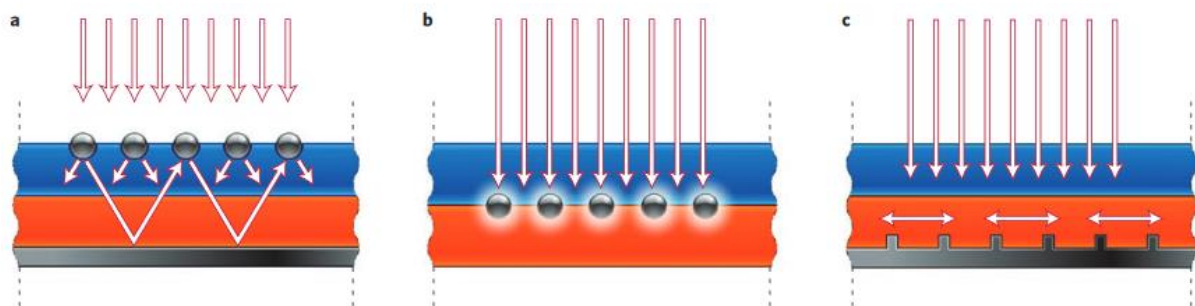


Figure 31. Plasmonic light-trapping geometries for thin-film solar cells. (a) metallic nanoparticles are placed on the “front” side of the device. Light is trapped in the semiconductor and scattered, resulting in an increase of the optical path length in the cell. (b) Nanoparticles are embedded in the semiconductor, and near-field results in exciton’s creation and separation. (c) Light is trapped by the coupling plasmon-polariton at the interface metal/semiconductor. [143]

Smaller particles close to the semiconductor layer can couple a larger fraction of the incident light to the semiconductor, and increase more the optical path length than bigger ones [143].

When the NPs are placed on the “back” side (close to metallic electrode), destructive interference effect between incident and reflected fields can be observed. Placing the NPs on the “front” side of the solar cell fixes this one precise point.

When metal stripes are placed on the surface of a solar-cell, the short-circuit can be enhanced by 45% [192]. To be efficient, light-trapping nanodisks arrays’ optimization must take into account the coupling between NPs, ohmic damping (non-radiative relaxation through phonons), grating diffraction effects [193] and the coupling between surface plasmon modes [194]–[196].

In the two articles addressing plasmonic NPs in perovskite solar cells mentioned above, spherical metallic nanoparticles are respectively on top of FTO or inside the active layer. In the first case, they were Ag-Au alloy popcorn-shaped, which were embedded in the mesoporous TiO₂ at a concentration of 0.7 wt %, and gave a relative PCE enhancement of 15.7%. In the second one they were Ag@TiO₂ core-shell nanoparticles that were integrated to the mesoporous Al₂O₃ scaffold layer. Nanospheres can be deposited by different techniques, including layer by layer deposition (followed

by annealing, which creates clusters [187]), evaporation [163] or spin-coating of NPs [176]. A higher control of the inter-particles distance and dispersity of the sizes of the metallic NP can be obtained using other techniques such as e-beam lithography [197] or nanoimprint [198].

E-beam lithography is a process which consists in the patterning of photosensitive resin through focused electron beam scanning. In a second time, the resin is developed and the exposed parts are removed. Then the metal is deposited, and the rest of the resin is removed. The metallic pattern only remains on the substrate. It has been investigated for organic solar cells [197], [199], [200][162][191], polymer [187], DSSC [189] or silicon [188]. The major drawback is the slowness of this process that includes many steps, and even more the maximal dimension of patterns: a pattern of 15 mm diameter was printed in 9h with a resolution of 200nm [201] (which is clearly too low for 200 nm-big disks), without mentioning the time of resin coating, developments and metal evaporation. This makes it unlikely to be used for industrialized process and even for a 0.1 cm² cell.

Nanoimprint is a method that requires the use of a PDMS (polydimethylsiloxane) mold whose shape fits the one to be printed. Then, again, two different methods exist. The first method is the degassing assisted patterning process, in which the mold is previously degassed and then applied on gel that has not dried yet (like sol-gel TiO₂ right after spin-coating) [202], allowing it to match the contours of the mold by soaking it. The other method consists in first thermally evaporating metal on the mold and then bringing it in contact with the substrate [203]. It's a very simple, scalable and cost-effective method, which however takes some time to experimentally master, without mentioning potential dependency to another laboratory for the mold's fabrication. Finally, the pattern is defined by the mold and cannot be tuned, unless another mold is fabricated, which is not the case for e-beam.

IV. Plasmonic enhanced upconversion – Case of a metallic nanosphere and an upconversion particle

The proximity between a metallic nanoparticle and an upconversion nanoparticle allows the enhancement of the emission and the absorption of the UCNPs [204] when LSPR matches UCNPs' absorption and/or emission. The other effects of surface plasmon close to an emitter are the increase of quenching and non-radiative decay rates of excited electrons, usually leading to losses, as well as the modification of energy transfer rates [205]. Quenching is a term that qualifies the decrease of fluorescence through its annihilation (for instance by an energy transfer from the UCNPs back to the metallic NPs).

In this part, we will focus on emission and absorption's enhancements. They rely on the strengthening of the local electric field intensity in the vicinity of an individual metallic nanostructure at the LSPR. The fluorescence enhancement can be maximized by optimizing the distance between the two particles and by tuning the LSPR of the metallic NP through shape modification.

Decay rates are parameters describing the relaxation of an electron to a lower electronic level. They are powerful indicators for the lifetime of an excited level, and thus most of luminescence enhancements can be quantified through decay rates modification.

Total decay rates are the sum of radiative decay rates Γ^R and non-radiative decay rates Γ^{NR} . We can write that, for any transition from level i to level f , $\Gamma_{if}^T = \Gamma_{if}^R + \Gamma_{if}^{NR}$.

Total and radiative decay rates were expressed by Kim et al. involving the exact electro-dynamical theory [206] for the case of a dipole (representing the UCNP as a single luminescent atom), close to a spherical metallic particle. The electro-dynamical theory uses Mie theory to express those rates.

In their simulation, the dipole/sphere interaction depends on the two possible orthogonal orientations: radial or tangential as shown [Figure 32](#). The upconverting property of the luminescent material was not taken into account.

More details on the expression of these rates are described in Ref [206].

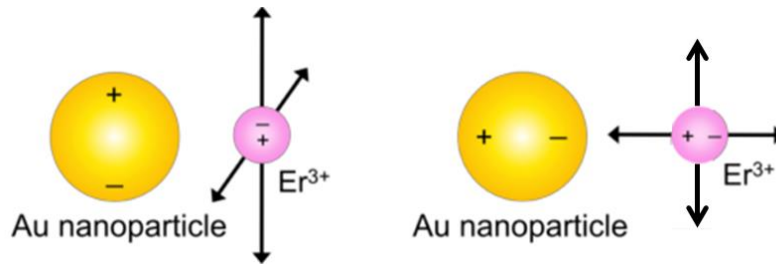


Figure 32. Tangential (left image) and radial (right image) oscillation of Er^{3+} regarding the metallic nanoparticle [207]

1. Luminescence enhancement outcome

We will refer to the Equations 29 to Equation 33 listed below from the work conducted by Liu et al. [204]. The expressions of excitation and emission enhancement factors come themselves from the work done by Esteban et al. [208]

Let's consider the simplified upconversion process described [Figure 19](#) with three levels and two possible mechanisms (GSA+ETU or GSA+ESA).

a. Excitation enhancement factor

The excitation enhancement factor for ESA can be expressed as followed:

$$f_{ex,ESA} = \frac{|\vec{\mu} \cdot \vec{E}|^4 \Gamma_{10}^{TO}}{|\vec{\mu} \cdot \vec{E}_0|^4 \Gamma_{10}^T} \quad 29$$

- $\vec{\mu}$ is the electric dipole momentum,
- \vec{E} and \vec{E}_0 are respectively the electric field under LSPR excitation and incident electric field
- Γ_{10}^{TO} is the total decay rate from level 1 to level 0 without the presence of the metallic particle
- Γ_{10}^T is the total decay rate from level 1 to the level 0 with the metallic particle

There are two competing processes in the ESA mechanism that can be associated with the two terms of this expression: on one hand, the first term is the positive contribution from the fourth power of near-field, which is the ESA enhancement factor. This means that when the local electromagnetic field is enhanced, ESA is enhanced at the fourth power. On the other hand, the negative contribution from the total decay rate of the intermediate state which is the inverse of the second term. We can say $f_{ex,ESA} = \text{ESA enhancement factor} / \text{decay rate of the intermediate level}$.

The excitation enhancement factor for ETU can be expressed as followed:

$$f_{ex,ETU} = \frac{|\vec{\mu} \cdot \vec{E}|^4}{|\vec{\mu} \cdot \vec{E}_0|^4} \left(\frac{\Gamma_{10}^{TO}}{\Gamma_{10}^T} \right)^2 \quad 30$$

Here, we ignore any change in efficiency of the ET process due to the metallic NP. We also assume identical field enhancement for the two atoms between which the transfer occurs. The negative contribution from the decay rate of the intermediate state has twice as much chance to occur, once to the sensitizer, and second to the absorber (thus the square power).

b. Emission enhancement factor

The emission enhancement factor can be expressed as followed:

$$f_{em} = \frac{\eta}{\eta_0} \quad 31$$

η and η_0 are quantum efficiency with and without the metallic particle respectively.

c. Total enhancement

We can thus distinguish the total enhancement factor for ESA and for ETU:

$$f_{tot,ESA} = f_{em} f_{ex,ESA} = \frac{|\vec{\mu} \cdot \vec{E}|^4}{|\vec{\mu} \cdot \vec{E}_0|^4} \frac{\Gamma_{10}^{TO}}{\Gamma_{10}^T} \frac{\eta}{\eta_0} \quad 32$$

$$f_{tot,ETU} = f_{em} f_{ex,ETU} = \frac{|\vec{\mu} \cdot \vec{E}|^4}{|\vec{\mu} \cdot \vec{E}_0|^4} \left(\frac{\Gamma_{10}^{TO}}{\Gamma_{10}^T} \right)^2 \frac{\eta}{\eta_0} \quad 33$$

d. Modification of transition coefficients

However, Fischer et al. showed that transition probabilities are indeed affected by the presence of the metallic nanoparticle in the vicinity of the UCNP [207]. We can thus express the modified Einstein coefficients in the presence of a plasmonic structure $A_{if,plasm}$ as

$$A_{if,plasm} = (\Gamma_{if}^R + \Gamma_{if}^{NR}) A_{if} \quad 34$$

2. Variation of the enhancement factor with distance

In the following part we will briefly describe the situation in [Figure 32](#) and vary the distance between the emitter and the metallic NP.

a. Comparing quantum efficiencies in the case of an optical emitter (Electrodynamic Theory)

Mertens et al. [209] considered the situation pictured on [Figure 32](#), the metallic NP being an Ag sphere of diameter 60nm, optical data taken from Palik [210], and the emitter emitting a simple luminescence due to a one-photon absorption. They averaged the dipole orientation over all solid

angles, which is representative of the case where transition dipole moments are randomly oriented. The emission wavelength was chosen in order to match the LSPR (433nm).

The results giving radiative and non-radiative decay rates (and thus quantum efficiency given by Equation 10) as a function of the distance between the two particles, calculated using the electrodynamic theory, are shown on Figure 33. We can observe the existence of an optimal distance at which the non-radiative decay is small enough whereas radiative decay is still high (quantum efficiency is defined as the ratio of radiative decay over the sum of radiative and non-radiative decays). Non-radiative decay is very high at small distances because of quenching is a short-range phenomena as we can see on Figure 33.c. At the separation of 6 nm, the quantum efficiency is multiplied by 10 (compared to the case in absence of the metallic nanoparticle). These results depend on the initial choice of quantum efficiency and on the shape and material of the nanoparticle.

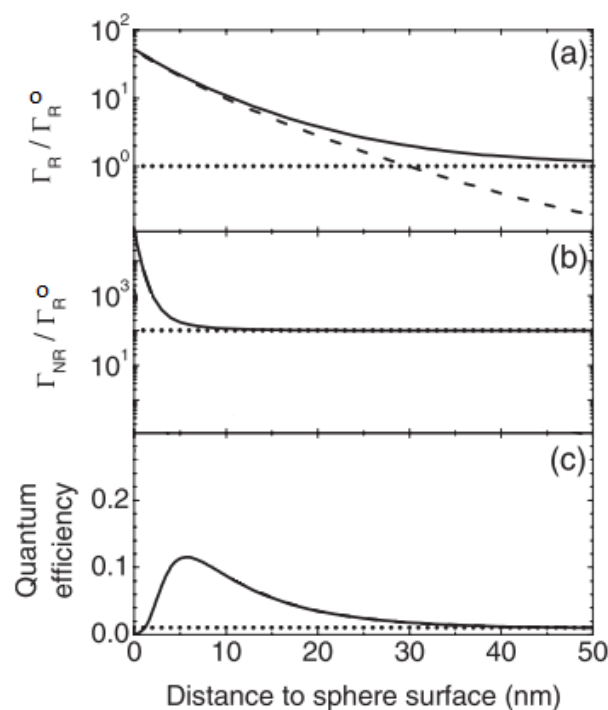


Figure 33. Those curves are obtained taking 60 dipole plasmon modes (corresponding to the biggest value taken by n in equations 24 and 25) (a) Radiative decay rate as a function of metallic NP-emitter distance (solid line). The contribution due to the presence of the metallic NP is the dashed line, and the radiative decay rate taken as reference (absence of metallic NP) is the dotted line. (b) Non-radiative decay rate as a function of metallic NP-emitter distance in the presence (solid line) and absence (dotted line) of the metallic NP. (c) Luminescence quantum efficiency of the emitter in the presence (solid line) and absence (dotted line, staging at 1%) of the metallic NP. [209] Quantum efficiency is defined as the ratio of radiative decay over the sum of radiative and non-radiative decays

b. Comparing relative luminescence – Case of an upconversion emitter (Electrodynamic Theory)

Also relying on electrodynamic calculations of radiative and non-radiative rates, Fischer et al. calculated relative luminescence [207] for different emission wavelengths in the case of a gold nanoparticle of radius 200nm. In this case, they used the calculation of Mertens et al (equations 24 and 25) described above to calculate the radiative and non-radiative decay rates, and then they used

relation 34 to calculate new transition coefficients, and using equations similar to the ones described in the Annex 2.A., they were able to calculate occupancy of any level and thus the luminescence L_i from this level, using the relation $L_i = n_i A_{if}$. They averaged on the two dipolar orientations and they obtained an optimal distance around 15 nm for most transitions, as shown on Figure 34. The UC model they use is different from the one exposed earlier in this chapter but will not be developed in this work.

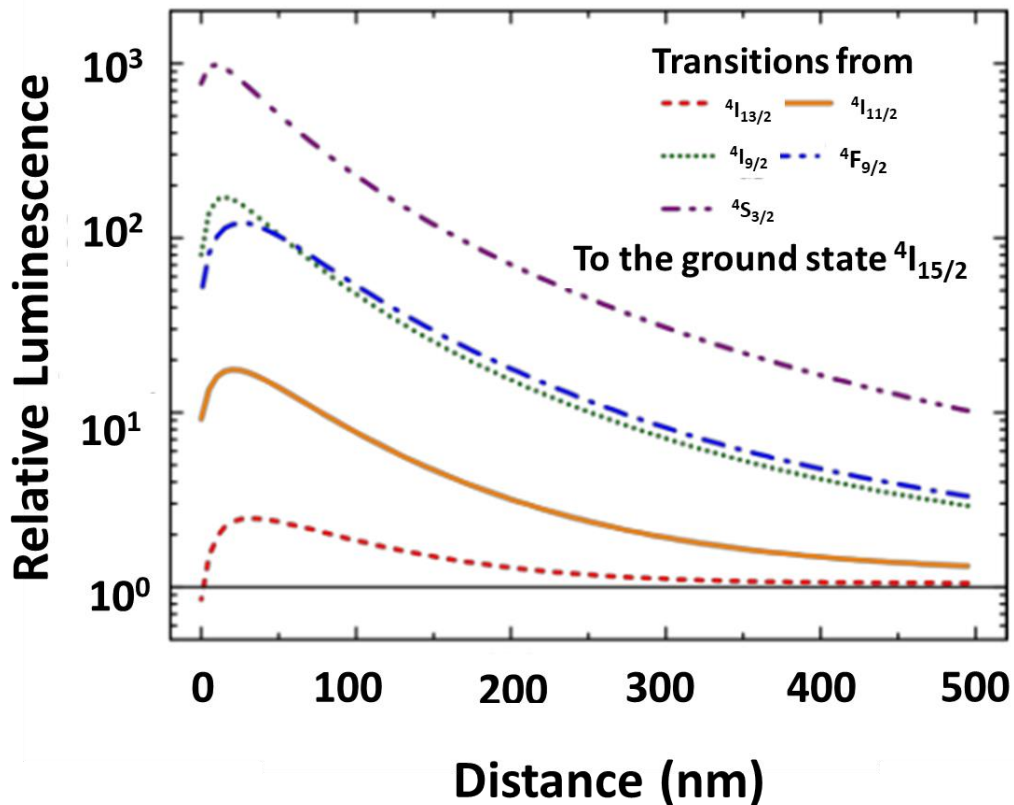


Figure 34. Relative luminescence of an erbium atom close to a gold NP for different NP-Er distances averaged for both polarizations [207]

Liu et al. obtained similar results by comparing enhancement factors (Equations 32 and 33, but they only took ESA into account) [204]. Since they considered both emission and absorption enhancement, which happen at different frequencies, the optimal distance for absorption and emission's maximal enhancement was different.

In all those cases, the LSPR is tuned in order to be the closest to the UC's absorption peak. An unpublished study was performed at the laboratory relates near-field experiments where gold nanodisks' near field is imaged using an upconversion nanocrystal as a surface scanning tip (just like picture in Figure 29). They noticed a difference between the wavelength at which the near-field intensity is maximum and the far-field resonance wavelength [211]. This shift between near and far-field has been addressed recently ([212],[213], [214]) and it was found that this difference increases for larger structures (above 100nm). This is the reason why a perfect match between absorption wavelength of the UC and the LSPR might not be the most effective way to enhance luminescence.

3.State of the art

Plasmonic enhanced upconversion is a widely addressed topic, and we will here only mention a few examples of systems and the enhancements that were predicted or measured.

By trying different shapes of plasmonic NPs, Sun et al. found the best shape for maximized fluorescence enhancement of $\text{NaYF}_4:3\%\text{Er}^{3+}:17\%\text{Yb}^{3+}$ was the pyramid (compared to linear gratings, bullseye, all on top of the UC material) [205].

Wang et al. compared numerical to experimental results in the case of several Ag Nano platelets surrounding an UC nanorod. In the case where the LSPR of the platelets is chosen to match the $\text{NaYF}_4:\text{Er}^{3+}:\text{Yb}^{3+}$ UC's emission, the enhancement ratio is 5 and in the case when it matches the UC's absorption, the enhancement ratio is 22. This way, they could deduce a quantitative estimation of the impact of a single platelet [215].

For the same upconverting material, an enhancement factor of 3.8 was found using single gold sphere [216] by Schietinger et al.

Lee et al. used downshifting (DS) material as well as upconversion, in a metal/insulator/metal (MIM) structure composed by silver film/UC layer/silver nanodisks/DS layer [203]. They measured a photoluminescence enhancement of 174 times for the UC and of 29 times for the DS.

In the theoretical approach of Liu et al., the maximal enhancement factors varied between 120 and 160 times for 640 and 540 nm respectively, in the case of a gold nanorod.

In the particular experimental configuration of UCNPs coated with 1-2 nm-big Au NPs, the emission was also increased 3 times [217]. The control of surface coverage and thickness was found to be crucial to obtain an effective enhancement: if the coverage is complete and/or the shell is too thick, it will act as a quencher.

Concerning the combination of both plasmonic and upconversion materials and their implementation in a photovoltaic device, it has been numerically predicted that the light absorption by the absorber would be enhanced 10 times with only UCNPs, and 100 times increased by upconverting dielectric cores with metallic nanocrescents silver shells [218]. Experimentally, it's been tried a few times: Meng et al. also coated $\text{Y}_2\text{O}_3:\text{Er}/\text{Au}$ with TiO_2 and they mixed the so obtained NPs to submicron TiO_2 in order to form a multifunctional scattering layer in DSSC. They obtained an improvement of 27.6% in PCE by comparison to the cell without this layer [219]. By trapping upconverted light generated by $\text{NaGdF}_4:\text{Yb}^{3+}:\text{Er}^{3+}:\text{Fe}^{3+}$ using reflecting silver NPs, an increase of 21.3% in PCE was observed in a DSSC [220]. The solar cell with both UCNPs and plasmonic NPs exhibited a higher PCE (7.1%) than the one with only UCNPs (6.2%), which exhibited itself a higher PCE than the reference solar cell (5.8%). The lack of any standard deviations for those two works mentioned above advises us however to be cautious when considering these results.

V.Finite Difference Time Domain (FDTD) Simulation principle

Finite Difference Time Domain (FDTD) is a rigorous resolution method using partial derivative that implies neither approximation nor theoretical restriction [144] [221]. It was developed by K.S. Yee in 1966 [222]. As calculation times and informatics tools became more and more accessible and fast, the number of studies applying FDTD grew rapidly.

A well-known application of FDTD method consists in Maxwell equation resolutions. They describe the temporal variation of electric or magnetic field as a function of magnetic or electric field. FDTD consists in solving a partial differential equations system (corresponding to Maxwell equations) by discretizing time and space.

The equations used to solve Maxwell equations are given in Annex 5.

A higher accuracy is obtained for smaller mesh lattice (the mesh lattice corresponds to the spatial division of the calculation region, as detailed in Annex 5). However, this implies a drastic increase of calculation time. In order to limit calculation time and informatics resources, the simulation domain can be restricted. In order to do so, several solutions exist when boundary conditions in simulation domain are defined:

- PML, Perfect Matched Layer: they allow simulating an artificial absorbing layer in order to truncate computational regions by including a damping factor
- periodic conditions lead to the infinite repetition of the structure using one simulation boundary as the other boundary.

Simulation can stop when convergence or divergence criteria is obtained. These criteria can be defined using different methods:

- when electric and magnetic field don't vary as function of time anymore
- when the integration in the simulation domain of the field is close to zero (all the waves have been reflected, transmitted or absorbed)
- when this same integral diverges
- when the maximal time for calculation is reached.

The software needs several inputs in order to run the simulation:

- refractive index, permeability and permittivity of used materials. For common material, there exists a library of those data, that we actually used in this work
- boundary limits of simulation domain
- meshing in the three directions
- time meshing

Total simulation time defined by the user that is cut into temporal steps of Δt . In this work we used a commercialized software called FDTD Solution © distributed by Lumerical ©.

This chapter allows us a better theoretical understanding of the phenomenon behind plasmonic enhanced upconversion as well as a good overlook on photovoltaic devices characterization.

In order to obtain the to most promising results regarding the incorporation of those two types of nanoparticles in a solar device, this one has to be as well optimized as possible. Next chapter will be dedicated to standard perovskite devices optimization.

Chapter 2. Fabrication and characterization of solar cells

This chapter mainly addresses fabrication processes of solar cells and their optimizations. Solar cells performances' analysis will first be discussed before exploring optimization leading to the device on which UCNPs implementation's optimization will be later operated.

I. Obtaining and comparing data for efficient optimization

Before describing the solar cell fabrication and different layers' optimizations, a little notice should be given on how to obtain results and analyze them in order to draw the most useful and reasonable conclusions.

We will first expose the measurement methods before critically discuss the best way to analyze the results.

1. I-V curve measurement

a. Set-up

The set-up used to measure I-V curve consists in a solar simulator, to which the cell is exposed through the transparent FTO/Glass side, and a computer-controlled Keithley 2612B source measurement unit. The solar simulator (ASTM model, class AAB from Abet Technology) delivers an AM1.5G operated at 1 sun. The light intensity was first calibrated by a calibrated Si reference solar cell.

Two pin-electrodes are connected to the two electrodes of the device (FTO and gold) by simple contact. The current is measured as the bias varies from 1.1V to 0V with 0,01 V steps in reverse and forward scanning directions. Each step lasts 50 ms, which implies a scan rate of 200mV/s. In this work, fewer attention was paid to hysteresis phenomenon or scan rate influence. The scan rate was fixed for all measurements. We mainly focused on the parameters obtained under those measurement conditions: J_{sc} , V_{oc} , FF and PCE, as described in Chapter 1.

The output files are Excel files delivering a column giving the current density and another giving the bias.

b. C- program data analyzer

In order to automatize the analysis of the results, a C-program was written. All the I-V curves are recorded and named with an integer from 1 to the maximal number of cells for the same experimental conditions and put in the same file document. The program then analyzes the data and gives, for each cell, J_{sc} , V_{oc} , FF and PCE.

From those results, three lines are printed in the output document: the parameters (J_{sc} , V_{oc} , FF and PCE) of the cell with the maximal PCE, the average for each parameter, and the standard deviation Σ for each parameter, calculated as

$$\Sigma = \sqrt{\frac{\sum_i (x_i - \bar{x})^2}{N}}$$

35

Where

- N is the total number of cells,
- \bar{x} the average of the parameter x,
- and x_j the values taken by the parameter x (I_{sc} , Voc, FF or PCE).

2. Extern Quantum Efficiency (EQE)

EQE is based on wavelength by wavelength current-measure. It is the ratio of the number of collected charge carriers to the number of incident photons for each wavelength. The monochromatic light beam was obtained from a white light source and an Oriel Cornerstone monochromator (and appropriate order sorting filters to eliminate higher order grating reflections). The monochromatic illumination was chopped at 37 Hz and calibrated by using a NIST-calibrated Si photodiode before each measurement session. The solar cell's short-circuit current I_{sc} under each monochromatic wavelength was measured in air by a Stanford

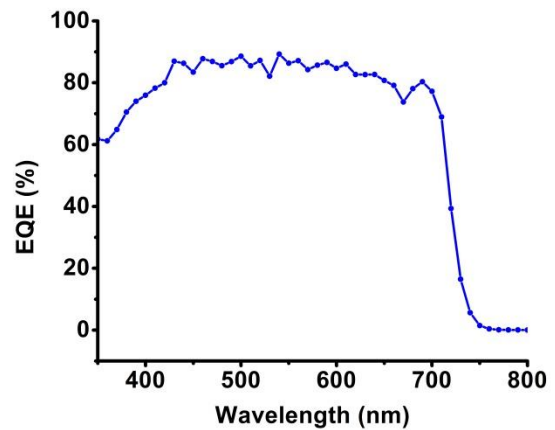


Figure 35. EQE of $FA_{0.83}Cs_{0.17}Pb(I_{0.6}Br_{0.4})_3$ measured in collaboration with Zhelu Hu.

Research systems SR570 low-noise current preamplifier and a SR810 DSP lock-in amplifier. The EQE spectrum was determined by

$$EQE(\%) = \frac{I_{sc}}{P} \frac{1240}{\lambda} \cdot 100$$

36

Where

- P (in W) is the power of the monochromatic illumination,
- λ the wavelength in nm and
- I_{sc} the short circuit current obtained at this wavelength.

An example of EQE obtained for $FA_{0.83}Cs_{0.17}Pb(I_{0.6}Br_{0.4})_3$ is shown [Figure 35](#).

In this work, the devices comparisons are mainly based on are I-V curves.

3. Data acquisition and analysis precautions

On which statistical tool can we rely in order to deduce that the experimental conditions of one set of data are more likely to give better performances in the long term?

a. Variability and repeatability of experiments

Experiments are run in batches. Each batch includes maximum 24 substrates. This number is imposed by the number of substrates that fit in the mask used for gold evaporation (we can use two masks at the same time which both have the room for 12 substrates, as we can see [Figure 48](#)). Each substrate has 5 pixels on it, and each pixel is considered as an independent cell of area fixed at 0.107 cm². The uncertainty on this measure is later discussed. However, often, one pixel or two are inoperable, either because the pixel is overlapping the FTO electrode (thus creating a short-circuit), or because of other local defects.

Every experimental condition (same cell architecture, spin-coating speeds, temperature and time of annealing), was repeated twice, or three times for results with a stronger statistical weight. We have in the best case up to 10 or 15 solar cells fabricated in the same conditions.

However, we observed strong variability for the same condition: if we look at [Table 2](#), which gives parameters obtained for 9 cells which have followed identical fabrication process, we can notice a deep variability between the device with the best PCE (16.3%) and the smallest (3.7%). In this example, we would assume the two worst devices are abnormal (local defects), and don't consider them in average calculation, but the threshold remains mainly subjective.

Device N°	Jsc	Voc	FF	PCE
1	16.1	0.79	38	4.8
2	20.8	1.07	56	12.6
3	25.2	1.08	59	16.3
4	17.5	0.65	32	3.7
5	19.0	1.06	59	12.0
6	19.5	1.06	51	10.6
7	22.3	0.88	54	10.7
8	20.8	1.0	48	10.0
9	23.1	1.0	54	13.4

Table 2. Experimental results for a perovskite solar cell with a TiO₂ compact layer and KY₇F₂₂ on the rear side, for which 3 substrates were fabricated on the same day and following the identical process.

Jsc stands for short-circuit current, Voc for open-circuit voltage, FF to Fill Factor and PCE to Power Conversion Efficiency

Those results come from only 9 pixels up on the 15 devices and the 6 other available pixels were inoperable for the reasons given above. For their definitions you can refer to Chapter 1 Section I.2.b. These differences are related to slight changes often not controllable or noticeable by the experimenter, creating local defects that affect the cell. Local defects can be due to inhomogeneity of thickness (too thick in the center of the substrate or too thin in the corners), dusts, hole created by a wrong position of the anti-solvent tip, processing temperature during fabrication, or solvent vapors affecting perovskite composition [223].

The variability of results from one batch to another using same experimental condition is even bigger, as shown [Table 3](#), which represents results for solar cells that followed the same experimental procedure than the ones in [Table 2](#), 27 days later (using fresh precursor solutions).

Device N°	Jsc	Voc	FF	PCE
1	18.4	0.8	38	5.6
2	12.0	0.9	41	4.5
3	11.9	0.9	44	4.9
4	11.4	0.9	42	4.5
5	11.2	0.8	38	3.5
6	13.0	0.9	42	5.0
7	13.8	0.9	43	5.7
8	12.8	0.9	42	5.2

Table 3. Experimental results obtained for identical experimental than the results given in Table 2, 27 days later.

These differences are still not fully understood and can be due to numerous factors from uncontrollable solution aging to meteorological conditions, or polydispersity of polymeric HTL [224]. Saliba et al. mention for instance the existence of a “bad batch” with low device efficiencies “without any easily discernible explanation” [223].

A lot of articles address the stability of perovskite solar cells, which are, as mentioned in the first Chapter, very sensitive to moisture, temperature, UV-light and oxygen [225][59][226], but fewer address reproducibility and batch-to-batch or in-batch variations. Reproducibility issues are sometimes quickly mentioned in the literature (“To avoid batch-to-batch variations”) [35][224][227], sometimes qualitatively (“large batch-to-batch as well as in-batch variations with such films” [228]), and sometimes considered as obstacles to data comparison (“the differences in Jsc observed in [figure 1] simply reflect batch-to-batch variation in the perovskite layer, rather than any significant difference between the two fabrication processes” [229]). The treatment of this phenomenon is disproportional to its reality, unfortunately strongly influenced by the long tradition of “positive publishing”. It is “hampering the entire research field [as] it is hard to pinpoint “hidden” variables influencing this system (apart from preparative errors)” [223].

It is however possible to address those high variations and inexactitudes by proceeding to a reliable, transparent and solid statistical analysis of the results.

b. Comparing results - Ideal case

Many statistical tests exist in order to determine the certitude with which we can assert the superiority of the results of the batch i compared to the batch j.

The level zero of the proof consists to verify the hypothesis

$$\bar{x}_i - \Sigma_i > \bar{x}_j + \Sigma_j$$

37

Where \bar{x}_k is the average of the value x for the batch k and Σ_k its standard deviation. Usually we can compare PCEs, however, the comparison of J_{sc} , V_{oc} of FF only can also bring interesting highlights about one specific aspect of the device.

A statistical test called student t-test can also be used to compare two Gaussian distributions. Those distributions follow Equation 38

$$f(x) = \frac{1}{\sqrt{2\pi\Sigma^2}} e^{-\frac{(x-\bar{x})^2}{2\Sigma^2}} \quad 38$$

The case where the distributions are not Gaussian will not be given here and different tests apply then. The t-test can be used to verify whether a distribution is Gaussian or not.

The null hypothesis is: the two batches i and j possess the same distribution (which imply the same mean value and standard deviation). The aim is to proof it's wrong. In order to do so, we calculate from the data of the batches a number called t-value, which can be calculated as

$$t = \frac{\bar{x}_i - \bar{x}_j}{s} \quad 39$$

With

$$s = \sqrt{\frac{\Sigma_i^2}{N_i} + \frac{\Sigma_j^2}{N_j}} \quad 40$$

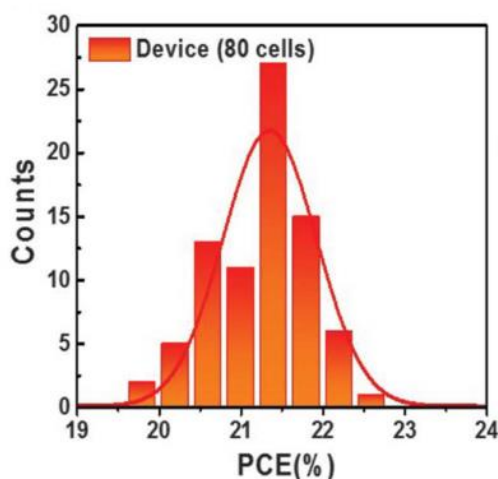
Where N_k is the number of samples in the batch k .

The absolute value t-value is then compared to a value available in the so called t-table, which we can find in Annex 6. This value depends on the number of samples in the batch, and on the confidence level, or p-value. The confidence level describes the confidence with which the null hypothesis can be rejected (and thus with which we can assert that one batch leads to higher efficiencies than the other one).

For instance, if the t-value for the comparison between two batches with 11 samples is equal to 1.8, there are 95% of chances that it is correct to say that the two batches are leading to different results. The case where the two batches have a different number of samples is briefly addressed in the Annex 6.

c. Comparing results – the reality

Most of the time, articles mention the number of devices they use to produce their results. (For instance : 18 for [230][223], 50 for [231], 48 for [172]). However, it happens often that authors compare best performing devices [47][232]. If any error bar is given, the number of devices to which it corresponds is not always precised [115].



In their paper showing the best-performing solar cell known as this work is written, Yang et al. used 80 devices (from different batches, which implicitly suggests a good reproducibility) and fit the results obtained by a curve (probably Gaussian, this was not precised), as shown in Figure 36. Even if cells with higher PCE were obtained, they chose to give the most reproducible result, displaying 21.6%, rather than the best performing one

[5]. A similar approach was also done by Zheng et al. [233] but with less samples (20).

Figure 36. Results obtained by Yang et al., displaying the distribution of PCE of their devices. 21.6% was chosen to be the reproducible average device.

d. Comparing results – what we chose to do

In this work we will be the most transparent on the comparison tools we used (even when they are under publishable expectations). Most of the time, we have at our disposal less than 10 operable cells for the same experimental condition. We will mainly compare best and average performing devices. In the optimization section in Chapter 4, student t-test will be run.

In the main text, best performing devices' I-V curves will be plotted, while Tables displaying the average, best and standard deviations values of J_{sc} V_{oc} FF and PCE will be given in the Annex 8. For the reasons mentioned above, compared results will always be from the same batch. We will usually compare 2 experimental conditions in which only one parameter has changed (spin-coating speed, concentration in UCNPs, precursor solution recipe, annealing time and temperature...) and the conclusion on relative improvement using one or the other condition will be qualitatively drawn by comparing both best performing devices and average values of J_{sc} V_{oc} FF and PCE for each condition. The number of devices used for this comparison will be given.

II. Solar cell fabrication

Solar cell fabrication is a complex procedure, and the slightest modification in any step can lead to drastic change in the resulting device. Any layer's purity, compactness, crystallinity, thickness easily vary as experimental parameters vary, and so does the performance of the device. This is the case for experimental parameters such as temperature and time annealing, spin-coating's speed ramps, solvent engineering timing, angle and relative position of the tip releasing the anti-solvent, and of course any difference of composition of precursor solutions. The measurement method (fixed in this work) can also influence the result: for instance, scan rate or measurement method (I-V set up or incident photon to current efficiency set up) has an impact on J_{sc} and V_{oc} [234].

Precision, high attention and transparency are required from the experimenter, and we shall endeavor to present results which possess those three qualities.

As mentioned in the first chapter, a perovskite solar cell as the one we can see on [Figure 37](#) is a stacking of several layers. In order to improve and optimize the incorporation of UCNPs in a solar cell, the standard device (to which the optimized ones will be compared) must be already as optimized, reproducible and mastered as possible. Even though this experimental investigation is a prerequisite step to the UCNPs and Au NRs implementation, it occupied a non-negligible experimental time and

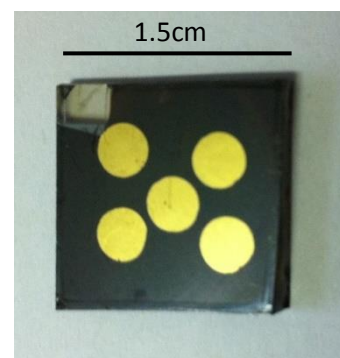


Figure 37. Photography of a standard perovskite solar cell

by giving the details of the standard device optimization journey, we hope to simplify further work addressing similar problematics.

In the upcoming part the experimental protocols of the depositions of those layers will be given, in the order of deposition, followed by their optimizations. UCNPs and Au NRs' deposition processes will be addressed in Chapter 4. Here is the list of the layers (as reminded [Figure 38](#)):

- Electron Transport Layer (ETL): in this work, we used compact and crystalline TiO_2 . Two compositions were compared before an optimum with ETL-free device was found.
- perovskite layer: four different perovskite compositions were tried out. The most reproducible results were obtained with $\text{FA}_{0.83}\text{Cs}_{0.17}\text{Pb}(\text{I}_{0.6}\text{Br}_{0.4})_3$.
- the Hole Transport Layer (HTL): Poly-TPD was compared to Spiro-oMeTAD, that was itself afterwards optimized.
- top electrode made of gold (no optimization).

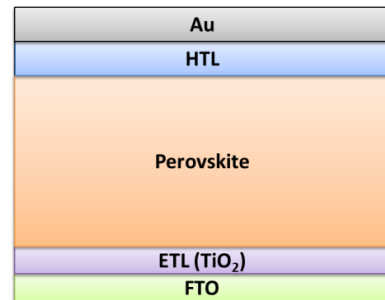


Figure 38. Schematic stacking of layers composing a solar cell

One of the difficulties of optimizing three layers is that a device's performance can be impacted if only one of them is deficient.

The consequence is that the optimization of a certain layer alone might not lead to fully optimized devices, and, worse, if we consider two layers are deficient, the improvement of the first one might not correspond to the optimal device as the second one is improved to, which implies back-and-forth optimizations steps.

1. Pre-treatment and general precautions

The substrates are FTO (Fluoride Tin Oxide, as in [Figure 39](#)) coated glass substrates purchased from Sigma Aldrich (resistivity sheet around $7\Omega/\text{square}$). It is the anode of the device. $1.5\text{ cm} \times 1.5\text{ cm}$ square substrates are cut from the bigger slice with a diamond tip.

In microelectronic fabrication processes, cleanliness is an absolute fundamental rule. Any contamination with chemical, dirt or dust leads to severe losses of performance for the device. Substrates must be hold by plastic tongs each time they are manipulated. Before cleaning the substrates, a number is engraved using a diamond pen on the backside of the substrates, which will be later used to differentiate them.

Substrates are cleaned through 5 steps of sonication lasting 30 minutes each, the first one in acetone, the second in isopropanol (IPA), the third one in deionized (DI) water and a last IPA cleaning bath. They are dried using an air gun and then conditioned in their boxes. Right before being used, the last cleaning step is executed: 10 min in oxygen plasma. It removes the last organic components on the surface.

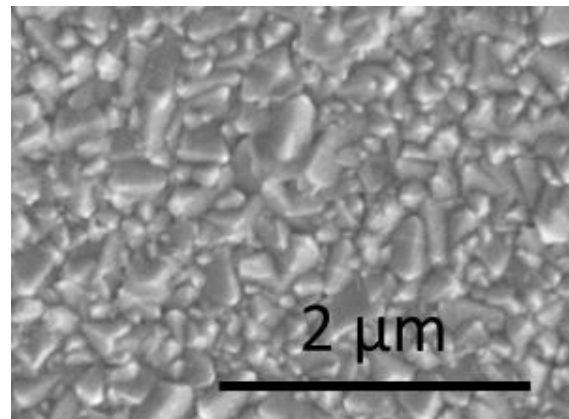


Figure 39. FTO microstructure on the SEM (Scanning Electron Microscope)

In order to be able to make a contact between the two electrodes, which is necessary for all electrical measurements, a tape is applied on a same corner of the substrate before each deposition, apart from gold, and removed after each deposition, ensuring an access to FTO layer.

All the layers apart from gold are deposited using a spin-coater. Spin-coating is a process relying on centrifuge force which deposits a thin layer using a solution precursor of this layer. It is usually followed by annealing for solvent evaporation and sometimes crystallization. Annealing can be a key step of the process, since high temperatures may degrade the material (so annealing time and temperature may have to be adjusted). For a given precursor solution concentration, the thickness of the layer is mainly determined by the rotation speed and speed ramps. The speed can be empirically adapted starting from literature's value and adjusting regarding thickness measurements and devices' performances. Thicknesses are measured using a profilometer Dektak. The chemical products providers can be found in Annex 8.

The best results are obtained when all the fabrication steps are executed in a row (starting from oxygen plasma) within 1,5 days and shortly after precursor solutions preparations, following this timetable:

Day -7 to Day -1: Perovskite solution preparation, HTL solution preparation

Day 1: Oxygen plasma, optional TiO₂ deposition and sintering, perovskite deposition, HTL deposition, stored in the dry box overnight in the case of spiro-OMeTAD as a HTL (for oxidation).

Day 2: Gold evaporation. Electrical measurements such as I-V curve measurement were also done in a row. Even if devices are further stored in a dry box (or in a glove-box when tests must be run long after the fabrication), performances can rapidly deteriorate because of air and humidity. TiO₂ solution has to be kept for duration of maximum 3 months, Spiro-OMeTAD for two weeks, perovskite solutions for one week.

2. Electron Transport Layer – TiO₂

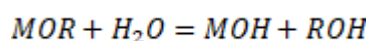
a. Sol-gel method

As explained in the first chapter, titanium dioxide is an n-type ETL. It is usually called blocking-layer, as it blocks holes which would short-circuit the cell by escaping through the FTO electrode [235]. It is the first layer deposited after cleaning the substrates. It's deposited by spin-coating, and later annealed in order to form the final titanium oxide phase (anatase) at 400°C. Surface morphology and film resistance are crucial for the performance of a device: any pin-hole represents a leakage route for holes and has to be avoided. We can sometimes observe cracks, examples shown [Figure 40\(a\)](#) and [\(b\)](#). This can happen when the film is subject to high humidity or because of inappropriate deposition speed, thermal shock, solution aging or internal stresses.

A flawless layer looks like [Figure 40\(c\)](#). It's a thin layer (thickness around 50 nm). We can see the FTO surface underneath.

The film formation is called sol-gel.

Sol-gel technique is a fabrication method often used for inorganic oxides that relies on two steps: hydrolysis and condensation, followed later by calcination. Hydrolysis is described by the reaction of an alcoholate M(OR)_n where M is a metal and R an alkyl (in our case, M=titanium, R=isopropyl and n=4), with water, leading to the component M(OH)_n (and the corresponding alcohol ROH):



41

Condensation relies on the formation of M-O-M bonds:

During the annealing process, water and alcohol are evaporated and the titanium dioxide solid remains and crystallizes.

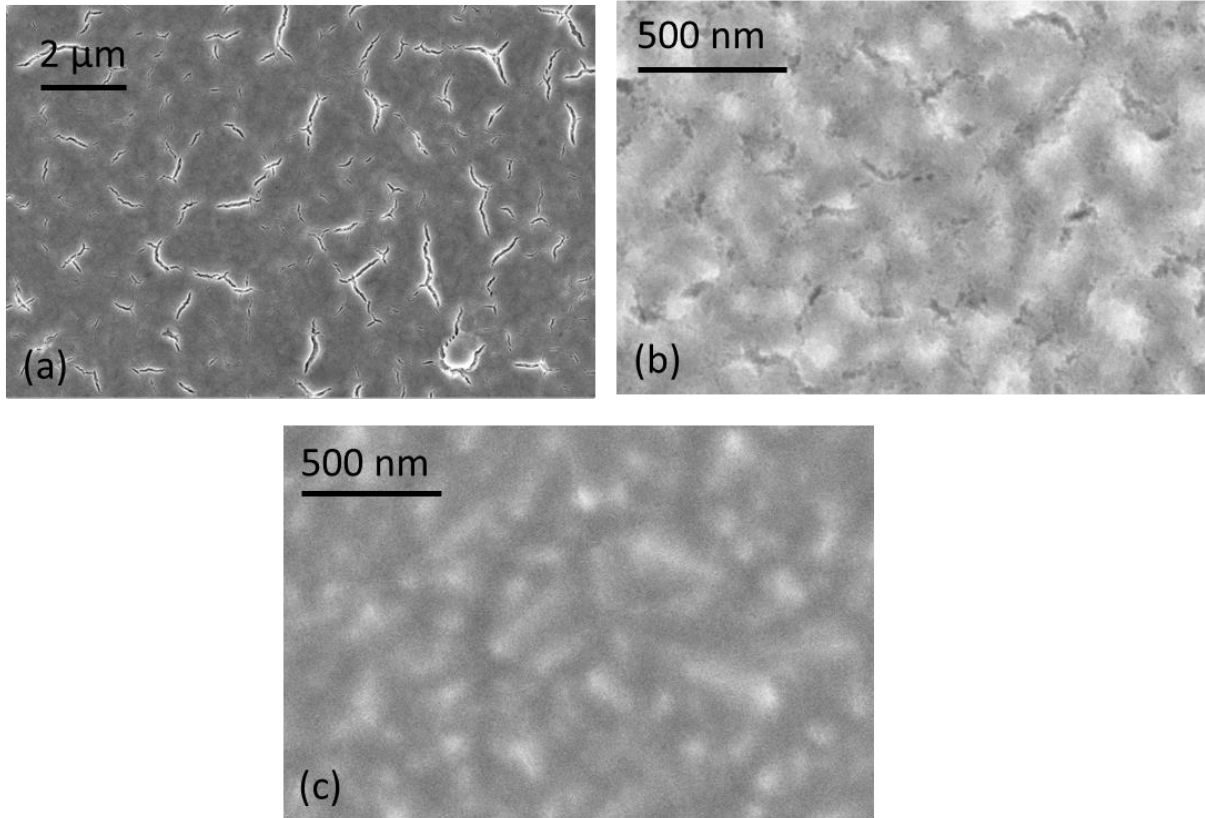


Figure 40. SEM pictures of TiO₂. (a) ³Ti recipe with a second step at 2000 rpm. We can observe long and deep cracks that are responsible of unusually low performance of the device. (b) ²Ti that was not further used for device fabrication. The surface is neither smooth nor compact (c) ¹Ti diluted in water 1:1. This detail is representative of the whole sample.

In this work we have carrier out some tests on three different recipes, summarized in the table below in the order of use:

Recipe's name	Solution preparation	Deposition speed	Annealing step 1	Annealing step 2	Thickness (/nm)	Ref
¹ Ti	10 mL DI water 100μL HNO ₃ 69 wt % 2mL TTIP stir in oil bath at 60°C for 6 hours	2000 rpm 60s	3 min 125°C	30 min 500°C	130 (50 in the reference)	[1][236]
² Ti	0.15 M Titanium diisopropoxide bis(acetylacetonate) in butan-1-ol	5000 rpm 30s	5 min 125°C then repeated twice with 0.3 M Titanium diisopropoxide bis(acetylacetonate)	15 min 500°C	300	[237]

			te) in butan-1-ol			
³ Ti	15 mL EtOH 100 μL HCl 37 wt % 0.9 mL TTIP	500 rpm 5s 5000 rpm 25s	15 min 200°C	1h 500°C	30/80	Adapted from [238]

Table 4. Summary of the compact TiO₂ recipes experimented in this work. TTIP = titanium isopropoxide. rpm = round per minute

The annealing process is a sensitive step: any temperature shock has to be avoided in order to reduce intern stress in the layer. Thus, before transferring the substrates from the hot plate to the oven, we would rather wait the sample to cool down, or to put them in an already preheated oven, using a preheated petri dish.

b. Optimization of two recipes ¹Ti and ³Ti

²Ti was not optimized as the whole process was longer and the first tries gave relatively mediocre performances (Figure 40(b)). ¹Ti and ³Ti were optimized and then compared. In order to do so, we compared results for different recipes or for the same recipe but varying many parameters:

- Concentration in TTIP (water dilution for ¹Ti, in order to decrease thickness that exceeds 100 nm)
- Spin-coating speeds for deposition and length of the ramp
- Age of the solution
- Recipes between them
- Annealing time and temperature (2 annealing steps);

We tried to draw conclusions in order to obtain the process and recipe giving the highest device performance.

We will only give results (consisting in IV curves) that concern speed optimization and comparing recipes between them. As described in the section I.1, this measure consists in measuring the current between the two electrodes as the voltage varies from 1,1 V to 0. We can notice that the open-circuit voltage presented here are relatively low. Voc values increased when perovskite's precursor solutions were later improved.

Speed optimization mainly relies on variation of thickness of the deposited layer. As a comparison, Wu et al. deposited TiO₂ by Atomic Layer Deposition (ALD) and the thickness was 50nm [239]. For a sol-gel deposition method, Wojciechowski et al. found optimized TiO₂ thickness of 45 nm [240].

¹Ti's deposition speed was optimized at 2000 rpm after having compared devices resulting from 2000 rpm and 4000 rpm. Jsc, Voc, FF and PCE average, best and standard deviation values are given in Table 10 and Table 11 of Annex 7. Best devices' IV curves are shown Figure 41(a) By looking in those tables, we can see that average PCE is around 3.5 times higher when a speed of 2000 rpm was used, which is surprising as the thickness of 190 nm obtained in this case (compared to 140 nm for 4000 rpm) is much bigger than the average TiO₂ thickness mentioned in the literature. This might be related to the existence of a thickness range that particularly has to be avoided and under or over which the resulting device is better (maybe because of destructive interference). A thickness of 190 nm leads to better devices than 140 nm.

A similar experience was conducted regarding ^3Ti 's deposition speed. We can see in [Table 12](#) and [Table 13](#) of Annex 7 which compare performances of devices on which ^3Ti was spun at 5000 rpm versus 2000 rpm, that the average for devices at 2000 rpm is 1.8 times the one at 5000 rpm. Best devices for both conditions are shown [Figure 41\(b\)](#). We notice that this increase of PCE is mainly due to a much larger J_{sc} (almost two times higher for 2000 rpm). The thicknesses are respectively 80

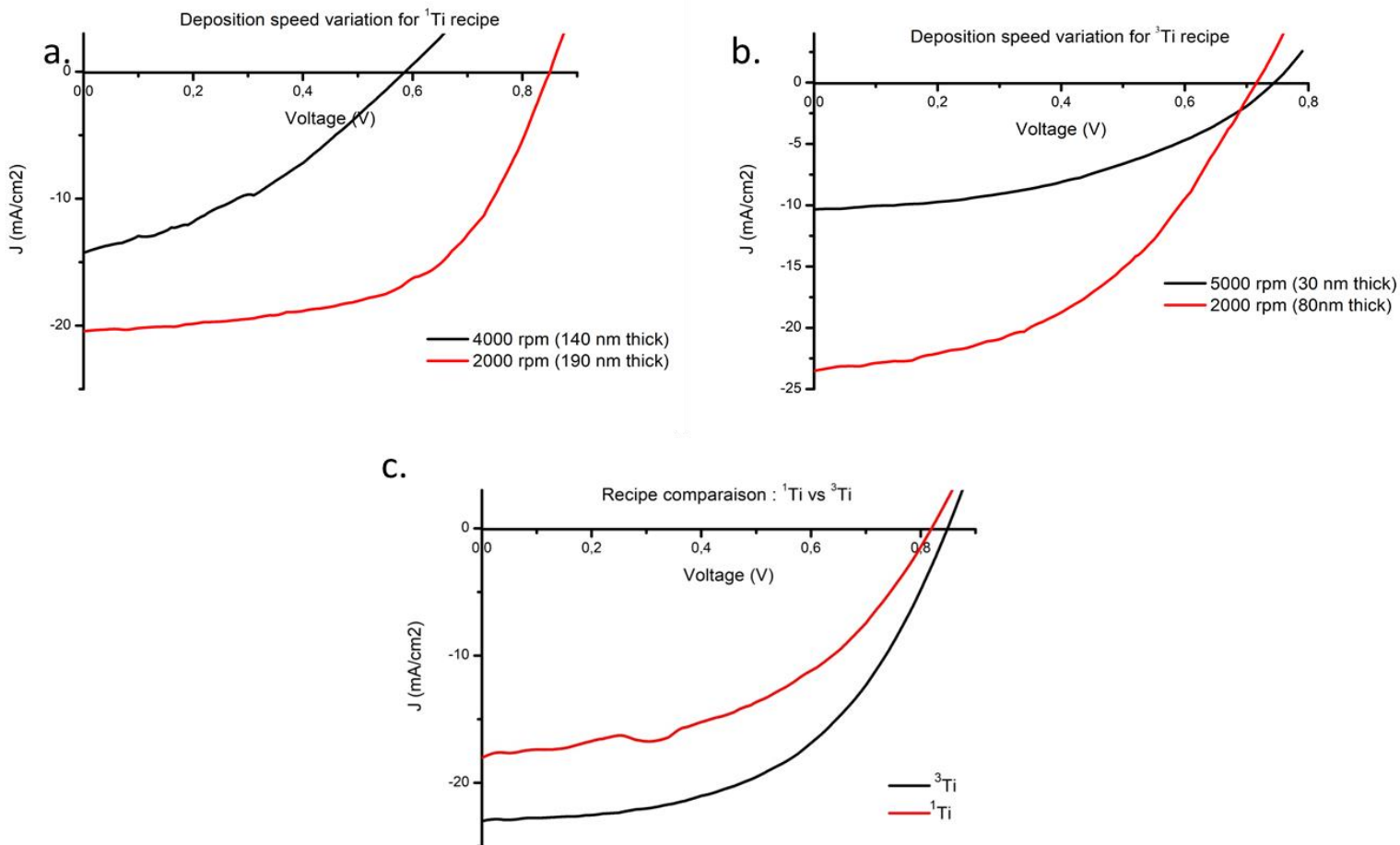


Figure 41 Best devices for a. ^1Ti deposition speed variation b. ^3Ti deposition speed variation c. Comparison between ^1Ti and ^3Ti .

(2000 rpm) and 30 nm (5000 rpm). It seems that 30 nm is not thick enough for this layer.

We finally compared ^1Ti and ^3Ti recipe, since thickness of ^1Ti seems to be too big compared to the optimal thickness reported in the literature. As we can see on [Table 14](#) and [Table 15](#) of Annex 7, the average PCE is 2 times higher for ^3Ti than for ^1Ti . The best devices for each respective condition are shown [Figure 41.c](#).

Those experiments led us to use ^3Ti for other parameters' optimization.

Some of our UCNPs-incorporated devices adopted an ETL-free device structure. It's well known that ETL-free structure devices can also lead to efficient devices (and represent a significant advantage to have a simpler structure) [13][241][242][243][244].

A mesoporous layer, often made of aluminum oxide or titanium dioxide nanoparticles can be deposited on top of the ETL. It acts as a scaffold that improves charge transport, perovskite

crystallinity and optimizes its thickness, by reducing the distance crossed by electrons before being injected in the TiO₂ [245]. Different mesoporous scaffold recipes were experimented during the early stage of this thesis work but unfortunately, we did not reach a satisfactory optimization. Therefore, we did not use mesoporous recipe for UCNP implementation.

3. Perovskite

We will now discuss the optimization of the absorber layer. 4 recipes will be related and discussed in this work. They are related in the [Table 5](#).

Recipe's name	Solution preparation	Deposition speed	Annealing process	Ref
MAPbI _{3-x} Cl _x	54 mg PbCl ₂ 103 mg MAI In 0.5 mL DMF	2000 rpm for 60 sec	100°C 50 min	[246]
¹ MAPbI ₃	202 mg PbI ₂ 70 mg MAI In 0.5 mL DMF	2000 rpm for 60 sec	100°C 20 min	[246]
² MAPbI ₃	333 mg PbI ₂ 182 mg MAI In 1 mL DMSO	1000 rpm for 15 sec 6000 rpm for 40 sec 100 μL CBZ dropped between the 10 th and the 15 th of the second step	115°C for 15 min	[247]
FA _{0.83} Cs _{0.17} Pb(I _{0.6} Br _{0.4}) ₃	178 mg FAI 55 mg CsI 208 mg PbI ₂ 275 mg PbBr ₂ 1 mL DMF 36 μL HBr 72 μL HI	2000 rpm for 1 min 100 μL of CBZ dropped between the 10 th and 15 th second.	70°C for 1 min 100°C for 40 min	[248]

Table 5. Summary of the perovskite recipes experimented in this work. CBZ = Chlorobenzene. DMF = Dimethylformamide. FAI = formamidinium iodide. MAI = methylammonium

Layers are prepared and annealed in an argon-filled glovebox. The thickness of the perovskite's layer is usually between 400 and 600 nm depending on the process and the precursor solution. The reason why so many different recipes were chosen is because each of them represented an improvement compared to the previous one: MAPbI_{3-x}Cl_x and ¹MAPbI₃ showed relatively low Voc and FF ([Figure 42.b.](#)), even when TiO₂ was optimized. Those problems were then partially solved by ²MAPbI₃, for which we obtained higher Voc (around 1V, [Figure 44](#)), but the FF remained low (around 50%). This is why we finally adopted the ETL-free FA_{0.83}Cs_{0.17}Pb(I_{0.6}Br_{0.4})₃ (which gave more satisfactory FF) to implement UCNPs.

a. HC(NH₂)₂I (FAI) and CH₃NH₂I (MAI) synthesis

FAI and MAI are either used in perovskite precursor solutions.

Synthesis of FAI (in collaboration with Zhelu Hu). FAI was prepared according to the method reported by Wozny et al. [249] with minor modifications. In a typical preparation, 12.60 g of formamidinium acetate was added to 125 mL of methanol in a 250-mL-volume Erlenmeyer flask that was immersed in an ice bath. 24 mL of hydriodic acid (57 wt %) was then added dropwise. The reaction was left stirring for approximately 2 hours at room temperature. The precipitate was collected by evaporating the entire reaction product at 55 °C during 2 hours. After evaporation, the obtained solid was dissolved in isopropanol and precipitated by adding diethyl ether and subsequent centrifugation. This precipitation and centrifuge procedure was repeated three times. The final white powders obtained were dried in a vacuum oven at 50 °C overnight before being transferred to an Ar-filled glovebox for storage.

Synthesis of MAI. CH₃NH₂I was synthesized according to a method described by Roldan-Carmona et al. [250]. In an ice bath for 2 hours, 21.6 mL methylamine (40 wt % in water) and 30 mL hydriodic acid (57 wt % in water) are mixed together. Solvent is evaporated once the mixture has recovered a room temperature using a rotatory evaporator. The so-obtained solid is then kept under vacuum at 50°C for 30 min, and then dissolved in IPA before being washed with diethyl ether, centrifuged, and washed again with EtOH/diethylether (volumic ratio 1:3), centrifuged, washed with pure EtOH, until the powder turns totally white. It's then further dried out in a vacuum oven at 50°C overnight, and then stored in argon-filled glove-box.

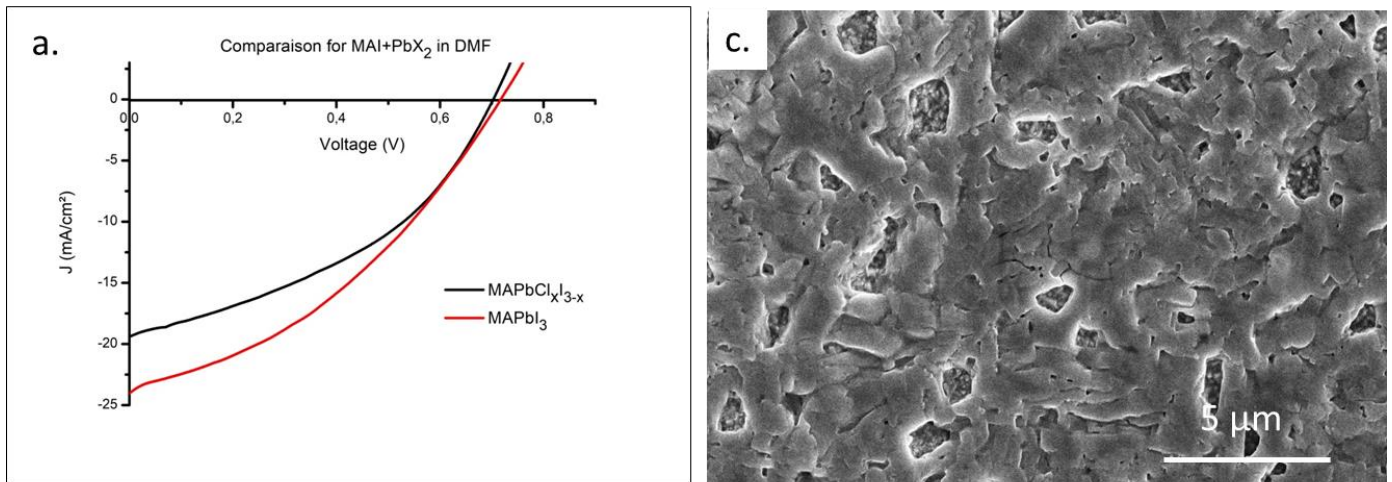
b. ¹MAPbI₃ and MAPbI_{3-x}Cl_x in DMF (N,N-dimethylformamide)

MAPbI₃ and MAPbI_{3-x}Cl_x are the two most commonly studied perovskites as solar converter [246]. The film deposition has a critical influence over the film morphology and on the cell performance [251]. The role of chlorine has been reported as a crucial actor to increase of the perovskite crystal size, resulting in an increase of the electron diffusion length [252][3].

The preparation of the precursor solutions for these two perovskites were inspired by a work from Tidhar et al. [246]. ¹MAPbI₃ precursor solution contains 202 mg of PbI₂ and 70 mg of MAI in 0.5 mL DMF (0.88 M equimolar), and MAPbI_{3-x}Cl_x precursor solution contains 54 mg of PbCl₂ and 103 mg of MAI in the same volume of DMF (0.88 M, molar ratio 3:1 MAI:PbCl₂, as described in [56], [253],[254]).

They were both deposited on the TiO₂ layer by spin-coating at 2000 rpm for one minute and annealed at 100 °C for 50 min (lead chloride case) and 20 min (lead iodide case) until they took a dark coloration. Both recipes give comparable results, as we can see from [Figure 42\(a\)](#) The PCE of the PbI₂ based device shown here is 6.4% and the one of the PbCl₂ device is 6.1% ¹Ti was used as TiO₂ layer, and ¹Spiro as HTL.

The PCEs of those devices are under lower than one would expect from this type of perovskite. This can be explained by the quality of the perovskite film, as we can see on a SEM picture of $\text{MAPbI}_{3-x}\text{Cl}_x$ (Figure 42.c): the discontinuity of the film and micrometer size holes allow a contact between the HTL and the ETL, and increase the probability of short circuits, thus decreasing J_{sc} and V_{oc} . Crystallographic investigation was run and let us conclude that the crystallographic structure itself of the perovskite film does not correspond to the one of the pure film from the literature, as we can see on Figure 43. The presence of impurities is observed (e.g. PbI_2 or MAPbCl_3).



	J_{sc} (mA/cm ²)	V_{oc} (V)	FF (%)	PCE (%)
$\text{MAPbCl}_x\text{I}_{3-x}$	21,5	0,7	40	6,1
MAPbI_3	24,0	0,7	37	6,4

Figure 42. a. I-V curves comparing best devices obtained with two different and not fully optimized perovskite formulas. b. Datas for curves plotted in a. There are no average data Tables available for these conditions since we only obtained one exploitable pixel for each device. c. SEM Image of $\text{MAPbI}_{3-x}\text{Cl}_x$ on FTO substrate.

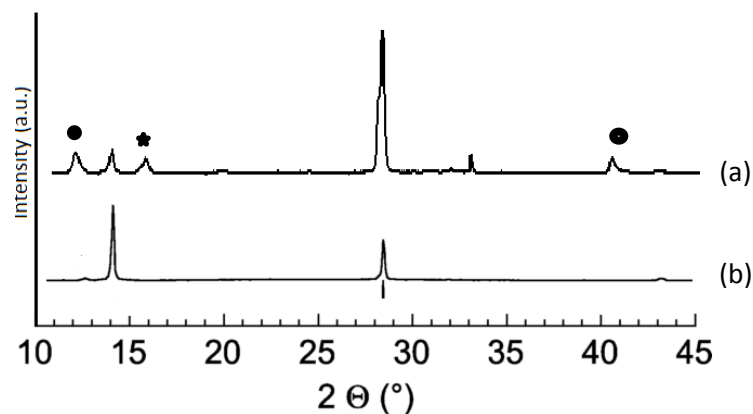


Figure 43. XRD of $\text{MAPbI}_{3-x}\text{Cl}_x$ (a) prepared as described above (b) from the literature [50]. The dot corresponds to the presence of PbI_2 and the star to the presence of MAPbCl_3 . The peak at 33° could be attributed to FTO.

For those reasons, we decided to improve the crystallinity of the perovskite layer and tested two solvent engineering methods. Such solvent engineering method consists in dropping 100 μL of anti-solvent (CBZ in this work) at a precise point of the spin-coating step. This solvent is chosen in order not to dissolve the perovskite. This drop-casting step improves crystallization because it prevents the precocious crystallization that happens during rotation which results into inhomogeneous islands with low coverage. The anti-solvent method forms a uniform and amorphous layer, with a full surface coverage and low roughness (as confirmed qualitatively and quantitatively by respectively its brilliance and XRD measurements by Jeon et al.) [255]

c. Solvent engineering methods - ${}^2\text{MAPbI}_3$ in DMSO, $\text{FA}_{0.83}\text{Cs}_{0.17}\text{Pb}(\text{I}_{0.6}\text{Br}_{0.4})_3$ in DMF

${}^2\text{MAPbI}_3$ was prepared following the method described in [247] by dissolving 333 mg PbI_2 and 182 mg MAI (1.2M equimolar) in DMSO (dimethylsulfoxide). The spin-coating deposition is run in two steps: first step at 1000 rpm for 15s with 10s acceleration, followed by a step at 6000 rpm for 40s with 3s acceleration. Between the 10th and the 15th second of the second step, 100 μL of CBZ was dropped on the center of the rotating sample. Substrates were annealed at 115°C for 15 min (temperature and time annealing were optimized but these optimizations won't be discussed here).

$\text{FA}_{0.83}\text{Cs}_{0.17}\text{Pb}(\text{I}_{0.6}\text{Br}_{0.4})_3$ was prepared as described in [248] by dissolving 178 mg of FAI, 55mg of CsI, 208 mg of PbI_2 , 275 mg of PbBr_2 in 1 mL DMF and adding 36 μL HBr and 72 μL of HI. The deposition was done at 2000 rpm for 55s. 120 μL of CBZ were dropped between the 10th and the 15th second of the process. Substrates were annealed 1 min at 70°C right after deposition and then on air at 100°C for 40 min. This recipe is compatible with an ETL-free device.

$\text{FA}_{0.83}\text{Cs}_{0.17}\text{Pb}(\text{I}_{0.6}\text{Br}_{0.4})_3$ was developed after we noticed some inexplicable and slow (over 4 months) degradation of the performance of ${}^2\text{MAPbI}_3$ - devices. $\text{FA}_{0.83}\text{Cs}_{0.17}\text{Pb}(\text{I}_{0.6}\text{Br}_{0.4})_3$ showed much higher V_{oc} and FF than ${}^2\text{MAPbI}_3$ as we can see on [Figure 44](#) and on [Annex 7 Table 16](#) and [Table 17](#) (1.06 against 0.87 V for average V_{oc} and 60 against 45 % for average FF).

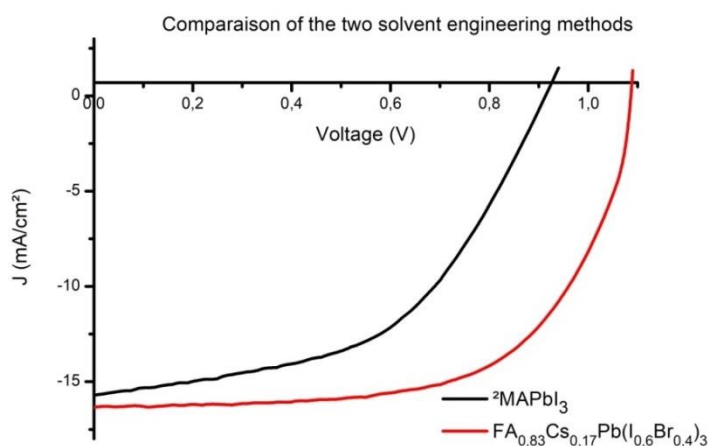


Figure 44. IV curve comparison between $\text{FA}_{0.83}\text{Cs}_{0.17}\text{Pb}(\text{I}_{0.6}\text{Br}_{0.4})_3$ and ${}^2\text{MAPbI}_3$. Jsc Voc FF and PCE tables can be found in [Annex 7 Table 16](#) and [Table 17](#).

4. HTL

The HTL is a matching layer whose HOMO (Highest Occupied Molecular Orbital) is chosen close to that of perovskite. In this work, we mainly used Spiro-oMeTAD (2,2',7,7'-Tetrakis[N,N-di(4-methoxyphenyl)amino]-9,9'-spirobifluorene) and Poly-TPD (Poly(N,N'-bis-4-butylphenyl-N,N'-bisphenyl)benzidine), both chemical formulas are given [Figure 45](#). HTLs are deposited in an Argon filled glovebox. The thickness of a HTL is between 200 and 400 nm.

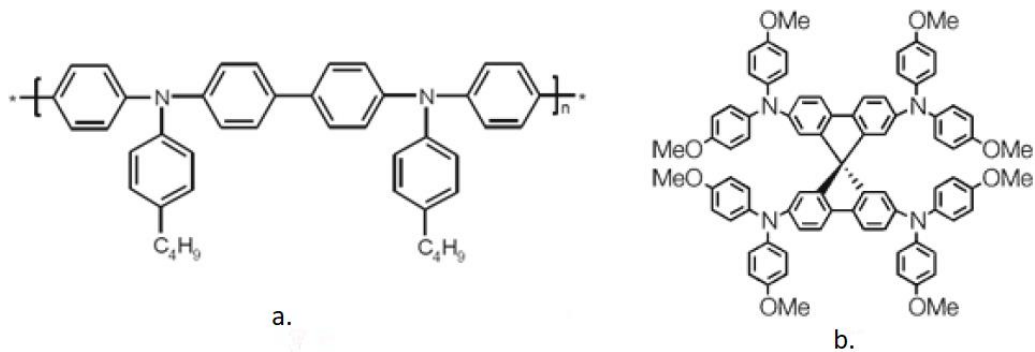


Figure 45.a.Poly-TPD b.Spiro oMeTAD. [1]

a.Poly TPD and ¹Spiro comparison

12mg of Poly-TPD were dissolved in 1mL DCB (dichlorobenzene) during 1 hour at 80°C following a method described in [1]. 40μL of the solution were deposited on the substrate and spun for 1 min at 4000 rpm, and the substrate was then annealed at 80 °C for 15 min.

¹Spiro was the first optimized Spiro-oMeTAD solution, and it was prepared by dissolving 67 mg of Spiro-oMeTAD in 1mL CBZ following a method described by [238]. 30 μL of TBP (4,tert-butylpyridine) were added to the solution, which was stirred for 1 hour before adding 20 μL of a Li-TFSI solution (520mg/mL in acetonitrile). The solution was kept 24h under stirring before being used. It was then deposited at 4000 rpm for 40s with 4s acceleration, and kept overnight in a dry box to allow oxidation.

Li-TFSI stands for Lithium bis(trifluoromethanesulfonyl)imide. Li-TFSI acts on the polymer film as a p-dopant [256]. It increases the conductivity of the film. Ambient air exposure results in a redistribution of Li-TFSI across the Spiro-oMeTAD layer and increases its conductivity [257]. Since water damages the perovskite layer, air exposure is replaced by oxidation in a dry box.

Comparison between the two recipes (all other parameters being equal) was run and lead to I-V curve comparison shown in [Figure 46](#). The device using Poly-TPD as HTL shows much worse performances than the one with ¹Spiro (average performance of 0.4% against 4.7%), as we can see on [Table 18](#) and [Table 19](#) of Annex 7.

The reasons of the unexpectedly low performance for the device with Poly-TPD have not been further inquired.

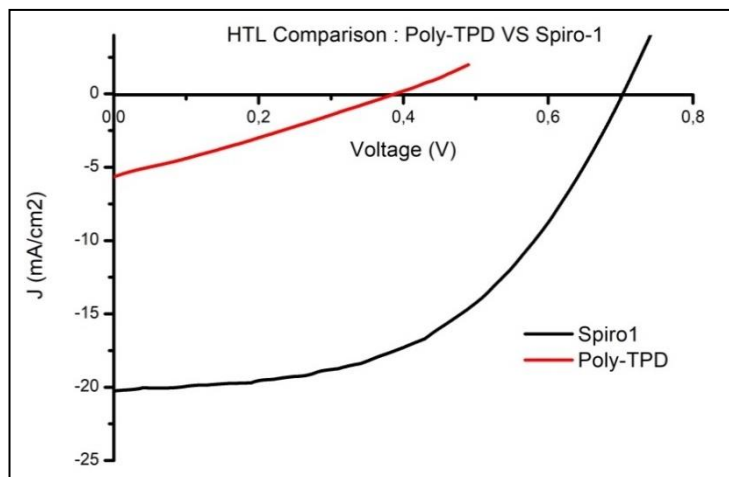


Figure 46. IV curve comparison for Poly-TPD and Spiro1. Jsc Voc FF and PCE tables can be found in Annex 7 Table 9 and 10.

b. ¹Spiro vs ²Spiro

²Spiro's recipe is similar than the one for ¹Spiro (it's more concentrated in Spiro-oMeTAD and contains slightly less TBP and Li TFSI): 96.5mg of Spiro-oMeTAD were dissolved in 1mL CBZ. 10 μ L of TBP and 32 μ L of LiTFSI (170 mg/mL in acetonitrile) are then added as described in Ref [258]. The comparison between ¹Spiro and ²Spiro is shown [Figure 47](#). We notice that the ²Spiro gives a higher PCE, Jsc and Voc than ¹Spiro (data available in [Table 20](#) and [Table 21](#) of Annex 7): 7.6 % against 4.7% for average PCE, 15.7 against 12.3 mA/cm² for Jsc and 1 against 0.9 V for average Voc.

We therefore applied ²Spiro as the HTL in all other experiments carried out in this work.

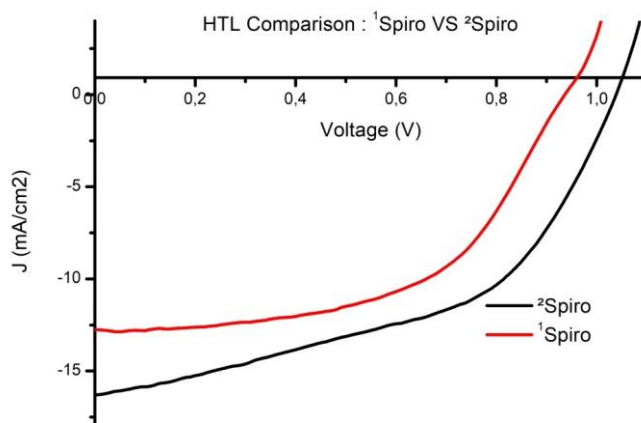


Figure 47. IV curve comparison for ¹Spiro and ²Spiro . Jsc Voc FF and PCE tables can be found in Annex 7 [Table 20](#) and [Table 21](#).

5. Gold

Gold is the top electrode. A thickness around 80 nm is deposited with a metal evaporator under vacuum (around $3 \cdot 10^{-6}$ mbar at the beginning of the deposition to 10^{-5} mbar at the end). A mask was fabricated at the workshop of the laboratory starting from a thin metal plate cut in a 15 cm x 15 cm square, in which 3.5 mm holes were drilled, as we can see in [Figure 48 \(a\)](#) . Holes measure an average of 3.7 mm after drilling, which makes a surface of 0.107cm². We estimate the error on the diameter to be around 0.2mm, which makes an error on the surface of 0.02cm².

5 holes per device's spot were drilled, and there are 12 spots for 12 devices on the mask. Devices were stuck on their edges to the mask using carbon tape. The mask with attached samples was then stuck to the top rotating plate in the evaporator with vacuum tape. The deposition rate was kept around $1\text{\AA}/\text{s}$.

The surface of a gold pixel is shown on a photograph taken with a microscope of magnification of 5 in [Figure 48 \(b\)](#). A few black holes can be observed on the surface.

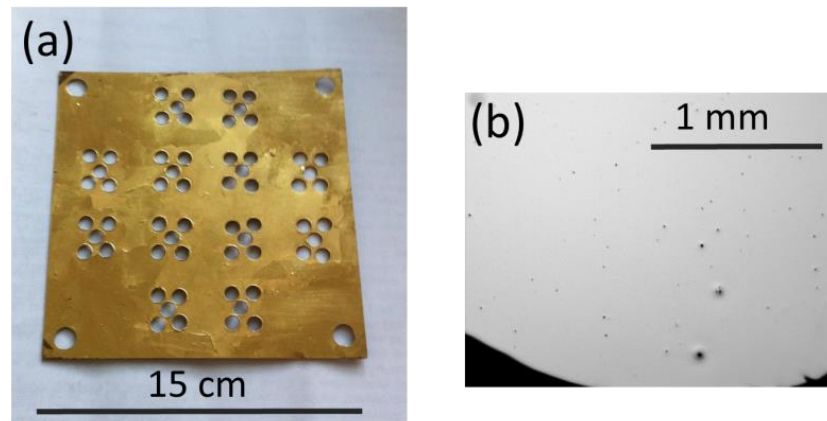


Figure 48. (a) Photography of the front side of the mask used for gold evaporation. (b) Photography of the surface of a pixel after gold deposition

The fabrication of solar cells, the data acquisition, and data analysis being now well defined, we can consider the synthesis of both nanoparticles (upconversion or plasmonic structures) that will later be implemented inside the devices.

Chapter 3. Synthesis, Optical and Structural characterization of nanorods and upconversion nanoparticles

This chapter is dedicated to the detailed protocols of upconversion nanoparticles and gold nanorods synthesis, as well as exposing the few methods that were used to characterize those two types of nanoparticles.

I. Nanoparticles characterization's methods

a. Absorbance measurements

On powder (UCNPs)

The Kubelka-Munk (KM) model describes the interaction of incoming light with a layer of highly scattering material, such as powder, supposed to be uniform, isotropic, non-fluorescent and non-glossy. The model is widely described by Džimbeg-malčić et al.[259] and is used in particular in diffuse reflectance spectroscopy.

The expression of the absorbance as a function of reflectance R is given by

$$F(R) = \frac{(1 - R)^2}{2R} \quad 43$$

The absorbance of $KY_3F_{10}:5\%Er^{3+}:20\%Yb^{3+}$ is shown [Figure 49](#).

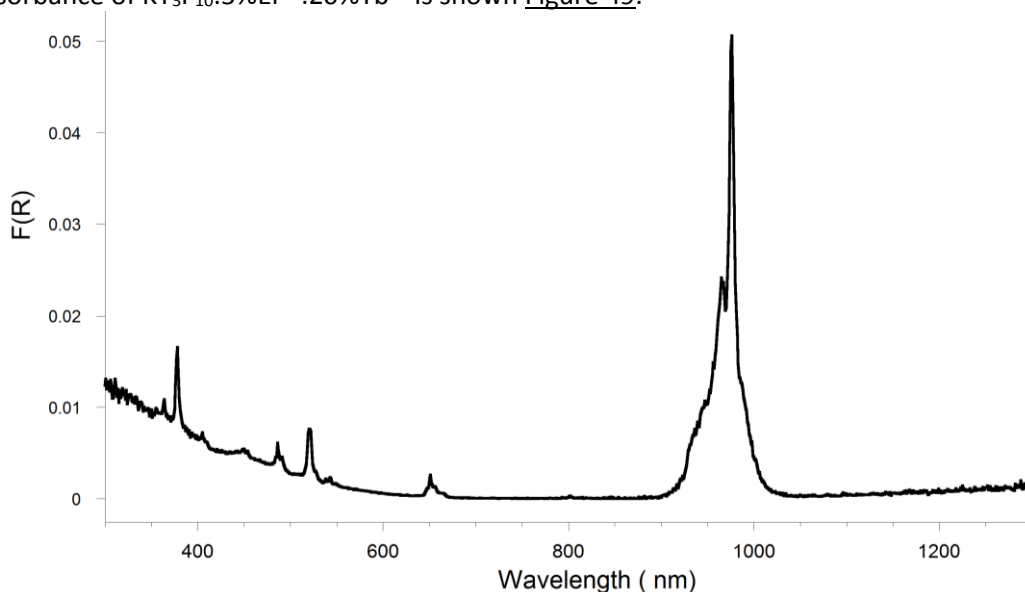


Figure 49. K-M Absorbance of $KY_7F_{22}:5\%Er^{3+}:20\%Yb^{3+}$ obtained by diffuse reflectance measurement.

The large absorption peak around 960 nm is the ytterbium's one. Peaks around 380, 480, 520 and 650 nm are attributed to absorption of Er^{3+} [260].

UV-vis Absorbance (for Au NRs)

UV-vis absorption spectra were measured in air using by an Agilent Cary 5E.

b. PhotoLuminescence Quantum Efficiency (PLQE)

The Photoluminescence Quantum Efficiency or PLQE defines the ratio of emitted photons on absorbed photons (in percentage). It can be measured through a set-up (Figure 50) that includes an integrating sphere, a NIR laser and a spectrophotometer covering the spectral range of emission and excitation, as described by Faulkner et al. [261].

In a typical experiment, two spectrums are recorded under the following conditions:

- Excitation source incident inside the empty sphere
- Sample inside the sphere and hit by the laser (in the beam path)

The PLQE is then expressed as

$$\eta = \frac{P_b}{L_a - L_b} \quad 44$$

Where

- P_b is the PL peak integrated over the emission range, and
- L_a and L_b the excitation peak in case of empty sphere (a) and with the sample inside (b) integrated over the excitation range.

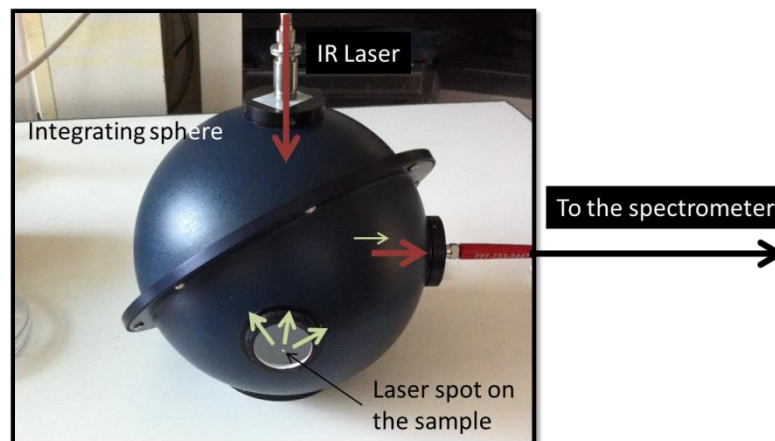


Figure 50. Photography of the PLQE set-up.

In our case, PLQE were measured on UCNP powder.

The PLQE of $\text{KY}_3\text{F}_{10} : \text{YF}_3 : 5\% \text{Er}^{3+} : 20\% \text{Yb}^{3+}$ was measured by using the 2MM (two Measurements Method, different from the 3MM which will not be given here), integrating the signal plotted in Figure 51, and a PLQE of 6.7% was found. This value is higher than the one found by van Veggel and Boyer, for $\text{NaYF}_4 : 2\% \text{Er}^{3+} : 20\% \text{Yb}^{3+}$ (around 4%) [101]. In that range of values, standard deviations are relatively high as we can see Figure 18, so we consider those two results as values belonging to the same order of magnitude.

This technique is limited by different experimental parameters:

- Spectrometer detection limits: luminescence being correlated to particles' size (see discussion Chapter 1.II.5), the luminescence of small particles is too small to be detected by the spectrometer. This was for instance the case for $\text{NaYF}_4 : \text{Gd}^{3+} : \text{Er}^{3+} : \text{Yb}^{3+}$, whose diameters

were between 20 and 40 nm. For the same reason (relative low luminescence), those particles are less likely to be good candidates for solar cells' improvement.

The topography of the powder also plays an important role: since the intensity changes radically when the laser hits a hill or a valley of the powder, only the spot hit by the laser might determine the possibility to measure PLQE or not.

- The fact that it's not possible to obtain at the same time no saturation of the excitation peak and a detectable luminescence peak led us to find a solution by changing integration time between the two measures (the luminescence with a long integration time 1 to 2s, the laser with a smaller integration time around 5ms. The background subtraction has to be done each time the integration time is changed). The signal is then corrected in order to obtain the same scale bar. This is allowed by the linear variation of intensity with integration time (a doubled integration time will lead to a doubled integrated intensity).

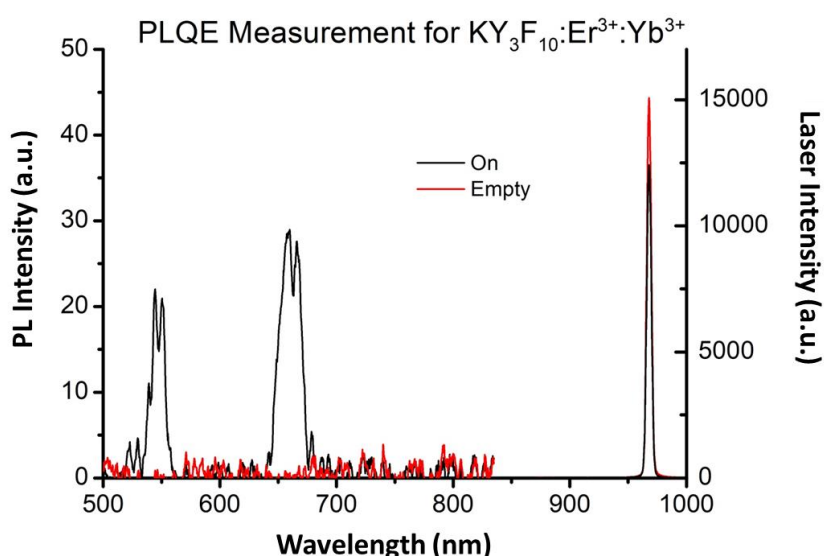


Figure 51. PLQE measurement: PL and excitation peak of a $KY_3F_{10}:YF_3:5\%Er^{3+}:20\%Yb^{3+}$ IPA solution are measured as the sample is either not placed in the sphere (empty) or is placed in front of 980 nm laser (on). For the sake of visibility, a different scale is used for emission and excitation intensities.

To have an idea on error bars on PLQE measurements with the set-up used in this work, the reader can have a look at [Figure 24](#) of Chapter 1. The error bar is around $\pm 2\%$ for a PLQE of 4%.

The PLQEs of all of the UCNPs on which it was measurable are given in the section II.6.b. of this chapter.

c. PhotoLuminescence (PL) spectrum

A PL spectrum corresponds to the emission of the UCNPs under excitation at a wavelength that corresponds to UC's absorption (980 nm in the case of ytterbium and erbium doped fluoride matrix). The normalized PL spectrum of doped $KY_3F_{10}:YF_3$ and KY_7F_{22} are shown [Figure 52](#).

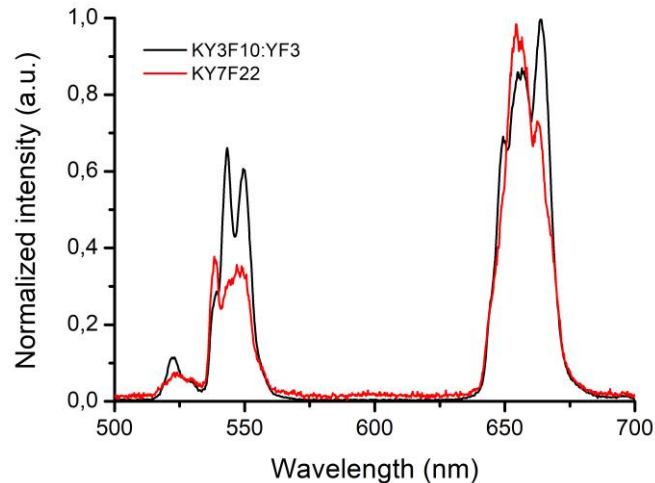


Figure 52. Normalized PL Spectrum of doped $KY_3F_{10}:YF_3$ and KY_7F_{22} . Excitation 975 nm.

The peaks around 650 nm and 550 nm correspond respectively to ${}^4F_{9/2} \rightarrow {}^4I_{15/2}$ and ${}^4S_{3/2} \rightarrow {}^4I_{15/2}$ (the small peak around 525nm corresponds to ${}^2H_{11/2} \rightarrow {}^4I_{15/2}$).

The different peaks observed on a PL spectrum correspond to the possible relaxations and their intensity is proportional to the population of the level from which the relaxation is emitted. The PL spectrum depends on the close surroundings of the UCNPs through its influence on the energy level's populations. Peaks' intensity ratio can also be of great interest for thermal measurements. For instance, levels ${}^2H_{11/2}$ and ${}^4S_{3/2}$ of Ytterbium are in thermal equilibrium [262].

PL spectrums were measured by exciting the substrate (glass slide with UCNPs deposited by spin coating on top) by a NIR laser at 980 nm. The laser spot (with a diameter of ~ 30 to $50 \mu\text{m}$) was focused onto the UCNPs with the help of a NIR sensitive camera: at low fluence, the laser's position was adjusted in order to obtain the smallest and most focused spot in the center of the image. Fluorescence spectrum was recorded by a Horiba Triax 180 spectrometer.

A high pass filter (< 800 nm) was put between the laser and the substrate in order to cut second order emission from the laser. A low pass filter was put between the substrate and the spectrometer in order to cut residual laser radiation.

Quantitative comparison between two PL spectrum measured on two different substrates is not reasonable: because of the high sensitivity of the measured intensity to the UCNPs' concentration, any aggregation will result in an artificially high intensity that might not be related to the UCNPs themselves. Another limitation is also caused by the slight change of focalization which inevitably happens by changing substrate, even if the laser is readjusted each time. For those reasons, only qualitative comparisons will be made.

However, a more precise comparison can be made in the case where the difference of experimental conditions concerns the same substrate: for instance in the case where nanorods are deposited first

on only half of the substrate (by covering the other half with a tape), and then UCNP deposited on the whole substrate. By measuring the two spectra while only displacing the substrate, we avoid the optical variation. This will be discussed in Chapter 4.

d. Excitation power dependence of luminescence intensity

As we mentioned in the first chapter, the power dependence of the luminescence intensity gives indications on the upconversion mechanism. The population level N (and thus the intensity of the luminescence peak emitted by it) is proportional to P_{exc}^x where P_{exc} is the excitation power and x an number. The number of photons implied in the process is the smallest integer above x .

A measurement set-up composed by a 980 nm laser focused on the glass substrate on which UCNP were deposited by drop-casting (maximizing the concentration of UCNP). High and low pass filters were used as in the PL measurement. The power of the laser was modified by using density filters. The power of the laser was measured with a power meter after the set of measures.

This technique has several limits. We therefore need to prudently consider its results:

- If the laser moves unintentionally (in particular at the moment when the density filter is changed), the laser spot on the substrate will inevitably move as well. In this case, the power density may change, and the resulting PL intensity may change as well.
- The displacement of the laser beam has an impact on the collection photons cone which might be reduced or increased, thus modifying the PL measure.
- The laser needs to be removed from the set-up for the power measure because of lack of space at emplacement of the substrate. There may be a small error between the measured power density and the one that reaches the sample.

The results of this measure carried out on $KY_7F_{22}:5\%Er^{3+}:20\%Yb^{3+}$ are shown Figure 53. It is obtained by plotting the logarithm of the PL intensity at two wavelengths (540 and 652 nm, corresponding respectively to $^4S_{3/2}$ and $^4F_{9/2}$ relaxation to $^4I_{11/2}$) as a function of the logarithm of the incident excitation power.

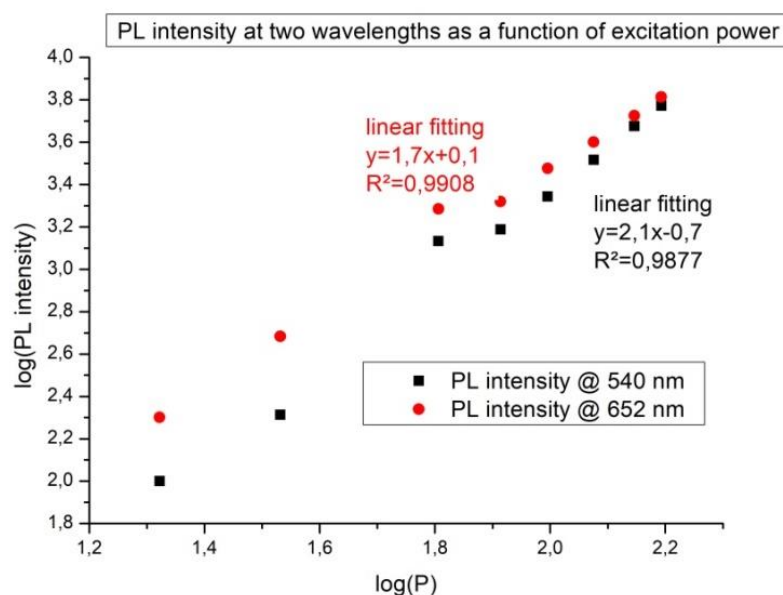


Figure 53. Power dependence of PL intensity for two luminescence wavelengths: 540 and 652 nm. The plots correspond to $\log_{10}(I_{lum})=f(\log_{10}P)$. The linear fitting gives a slope of 2.1 for the emission at 652 nm, and 1.7 for the one at 540 nm.

A linear regression approaches the points by a straight line with relatively good determination coefficients (0.9908 and 0.9877). The slopes are respectively of 1.7 and 2.1. Even if the smallest integer below 1.7 is 1, the theoretical model predicts that those relaxations are 2-or-more photons phenomenon. This difference might be explained by the points mentioned above.

However, it's worth noticing that in the literature, both linear and non-linear behavior were observed: Ye et al. observed a linear increase of PL intensity with excitation power for NaYF₄:Yb,Er [263], whereas Nigoghossian et al. observed a non-linear (n=2.5) behavior for NaGdF₄:Yb³⁺:Er³⁺ [264]. Both behaviors can even be observed for the same particles at different laser powers: for instance, Lu et al. noticed an evolution from quadratic to linear dependence as the excitation power increased, which suggests a phenomenon of saturation at high power [265]. This prevents us from generalizing the evolution of PL intensity with incident excitation power.

e. Transmission and Scanning Electron Microscopy

Scanning Electron Microscopy (SEM) is an imaging technique in which an electron beam scans the surface of the substrate. Briefly, the incidence angle will determine the amount of secondary electrons that can be collected by the detector, and counting those electrons gives access to the topology of the material. SEM images were acquired by a FEI MAGELLAN 400 SEM with standard field emission gun source, operated using the Through the Lense Detector, with a working distance usually around 4 mm, an acceleration for electrons of 5 kV and a current of 13pA.

Transmission Electron Microscopy (TEM) is also an imaging technique that collects electrons, but those ones are simply transmitted through an ultrathin sample (less than 100 nm). TEM characterizations were performed by a JEOL 2010 microscope operated at 200kV. All TEM measurements were executed with the help of Xiangzhen Xu who is in charge of the use and maintenance of the instrument.

f. X-Ray Diffraction method

The X-Ray Diffraction (XRD) is a structural characterization technique that determines the crystal structure of a solid. In our case experiments were executed on powders. Analysis of the intensity of diffracted X-rays at a specific angle that varies along the measure allows the deduction of the distances between lattice planes and allows the deduction of the crystallographic structure.

XRD spectrum were obtained by a PANalytical X'Pert X-ray diffractometer using Cu-K α ($\lambda = 1.5406 \text{ \AA}$) radiation for most of the XRD diffractograms presented in this work.

The reference diffractogram of KY₇F₂₂ that was measured at the European Synchrotron Radiation Facility (ESRF) at a working wavelength of 0,501234 \AA (Figure 59 discussed on page 78), and the diffractogram of KY₃F₁₀ (Figure 59 (b) discussed on page 78), that was measured with a D8 Bruker diffractometer using a Co-K α ($\lambda = 1.788965 \text{ \AA}$).

The diffraction patterns were scanned with a 2θ angular resolution of approximately 0.04°.

g. Fluorescence lifetime

Fluorescence decay measurement, or fluorescence lifetime, allows a dynamic and absolute description of fluorescence, when PL only gives an average and relative description. An electronic level's lifetime is defined as the inverse of the sum of the radiative and non radiative rates which are implied in relaxation starting from this level.

The sample was excited by a pulsed Nd:YAG Q-switched laser (Ekspla NT342B-SH) with 6 ns laser at 970nm and the emission's intensity was measured by placing a Jobin-Yvon HR250 monochromator between the sample and the photomultiplier tube in order to filter out the targeted relaxation.

II. Upconversion nanoparticles : characterization and synthesis

UCNPs synthesized for solar cells improvement must possess several characteristics:

- High PLQE. This implies UCNPs size above circa 70 nm, for the reasons given in the discussion on relation between size and luminescence in chapter 1.
- Size upper limit. The size of the UCNPs should not exceed the perovskite or HTL's one in order to be entirely covered by it. Typically, the perovskite layer has a thickness around 400 and 600nm and the spiro-OMeTAD on top around 400 nm).
- Ease to disperse in a perovskite-compatible solvent.
- Preferably clean UCNPs surface (organic ligands may create charge-collection barriers).

Four different types of particles were thus synthesized, analyzed and compared in order to find the best compromise for devices fabrication.

1. NaYF₄ :1%Er³⁺ :10%Yb³⁺ hydrothermal

a. Syntheses A to C - Sodium citrate ligand

This recipe is adapted from Zhao et al. [266]. Here is the protocol for Synthesis A (B and C follow). The total volume of the solution is 15 mL. The molar ratio NaF/citrate/Ln ratio is 12/0.5/1. 5 mL of lanthanide aqueous solution with a total molar quantity of 5 mmol in rare earth is prepared with the ratio 89/10/1 in Y/Yb/Er by mixing 1704.4 mg of yttrium nitrate hexahydrated (4.45 mmol), 224.6 mg of ytterbium nitrate pentahydrated (0.5 mmol), and 22.2 mg of erbium nitrate pentahydrated (0.05mmol) into 5mL water. 5mL of water containing 735.2 mg of sodium citrate is then added. 5mL of aqueous solution of NaF at 60 mM is then added within 2 minutes. The milky white solution is stirred for an hour and then put in an autoclave for 2 hours at 200°C.

After thermal treatment, the solution is washed twice with DI water and redispersed in water. The dried powder has to be annealed at 300°C for 30 minutes to reduce quenching centers and improve luminescence as we can see on [Figure 54\(d\)](#) The fact that the product is in a form of a UCNPs powder allows the preparation of solutions with known mass concentration.

This synthesis is based on the dissolution-recrystallization mechanism [266]. The phase control of the final products is tuned by the growth regime (thermodynamic vs kinetic). The ligand is the key to the size of particles and to the anisotropic growth. The ratio citrate/Ln has an impact on the crystallography of the NPs: with a ratio of 0.5, a mixture of cubic and hexagonal UC submicroplates is obtained, whereas for a ratio between 1 and 1.5, pure UCNPs with a narrow size distribution are

obtained, implying that the crystal growth is restricted. As for NaF, it affects the shape, the size and the crystal structure. F⁻ anions act as reactant as well as mineralizer and its presence in excess lowers the crystallization temperature. Hydrothermal time and temperature also play a major role in the size shape and crystallization of the UCNPs: lower hydrothermal temperatures favors the formation of smaller size UCNPs, and higher temperature benefits the formation of mix-shaped UCNPs. Extending hydrothermal time increases NPs size slightly and their surface becomes smooth. It also improve crystallization [266].

This synthesis A is indicated as the one exclusively leading to the hexagonal (β) phase of NaYF₄ crystal, which is more luminescent than the cubic one (α) [267]. However, the size of the synthesized particles is too large (1 μ m long and 500 nm large) for the purpose they're designated for, as we can see on [Figure 54\(a\)](#). For this reason, the identical synthesis was repeated twice by changing temperature and NaF/citrate/Ln ratio in order to obtain smaller particles, as predicted in the observations made in the paragraph above.

Smaller particles (300 nm) were obtained for a higher concentration in citrate ([Figure 54\(b\)](#)), but this size being still too large for the implementation in solar devices, the hydrothermal time was then reduced. But instead of leading to smaller particles, this synthesis only lead to the separation between big particles of 1 μ m and small particles of 20 nm ([Figure 54\(c\)](#)).

The different synthesis and resulting particles' sizes can be found in Table 6.

	NaF/citrate/Ln ratio	Annealing time and temperature	Average size (length) and size distribution
Synthesis A	12/0.5/1	200°C 2 hours	1 μ m. Narrow size distribution.
Synthesis B	12/1.5/1	180°C 2 hours	300nm. Narrow size distribution.
Synthesis C	12/1/1	180°C 1 hour	1 μ m and 20 nm. Two types of particles.

Table 6. Summary of hydrothermal syntheses of NaYF₄ :1%Er³⁺ :10%Yb³⁺ with sodium citrate ligand

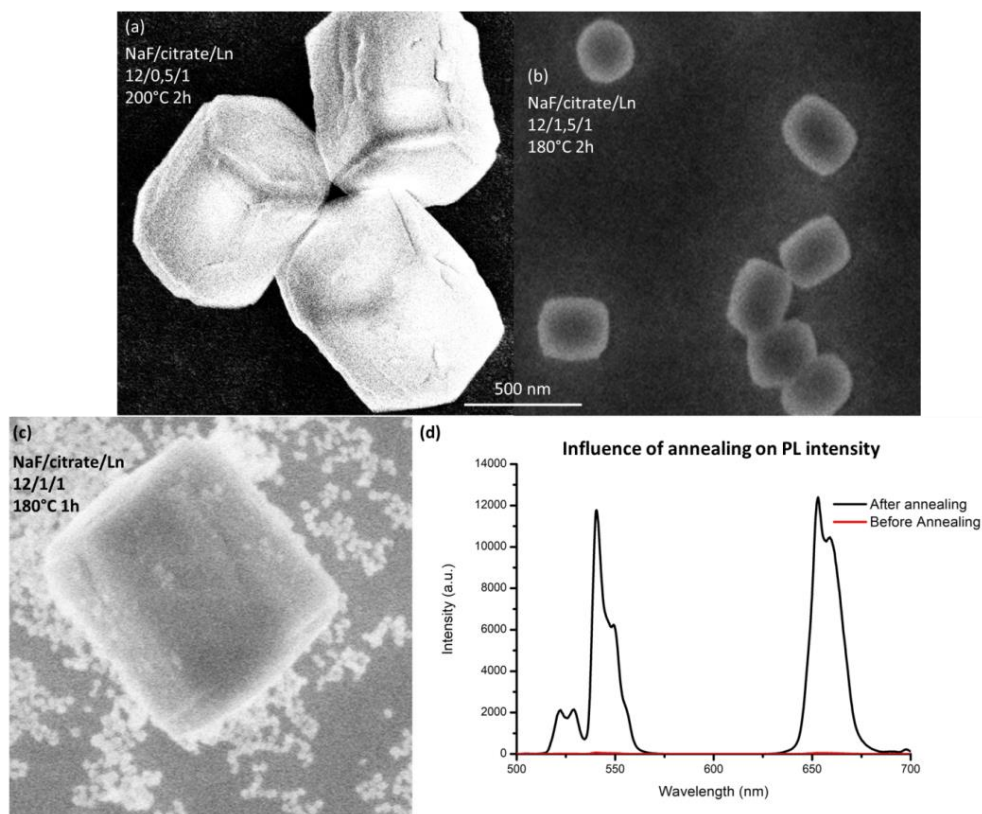


Figure 54. SEM images of (a) synthesis A (b) synthesis B (c) synthesis C. The scale bar is accurate for the three images (d) Influence of annealing at 300°C for 30 min on PL intensity.

Since the two variants did not lead to reasonable size (70-150 nm), citrate sodium was replaced by EDTA (ethylene diamine tetra-acetic), which is supposed to give smaller UCNPs, as described in [268].

b.Synthesis D and E - EDTA ligand

In order to decrease the size of the UCNPs, we performed in collaboration with Hengyang Xiang a similar synthesis with other ligands.

1 mmol EDTA (372 mg) in 5 mL DI water is mixed with 1 mmol lanthanide solutions in 5 mL DI water. Two lanthanide ratios were tried out in synthesis D and E as summarized in Table 7.

	Molar ratio $Y^{3+}:Yb^{3+}:Er^{3+}$	Mass of $Er(NO_3)_3 \cdot 5H_2O$	Mass of $Yb(NO_3)_3 \cdot 5H_2O$	Mass of $Y(NO_3)_3 \cdot 6H_2O$
Synthesis D	89:10:1	4.4 mg	44.9 mg	340.8 mg
Synthesis E	78:20:2	8.9 mg	89.8 mg	298.7 mg

Table 7. Summary of hydrothermal syntheses of $NaYF_4 : 1\%Er^{3+} : 10\%Yb^{3+}$ (EDTA ligand)

12 mmol NaF (1007.7 mg) was then added to the solution that was then stirred for one hour, and put in the autoclave for one hour at 120 °C. The last step to obtain the powder was the same than in the case with citrate sodium as ligands.

The so-obtained UCNPs have lower average diameter: from around 65 to 130 nm for Synthesis D, and from 70 to 120 nm for Synthesis E, as we can see on SEM pictures (Figure 55).

As described by the DLVO theory (from Derjaguin Landau Verwey and Overbeck), for smaller particles' radius (the critical radius depending also on the geometry of the particles and their

chemical nature), the attractive Van der Waals force becomes stronger than the repulsive coulombic one, and they tend to aggregate [269]. Obtaining a homogeneous suspension was more difficult in the case of those two syntheses and the sonication time had to be increased up to a couple of hours in order to obtain a temporarily stable solution.

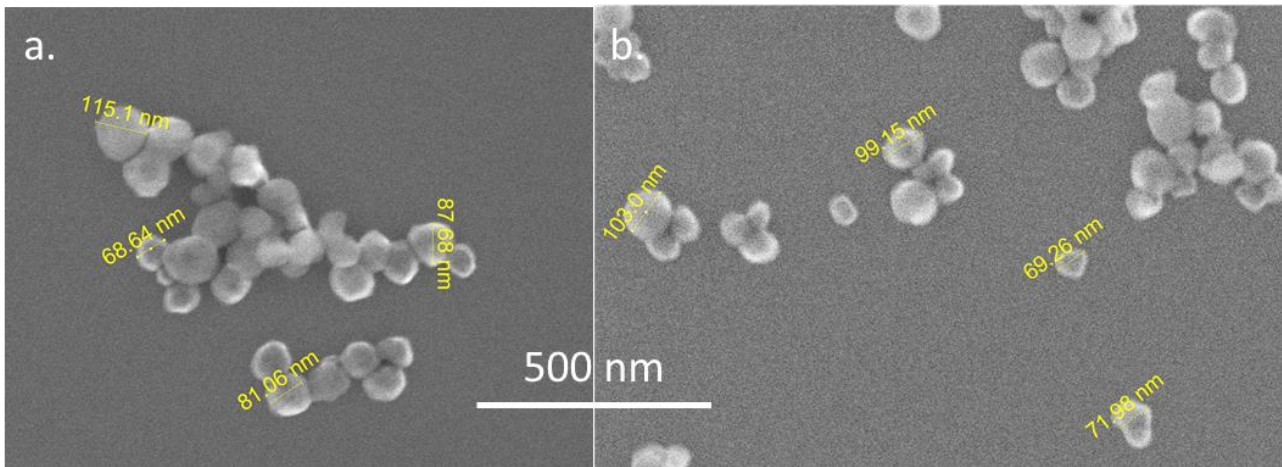


Figure 55. SEM images of (a) synthesis D (b) synthesis E

c.XRD

The good correspondence between the measure diffractogram and the one from the literature suggests that this synthesis majorly lead to the formation of hexagonal NaYF_4 matrix, as we can see on [Figure 56](#) that compares both diffractograms. The peak around 37° can be attributed to FTO substrate.

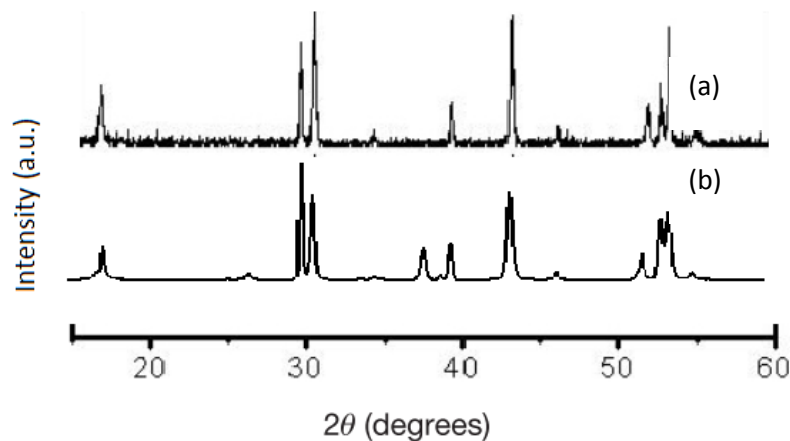


Figure 56. XRD Diffractograms of hexagonal phase $\text{NaYF}_4 : 1\% \text{Er}^{3+} : 10\text{Yb}^{3+}$ Synthesis A (a) from the literature [266] (b) measured.

2. KY_7F_{22} and $\text{KY}_3\text{F}_{10}:\text{YF}_3 : 5\% \text{Er}^{3+} : 20\% \text{Yb}^{3+}$ Coprecipitation

The two following recipes were experimented and characterized in collaboration with Patrick Gredin and Karmel de Oliveira at Institut de Recherche de Chimie Paris. The presence of hydrofluoric acid requires specific equipments (air glove box), as well as extra care paid during the synthesis.

a.Synthesis

KY_7F_{22} : 5 mol % Er^{3+} : 20 mol % Yb^{3+} NPs were synthesized by coprecipitation of an aqueous solution (10mL) of potassium fluoride, yttrium, erbium and ytterbium nitrates in stoichiometric proportion in a large excess (10mL) of hydrofluoric acid 40% at room temperature (58.9mg of KF, 1.817mg of $Y(NO_3)_3 \cdot 4H_2O$, 630mg of $Yb(NO_3)_3 \cdot 5H_2O$ and 157mg of $Er(NO_3)_3 \cdot 5H_2O$). After centrifuging the as-obtained solution and removing the supernatant, the obtained powder was rinsed and centrifuged again four times in deionized water before the final centrifugation. The final obtained UCNPs were dried in air at 60°C for two days followed by thermal annealing at 300°C for 3 hours under dried argon atmosphere to remove hydroxyl and/or nitrate groups adsorbed at the surface of the nanoparticles.

KY_7F_{22} decomposes in $KY_3F_{10}:YF_3$ when the annealing temperature exceeds 385°C. This can be justified by thermogravimetric analysis/differential thermal analysis (TGA/DTA), which consist in annealing a substrate while measuring the temperature on the substrate and in the annealing chamber. These analysis were run on KY_7F_{22} (Figure 57) and show a decomposition peak at 385°C as well as continuous weight losses between 100 and 400°C, attributed to adsorbed groups' desorption. The products of the decomposition were determined by XRD run before and after annealing.

We will from now on refer to KY_7F_{22} or $KY_3F_{10}:YF_3$ for products of this synthesis. The mass ratio KY_3F_{10}/YF_3 was estimated around 50% by calculations relying on molar quantities.

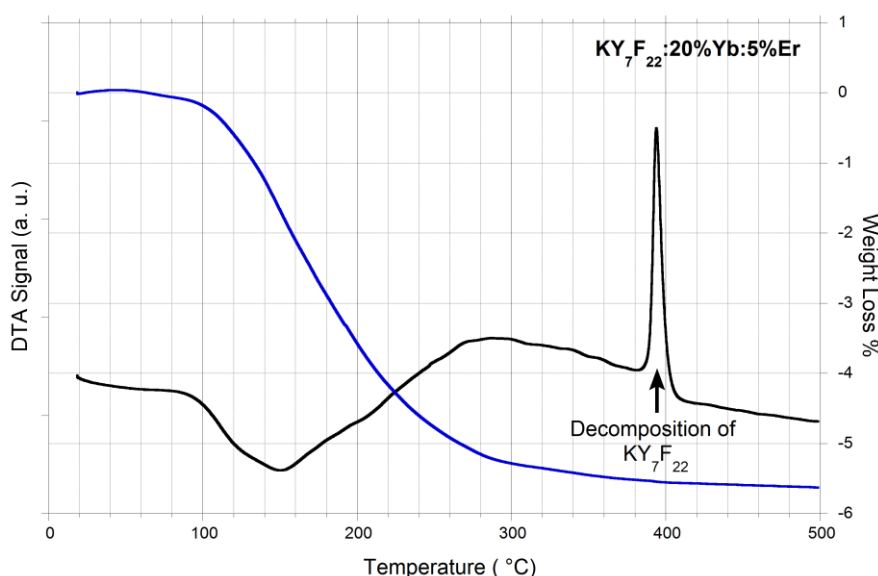


Figure 57. TGA/DTA analyses of Yb^{3+} and Er^{3+} co-doped KY_7F_{22} . The dash curve corresponds to the weight loss (%) and the plain curve to the DTA signal. The strong sharp peak centered at 385°C is attributed to the decomposition of the KY_7F_{22} phase (which is endothermic).

The synthesis of these monocrystalline (confirmed by TEM observation) nanoparticles relies on the germination followed by growth (this does not exclude aggregation).

The use of potassium fluoride as potassium source rather than potassium nitrate results in the decreasing number of impurity (YF_3), but UCNPs are of a smaller diameter and less well crystallized (atoms are not as well aligned as in well-crystallized particles) in that case. This might be related to K-F bond stability in presence of hydrofluoric acid. Size is controlled by many different factors from

initial number of seeds, reaction's speed, ions' availability, solution stirring, surface energy and charge...

During the synthesis, nitrate and water molecules are adsorbed at the surface of the UCNPs. If they are left on the surface of the UCNPs, they would quench the luminescence. Therefore, getting rid of them through annealing is a compulsory step of the synthesis. During the annealing, the desorption of nitrate groups occurs and they are probably evacuated under the form of nitric acid by reacting with water, and probably of nitrogen oxide as well. Hydroxide groups are also adsorbed but are less harmful to luminescence.

The annealing temperature has to be very carefully chosen in order to avoid phase transition.

b.XRD

The X-ray powder diffraction pattern was indexed by comparing the XRD pattern with the one from a sample of KY_7F_{22} previously synthesized and used as reference ([Figure 58](#)

[Figure 59\(a\)](#)). The chemical formulation of this reference compound was confirmed by energy dispersive X-ray fluorescence spectrometry and the reference diffractogram was recorded at the European Synchrotron Radiation Facility (ESRF). The analysis of this X-ray pattern revealed that KY_7F_{22} crystallizes in a cubic system with a cell parameter of $15.4655(1) \text{ \AA}$.

Figure 59. Measured (points) and calculated (full curve) X-ray powder patterns of (a) KY_7F_{22} . Reference pattern measured at Synchrotron. (b). doped KY_7F_{22} , presenting additional resulting from the doping. The short vertical lines below the profile curve mark the positions of all possible Bragg reflections. The lower curve shows the difference between measured and calculated profiles. The matching between measured and calculated curves shows that the phases are pure. The angular coverage is different because the two diffractograms are not obtained at the same emission wavelength.

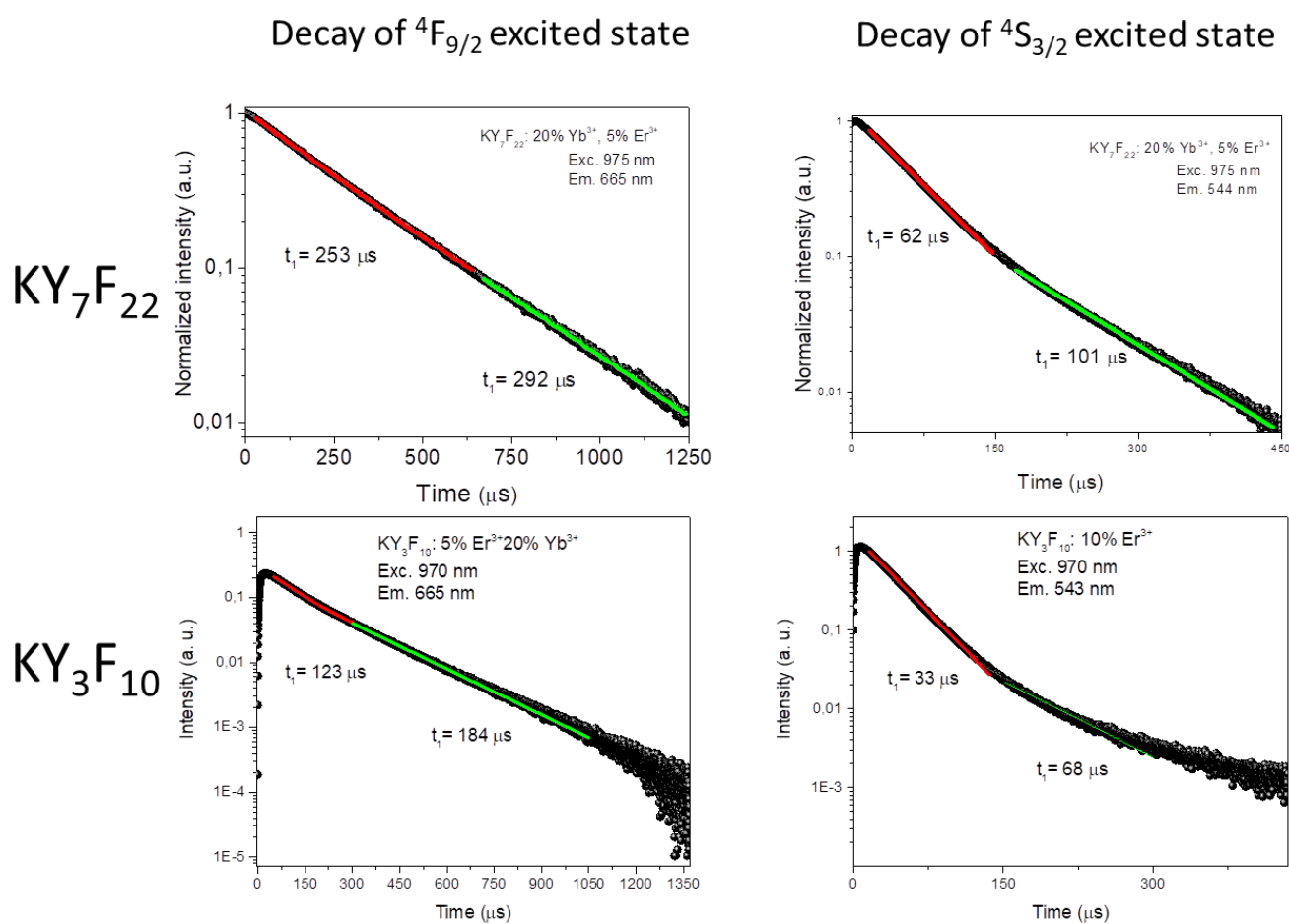
(c) doped $KY_3F_{10}:YF_3$.

c. PL Lifetime

PL lifetimes were measured for both doped KY_7F_{22} and $KY_3F_{10}:YF_3$ ([Figure 60](#)). The measurements underline the fact that KY_7F_{22} exhibit longer lifetimes both at 656 and 543 nm than KY_3F_{10} : 556 μs and 266 μs at respectively 656 and 543 nm for KY_7F_{22} , against 123 and 33 μs for $KY_3F_{10}:YF_3$. This represents an advantage once implemented in a solar cell: longer lifetimes imply an increased probability of energy transfer from the UCNPs to the perovskite.

PL spectrum of KY_7F_{22} is shown [Figure 52](#).

Figure 60. PL lifetime measurements obtained for two relaxations (starting from level $^4F_{9/2}$ and $^4S_{3/2}$ for KY_7F_{22} and $KY_3F_{10}:YF_3$. The red and green curves represent the two single exponential fits (at short and long time) of the experimental data.



d. SEM

SEM characterization was done and the resulting SEM pictures are shown [Figure 61](#). Their diameters are between 200 and 250 nm with relatively narrow size dispersion.

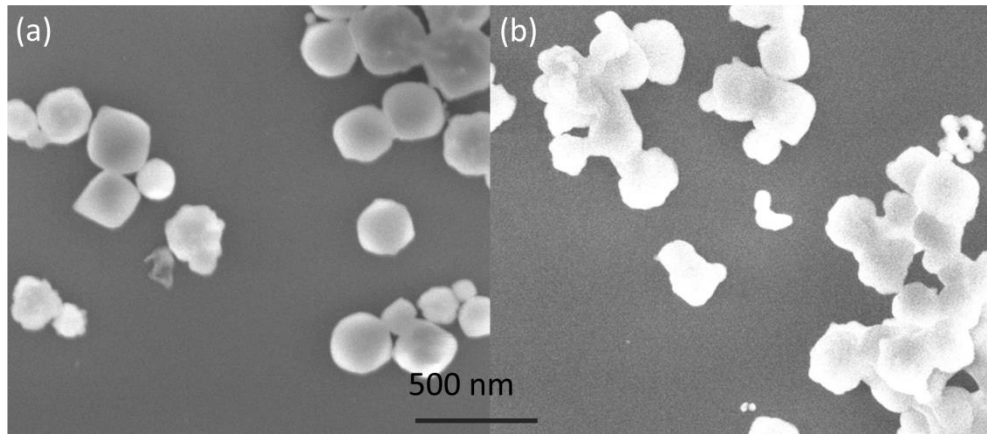


Figure 61. SEM pictures of (a) KY_7F_{22} and (b) $KY_3F_{10}:YF_3$

3. $KY_3F_{10}:5\%Er^{3+}:20\%Yb^{3+}$ hydrothermal

This synthesis and the characterization were done in collaboration with Karmel De Oliveira.

a. Synthesis

KY_3F_{10} : 5% Er^{3+} , 20% Yb^{3+} particles was performed by a polyethylene glycol (PEG) assisted hydrothermal method. 2 mmol of $RE(NO_3)_3$ was dissolved in 10 mL of water, and 5 wt % PEG aqueous solution was introduced to form a clear solution by stirring. Afterwards, 25 ml of aqueous solution containing 8 mmol of KF was dropwise added. After agitation for another 15 min, the as-obtained milky solution was transferred into a Teflon bottle held in a stainless steel autoclave, and maintained at $220^\circ C$ for 12 h. After this time, the particles were separated by centrifugation, washed with ethanol and deionized water, and then dried in air at $80^\circ C$ for 24 h.

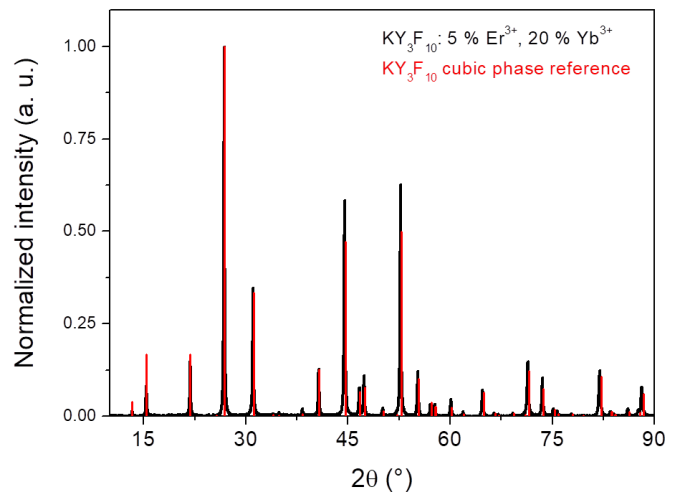


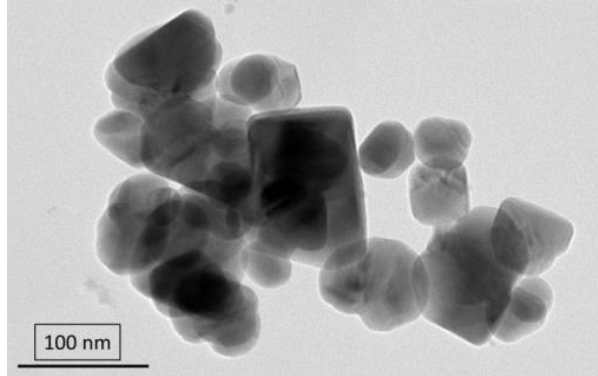
Figure 62. XRD Pattern of KY_3F_{10} synthesized by hydrothermal route

The mechanism of reaction is similar to that of $NaYF_4$ hydrothermal described page 72/74.

Contrary to the coprecipitation synthesis, this synthesis only led to pure KY_3F_{10} , as a XRD diffractogram proves it (Figure 62).

b. TEM

The size distribution obtained for this synthesis is much wider than the one obtained by coprecipitation. The particles are irregular, cubic or spherical, and their size varies from 20 to 150 nm (Figure 63).



c. Infrared vibrational

whether PEG ligands surface of the UCNPs

Figure 63. TEM Picture of $KY_3F_{10}:5\%Er^{3+}:20\%Yb^{3+}$ synthesized via hydrothermal synthesis

vibrational spectra was carried out on those particles (Figure 64(a)). The absorption around 3400cm^{-1} can be attributed to $-OH$ stretching vibration from water and PEG. The absence of absorption at 2960 , 2930 or 2855 cm^{-1} , characteristic to asymmetric and symmetric stretching of methylene [270], [271] would tend to confirm the absence of PEG on the surface of the UCNPs.

spectra

In order to verify are still adsorbed on the after annealing, infrared

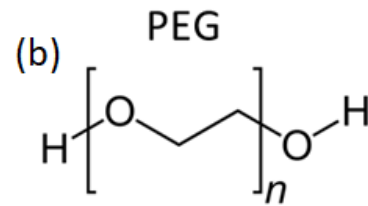
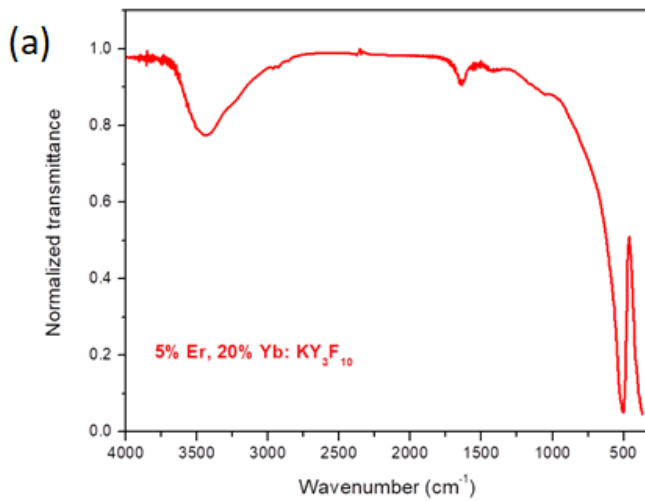


Figure 64. (a) IR vibrational spectra of KY_3F_{10} hydrothermal. (b) Chemical formula of PEG.

4. $NaYF_4:30\%Gd^{3+}:2\%Er^{3+}:18Yb^{3+}$

a.Synthesis 1 – Octadecene ligand – Solvothermal

This recipe is adapted from Wang et al. [272]

3 mL of oleic acid, 7 mL of octadecene, and respectively 1mL of YCl_3 , 0.6mL of GdCl_3 , 360 μL of YbCl_3 and 40 μL of ErCl_3 , all at 0.2M in methanol were mixed under vacuum for an hour at 90°C. Then, it cooled down to room temperature.

5mL of methanol with a concentration of 1.6 mmol of NH_4F and 1 mmol NaOH are then added under argon. The solution was then put again under vacuum. It turned milky white. It was heated up again to 100°C for 30 min (starting from the moment when it reaches 100°C), and then to 300°C for 1h30. It was then cooled down to room temperature, purified three times with methanol and ethanol, and then dispersed in cyclohexane.

During the first step of the synthesis, methanol was evaporated and rare earths were solvated by the ligands. During the second step, the UCNPs' formation and growth occurred, controlled by the presence of two types of ligands. The basicity of the solution helped ionizing the ammonium fluoride to free F^- for reaction.

b.Synthesis 2 – oleic acid ligand – Hydrothermal

This recipe was adapted from Li et al. [217]3.375mL of DI water, 0.0675g of NaOH , 11.25 mL of ethanol and 11.25 mL of oleic acid were mixed together. 136.8 mg of YCl_3 , 62.8 mg of YbCl_3 , 71.1 mg of GdCl_3 were dissolved in 4.5 mL of an aqueous solution prepared by mixing 17.9mg of ErCl_3 and 12 mL of DI water. The solution stirred until complete dissolution and was then put in the autoclave at 200°C for 2 hours. It was washed with Ethanol three times and dispersed in cyclohexane.

Its mechanism is similar to that of hydrothermal $\text{NaYF}_4:1\%\text{Er}^{3+}:10\text{Yb}^{3+}$

The characterizations below correspond to Synthesis 1.

b.TEM

The TEM images for two different tests of Synthesis 1 show a relative good reproducibility, as we can see by comparing [Figure 65\(a\)](#) and [\(b\)](#). We can notice that this synthesis seems to lead to a narrow size dispersion.

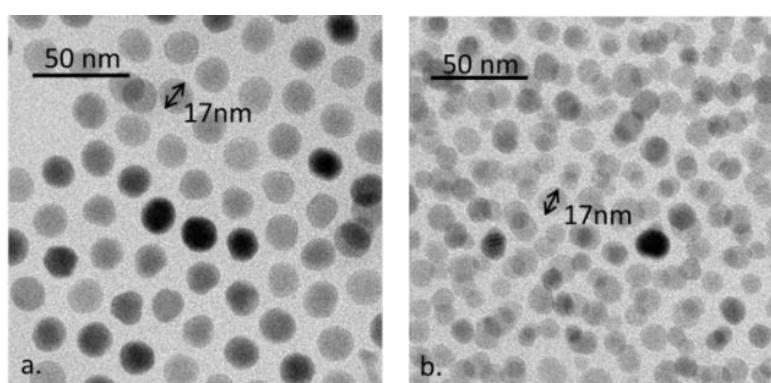


Figure 65. (a) and (b)TEM Images of $\text{NaYF}_4:30\%\text{Gd}^{3+}:2\%\text{Er}^{3+}:18\text{Y}^{3+}$ (two different batches)

c.XRD

The good correspondence between the measured diffractogram and the reported one suggests that this synthesis principally leads to the formation of hexagonal NaYF₄ matrix, as we can see on [Figure 66](#). The presence of the cubic phase is also confirmed by XRD.

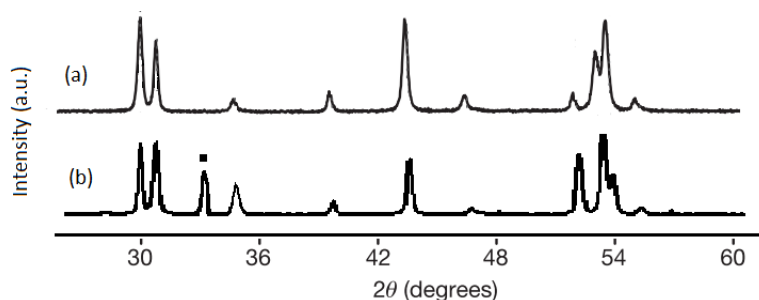


Figure 66. XRD Diffractograms of hexagonal phase NaYF₄:30%Gd³⁺:2%Er³⁺:18Yb³⁺ (a) from the literature [267] (b) measured. The diffraction peak corresponding to cubic NaYF₄ is marked with a square box.

5. Ligands' problematic

Ligands are usually organic molecules (PEG, EDTA, citrate sodium, oleic acid, dodecanethiol are the five ones that were used in this work, whose chemical formula are shown on [Figure 67](#)). They are used to allow and control NP's growth. However, in order to minimize the number of defects they could introduce in the devices (charge recombination, trapping states incorporation, charge-transfer barriers...), we have to make sure that they are eliminated at some point of the solar cell fabrication process.

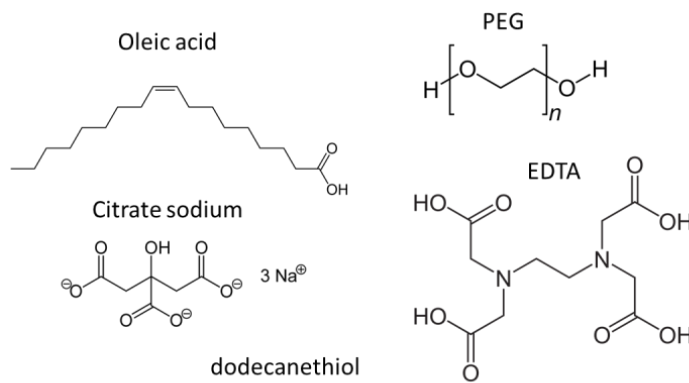


Figure 67. Chemical formula of ligands used in this work

The ability of UCNPs to cluster and the wettability of the upcoming layer depend, amongst others, on the size of the UCNPs, their volume to surface ratio, but also on the presence of ligands [273]. Annealing between 300 and 400°C allows to burn ligands and eliminate defect sites and quenching centers [266], which can enhance the photoluminescence intensity. Annealing can also result in a possibly irreversible aggregation of the UCNPs. The annealing temperature has to be cautiously chosen because it can modify the crystallographic phase.

This was the route chosen for KY₃F₁₀:5%Er³⁺:20%Yb³⁺, KY₇F₂₂:5%Er³⁺:20%Yb³⁺ and NaYF₄:1%Er³⁺:10%Yb³⁺ (in the case of synthesis by coprecipitation, it's not ligands that are covering the particles, but rather adsorbed nitrate groups).

But due to their small diameters, this approach was not applied for NaYF₄:30%Gd³⁺:2%Er³⁺:18Yb³⁺ (aggregation occurs for smaller particles, as explained in section II.1.c, and obtaining a powder could

have resulted in irreversible aggregation). We thus decided for those UCNPs to get rid of ligands after deposition.

In order to do so, the best option is oxygen plasma treatment, as we can see on [Figure 68](#), where PL intensities are compared for different post-deposition treatments.

The case where both oven and plasma treatments are operated on the sample shows much lower PL intensity as in the case of plasma treatment alone (around 2500 counts against 15000 for the PL intensity at 530 nm). If the plasma treatment is followed by oven annealing, the PL intensity is even lower, which suggests that oven annealing has for this type of particles an irreversible damaging on the luminescence of the particles.

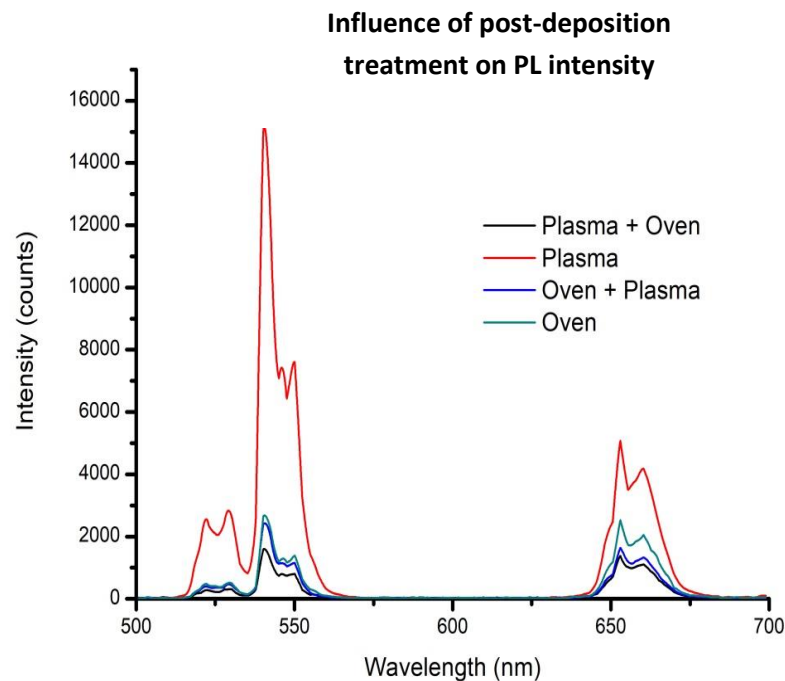


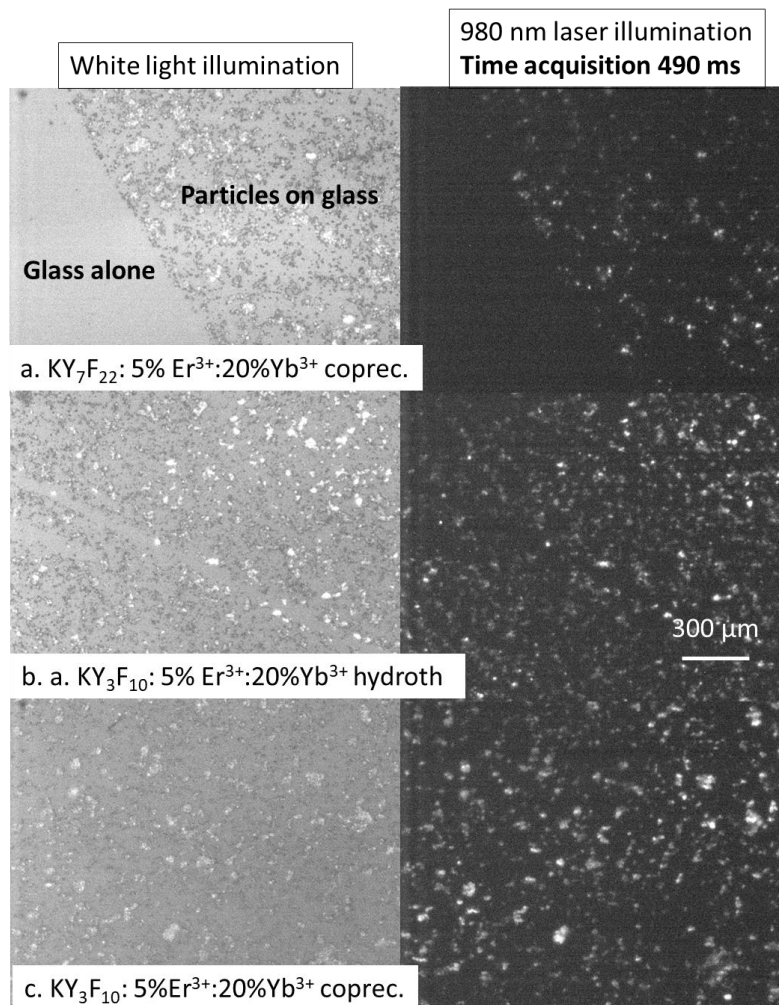
Figure 68. Influence of post-deposition treatment on PL intensity for $\text{NaYF}_4:30\%\text{Gd}^{3+}:2\%\text{Er}^{3+}:18\text{Yb}^{3+}$ solvothermal synthesis. UCNPs were deposited by spin-coating (2000 rpm for 30 sec, annealing at 100°C for 10 min). Oven treatment corresponds to 45 min at 300°C followed by plasma treatment to 45 minutes of oxygen plasma.

6. Qualitative comparison

a. Ratio of luminescent particles

6 types of particles from different synthesis were compared on microscope pictures taken under white light illumination and NIR laser illumination (Figure 69). The aim is to qualitatively characterize the luminescent centers portion of a sample. The concentration depositions are different, which implies different surface coverages. We can observe on these optical images a relatively high ratio of luminescent particles for KY_3F_{10} , $KY_3F_{10}:YF_3$ and for KY_7F_{22} . The ratio seems also quite high for $NaYF_4:1\%Er^{3+}:10\%Yb^{3+}$ synthesis A (even if the time acquisition is longer), but a relatively low ratio for $NaYF_4:30\%Gd^{3+}:2\%Er^{3+}:18\%Yb^{3+}$ and $NaYF_4:1\%Er^{3+}:10\%Yb^{3+}$ synthesis C (for which a non-negligible ratio of the particles is below 20 nm). The substrate used in the image with KY_7F_{22} presents a part on which there are no particles and a part on which there are particles, in order to clearly see the difference between the two cases.

From this experiment, we would conclude that KY_3F_{10} , $KY_3F_{10}:YF_3$ and KY_7F_{22} seem to be the most promising samples.



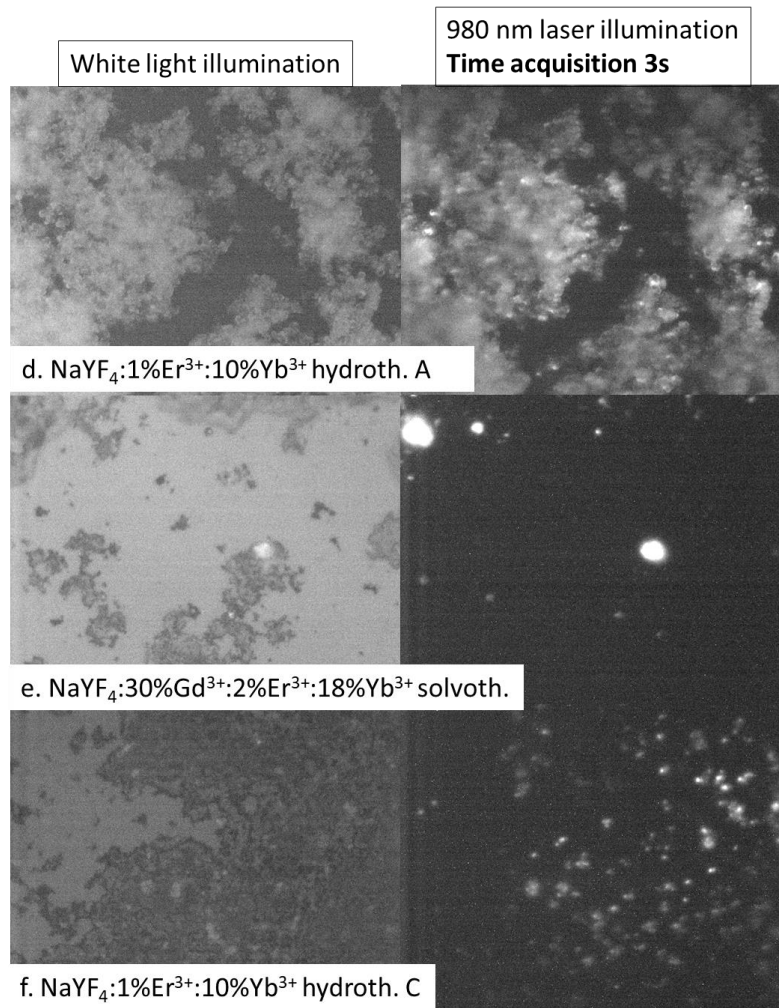


Figure 69. Microscope pictures of 6 different UCNPs on glass, under white light illumination (left columns) and 980 laser illumination (right columns). The acquisition time of the one acquired under 980 laser illumination is different for the two series: 490 ms for the a-c serie, 3s for the d-f.

b. The elimination

Among the four types of UCNPs that were synthesized for this work, two types were eliminated because they did not fit the prerequisite for device implementation:

- $\text{NaYF}_4:30\%\text{Gd}^{3+}:2\%\text{Er}^{3+}:18\%\text{Yb}^{3+}$ showed low fluorescence, probably because of their small size (below 70nm) which implies a low luminescence intensity. Getting rid of their ligands was also a supplementary step in the device fabrication, which was not the case for the three other UCNPs.
- $\text{NaYF}_4:1\%\text{Er}^{3+}:10\%\text{Yb}^{3+}$, synthesis A B and C, because their size were too large to be inserted in the device.

For reasons given in III.1.c, comparison of samples is not fully accurate when based on PL intensity only. PLQE is the most suitable technique in order to compare sample synthesized by different synthesis. The PLQEs for the different samples are shown [Table 8](#).

We mainly focused our device fabrications on the incorporation of KY_7F_{22} and $KY_3F_{10}:YF_3$, which both exhibit similar PLQE, and were both synthesized in collaboration with Patrick Gredin and Karmel de Oliveira. One attempt was also made by incorporating $NaYF_4$ (synthesis D) and KY_3F_{10} to solar devices.

UCNP	PLQE
$NaYF_4 :1\%Er^{3+} :10\%Yb^{3+}$ hydrothermal A	3.3%
$NaYF_4 :1\%Er^{3+} :10\%Yb^{3+}$ hydrothermal B	2.1%
$NaYF_4 :1\%Er^{3+} :10\%Yb^{3+}$ hydrothermal C	2.3%
$NaYF_4 :1\%Er^{3+} :10\%Yb^{3+}$ hydrothermal D	2.3%
$KY_3F_{10}:YF_3:5\%Er^{3+}:20\%Yb^{3+}$ coprecipitation	6.7%
$KY_7F_{22}:5\%Er^{3+}:20\%Yb^{3+}$ coprecipitation	5.1%
$KY_3F_{10}:5\%Er^{3+}:20\%Yb^{3+}$ hydrothermal	Not measurable
$NaYF_4:Gd^{3+}:Er^{3+}:Yb^{3+}$	Not measurable

Table 8. Comparison of PLQEs for the different synthesized UCNPs. The two last lines correspond to the smallest UCNPs and their luminescence was detected but too noisy to make any trustworthy calculation. Excitation source : 975 nm.

In order to enhance upconversion's absorption, gold nanorods were synthesized. The next part will address this synthesis and its problematics.

III. Nanorods (NRs) synthesis and characterization

Metallic gold NRs were synthesized following a seed-mediated growth synthesis. The targeted properties of the synthesized NRs concern both their insertion in solar devices and the upconversion enhancement. We target NRs that fit the following criterion:

- A LSPR (Localized Surface Plasmon Resonance) close to the absorption of the UCNPs (900-1000 nm)
- A low absorption in the absorption range of the perovskite (below $\lambda=800$ nm)
- A surface chemistry compatible with the fabrication of an efficient device (easily removable ligands)
- Dispersed in solvent compatible with perovskite in the case where they are inserted on top of perovskite (thus non-aqueous)

These 2 last points are in particular important in the case of NRs, since they are inevitably surrounded by ligands that allow their dispersion in water. Without ligands, they would immediately aggregate. But as we saw in the case of UCNPs, any chemical impurity such as long organic molecules decrease charge transport and contribute to lower the performance of the device, without mentioning the wettability of the perovskite precursor solution on the surface of the NRs layer.

1.Synthesis protocols

The aspect ratio (AR) of a gold nanorod is defined as the ratio of its length over its diameter. It is a well known theoretical and experimental fact that LSPR shifts to long wavelength when the aspect ratio is increased [274]. An AR around 4.5 will give a LSPR in water around 900 nm, and a one of 5.5 around 980 nm [275]. We thus chose recipes and material quantities leading to the synthesis of Au NRs with such ARs.

a.Seed Mediated Growth

NRs synthesis was adapted from the work of YE et al. [276] The solvent is DI water.

Seed solution.

In a typical synthesis, 5mL of 0.5 mM HAuCl_4 (84,9 mg for 50mL at 5mM) was mixed with 5 mL of 0.2M CTAB (hexadecyltrimethylammonium bromide) (3.645g for 50 mL at 0.2M). 0.6 mL of fresh 0.01M NaBH_4 (37.8 mg for 100mL at 0.01M) was then injected to the solution under vigorous stirring for 2 minutes. The solution color changed from yellow to brownish yellow. The seed solution was aged at room temperature for 30 minutes before use (during which the growth solution is prepared).

Growth solution . The total volume was later reduced for smaller batches (every measure divided by 25 for a total volume of 20 mL).

9g of CTAB and 1.234 of NaOL were dissolved in 250 mL of warm water (50°C). The solution cooled down to 30°C and 24 mL (for Synthesis 1 and 36mL for Synthesis 2) of 4mM AgNO_3 was added. The mixture was kept undisturbed at 30°C for 15 min after which 250 mL of 1mM HAuCl_4 solution was added. The solution became colorless after 90 min of stirring and 3 mL (for Synthesis 1 and 2.1 mL for Synthesis 2) of HCl (37 wt % in water) was then introduced to adjust the pH.

After 15 min of moderate stirring, 1.25 mL of 0.064 M of ascorbic acid was added and the solution was vigorously stirred for 30s. 0.2 mL of seed solution was then injected, stirred for 30s, and then left undisturbed at 30°C for 12h for NR growth. The NRs were obtained by centrifugation and were washed three times with water to remove excess ligands and other chemicals. More washing procedures could critically reduce the dispersivity of the NRs, which would aggregate.

b.Growth mechanism

The first step of this synthesis implies the reduction of gold(III) chloride by sodium borohydride in the presence of CTAB. Cationic surfactant CTAB has been widely used for colloidal seeded growth Au NRs synthesis [277]–[291].

In the growth solution, Au(III) is reduced by NaOL with its double bond (disappearance of the orange/yellow color) in presence of ascorbic acid, HCl, CTAB and silver nitrate. The role of Ag^{3+} in such a synthesis has been reported as crucial as it interacts with CTAB to form elongated templates and hinders the growth of certain crystallographic facets of Au NRs [288][292]. Increasing the amount of Ag^{3+} from the optimum value however led to a decrease of AR due to the thickened NR width [275]. The use of a second surfactant participates to the oxidation as well as it

circumvents the limitations in NRs' dimensions and allow them having LSPR from 650 to 1150 nm [276]. Various parameters control the size of the NRs and several trends are noticeable: lowering pH of growth leads to a higher AR, as well as reducing the amount of seed particles (more growth material per seed). A high concentration of CTAB may block NR formation along certain directions.[276]

c.Optimization of the synthesis – Variation of Silver nitrate volume

The first synthesis led to the formation of nanospheres only, as we can see on [Figure 70\(a\)](#) This might be related to the large volume of solution and inhomogeneous stirring. For this reason, the protocol was adjusted in order to obtain higher AR, and the volume of silver nitrate of Synthesis 2 was increased to 36 mL. The amount of HCl was also reduced to 2.1 mL as suggested in the Table 2 of Support Information of [276].

NRs were obtained with a LSPR around 940 nm, that were 95 ± 12 nm long and 18 ± 4 nm diameter (AR=5.3, average and standard deviation calculated with Image J on 23 nanorods). As we can see on [Figure 70\(b\)](#), many nanospheres still remain at the end of the synthesis. The absorption peak around 550nm can be attributed for Synthesis 1 to the nanospheres, whereas the one at 525 nm for Synthesis 2 can be attributed to the absorption peak of the nanospheres remaining in the solution and the one around 650 nm to the transverse resonant mode of the NRs [291].

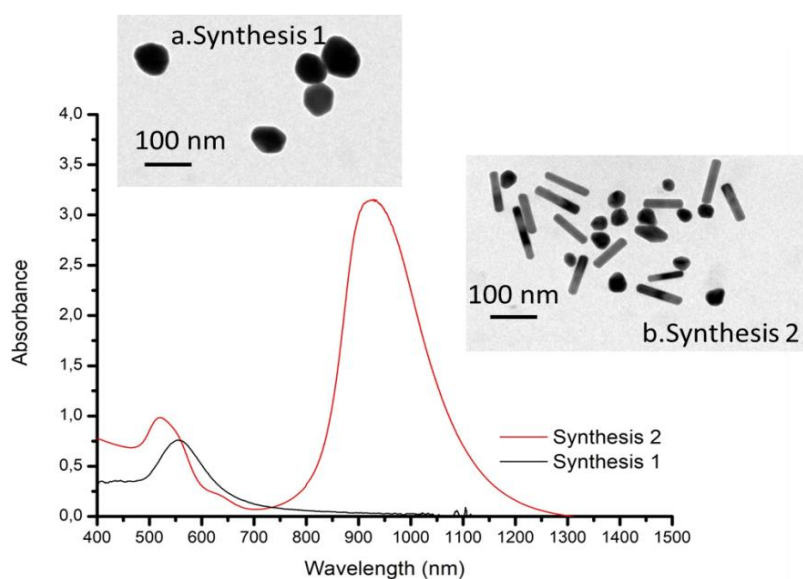


Figure 70. TEM Images and absorption spectrum of (a) Synthesis 1 (b) Synthesis 2.

Further work on the optimization of the synthesis was conducted by Tingting Niu that led to high reproducibility of synthesis of tailored NRs with a LSPR between 900 and 1300nm with very few nanospheres, (Chapter 4 I.1.b).

Several attempts to grow fold directly on UCNPs were carried and more information on the protocol and the results can be found in Annex 9.

2. Ligands and solvent problematics

Just like for UCNPs, getting rid of ligands attached to NRs in order to implement them in device is a necessity. We can see how thick and visible the organic film is after NRs deposition ([Figure 71](#)). In the case of NRs, the possibility to get rid of them before the deposition involves more complex steps than after deposition: ligands are necessary to avoid aggregation. They can be eliminated after deposition using oxygen plasma.

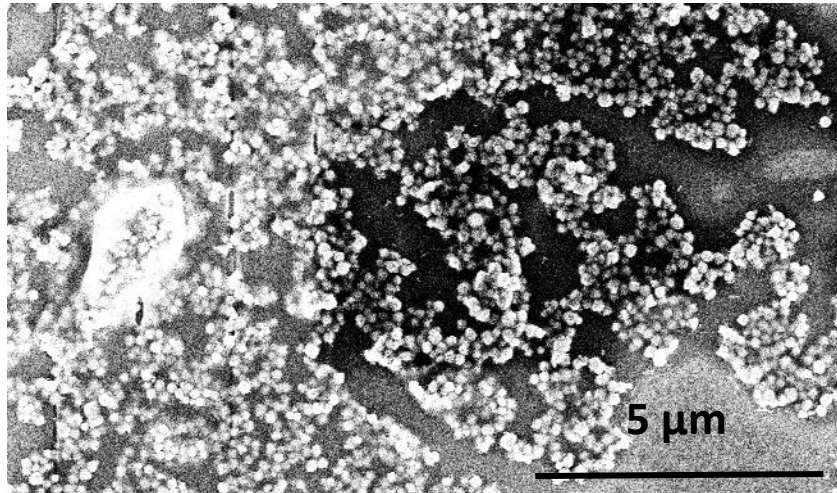


Figure 71. SEM Image of UCNPs on top of which NRs were deposited. The darker spots indicate where the electron beam previously burnt the organic film that otherwise covers the rest of the surface

If the NRs are dispersed in water, it will not be possible to deposit them on top of the perovskite layer because perovskite decomposes when in contact with water. One of the solution to make them solvable in another type of solvent (chloroform, hexane...) consists in exchanging their ligands from CTAB to ligands such as dodecanethiol or PEG-SH [293], [294].

A few attempts of ligand exchange have been carried out and did not lead to successful NRs dispersion in non-aqueous solvents. For this reason, we only used NRs under the perovskite layer and managed to get rid of ligands with oxygen plasma treatment.

After having synthesized and characterize those two types of particles, they were implemented in perovskite solar cells in order to enhance them.

The next and last chapter will be addressed to this implementation and the characterization of the devices.

Chapter 4. Incorporation of nanoparticles in perovskite solar cells

I. Plasmonic NPs and nanostructures, simulation and incorporation in solar devices

1. Choice of NRs aspect ratio : comparison between experiment and simulation

a. Model of absorption for a gold NRs on a glass substrate

We decided to simulate plasmonic resonance for gold nanorods placed on a glass surface (a situation close to gold nanorods dispersed on FTO, as they would be once integrated in a device). For this purpose, we used the commercial FDTD software Lumerical ©.

The glass substrate has to be larger than the calculation region. A parallelepiped box represents the source (plane wave with a wavevector normal to the rod) surrounding the rod (grey box in [Figure 72](#)), and another parallelepiped in charge of measuring the absorbed field (yellow box in [Figure 72](#)).

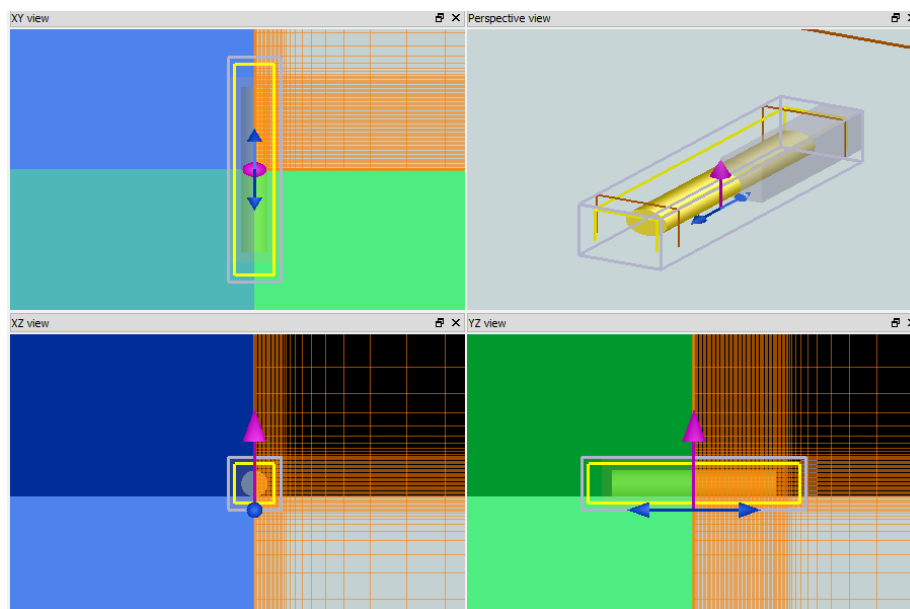


Figure 72. 4 points of views of the simulation of a gold nanorod on a glass substrate on Lumerical ©

The absorption of the metallic structures was plotted in order to obtain the variation of the simulated Localized Surface Plasmon Resonance (LSPR) as a function of the size of the rod. Eleven different sizes were tested (the first number refers to the diameter and the second the length of the rod, both in nm) : 20x50, 20x75, 10x50, 20x115, 20x125, 10x75, 20x150, 10x85, 10x95, 10x100 and 10x110, which correspond to ARs (Aspect Ratios, the length over the diameter) between 2.5 and 11 ([Figure 73.b](#)).

Those absorbances were compared to the one obtained experimentally by Xiang et al. [275] for nanorods whose ARs are in the same range ([Figure 73.a](#)). Let's note that the absorption feature at 1400 nm originates from the absorption of water.

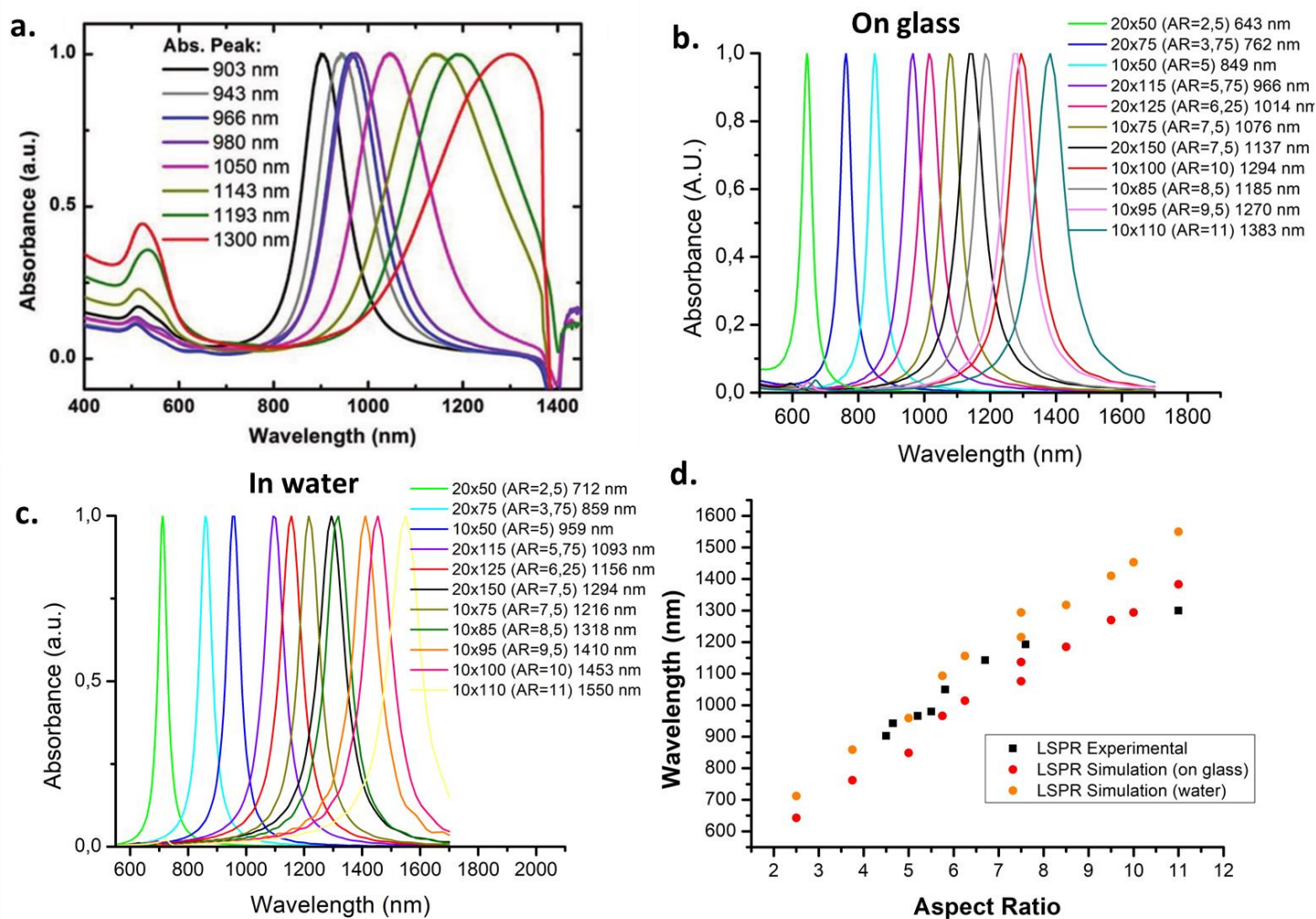


Figure 73. Absorbance for gold nanorods of different sizes (a) Experimental results obtained by Xiang et al. [275] (b) Normalized absorbances for different Au NRs' AR obtained from simulation using Lumerical ©. Case where the rod is on glass substrate (c) Case where the rod is in water (d) Comparison of LSPRs as a function of Aspect Ratio for experimental and simulated results.

Figure 73.d. shows the variation of LSPR as a function of AR obtained through experiments and simulations. We can observe a good match between the experimental and the simulated absorbances. The difference of LSPRs that we could observe between the simulation (on glass substrate) and the experiments becomes smaller in the case where the rod is surrounded by water. This difference was indeed explainable by the difference of index of the surrounding medium: water in the case of the experimentally measured absorbances ($n=1.33$), air in the case of simulated ones ($n=1,00$), as well as the presence of a glass substrate in the case of the simulation.

In order to be closer to the experimental measurement conditions, we run the same simulation by replacing the surrounding medium by only water (Figure 73.c.). We can notice that the change of surrounding medium only implies a vertical shift of the LSPRs towards longer wavelengths.

At high aspect ratio (11), both LSPRs predicted by the simulation are over the experimental one.

Those results validate the use of the simulation model in order to predict the LSPR of a specific batch of gold nanorods for ARs under extreme values (<11).

We also notice that LSPR does not depend on AR alone, since two rods of the same AR (7.5) can exhibit slightly different LSPRs.

b. Field distribution around a gold nanorod

On top of the simulation results mentioned above, two monitors cutting the rod in two in the transversal direction were added in order to visualize the electric field distribution in the close vicinity of the rod at his LSPR. The result for a rod whose dimensions are 20nm x 115nm (corresponding to a LSPR of 966 nm) is shown [Figure 74.c.](#)

As we can see on [Figure 74.a. and b.](#), the electric field is enhanced in the close surrounding of the nanorod, principally around the edges of the rod. The maximal electric field enhancement ratio that is obtained is around $3 \cdot 10^4$.

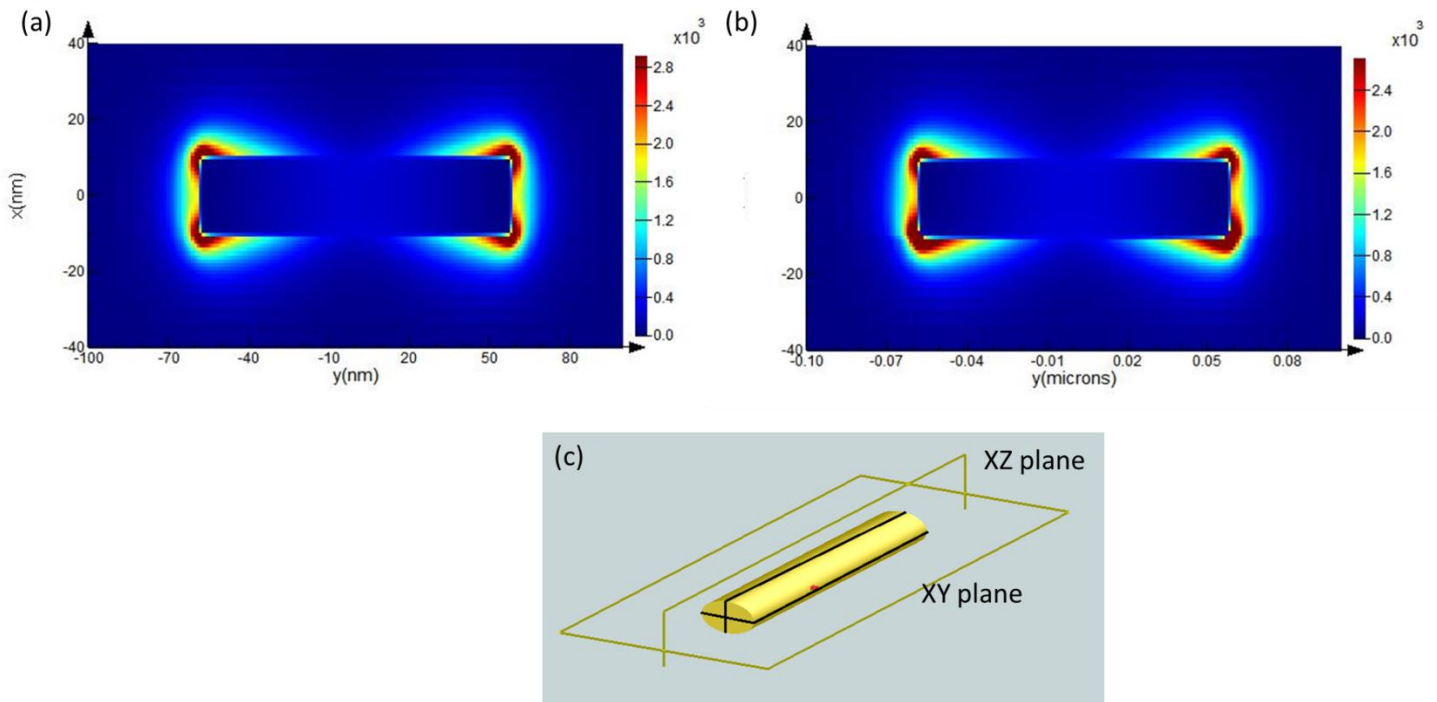


Figure 74. Electric field visualisation a. on a XY plane (parallel to the glass substrate) b. on a ZY plane (normal to the glass substrate) c. Scheme of the position of the planes relative to the rod.

The visualization of the field allows us to see that the maximal upconversion enhancement would occur when the UCNPs volume overlap with the concentrated electromagnetic field volume would be maximal. We thus see that optimizing the size of a gold nanorod for an optimal enhancement of the upconversion effect implies both LSPR matching and maximizing the volume of electromagnetic field concentration.

2. Case of gold nanodisks in array : Radius impact on LSPR

a. Far-field absorption

Gold nanodisks arrays were deposited on a glass substrate using a process called e-beam lithography. This process can be described as followed: a photosensitive resin was first deposited on a substrate. The resin was locally exposed to e-beam according to the pattern of arrays. The resin was then developed, and this way, the exposed parts were removed. An adhesion layer of 2 nm of Cr was deposited followed by the deposition of 50 nm of gold by thermal evaporation. Finally, the second development occurred and the unexposed parts were removed. The pattern remained on the glass substrate, as we can see on [Figure 75 \(a\)](#). This work was done in collaboration with Laurent Billot.

The optical measurement set-up consists in a white-light source transmitted through the sample. The transmitted beam can then either be directed to the microscope used adjust the position of the sample, or to the spectrometer ([Figure 75 \(b\)](#)). The absorption of arrays of nanodisks of for three different diameters is shown [Figure 75\(c\)](#) .

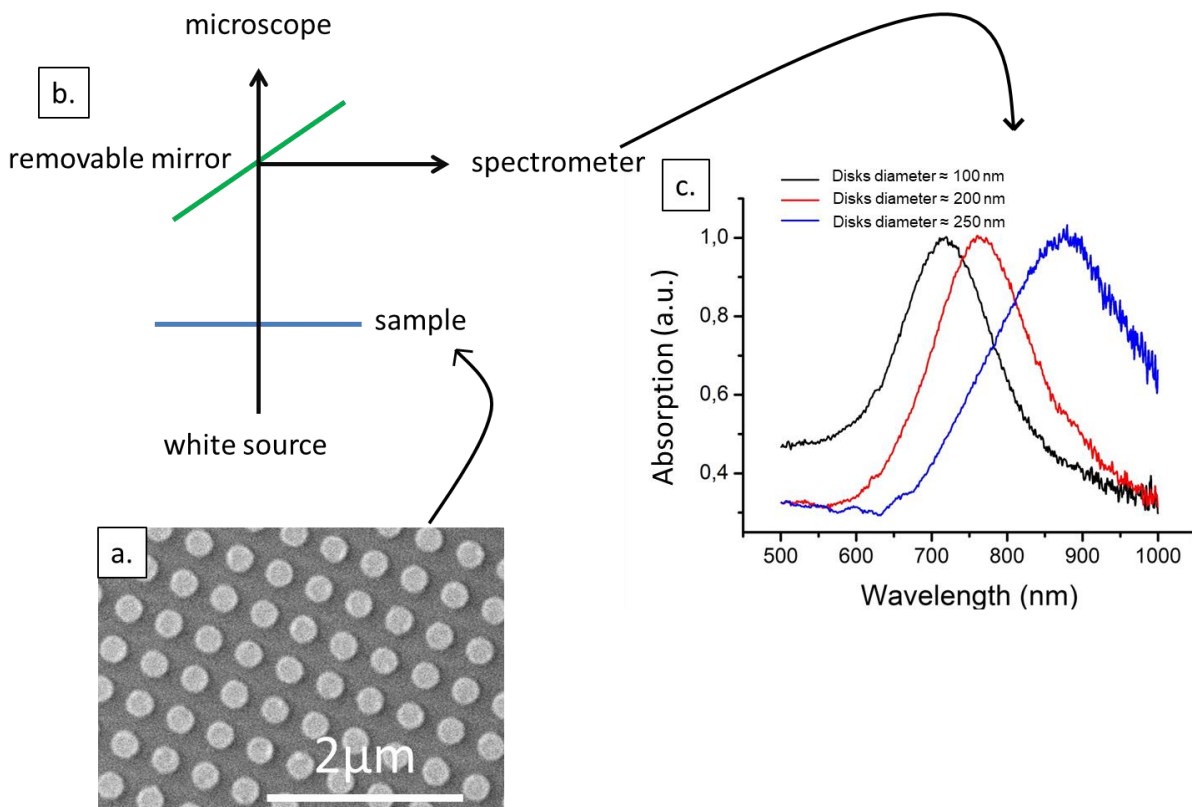


Figure 75. (a) SEM image of nanodisk arrays of diameter ≈ 250 nm. (b) Simple scheme of the set-up. (c) Absorption spectrum of arrays of nanodisks of different diameters. The signal over 1000 was cut because it was too noisy (limit of detector).

We can observe that the plasmonic resonance shifts to the blue side as the diameter of the disks decreases: for 200 nm diameter, the resonance is around 860 nm, 760 nm for 150 nm diameter and 710 nm for 75 nm diameter.

b. Near-field localization

As briefly mentioned in the first chapter (section II.2.a), a near-field imaging technique was used in order to visualize the electromagnetic field close to gold nanodisks. This technique consists in scanning the surface of a substrate on which gold nanodisks had been deposited with a sharp tip at the end of which an UCNP had been stuck (Figure 76 (a)). The UCNP (Er^{3+} and Yb^{3+} doped KY_3F_{10}) is excited by a 975 nm laser. The fluorescence emitted by the UCNP is proportional to the local electromagnetic field intensity, and measuring the fluorescence intensity allows the creation of such electromagnetic field intensity maps.

We can observe the formation of two lobes around the gold nanodisks, oriented in the direction of incident polarization (Figure 76 (b) (c) and (d)). Those lobes do correspond to the enhanced local field as confirmed by FDTD simulation of a nanodisk (Figure 76 (e)).

Figure 76 (f) to (j) show the variation of the intensity of the electromagnetic field as the diameter of the disks increase. We can see that as the diameter increases, the electromagnetic field is less intense than for smaller disks.

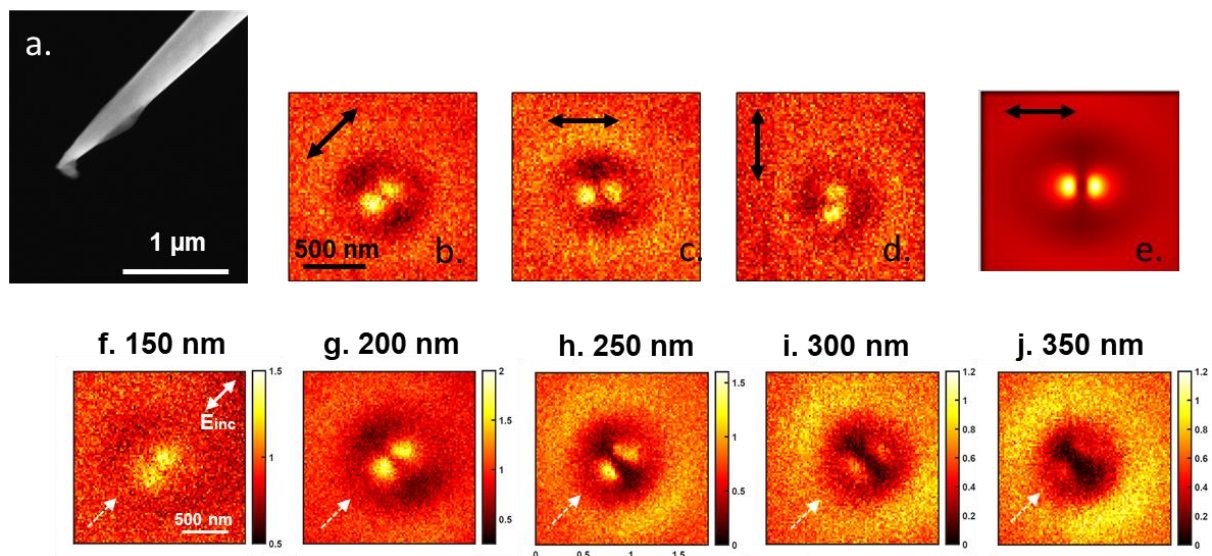


Figure 76. (a) UCNP at the top of the needle that scans the substrate. (b) (c) (d) Near field images for different polarization directions . (e) to (i) Near field of nanodisks whose diameter varies between 150 and 350 nm.

The ideal diameter of nanodisks for the optimal upconversion enhancement (LSPR around 900/1000 nm) is between 250/300 nm. Such large (compared to the scale of the perovskite layer for instance) nanodisks would however introduce perturbations in the devices more than nanorods exhibiting a LSPR in the same range for a much smaller size.

Furthermore, the complexity of e-beam lithography prevents it to be applied for large-scale production, and the patterns printed within a reasonable time cannot exceed a couple of mm^2 (9 hours for 15 mm^2 fabrication).

For those two reasons, we decided to mainly focus on NRs as plasmonic structures to incorporate in perovskite solar cells.

3. Deposition processes – Morphological optimization

a. NRs alone

In order to implement NRs together with UCNPs in perovskite solar cells, several preliminary tests were carried out on the deposition processes of NRs only. The characterization tool we used is based SEM. The NRs were deposited on compact TiO₂ (typical ETL used in perovskite solar cells). The challenge was to obtain non-agglomerated NRs and a homogeneous dispersion of rods on the substrate. There were several parameters we could adjust:

The first one is deposition process: as we can see [Figure 77 \(b\)](#), drop casting led to big agglomerated NR clusters. We thus preferred to apply spin-coating as a deposition method. However, NRs from the original aqueous solution had no adhesion on the substrate ([Figure 77 \(a\)](#)), which is a well-known issue when it comes to nanorods dispersion on a smooth substrate [295]. For this reason, we applied a method based on a mixture of different solvents to disperse NRs.

Ethanol (EtOH) or Tetrahydrofuran (THF) was then added to the aqueous solution in order to increase NRs' adhesion on the substrate. CTAB is unstable in THF, and adding such solvent results in increasing van der Waals interactions between rods themselves or with the substrate [296]. At high THF volumic ratio, nanorods become so unstable that they tend to form self-assembled structures [297].

For this reason, the solvent mix has to be adjusted. For instance, when the NRs were redispersed in EtOH and then diluted in THF with a 50/50 volumic ratio, the NRs still agglomerated, as we can see on [Figure 77 \(c\)](#). The use of EtOH as a solvent is not as efficient as THF in terms of prevent agglomeration as we can see by comparing [Figure 77 \(d\)](#) and [Figure 77 \(e\)](#). The use of THF at 10-20 % allowed a compromised result ([Figure 77 \(e\)](#))

One difficulty encountered in the manipulation of NRs is the high incertitude on the concentration of the solution: since NRs cannot be dried and then be redispersed (because they would irreversibly agglomerate), the concentrations of the solutions have to be estimated by other means.

One way is to rely on the correlation between the optical absorbance and the concentration as explained by Haiss et al. [298]

We decided to choose a second way: to weight a glass substrate without and with a known volume of the NR solution deposited on top with the solvent evaporated.

All NRs used in this work from now on were synthesized by Synthesis 2 (Chapter 3) and have a mass concentration around 1mg/mL.

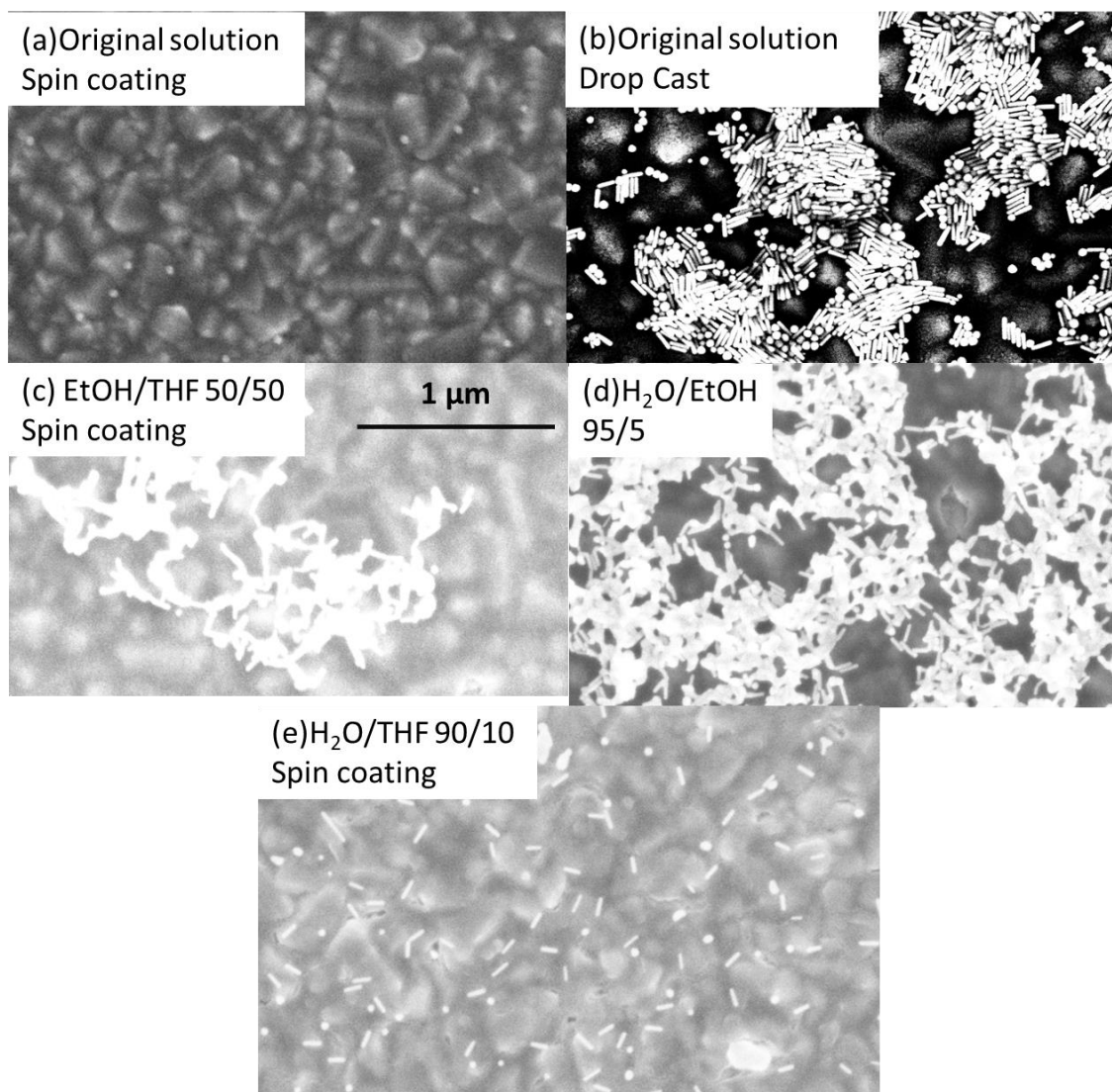


Figure 77. Different SEM images obtained from NRs dispersion on compact TiO_2 . The original aqueous solution is the one obtained directly after the synthesis 2 as described in Chapter 3. The spin coating is run at 2000 rpm for 30 sec. Any deposition is followed by 2 min annealing at 100°C . (a) Original solution, spin coated. (b) Original solution, drop casting. (c) NRs in EtOH/THF volumic ratio of 50/50. (d) $\text{H}_2\text{O}/\text{EtOH}$ 95/5 (e) NRs in $\text{H}_2\text{O}/\text{THF}$ of 90/10

b. UCNPs and NRs

In order to add both UCNPs and gold NRs, several deposition methods were tried:

- The deposition of NRs following the deposition of UCNPs.
- The deposition of UCNPs following the deposition of NRs.
- The deposition of a mixed solution of UCNPs and NRs.

As mentioned in Chapter 1, the distance between the plasmonic nanoparticle and the UCNP is crucial for plasmonic enhanced upconversion. A too small distance between these two types of particles could result in the quenching of the luminescence. At a too high distance, no enhancement occurs. 6-15 nm is the optimal distance in the case of a silver nanosphere [209].

Morphological characterizations were first carried out on smooth surfaces such as silicon wafer or compact TiO₂ (both having roughness under 50 nm, which is in the first approximation equivalent for any particle below this size). The choice of UCNPs is also important impacting their surface distribution and NP interactions: as we can see by comparing [Figure 78 \(a\) and \(b\)](#), NRs tend to stick less to the surface of KY₇F₂₂ than KY₃F₁₀ UCNPs, probably due to different surface energy. In the first case, NRs were rather far from the UCNPs, at a distance where any plasmonic enhancement is unlikely to happen whereas in the second case, they were stick to them (NRs are highlighted in red in [Figure 78.b](#)).

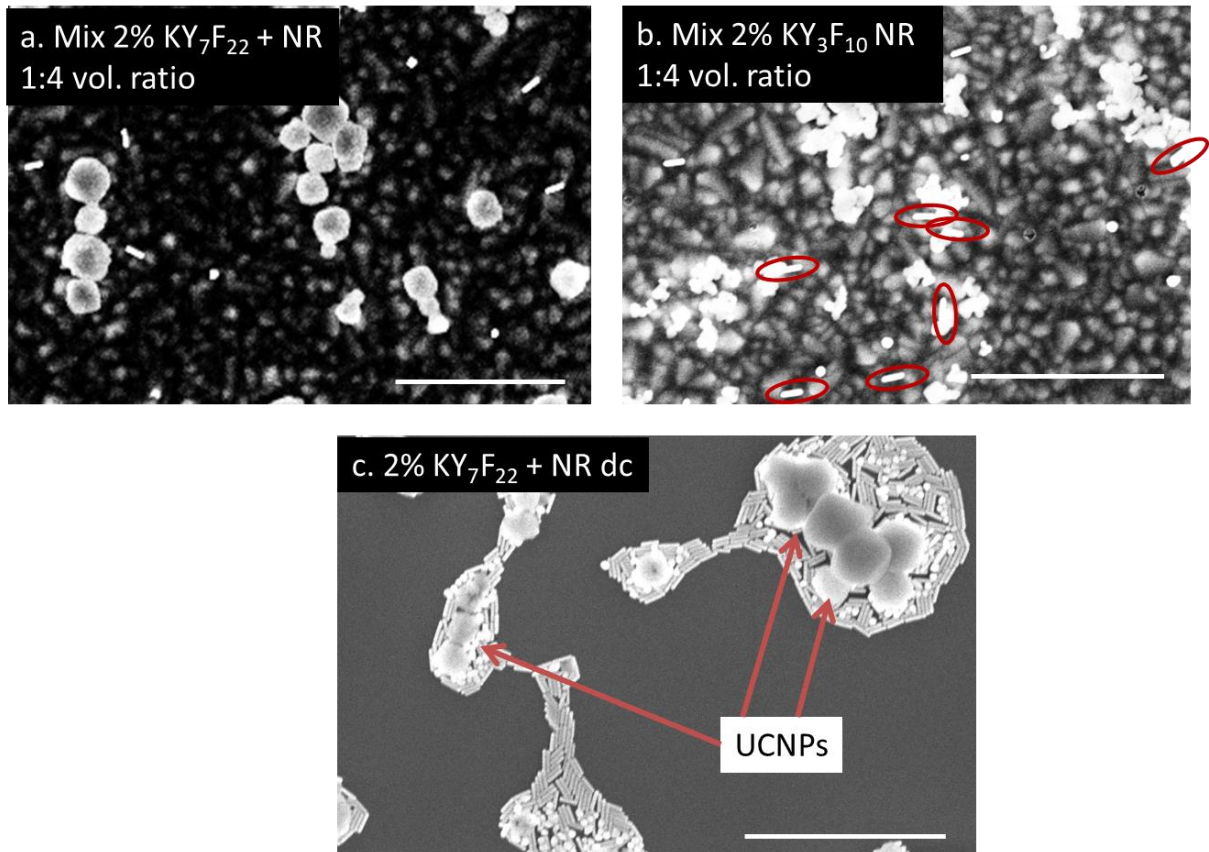


Figure 78. SEM images of different UCNPs/ gold NR combinations. Scale bar = 1 μm. (a) Mixed solution prepared with a volumic ratio of 1:4 of 2 wt % KY₇F₂₂ and NRs. (b) Mixed solution prepared with a volumic ratio of 1:4 of 2 wt % KY₃F₁₀ and NRs. (c) NRs drop casted on top of 2% KY₇F₂₂ on Si wafer. Mixed solutions are deposited by spin coating. Spin coating processes are done at 2000 rpm for 30 sec and followed by 100°C annealing for 3 min. Substrates have to go through 5 minutes oxygen plasma treatment before any observation in order to eliminate ligands.

We drop-casted some NRs solution on top of KY₇F₂₂ and obtained aggregates of NRs and UCNPs as we can see on [Figure 78 \(c\)](#). Such an aggregate of NRs is not an optimized distribution on a surface because the aggregate of NRs could behave as charge carrier barriers.

Since ETL-free devices were also experimented in this work, we chose to test the deposition of UCNPs/NRs on FTO. Being much rougher than compact TiO₂, nanoparticles behave differently on this surface.

Two NRs depositions were carried out: drop-casting in the first case (Figure 79(a)), spin-coating (for 5 seconds) in the second (Figure 79(b)).

FTO, due to its higher roughness (compared to Si or TiO₂), tends to retain more NRs on its surface (Figure 79(a) and (b)). For this reason, we deposited NRs before UCNPs and assumed NRs would be retained better on FTO before being covered by UCNPs.

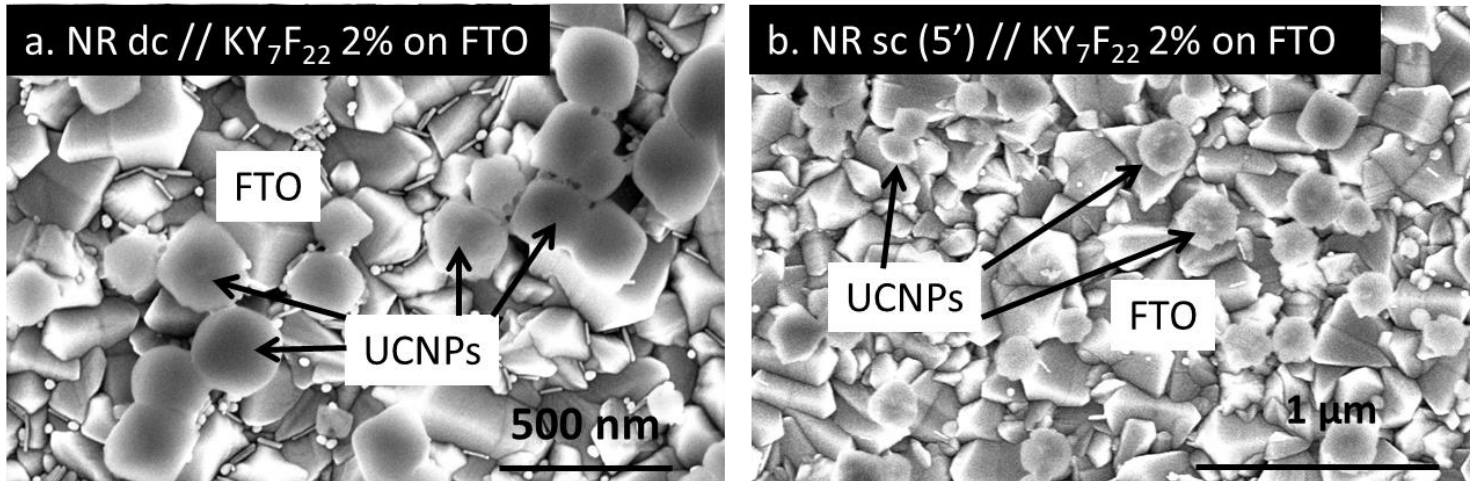


Figure 79. SEM Images a. NRs drop-casted on FTO with KY₇F₂₂ on top, spin coated (30 seconds at 2000 rpm). b. Same deposition except that NRs are deposited by spin coating (5 seconds)

4. Plasmonic enhanced upconversion – Preliminary studies

In order to see whether the presence of NRs has an effect on PL intensity, we measured the PL intensity of a sample with a part of it covered by NRs and UCNPs, and another part covered by UCNPs only. This sample was prepared by placing a tape covering half of the substrate during NRs deposition.

The substrate used here was a glass substrates with compact TiO₂ deposited on top. The NRs solution was diluted using THF 20 vol. %.

The UCNPs (NaYF₄ solvothermal) were then deposited by spin coating (2000 rpm for 1 min followed by 10 min annealing at 100°C), and 45 min oxygen plasma followed.

As we can see on [Figure 80](#), the intensity of the PL is higher in the presence of NRs, which confirms a macroscopic plasmonic enhancement of upconversion.

We warned the reader several times regarding PL intensity comparison. However here, the fact that the measure was made on the same substrate for both situations (with and without NRs) minimized the error induced by the change of focalization occurring when the substrate was replaced. Here, the only experimental condition changing from one measure to another is the sample's composition. Furthermore, similar results were obtained in the same type of experiment when another batch of UCNPs was used (KY₃F₁₀:YF₃).

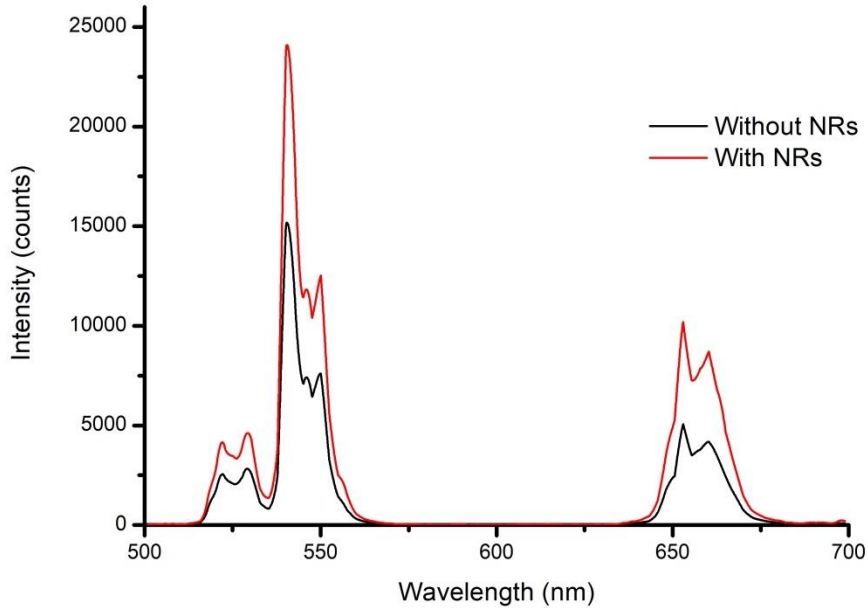


Figure 80. Influence of the presence of NRs on the PL intensity.

The enhancement ratios are 1.6 for the green (541nm) luminescence and 2 for the red one (652nm). This small difference between the two ratios could be attributed to the LSPR of the NRs that is closer to 900 nm (so the electromagnetic field is supposedly higher at wavelengths closer to 900nm). The device where these two types of particles were inserted will be discussed p 119.

II. UCNPs implementation in perovskite solar cells

UCNPs were inserted in solar devices. As we concluded in the chapter 3, we focused our optimization on KY_7F_{22} and $KY_3F_{10}:YF_3$. Attempts were carried out with KY_3F_{10} and $NaYF_4$ (hydrothermal).

The optimization was obtained by varying three parameters:

- The type of UCNPs
- The concentration in UCNPs
- Configuration: UCNPs are deposited either on the front side (on FTO) or on the rear side (on the perovskite layer) as shown [Figure 81](#).

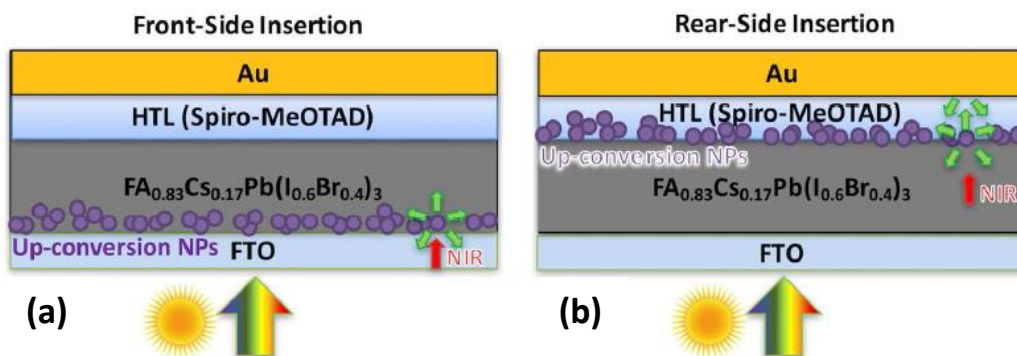


Figure 81. Schemes displaying the insertion of UCNPs in the device (a) in the case of the front-side insertion (b) in the case of the rear side insertion.

Only the optimization on KY_7F_{22} will be given in the main text, and the results regarding to three other types of NPs will be given in the Annex 11.

UCNPs were always deposited by a spin-coating process at 2000 rpm for 30 sec after which samples were annealed at 100°C for 3 min. UCNP solution have to be freshly sonicated for 1h at 50°C before use.

Here we aim to obtain an optimal amount of UCNPs to incorporate on the optimal side of $FA_{0.83}Cs_{0.17}Pb(I_{0.6}Br_{0.4})_3$ perovskite solar cells allowing a macroscopic photovoltaic characteristic enhancement. We then applied this optimal condition for microscopic studies.

1. Considering the morphology of the device

a. Impact of the presence of the UCNPs on perovskite surface coverage

We can notice a difference between the wettability of the perovskite precursor solution on FTO and on KY_7F_{22} , as shown on [Figure 82](#). The presence of a layer of UCNPs resulted in a reduced surface coverage of perovskite.

The anti-wetting property of KY_7F_{22} would rather be related to a physical reason such as surface morphology (high roughness at low surface coverage). This is similar to the reason why lotus leaves are hydrophobic [299]. Those UCNPs do not possess ligands, so the hypothesis of repulsive interactions between ligands and precursor solutions is unlikely.

Drop of perovskite precursor solution on
(a) FTO
(b) FTO + UCNP

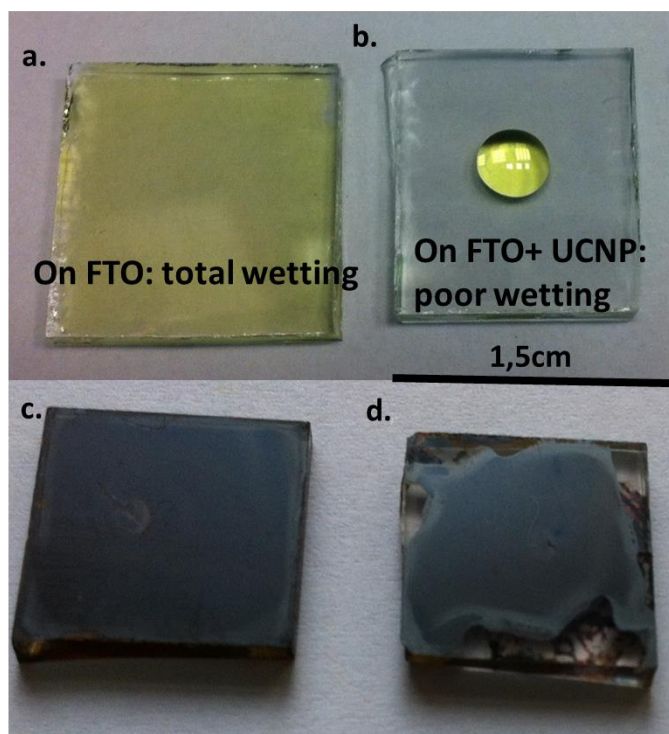


Figure 82 Qualitative comparison between the wettabilities of perovskite precursor solution ($FA_{0.83}Cs_{0.17}Pb(I_{0.6}Br_{0.4})_3$) on (a) FTO (b) $KY_7F_{22}:5\%Er^{3+}:20\%Yb^{3+}$, 2wt% in IPA. Resulting films after spin-coating and annealing (b) and (c).

b. Study of the impact of the concentration of UCNP's dispersions on their surface distribution on FTO and on perovskite

By increasing the mass concentration of the UCNP solution, we increase the concentration of the particles on the surface. This phenomenon is well illustrated by the SEM images for 2 and 7% KY₇F₂₂ on perovskite and FTO shown in [Figure 83](#).

We observe a good homogeneity of the distribution of KY₇F₂₂ on the substrate surface. However, homogeneity was not observed in the case of KY₃F₁₀, probably due to their surface property, as we can see [Figure 84](#).

For this reason, we focused the optimization of implementation of UCNP's in solar devices on KY₇F₂₂.

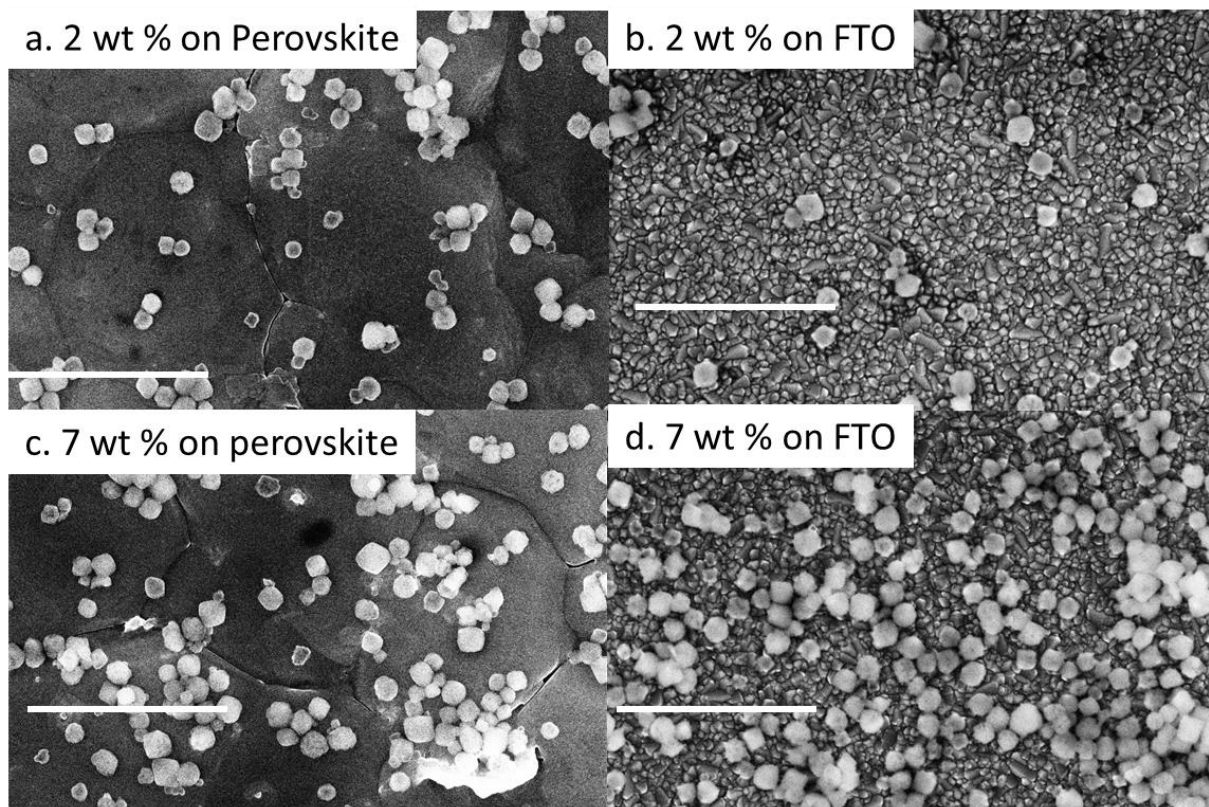


Figure 83. SEM images of KY₇F₂₂ (a) on FA_{0.83}CS_{0.17}Pb(I_{0.6}Br_{0.4})₃. Concentration: 2 wt %. (b) on FTO. Concentration: 2 wt %. (c) on FA_{0.83}CS_{0.17}Pb(I_{0.6}Br_{0.4})₃. Concentration : 7 wt %. (d) on FTO. Concentration: 7 wt %. Scale bar 2μm.

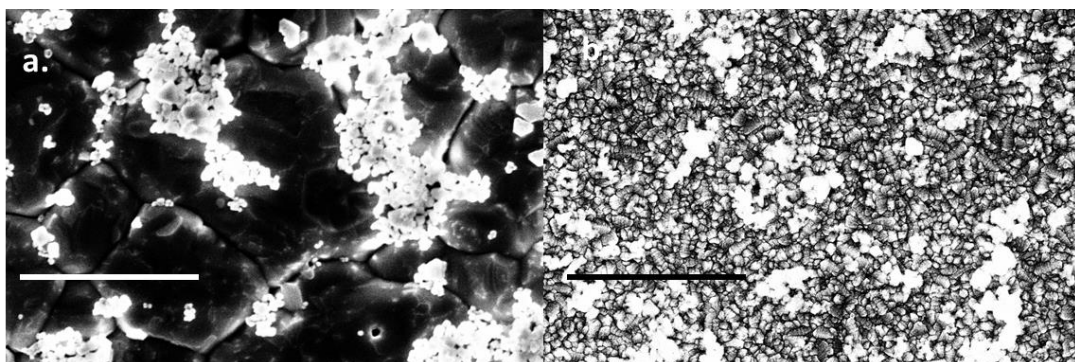


Figure 84. SEM images of KY₃F₁₀ 2 wt % in IPA a. on (FA_{0.83}CS_{0.17}Pb(I_{0.6}Br_{0.4})₃). b. on FTO. Scale bar 2μm.

c. Influence of the presence of UCNPs on device's roughness

No matter whether the UCNPs are placed on the front side (on FTO) or on the rear side (on the perovskite layer), they will inevitably have an impact on the morphology of the device. Photographs at different fabrication steps of devices in which UCNPs are implemented in the front and rear sides are shown [Figure 85](#). The surface of the top gold electrode is much rougher in the presence of the UCNPs than the pristine device. This tendency is even stronger in the case where the UCNPs are inserted in the rear side of the device. This is due to the fact the only layers that could smoothen the surface are the HTL and gold layer, whereas in the case of the front configuration, the perovskite layer can somehow cover the roughness of the UCNP layer.

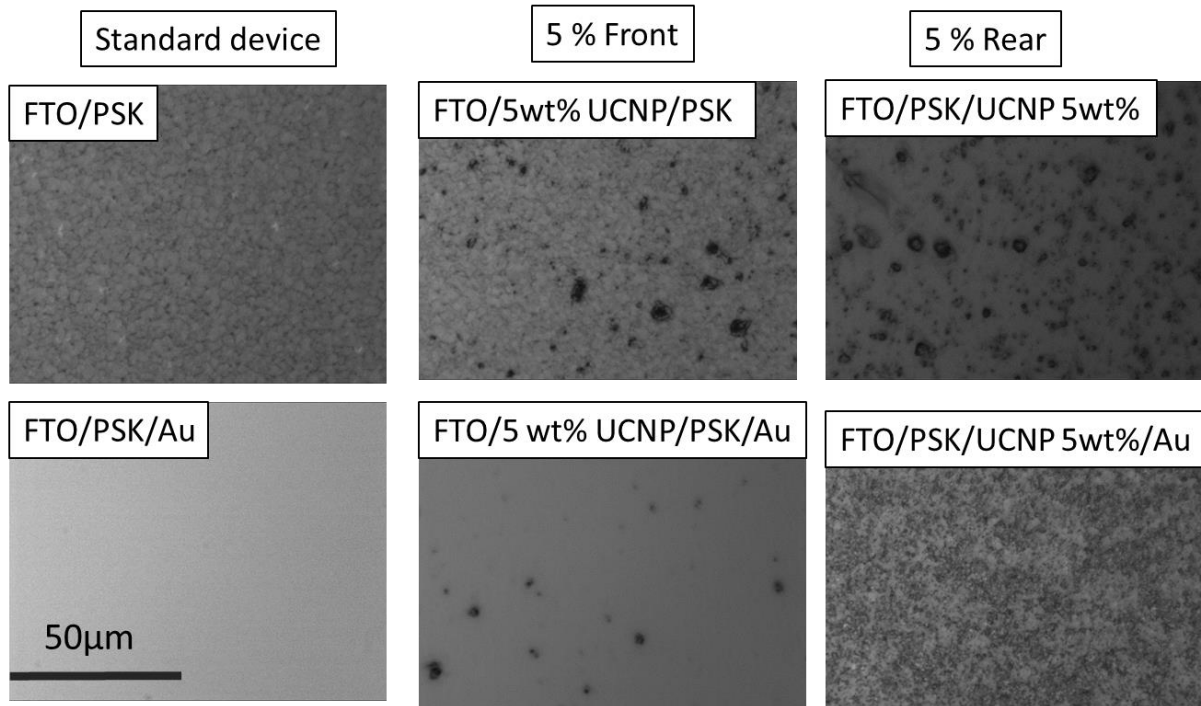


Figure 85 Optical images taken with a camera mounted on a microscope of devices in which UCNPs ($\text{KY}_3\text{F}_{10}:\text{YF}_3$ 5 wt % in IPA) were implemented in the front (in the middle) and the rear (right) side compared to standard device (left) at two different magnifications. PSK = $(\text{FA}_{0.83}\text{Cs}_{0.17}\text{Pb}(\text{I}_{0.6}\text{Br}_{0.4})_3)$

Some AFM (Atomic Force Microscope) measurements were run in order to quantify roughness, as we can see in [Table 9](#). Those measurements confirm the bigger impact on roughness when the UCNPs are inserted on the rear side.

Type of device	Standard	2 % Rear	5% Rear	10% Rear	2% Front	5% Front	10% Front
Roughness	14	82	96	152	22	32	49

Table 9. Values of root mean squared roughness measured on the gold layer of devices prepared with 0, 2, 5, or 10% of UCNPs ($\text{KY}_3\text{F}_{10}:\text{YF}_3$) inserted on the rear and front side respectively.

This impact on the morphology was also qualitatively observed for different concentrations of particles, as we can see in [Annex 10](#).

Considering the thickness of the perovskite layer being between 300 and 500nm, and the particles' diameter between 100 and 150nm for KY_7F_{22} , a cluster of two particles of KY_7F_{22} can be uncovered by

the perovskite layer: the formation of a huge agglomeration that the upper layer might not be able to cover results in the formation of micrometer-large holes as we can see by comparing [Figure 86\(b\)](#), showing perovskite deposited on UCNPs to [Figure 86\(a\)](#), perovskite deposited on FTO. Let's however note that this is not predominant behavior. In general, the perovskite is predominantly defects-free ([Figure 86\(c\)](#)).

We can clearly see that the morphological perturbation (increasing with concentration) will not play in the favor of a high concentration of inserted UCNPs in the device. Visible defects could act as recombination sites or prevent smooth charge extraction.

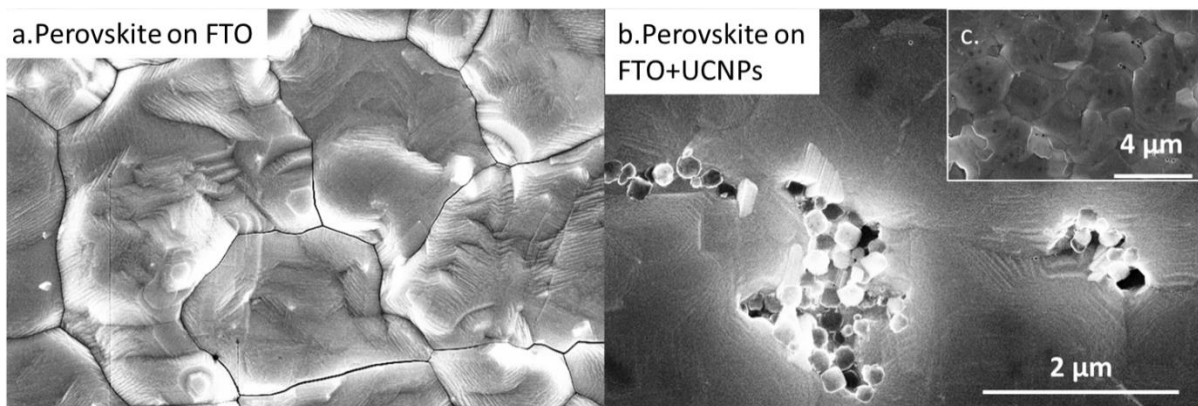


Figure 86 SEM image of a perovskite ($\text{FA}_{0.83}\text{CS}_{0.17}\text{Pb}(\text{I}_{0.6}\text{Br}_{0.4})_3$) layer deposited (a) on FTO (b) and (c) on 2 wt % KY_7F_{22}

2. Electrical characterizations

While from the morphological point of view, it seems that the presence of UCNPs introduces defects, irregularities and pinholes that would tend to decrease the device's performance, the electrical characterizations showed however improved solar cell efficiencies when an optimal amount of UCNPs were inserted. This improvement is mainly due to an increase of the short circuit current. A study on the impact of UCNPs insertion on the performances of perovskite solar cells was carried out by varying the concentration of UCNPs. Two different configurations (rear- and front-side insertion) were compared. The following part discusses the results when KY_7F_{22} NPs were inserted in an ETL-free $\text{FA}_{0.83}\text{CS}_{0.17}\text{Pb}(\text{I}_{0.6}\text{Br}_{0.4})_3$ perovskite device with $^2\text{Spiro}$ as HTL. Other optimization regarding the insertion of $\text{KY}_3\text{F}_{10}:\text{YF}_3$, KY_3F_{10} , and NaYF_4 (hydrothermal synthesis) are given in Annex 11 and will be discussed in section c of this subsection.

a. Influence of concentration and configuration – KY_7F_{22}

Doped KY_7F_{22} were inserted in the rear- and front- sides of the devices using a dispersion of four different concentration (2, 5, 7 and 10 wt % in IPA) were tested. I-V curves were measured on those devices. Average J_{sc} , V_{oc} , FF and PCE for solar cells coming from the same batch realized on the same day are compared in [Figure 88](#). [Figure 87](#) displays three IV-curves, corresponding to the best performing devices (standard witness solar cell, 5 wt KY_7F_{22} % front- and rear-side insertions).

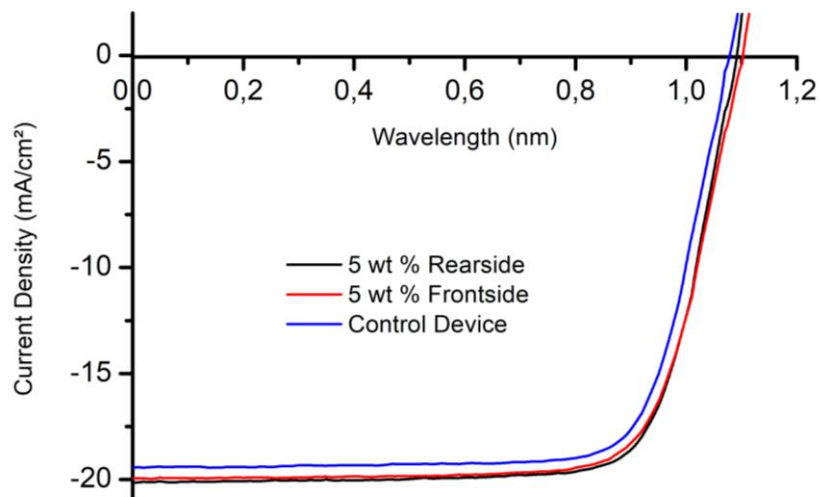


Figure 87. IV curve for the best performing devices with KY_7F_{22} in front- and rear-side insertion (5 wt %) in collaboration with Zhelu Hu

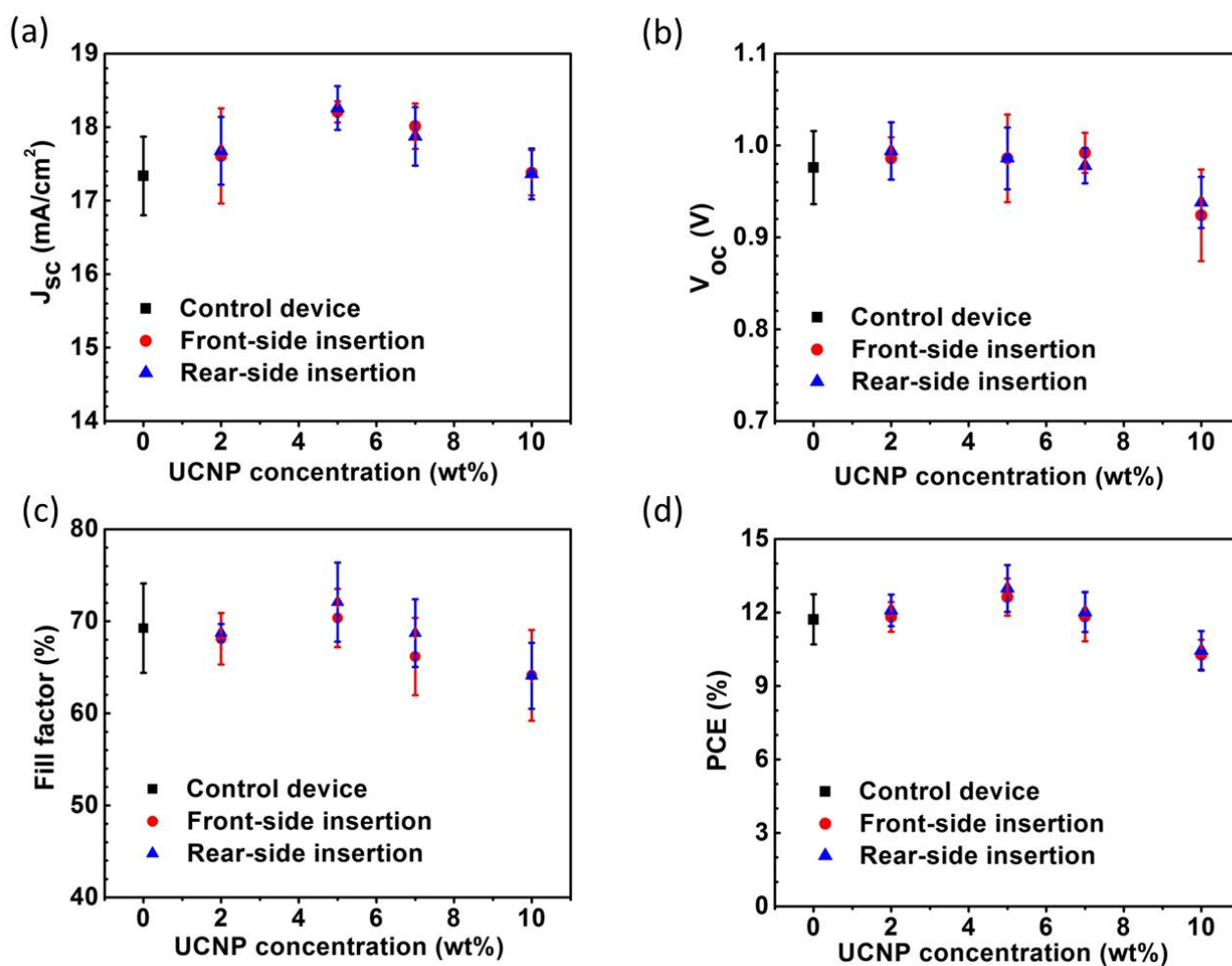


Figure 88. J_{sc} , V_{oc} , FF and PCE evolution for different concentrations of KY_7F_{22} in front and rear configurations. At least 5 devices are used for each point. In collaboration with Zhelu Hu.

About 4% and 5% averaged J_{sc} enhancement was obtained when a 5 wt % UCNP solution was applied in the front- and rear-side NP insertion configuration. Such J_{sc} enhancement, however, starts to decrease with the use of a UCNP solution of a higher concentration (> 5 wt%). While a larger amount of UCNPs can result in a higher upconversion current contribution, the formation of large insulating UCNP clusters can increase the solar cell series resistance. These factors thus lead to the observed progressive reduction of J_{sc} when the UCNP solution concentration was beyond the optimal value (~ 5 wt %). Concerning V_{oc} , on both front- and rear-side insertion configurations we observed negligible effect when the UCNP concentration is small or moderate (≤ 7 wt%) and a reduction of V_{oc} when a 10 wt % UCNP concentration was applied.

Such a reduction of V_{oc} can be due to the formation of large UCNP clusters at the interface which acts as charge recombination centers and perturbs the morphology of the perovskite or HTL layer formed on top. The perturbation of perovskite has a bigger impact on the device's performance and that is why V_{oc} decreases further in the front configuration. Furthermore, V_{oc} has been related for the case of a perovskite solar cell to the difference between the quasi-Fermi level of the electron at the FTO/perovskite interface and the quasi-fermi level of the hole at the HTL/Au interface under [300]. Creating pin holes as well as introducing defect in the perovskite layer will create intra bandgap electronic levels, which will contribute to decrease V_{oc} .

In terms of fill factor (FF), similar FF values as the control device were observed when the UCNP concentrations were ≤ 5 wt% for both front- and rear-side configurations, suggesting minor deterioration of series and shunt resistances due to the insertion of UCNPs as long as their concentration was relatively low. At a higher UCNP concentration (≥ 7 wt%), however, a reduction of FF can be observed in both device configurations, suggesting increased series resistance and recombination losses due to the formation of large insulating UCNP clusters. Overall, by comparison to the control device, about 5.7% and 7.4 % of averaged PCE enhancement was observed respectively in the front- and rear-side UCNP insertion configuration when an optimal UCNP solution concentration (5 wt%) was applied.

The t-test applied on PCEs' distributions testify that the control device distribution has a probability of respectively 0.85 and 0.90 to effectively belong to different distributions than the distribution of the 5 wt% rear- and front-side insertion.

This general tendency for V_{oc} , J_{sc} and PCE to increase until the optimum concentration is obtained, and decrease at a higher concentration seems to be related to a balance between at least three different effects:

- upconversion and scattering effects which contribute to increase the photocurrent: at higher UCNP concentration, the PL intensity increase (Section II.3.b.), the emitted light is more intense. More charge carriers can be generated if the emitted light is absorbed by the perovskite.

Furthermore, nanoparticles also play the role of light scatterers, which contribute to increase light paths and thus the number of photogenerated charge carriers due to an increased absorption.

- Structural impacts of the presence of UCNPs. UCNPs could lead to a decrease of cell efficiency due to an increased roughness and the formation of defects in the solar cell. At high surface coverage, charge recombination might occur at a higher rate and the UCNP will act as a blocking layer.

- If the parameters of the device benefit from light scattering caused by the presence of nanoparticles, it can also suffer from the shadowing of the particles, especially in the front configuration. It is a balance between scattering and absorption cross sections, even if absorption of UCNPs (Figure 49) is small in the absorption range of the perovskite material.

All these effects have a bigger impact at high UCNP concentration.

b. External Quantum Efficiency (EQE) of the device – in collaboration with Zhelu Hu

The EQE of a device with 5 wt % KY₇F₂₂ in the rear-side (Figure 89) exhibit an increase of EQE between 0 and 1% between 950 and 1000 nm, which confirms that the increase of J_{sc} observed in the previous part is partially related to the absorption of the NIR part by the device.

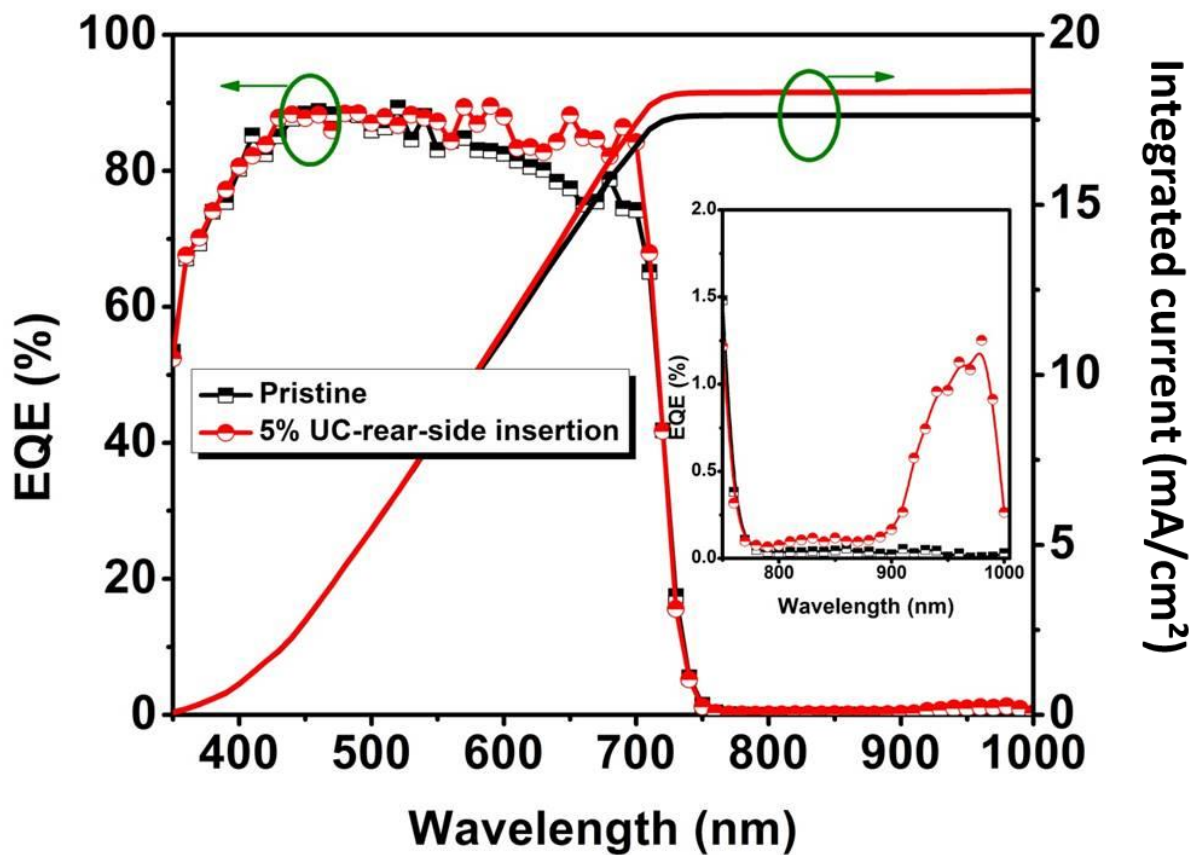


Figure 89. EQE spectra of two planar ETL-free FA_{0.83}CS_{0.17}Pb(I_{0.6}Br_{0.4})₃ perovskite solar cells with and without (“pristine”) co-doped KY₇F₂₂ 5 wt % inserted at the interface between the perovskite layer and the HTL polymer layer. The inset figure exhibits the zoom-in view of the spectrum range between 750 nm and 1000 nm. In collaboration with Zhelu Hu.

The integrated current for the current devices is worth:

17.61 mA/cm² from 350 to 740 nm,

0.02 mA/cm² from 740 to 1000 nm.

For the 5 wt % in the rear-side, the integrated current is worth:

18.3 mA/cm² from 350 to 740 nm:

0.05mA/cm² from 740 to 1000 nm.

The main difference between the two curves thus occurs between 500 and 700nm. This suggests that the absorption at 980 nm in the ytterbium absorption's region is not the main contributor to current enhancement. This enhancement is mainly due to scattering effect.

However, the incident power around 1000 nm delivered by the monochromator is around $10^{-5}\text{W}/\text{cm}^2/\text{nm}$. Since upconversion is a non-linear effect, the contribution to the photocurrent at higher densities (the solar irradiance at this wavelength is about 10^4 times higher) would probably be significantly higher.

c. Comment on others UCNPs

In Annex 11, the same optimization on concentration and configuration were carried out on $\text{KY}_3\text{F}_{10}:\text{YF}_3$ (Annex 11.A, in collaboration with Zhelu Hu), KY_3F_{10} (Annex 11.B.), and NaYF_4 (hydrothermal synthesis, Annex 11.C).

We observed similar behaviors in the case of $\text{KY}_3\text{F}_{10}:\text{YF}_3$ insertion as in the case of KY_7F_{22} . We observe for those UCNPs the same tendency of first an increase and then a decrease of J_{sc} , V_{oc} and PCEs with the concentration. The t-test was carried out on the PCE's distributions for standard devices compared to the distributions of devices with 5 wt % front- and 5 wt % rear-side insertions. The distributions of PCEs for a front-side and rear-side insertion (5 wt %) have a probability of 0.95 and respectively 0.99 to effectively belong to different distributions than the one corresponding to standard devices.

In Annex 11.B, the standard device displays a lower average efficiency than the device with 5wt% doped KY_3F_{10} inserted on the rear-side. The standard deviations for the parameters are much bigger. The t-test carried out for the insertions of those UCNPs showed a probability of 0.05 that the PCE's distributions effectively belong to different distributions between standard and UCNP devices.

This does not allow us to conclude on the improvement of the devices in which KY_3F_{10} had been inserted.

This might be explainable by the low optical activity of those particles, which made it difficult to measure their PLQE. Their lower size that implies high particle-to-particle attractions (as discussed in Chapter III section 2.1) also played the role in the difficult to obtain homogeneous dispersion in IPA. The insertion of NaYF_4 (hydrothermal, synthesis D, Annex 11.C.), did not show any improvement as compared to the standard device. This might be related to the difficulty to obtain an homogenous dispersion of the UCNPs on top of TiO_2 .

d. Plasmonic enhanced upconversion in a solar device – Preliminary study

Encouraging results were obtained by comparing UCNPs insertion alone with the insertion of UCNPs together with NRs. The table displaying the best, average and standard deviation values for J_{sc} , V_{oc} , FF and PCE are available in the Annex 11.D, and they correspond to three different compositions of UCNP/NR deposited on TiO_2 : (A) KY_3F_{10} 2 wt % alone, (B) KY_3F_{10} 2 wt % followed by deposition of NRs by spin coating, and (C) spin-coating of a mixed solution (volumic ratio 1:4 KY_3F_{10} 2 wt %:NRs equivalent to weight ratio 500:1).

As we can see on the resulting I-V curves of the best performing devices for those three experimental conditions (Figure 90), (C) leads to a higher average value of short circuit current (22.4 mA/cm^2) than (B) and (C) (20.9 and 20.3 mA/cm^2).

In this experiment, standard device (without any particles) had higher PCEs than devices with nanoparticles inserted. Obtaining higher PCEs for those experimental conditions than for standard devices would give to these results a much stronger weight.

An interesting direction would consist in obtaining similar statistical proofs as the ones used of UCNP insertions by comparing standard devices to devices with UCNPs, NRs, and both. But in this work thesis, we did not have enough time to carry further experiments in that direction.

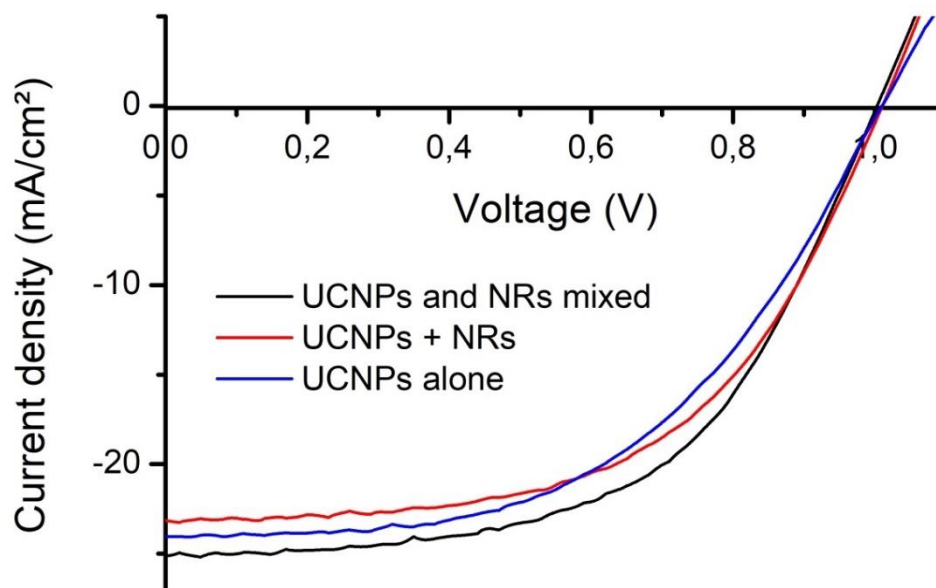


Figure 90. I-V curve comparison between three different devices in which UCNP/NR based layers were deposited on TiO_2 : KY_3F_{10} 2% spin coated (2000 rpm 30 seconds followed by 1 min annealing at 100°C), same followed by NRs spin coating (same deposition speeds and annealing), and deposition of a mixed solution 1:4 volumic ratio of KY_3F_{10} 2% and NRs.

3. Optical characterizations

a. LBIC/fluorescence mapping under NIR excitation

Besides the optimizations on the amount of UCNPs based on macroscopic photovoltaic characteristics, we performed detailed microscopic characterizations by the light-beam induced current (LBIC)/fluorescence mapping technique on solar cells with only half of their interface decorated by UCNPs fabricated on purpose. Such mapping experiments provided detailed microscopic and spectroscopic evidence allowing one to correlate the electrical and optical contribution of UCNPs together with the solar cell morphology. We note that the results from the macroscopic solar cell characterization in the previous section represent a global consequence of UCNP insertion on the perovskite solar cells where multiple effects play together. In order to quantify the upconversion contribution, here we further performed a microscopic solar cell characterization by the LBIC technique to correlate UCNP emission with upconversion-contributed photocurrent

under the excitation of a NIR laser (at 975 nm). Due to experimental limitations in the case of the front-side UCNP insertion (principally due to the shadowing), we focused on the rear-side UCNP insertion configuration to carry out the following microscopic studies. The shadowing of the particles is related to their (small) absorption. The UCNPs being placed on the light path of the laser (in the case of the front configuration), the increase of current can be cancelled out by the reduced absorption of the perovskite.

In order to facilitate LBIC-microstructure correlation, half of the perovskite/HTL interface was masked on purpose during the deposition of UCNPs (KY₇F₂₂ 5 wt % solution used here) and thus creating solar cells with half of their perovskite/HTL interface decorated by UCNPs (Figure 91 (b)).

The LBIC/fluorescence mapping in this work was achieved by focusing a 975 nm NIR laser through the transparent side (FTO) of the solar cell at the perovskite/HTL interface where UCNPs were inserted for half of the device (Figure 91 (a)). The laser spot diameter was about 30 – 50 μm and the total power of the laser spot was about 7 mW (which gives a power density around 360 W/cm²/nm, so 700 times higher than the one at 975 nm the solar emission). While the laser spot was fixed during mapping experiments, the position of the solar cell was controlled by a piezoelectric scanning stage. At each point, we recorded simultaneously the short-circuit current of the solar cell together with a fluorescence spectrum. A rectangular area (100 μm by 25 μm) at the border between the two zones was chosen for LBIC/fluorescence mapping experiments (indicated as the dark dashed line square in (Figure 91 (b)).

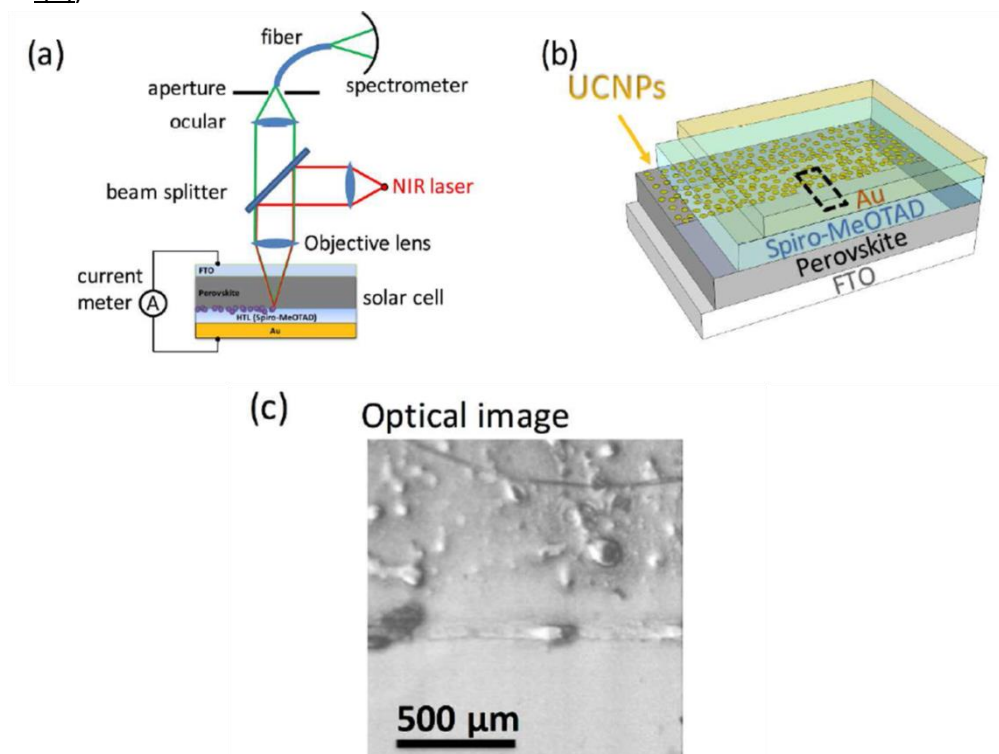


Figure 91. (a) Schematic of the LBIC/fluorescence mapping experimental set-up and the cross sectional schematic of the UCNP (KY₇F₂₂)-incorporated solar cell used in this work. The NIR laser (975 nm) was focused at the perovskite/HTL interface through the FTO side. (b) Schematic (not to scale) of the UCNP-incorporated perovskite solar cell structure where half of the perovskite/HTL interface was decorated by UCNPs. The dark dashed square represents the device area where LBIC/fluorescence mapping was carried out. (c) Optical image of the top-view (imaged from the gold electrode side) of the UCNP-incorporated perovskite solar cell. The interface between the part with and without UCNPs is clearly visible.

A typical LBIC and fluorescence mapping results are shown in [Figure 92](#). When the laser spot mapped from the part of device without UCNPs to the part with UCNPs, we observed a J_{sc} about 3 times higher. This increase of J_{sc} represents both the upconversion contribution from UCNPs excited by the 975 nm laser and the scattering contribution.

During this experiment, it's worth to note that any behavior attributed to defect in perovskite should be identical for both parts of the device with or without UCNPs.

In coherence with the J_{sc} mapping, an appearance of fluorescence of UCNPs was observed when the laser spot travelled from the part without to the part with UCNPs. These trends are clearly visible from the dashed line profile of the mapping results, plotted in [Figure 92](#).

The fluorescence spectrum recorded on the part with UCNP ([Figure 92\(b\)](#)) exhibited two fluorescence peaks located respectively around 540 nm (green fluorescence) and 660 nm (red fluorescence). By comparison to the fluorescence spectrum recorded from stand-alone UCNPs deposited on a glass substrate ([Figure 52](#) and [Figure 18](#)), the green/red fluorescence intensity ratio recorded in LBIC/fluorescence mapping experiment is largely reduced. This is due to the fact that the fluorescence signal must travel through the perovskite layer before being detected during LBIC/fluorescence mapping. As the perovskite layer has a larger absorption coefficient at the green fluorescence wavelengths than red fluorescence ones, the fluorescence signal detected exhibited a reduced proportion of green/red fluorescence.

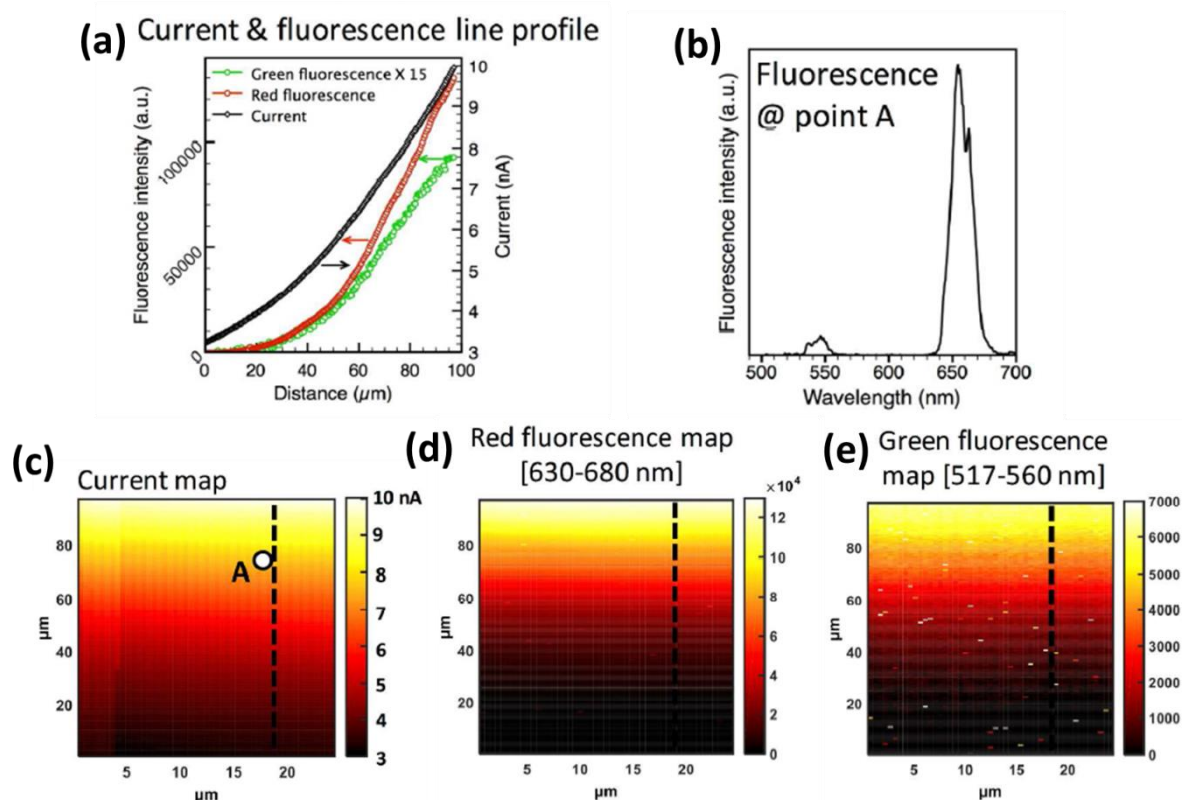


Figure 92. (a) J_{sc} and fluorescence line profile of the dashed line shown in (c), (d) and (e). (b) The upconversion fluorescence spectrum recorded during the LBIC mapping at the point A (labelled in (c)). (c) Short-circuit current J_{sc} mapping under the excitation of a 975 nm NIR laser. (d) and (e) The red and green fluorescence mapping recorded simultaneously during LBIC mapping. Each pixel represents the fluorescence signal integrated between 630 nm and 680 nm for red fluorescence (d) and between 517 nm and 560 nm for green fluorescence (e).

This reduced UCNP green fluorescence observed therefore is related to the optical contribution of the UCNPs in a perovskite solar cell where upconversion fluorescence was absorbed by the perovskite layer. The above-described LBIC/fluorescence mapping experiments thus offer a detailed microscopic picture, by which one can find the electrical and optical contribution of UCNPs together in excellent agreement with the solar cell morphology.

This experiment was also conducted on 5 wt % $\text{KY}_3\text{F}_{10}:\text{YF}_3$ and gave similar results that accessible in the Annex 12.A. In this experiment, however, the dark current was higher than in the experiment above (around 17 nA), and the increase of J_{sc} is only around 1.5 times. This is related to the poor quality of the device used for this measurement (showing only around 1% efficiency). This did not prevent us however to measure the microscopic effect of the presence of UCNPs on the current.

b. Under laser irradiation: variation of current with excitation power

In order to measure the influence of the excitation power of the 975 nm-laser on the current generated in the device, we used a similar set-up than the one represented [Figure 91 \(a\)](#). The current generated by the device was measured as the laser spot is entirely focused inside the pixel. The excitation power varied by changing the power delivered by the laser controller. This measure was executed on devices with 2, 5 and 10 wt % of $\text{KY}_3\text{F}_{10}:\text{YF}_3$ inserted in the rear-side of $\text{FA}_{0.83}\text{Cs}_{0.17}\text{Pb}(\text{I}_{0.6}\text{Br}_{0.4})_3$ perovskite devices. The results of this experiment are shown [Figure 93](#). The power of the laser was measured by a power meter.

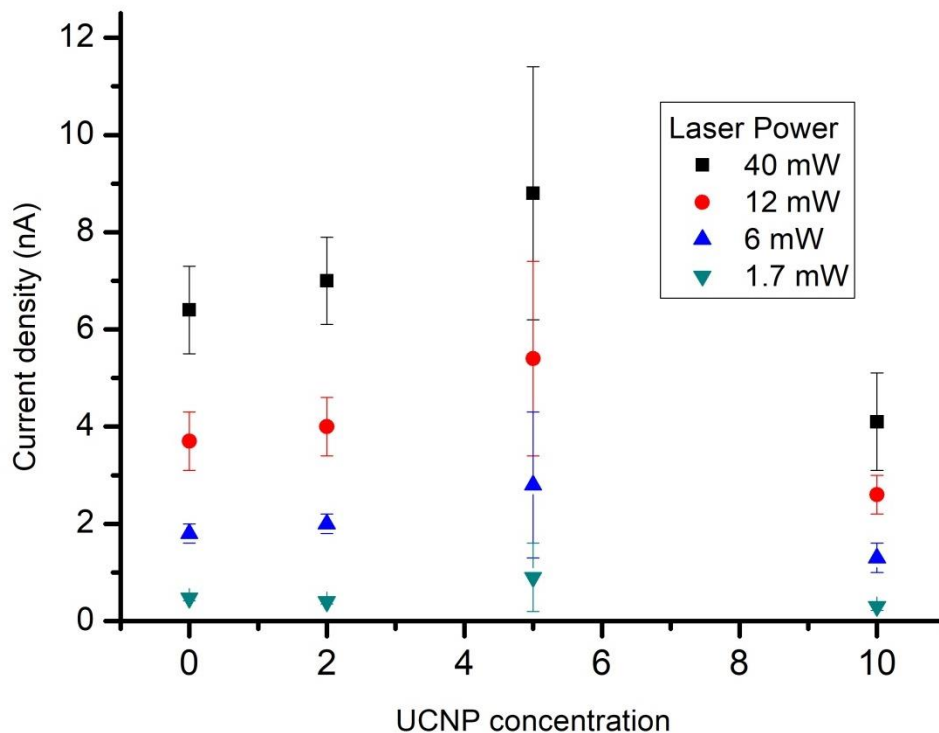


Figure 93. Variation of current density measured on a UCNP implemented perovskite solar cell for different UCNP concentration and excitation power

We observe an increase of short-circuit current with excitation power. The pristine device (no UCNPs) adopts this behavior too, which suggests a small absorption of the NIR by the perovskite

material. We can also observe a similar behavior as the one observed previously in the UCNP concentration optimization (section II.2.a of this chapter): the current density increases as the UCNP concentration increases until it reached a maximum value, for 5% UCNP. At higher concentration, it decreases, which was previously attributed to the formation of charge transport barriers and possible recombination centers.

As a comparison between the order of magnitude of excitation power and solar power at this wavelength, if the solar irradiance at 980 is $550 \text{ mW/cm}^2/\text{nm}$, it represents a power of 55 mW/nm on a solar cell (whose surface is 0.1 cm^2).

c. In situ luminescence variation with UCNP concentration

In order to investigate further about the effects of upconversion and the other parameters on the increase of device short-circuit current increase, we decided to measure qualitatively and quantitatively the variation of PL intensity of the devices used in the previous section. These measurements were operated on $\text{KY}_3\text{F}_{10}:\text{YF}_3$ implemented in ETL-free $\text{FA}_{0.83}\text{Cs}_{0.17}\text{Pb}(\text{I}_{0.6}\text{Br}_{0.4})_3$ perovskite devices, by similar experimental conditions than the one in [Figure 91 \(a\)](#). It is schematized [Figure 94\(a\)](#). The laser is focused on a device area not covered by the gold top electrode. The transmitted beam was recorded by a spectrometer. Three different devices were tested for each condition.

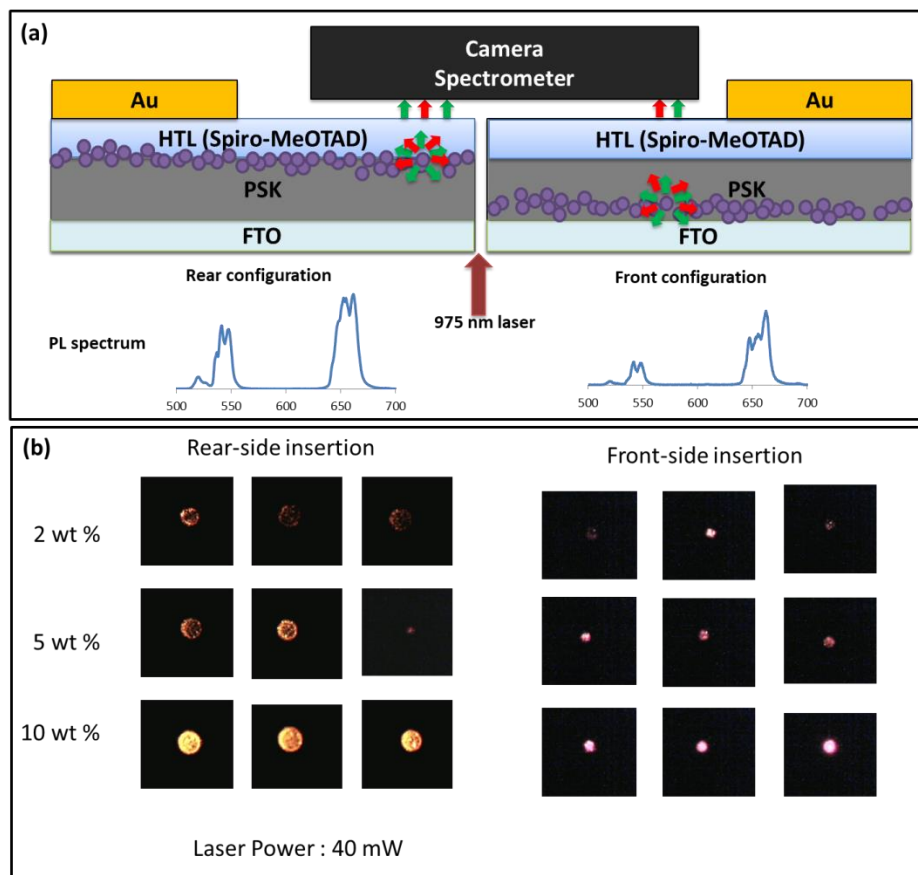


Figure 94. (a) Schematic representation of the set-up for the measurement of qualitative and quantitative variation of photoluminescence for devices with different UCNP concentration and in different configurations. (b) Pictures of the devices under laser excitation for rear- (left pictures) and

front-side (right pictures) insertion. Three different devices for each condition were tested. The diameter of the laser spot is around 20 μm .

Qualitative variation: camera detection

Pictures of the devices under laser excitation were taken (Figure 94(b)). We notice a stronger luminescence in the rear configuration, which is coherent with the fact that in that case, the luminescence is less absorbed by the perovskite material than in the front configuration.

We also notice an increasing PL intensity as the UCNP concentration increases for both configurations.

Quantitative luminescence intensity variation

In order to quantify those results, we measured the PL intensities at 545 and 662 nm (corresponding to green and red emissions respectively).

The averaged (over three devices) spectrums clearly show an increase of PL intensity associated with an increased amount of UCNPs in both configurations (Figure 95). The intensity at 662 nm for 10wt% is a little less than 3 times higher than the one at 5 wt %, which is itself 4 times higher than the one at 2 wt %, in the front configuration. Those ratios are both around two in the rear configuration. We can also note that here the green PL is absorbed in the case of the front-side insertion than the rear-side, as previously already observed (in the LBIC/fluorescence measurement).

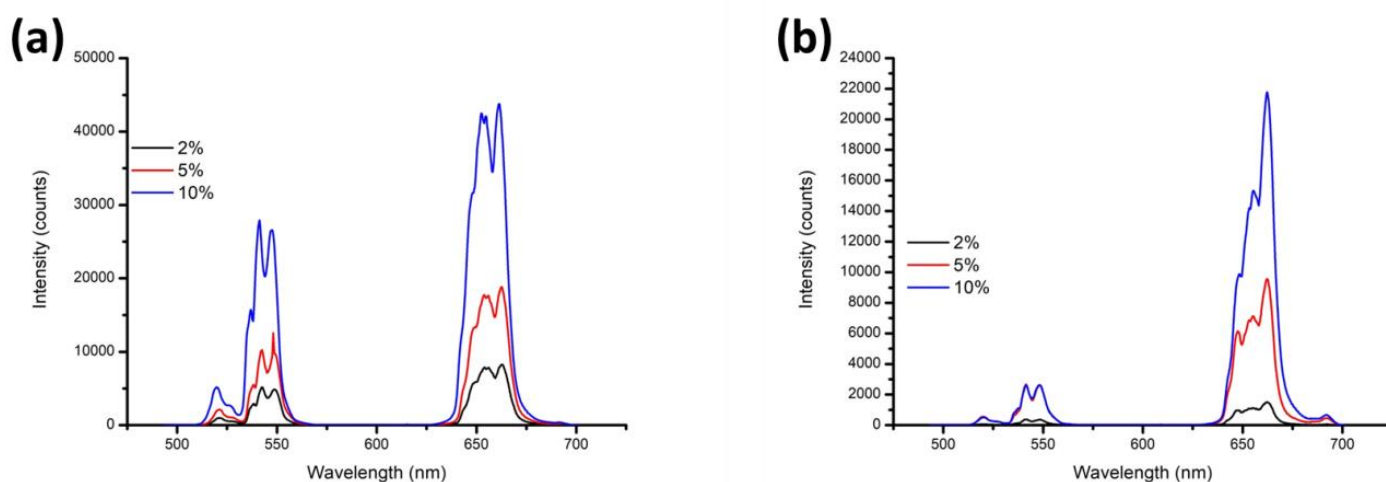


Figure 95 PL spectra (transmission) as a function of UCNP concentration for front-side (a) insertion and rear-side (b) insertion. Spectrums are averaged over 3 substrates.

Those measurements were quantified and the values of the intensities at 545 nm and 662 nm as a function of the concentration and configuration are shown Figure 96. They corroborate the results discussed above.

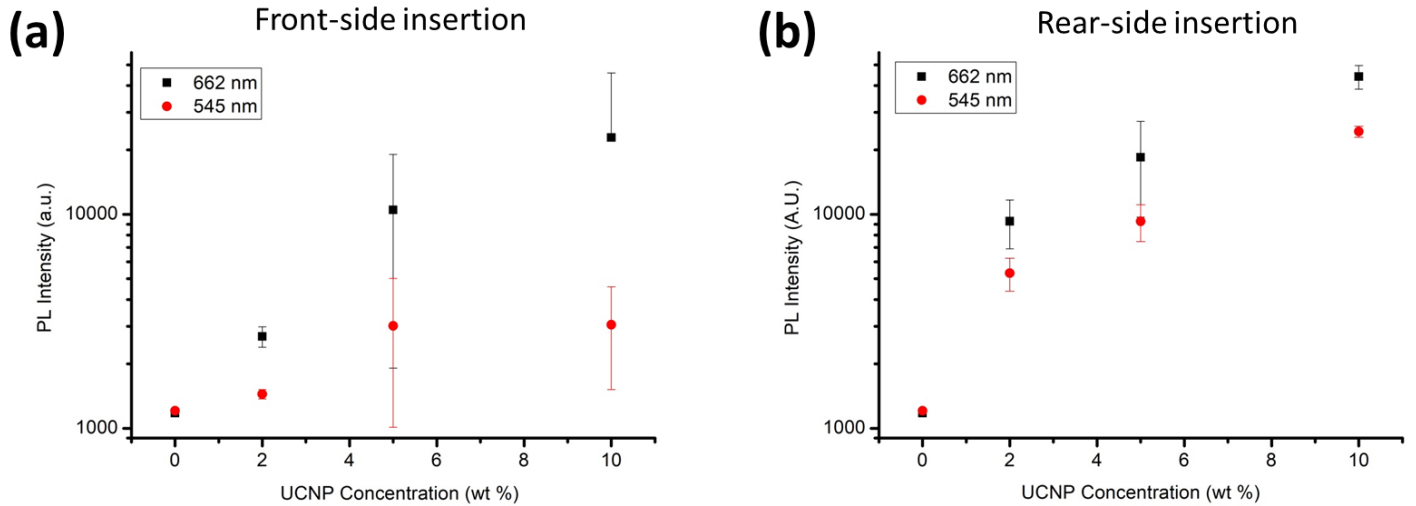


Figure 96 Logarithmic variation of PL intensity at 454 and 662 nm as a function of UCNP ($KY_3F_{10}:YF_3$) concentration for front-side (a) insertion and rear-side (b) insertion. Each point corresponds to a different substrate.

Those results showing a clear increase of PL intensity as the UCNP concentration increases would suggest that the optical contribution to the short circuit current only increases as the UCNP concentration increases. However, at higher concentrations of UCNPs (>5%), other effects related to the presence of UCNPs that rather contribute to current decrease start to play a preponderant role.

In this Chapter, we incorporated UCNPs in solar devices and the resulting devices exhibited increased performances. The concentration of UCNPs had to be adjusted in order to maximize this enhancement. Thanks to optical characterizations, we were also able to highlight this upconversion contribution and understand more precisely the different mechanisms under this variation of performance.

Conclusion and perspectives

In this thesis work, we first introduced concepts behind upconversion effect, plasmonic effect, plasmonic enhanced upconversion and current photogeneration in photovoltaic devices. The introduction of upconversion nanoparticles together with plasmonic structures in perovskite solar cells can help converting *in situ* one part of the solar spectrum into visible light, and increase the absorption of the solar cell and thus its performance.

In order to implement those nanoparticles, photovoltaic devices have to be as optimized as possible. For this reason, different deposition methods and recipes were experimented, for the Electron Transport Layer (ETL), the perovskite layer and the Hole Transport Layer (HTL). The structure later chosen for nanoparticles insertions was an ETL-free device, with Spiro-OMeTAD as HTL and $\text{FA}_{0.83}\text{Cs}_{0.17}\text{Pb}(\text{I}_{0.6}\text{Br}_{0.4})_3$ as the perovskite composition.

Different types of upconversion nanoparticles (UCNPs) were synthesized following different synthesis methods (coprecipitation, hydrothermal and solvothermal synthesis for both sodium and potassium fluoride matrixes such as NaYF_4 and KY_7F_{22}).

Plasmonic gold nanorods were synthesized. The synthesis was adjusted in order to obtain a Localized Surface Plasmonic Resonance close to the absorption region of the UCNPs (980 nm).

UCNPs were successfully inserted in perovskite devices, and the average solar cell power conversion efficiency (PCE) enhancement was around 6%. Complementary optical characterizations such as LBIC/fluorescence mapping method allowed us to improve the understanding of the mechanism behind this enhancement: the presence of UCNPs improves short-circuit currents both by their optical contribution in the absorption of the active layer and by the scattering that results from the presence of nanoparticles on incident light beam. At high UCNP concentration, however, the different morphological perturbations introduced by UCNPs result in the inverted effect and PCE tend to decrease.

Preliminary studies were also carried out by inserting Au NRs in solar devices together with UCNPs. These give a bright perspective on the following work to obtain a statistical proof on the repeatability of the trend observed (higher PCE when both nanoparticles were inserted than when only UCNPs were inserted), and to compare such results to control devices (i.e. no nanoparticles).

The contribution of the optical effect under the measuring conditions was rather small. But upconversion is a non-linear effect. UCNP insertion in solar cells would gain more advantages in the presence of a solar concentrator, whether for perovskite-based photovoltaic devices or for other structures showing low absorption in the near-infrared spectrum.

The results of this thesis work provides an experimental basis and interesting perspectives to the future application of other upconversion approaches (e.g. to efficiently upconvert other near-infrared wavelength than 980 nm) in solar cells based on other materials than perovskite.

Annexes

Annex 1 - Current-voltage equation for the case of an ideal diode

We consider an ideal p-n junction, which means two semiconductors with the same bandgap assembled. One, on the left in this study, is n-doped, which means doped with donors that are atoms with a higher number of electrons, and the other is p-doped, which means doped with acceptors that are atoms with a lower number of electrons. Both materials are neutral. We call N_d and N_a the respective concentrations of those elements. They thus also represent the concentration in major free carriers in their respective regions: electrons on the n side, holes on the p side. They are free because they are binding electrons not involved in any chemical bond.

Let's consider this junction at equilibrium: it's under constant temperature and it's disconnected from all external current or voltage source. The current in the diode is equal to zero and potential difference is equal to zero.

Depletion zone – electric field and potential [301]

Due to concentration gradient, free charges diffuse (electrons from n to p zone, holes from p to n zone) as shown in Figure 97.

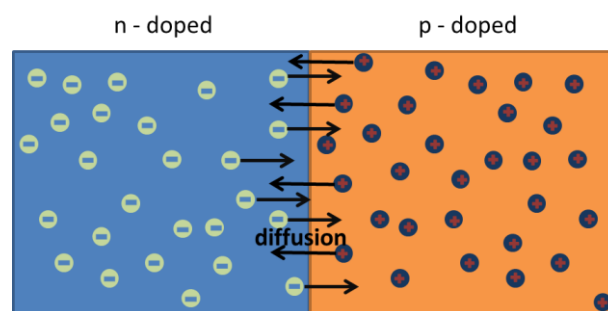


Figure 97. Scheme of pn junction. Free charges diffuse under concentration gradient.

This diffusion results in the creation of a zone called charge depletion zone as shown in Figure 98, which is a zone positively charged on the n side, and negatively charged on the p side, but overall neutral. Holes on the n-side and electrons on the p-side become minor carriers. The concentration of minor carriers is equal to the one of major ones: N_a electrons on the p-side and N_d holes on the n-side.

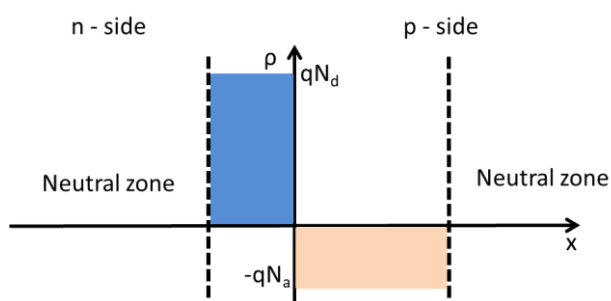


Figure 98. Space charge in the depletion zone.

The space charge in both zones is equal to the charge of the minority charge carrier (q for a hole, $-q$ for an electron) times the concentration of those charge carriers: qN_d electrons in the p side, $-qN_a$ holes on the n side, as we can see on Figure 97.

The difference of the local charge in this zone creates an electric field from the zone positively charged to the zone negatively charged. Those carriers are themselves subjected to a Coulomb force, which drifts charge minor carriers as we can see on [Figure 99](#).

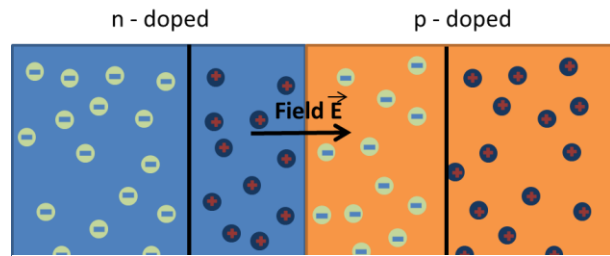


Figure 99. PN junction under equilibrium. The depletion zone is at the interface between both semiconductors.

We make the Shockley hypothesis that

- there are no major free charge carriers in the depletion zone anymore, but only fixed minor charge carriers,
- the depletion zone goes from $-x_n$ on the n-side to $+x_p$ on the p-side, with $W = x_p + x_n$ being the space charge layer width,
- at $x = x_p$, and $x = -x_n$, the semiconductor becomes neutral

And the ideal pn junction hypothesis allows us to neglect the generation and recombination in the depletion zone.

Due to Maxwell's first equation $\Delta E = \frac{\delta(x)}{\epsilon_0}$ giving the relation between the electric field E , the space charge δ and the permittivity of vacuum ϵ_0 , we can deduce the electric field profile, shown on [Figure 100 \(a\)](#), from this space charge profile. By integrating $\delta(x)$ on the n-side, given the boundary condition $E_n(-x_n) = 0$, we obtain

$$E_n(x) = \frac{qN_d x_n}{\epsilon_0} \left(1 + \frac{x}{x_n} \right) \quad 45$$

On the p-side, given the boundary condition $E_n(x_p) = 0$, we obtain

$$E_p(x) = \frac{qN_a x_p}{\epsilon_0} \left(1 - \frac{x}{x_p} \right) \quad 46$$

Continuity in $x = 0$ gives us $N_a x_p = N_d x_n$, which means the depletion zone is more extended on the less doped side of the junction.

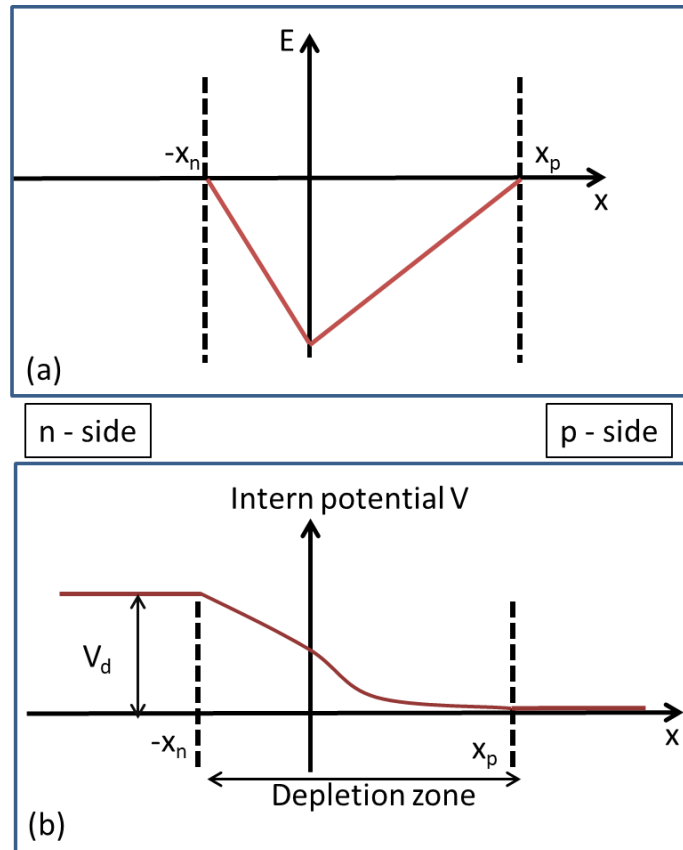


Figure 100. (a) Electric field profile (b) Internal potential profile x_n and x_p are the borders of the depletion zone and V_d is the diffusion tension.

By using the expression binding the energy to the potential $E = -q \frac{dV}{dx}$, we can also plot the internal potential inside the pn junction, which is shown [Figure 100\(b\)](#).

Fermi function and charges concentrations for intrinsic semiconductor [302]

The fermi function F_n represents the probability of occupancy of an electron at the energy E :

$$F_n(E) = \frac{1}{1 + e^{\frac{E-E_f}{kT}}} \quad 3$$

Where E_f is the fermi level of the intrinsic semiconductor, which is the energy level at which the probability of occupancy is $\frac{1}{2}$ at thermodynamic equilibrium. In a semiconductor, the fermi energy is usually within the bandgap.

For high values of energies ($E \gg E_f$), since the exponential is much larger than 1, we have

$$F_n(E) \approx \frac{1}{e^{\frac{E-E_f}{kT}}} = e^{-\frac{E-E_f}{kT}} \quad 47$$

The average number of electrons can be obtained by multiplying the fermi function by the density of state $g(E)$, which we can consider being a fixed number called N_c , the effective density of states for

electrons.

We can thus write

$$n(E) = N_c e^{\frac{E-E_f}{kT}} \quad 48$$

If we consider the valence band ($E \ll E_f$), the exponential will be much smaller than 1, and so we can use the approximation

$$F_n(E) = \frac{1}{1 + e^{\frac{E-E_f}{kT}}} \approx 1 - e^{\frac{E-E_f}{kT}} \quad 49$$

Since the probability of occupancy of holes is the probability of absence of electrons ($F_p = 1 - F_n$), we have

$$F_p(E) \approx e^{\frac{E-E_f}{kT}} \quad 50$$

And so we can also deduce that the distribution of holes in the valence band can be written as

$$p(E) = N_v e^{\frac{E-E_f}{kT}} \quad 51$$

Where N_c is the density of states of holes.

At thermal equilibrium, Fermi energy must be the same everywhere. We then have

$$n(E)p(E) = N_c e^{\frac{E-E_f}{kT}} N_v e^{\frac{E-E_f}{kT}} = N_v N_c e^{\frac{-2E_f}{kT}} = n_i^2(T) \quad 52$$

where n_i is the number of electrons and holes, which are equal, in a neutral intrinsic semiconductor, which depends on temperature.

We still consider an intrinsic semiconductor and we write this equation for $x = -x_n$ and $x = x_p$, and if we define n_{n0} , n_{p0} as electron concentration respectively as major and as minor charge carriers (electron concentrations at $-x_n$ and $+x_p$), and p_{p0} and p_{n0} the same for holes (at $+x_p$ and $-x_n$), we can obtain

$$n_{n0} p_{n0} = n_{p0} p_{p0} = n_i^2 \quad 53$$

PN junction under equilibrium ($V = 0$) [302]

When a n-doped and a p-doped semiconductor are put in contact, we admit the concentration in electrons and holes respectively at $-x_n$ and $+x_p$ are described by these equations (this can be deduced from fermi-dirac distribution law but we won't demonstrate it here)

$$n_{n0} \approx N_d = N_c e^{\frac{E_{c,n}-E_f}{kT}} \quad 54$$

$$p_{p0} \approx N_a = N_v e^{\frac{E_{v,p}-E_f}{kT}} \quad 55$$

Where $E_{c,n}$ is the conduction band energy on the n-side and $E_{v,p}$ is the valence band energy on the p-side, as pictured [Figure 101](#).

If we define two potentials ϕ_{p0} and ϕ_{n0} defined as respectively $e\phi_{p0} = E_f - E_{v,p}$ and $-e\phi_{n0} = E_{c,n} - E_f$ and ϕ_{bi} the built-in potential, with $e \cdot \phi_{bi} = E_g - e(\phi_{p0} - \phi_{n0}) = E_g - (E_{v,p} - E_{c,n})$, as shown on [Figure 101](#).

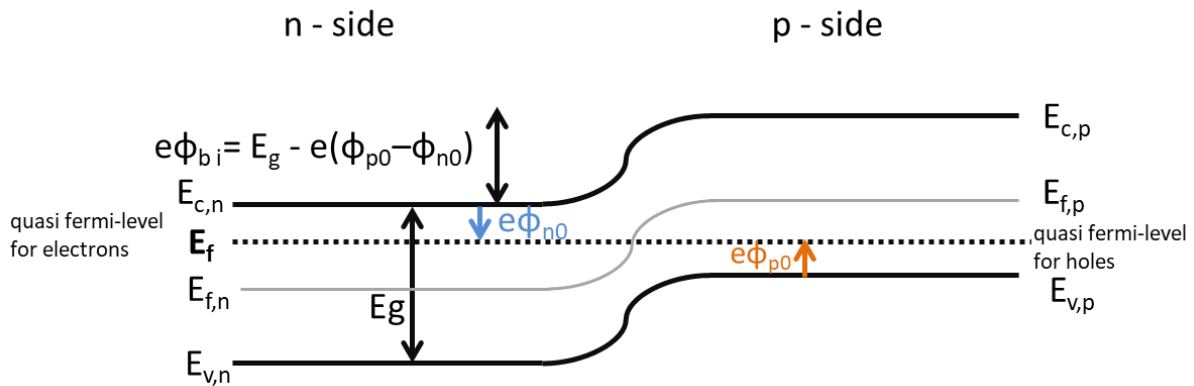


Figure 101. Band diagram of a pn junction

By deducing $E_{v,p}$ and $E_{c,n}$ expressions from [Equations 54 and 55](#) We thus have

$$e \cdot \phi_{bi} = E_g - kT \ln \frac{N_c N_v}{N_a N_d} \quad 56$$

By replacing in this equation N_c and N_v by their expression obtained from [Equations 48 and 51](#), and complete it with [equation 53](#), and we get

$$\phi_{bi} = kT \ln \frac{N_a N_d}{n p} = kT \ln \frac{n_{n0} p_{p0}}{n_i^2} = kT \ln \frac{n_{n0}}{n_{p0}} = kT \ln \frac{p_{p0}}{p_{n0}} \quad 57$$

Which in the end gives us the expression of minor charge carrier concentrations with built-in potential:

$$n_{p0} = n_{n0} e^{-\frac{e\phi_{bi}}{kT}} \quad 58$$

$$p_{n0} = p_{p0} e^{\frac{e\phi_{bi}}{kT}} \quad 59$$

Polarized junction [303]

When a positive bias ϕ is applied between both electrodes of the pn junction, the potential difference decreases, and so does the electric field, as shown on Figure 102.

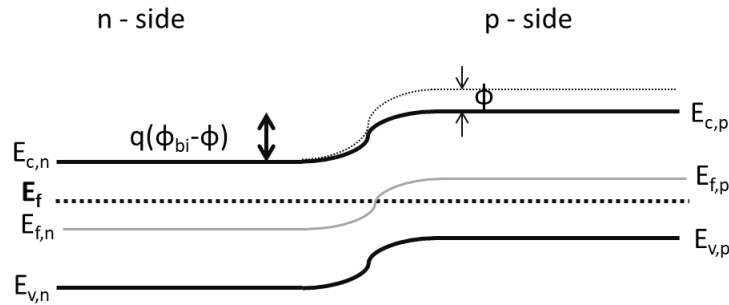


Figure 102. PN junction under forward bias

We will thus replace ϕ_{bi} by its new value $\phi_{bi} - \phi$, and if we define n_p and p_n as the concentration in minor charge carriers (so for electrons within $0 < x < x_p$ and holes $-x_n < x < 0$), we have

$$p_n - p_{n0} = p_{n0} \left(e^{\frac{e\phi}{kT}} - 1 \right) \quad 60$$

$$n_p - n_{p0} = n_{p0} \left(e^{\frac{e\phi}{kT}} - 1 \right) \quad 61$$

Let's write the continuity equation in the neutral layers: the temporal variation of electron concentration

$$\frac{dn}{dt} = \frac{1}{q} \frac{dJ_n}{dx} + G_n - R_n \quad 62$$

with G_n and R_n respectively the generation and recombination rates, and J_n the electron density current. The difference between generated and recombined electrons logically equals the number of created electrons. It is the deviation to equilibrium, the difference between current electrons concentration and electrons concentration at equilibrium, divided by the lifetime of the electrons:

$$G_n - R_n = \frac{n - n_0}{\tau_n} \quad 63$$

Current density is the sum of drift current density, which is proportional to the electric field intensity, and the diffusion current, which is proportional to the concentration gradient, following Fick's rule. We can thus write

$$J_n = \mu_n \left(enE + kT \frac{dn}{dx} \right) \quad 64$$

With μ_n the mobility of the electron in $m^2 \cdot V^{-1} \cdot s^{-1}$. Since the electric field is equal to zero outside the depletion zone, we combine 63 and 64 and we obtain

$$\frac{d^2 n_p}{dx^2} - \frac{n_p - n_{p0}}{D_n \tau_n} = 0 \quad 65$$

By integrating this equation with the boundary conditions stating $n_p = n_{p0}$ for $x \rightarrow +\infty$ and the limit for $x = x_p$ being defined by Equation 61, we get

$$n_p - n_{p0} = n_{p0} \left(e^{\frac{e\phi}{kT}} - 1 \right) e^{-\frac{x_p - x}{L_n}} \quad 66$$

With L_n being defined as $\sqrt{D_n \tau_n}$ which is diffusion length where D_n is defined as $q/\mu_n kT$.

We can then plot J_n and J_p profiles, as shown on Figure **103**.

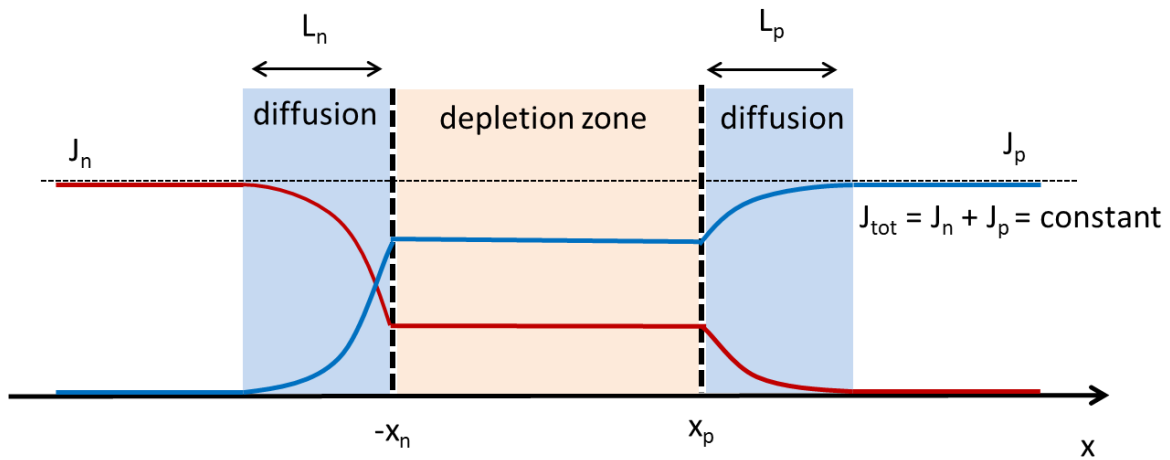


Figure 103. Current profile in a p-n junction (p on the right side)

We can now give the expression of the current in a pn ideal junction by calculating the sum of electron and hole current densities on specific points:

$$J = J_n + J_p = J_n(x_p) + J_p(-x_n) = \frac{qD_n n_{p0}}{L_n} \left(e^{\frac{e\phi}{kT}} - 1 \right) + \frac{qD_p p_{n0}}{L_p} \left(e^{\frac{e\phi}{kT}} - 1 \right) = J_s \left(e^{\frac{e\phi}{kT}} - 1 \right) \quad 67$$

With

$$J_s = \frac{qD_n n_{p0}}{L_n} + \frac{qD_p p_{n0}}{L_p} \quad 68$$

For a solar cell, we just have to subtract the photocurrent, which is caused by charge generation due to photons absorption.

$$J = J_s \left(e^{\frac{e\phi}{kT}} - 1 \right) - J_{ph} \quad 69$$

This potential-current equation for a p-n polarized junction is used as a prediction of the potential-current equation for a solar cell.

Annex 2. Upconversion models

A.Upconversion mechanism: electronic population level time derivative equations [98]

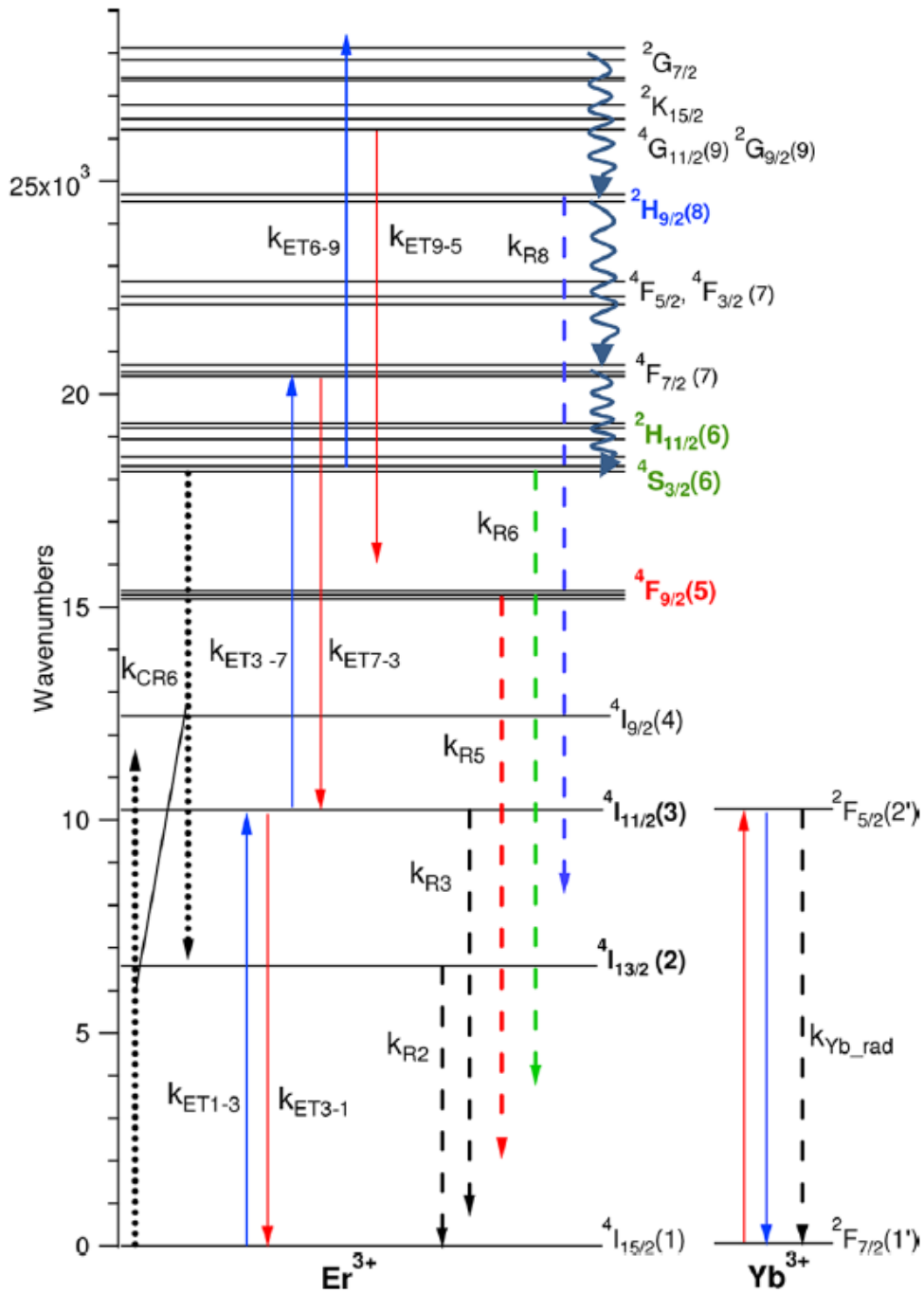


Figure 104. Schematic electronic transitions implied in upconversion process in ytterbium erbium doped NaYF_4 [98].

The number in brackets next to the level's name used in the description of the upconversion model in [Figure 104](#) will be used in the upcoming equations describing the level's population evolutions.

The transition rate related to ytterbium's absorption is defined to be $F \cdot \sigma_{Yb}$, F being the photon flux and σ_{Yb} the absorption cross section.

For an energy transfer from ytterbium to erbium, it will occur between level n_2' of ytterbium and two levels i and f of erbium, $i = (1,2,3,5,6)$ and $f = (3,5,7,8,9)$, the term added will be $k_{ETi-f}n_i n_2'$ (ET rate constant, times "departure" level of Yb, n_2' times "departure" level of Er n_i). For a back energy transfer from erbium to ytterbium, between two levels l and f of erbium, with $i = (3,4,7,9)$ and $f = (1,2,3,5)$, the term added is equal to $k_{ETi-f}n_l n_1'$.

For a non radiative contribution, the term added to \dot{n}_x is $+k_{NR,x}n_x$ if x is the final state level and $-k_{NR,x}n_x$ if x is the initial state level.

We consider also the case where two adjacent erbium atoms both excited in $^4I_{13/2}$ result in one excited erbium at $^4I_{11/2}$ and one in the ground state $^4I_{15/2}$. The rate of this process is called $k_{UC,2}$. We thus have the following set of ten equations:

$$\dot{n}_2' = F\sigma_{Yb}n_1' - k_{Yb}n_2' - k_{ET1-3}n_1n_2' - k_{ET2-5}n_2n_2' - k_{ET3-7}n_3n_2' - k_{ET5-8}n_5n_2' - k_{ET6-9}n_6n_2' + k_{ET3-1}n_3n_1' + k_{ET7-3}n_7n_1' - k_{ET9-5}n_9n_1' \quad 70$$

$$\dot{n}_1' = -\dot{n}_2' \quad 71$$

$$\dot{n}_9 = k_{ET6-9}n_6n_2' - k_{ET9-5}n_9n_1' - k_{NR9}n_9 \quad 72$$

$$\dot{n}_8 = k_{ET5-8}n_5n_2' + k_{NR9}n_9 - k_{NR8}n_8 - k_{R8}n_8 \quad 73$$

$$\dot{n}_7 = k_{ET3-7}n_3n_2' - k_{NR7}n_7 + k_{NR8}n_8 - k_{ET7-3}n_7n_1' \quad 74$$

$$\dot{n}_6 = -k_{ET6-9}n_6n_2' + k_{NR7}n_7 - k_{NR6}n_6 - k_{R6}n_6 - k_{CR6}n_6n_1 \quad 75$$

$$\dot{n}_5 = k_{ET2-5}n_2n_2' + 0.04k_{R8}n_8 + k_{NR6}n_6 - k_{ET5-8}n_5n_2' - (k_{NR5} + k_{R5})n_5 + k_{ET9-5}n_9n_1' \quad 76$$

$$\dot{n}_4 = k_{NR5}n_5 + k_{UC2}n_2n_2 - k_{CR4}n_4n_1 - k_{NR4}n_4 \quad 77$$

$$\dot{n}_3 = k_{NR4}n_4 + k_{ET1-3}n_1n_2' + k_{ET7-3}n_7n_1' + k_{CR6}n_6n_1 + 0.05k_{R5}n_5 + 0.05k_{R6}n_6 + 0.14k_{R8}n_8 - k_{ET3-1}n_3n_1' - (k_{R3} + k_{NR3})n_3 - k_{ET3-7}n_3n_2' \quad 78$$

$$\dot{n}_2 = k_{NR3}n_3 + 0.19k_{R3}n_3 + 0.05k_{R5}n_5 + 0.25k_{R6}n_6 + 0.42k_{R8}n_8 + k_{CR6}n_6n_1 + 2k_{CR4}n_4n_1 - 2k_{UC2}n_2n_2 - k_{R2}n_2 - k_{ET2-5}n_2n_2' \quad 79$$

$$\dot{n}_1 = k_{R2}n_2 + 0.81k_{R3}n_3 + 0.90k_{R5}n_5 + 0.7k_{R6}n_6 + 0.4k_{R8}n_8 - k_{CR6}n_6n_1 - k_{CR4}n_4n_1 + k_{UC2}n_2n_2 - k_{ET1-3}n_1n_2' + k_{ET3-1}n_3n_1' \quad 80$$

The article does not mention any reason why CR occurring between level 6 and 1 affects level 3. The premultipliers of the radiative rate constants were measured from emission spectra and calculated from Judd-Ofelt parameters.

B.Parameters for the UC model developed by Anderson et al.[98]

$k_{Yb} (s^{-1})$	613
$k_{ET1-3} (cm^{-3} s^{-1})$	1.18×10^{-14}
$k_{ET2-3} (cm^{-3} s^{-1})$	0.0×10^{-15}
$k_{ET3-7} (cm^{-3} s^{-1})$	1.54×10^{-15}
$k_{ET5-8} (cm^{-3} s^{-1})$	1.76×10^{-15}
$k_{ET6-9} (cm^{-3} s^{-1})$	6.07×10^{-15}
$k_{ET3-1} (cm^{-3} s^{-1})$	2×10^{-16}
$k_{ET5-2} (cm^{-3} s^{-1})$	0.00×10^{-16}
$k_{ET7-3} (cm^{-3} s^{-1})$	2.04×10^{-16}
$k_{ET9-5} (cm^{-3} s^{-1})$	2.84×10^{-16}
$k_{NR9} (s^{-1})$	1.76×10^6
$k_{NR8} (s^{-1})$	43450
$k_{NR7} (s^{-1})$	1.0×10^6
$k_{NR6} (s^{-1})$	26
$k_{NR5} (s^{-1})$	0.0
$k_{NR4} (s^{-1})$	22120
$k_{NR3} (s^{-1})$	61
$k_{R8} (s^{-1})$	2330
$k_{R6} (s^{-1})$	1510
$k_{R5} (s^{-1})$	2039
$k_{R3} (s^{-1})$	73
$k_{R2} (s^{-1})$	110
$k_{CR6} (cm^{-3} s^{-1})$	2.79×10^{-17}
$k_{CR4} (cm^{-3} s^{-1})$	8.04×10^{-19}
$k_{UC2} (cm^{-3} s^{-1})$	2.31×10^{-17}

Annex 3. Drude's model

We will describe here the Drude's model.

For more extended information, the reader can refer to [144].

We consider the interface metal/air under electromagnetic field $\vec{E}_0(\vec{r}, t) = \vec{E}_0 e^{i\omega t}$. Electrons are submitted to Lorentz force as well as a friction force \vec{F}_f which corresponds to collisions with atomic nucleus. It can be expressed as $m\gamma d\vec{\delta}/dt$, where γ is a damping constant and $\vec{\delta}(\vec{r}, t) = \vec{\delta}_0(\vec{r}) e^{i\omega t}$ is the displacement of the electron.

Writing Newton's second law, we have

$$-e\vec{E}_0 + \vec{F}_f = m\vec{a} \quad 81$$

$$-e\vec{E}_0 + m\gamma \frac{d\vec{\delta}}{dt} = m \frac{d^2\vec{\delta}}{dt^2} \quad 82$$

If we use the complex notation ($d/dt=i\omega$), we obtain

$$-e\vec{E}_0 + i\omega m \gamma \vec{\delta} = -m\omega^2 \vec{\delta} \quad 83$$

Which gives us the expression of the displacement of the electron

$$\vec{\delta} = \frac{e\vec{E}_0}{m(\omega^2 + i\omega\gamma)} \quad 84$$

The electron thus moves as the electric field changes direction. If electrons move, the metal becomes polarized and the barycenter of electron and ionic processions split from each other. The volumic polarization can be expressed as volumic density of electrons times their charge (-e) times their displacement:

$$\vec{P} = -ne\vec{\delta} \quad 85$$

On the other hand, we can write that the volumic polarization is equal to

$$\vec{P} = \epsilon_0 \chi_{metal} \vec{E}_0 \quad 86$$

Where ϵ_0 is the permittivity constant of vacuum, in F/m,

and χ_{metal} the susceptibility of the metal linked to its permittivity through $\chi_{metal} + 1 = \epsilon_{metal}$.

We can thus write, by combining Equations 84, 85, and 86

$$\epsilon_{metal} = 1 - \frac{\omega_p^2}{\omega^2 + i\gamma\omega} \quad 87$$

Where ω_p is the plasma frequency defined as

$$\omega_p = \sqrt{\frac{ne^2}{\epsilon_0 m}} \quad 88$$

Where

- n is the number of electrons
- e their charge, in C,
- ϵ_0 permittivity of vacuum, in F/m,
- m their mass, in kg,
- γ a constant characteristic of the material describing its damping, in s^{-1} .

If we express the complex form for the permittivity of the metal we have

$$\epsilon_{metal} = 1 - \frac{\omega_p^2}{\omega^2 + \gamma^2} + i \frac{\omega_p^2 \gamma}{\omega(\omega^2 + \gamma^2)} \quad 89$$

Annex 4. Localized Surface Plasmon Resonance 's condition for a sphere[144].

We will consider all the metallic ions as a ionic sphere and all the conduction electrons as an electronic ball. Let's express electric fields created by these balls. Using Gauss theorem that links the electric field flux through a surface and the quantity of charges in a volume V, we can write two equations for ions (\vec{E}_+) and for electrons (\vec{E}_-), which we summarized by only one:

$$\frac{\sum Q_{int}}{\epsilon_0} = \oiint_S \vec{E}_{\pm} \cdot \vec{dS} \quad 90$$

Where

- $Q_{int} = q.n.V$ is the total charge in the sphere (of electrons, in the case of \vec{E}_- and of cations in the case of \vec{E}_+), in C,
- V is the volume of the sphere, equal to $4/3.\pi.r^3$, in cm^3
- ϵ_0 permittivity of vacuum, in F/m,
- n is electron concentration, in cm^{-3} ,
- q the charge, in C.

By deriving twice the equations, we thus obtain

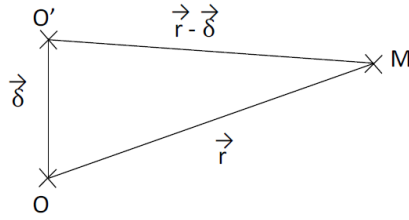
$$\vec{E}_+ = \frac{en}{3\epsilon_0} \vec{r} \quad 91$$

For electric field created by ions, and

$$\vec{E}_- = -\frac{en}{3\epsilon_0} \vec{r} \quad 92$$

For electric field created by electrons.

These two spheres can move under an electric field : the ions, under the electric field created by electrons, and the electrons, under the electric field created by ions. Let's however consider that due to the difference of mass between ions and electrons, only electrons are moving. Let's consider the ball of electrons goes from point O (on which the ions ball is centered) to point O', and let's look at total electric field at point M, as described on this figure:



Electric field on point M is the sum of electric field of ions coming from point O and from electrons coming from point O':

$$\vec{E}_M = \vec{E}_+(\vec{r}) + \vec{E}_-(\vec{r} - \vec{\delta}) = \frac{en}{3\epsilon_0} \vec{r} - \frac{en}{3\epsilon_0} (\vec{r} - \vec{\delta}) = \frac{en}{3\epsilon_0} \vec{\delta} \quad 93$$

We will use this relation later.

Let's now write the equation of movement for a conduction electron located in O' which is submitted to the force related to two electric fields: from ions on one hand, and the electric field of incoming wave \vec{E}_0 on the other hand. The electron is also submitted to a friction force called \vec{F}_f already mentioned in Drude's model Equation 82.

We can thus write

$$-e(\vec{E}_+(\vec{\delta}) + \vec{E}_0) + \vec{F}_f = m\vec{a} \quad 94$$

$$-e \frac{en}{3m\epsilon_0} \vec{\delta} - \frac{e}{m} \vec{E}_0 + \gamma \frac{d\vec{\delta}}{dt} = \vec{a} \quad 95$$

By substituting expression of ω_p given by Equation 88 and by defining electron's displacement $\vec{\delta}(\vec{r}, t) = \vec{\delta}_0(\vec{r})e^{i\omega t}$ we have $d/dt = i\omega$ and we can write

$$- \frac{\omega_p^2}{3} \vec{\delta} - \frac{e}{m} \vec{E}_0 + i\gamma\omega\vec{\delta} = -\omega^2 \vec{\delta} \quad 96$$

We recognize the expression of a harmonic oscillator whose natural frequency is $\omega_0 = \omega_p/\sqrt{3}$, and we can express electron displacement

$$\vec{\delta} = \frac{e\vec{E}_0}{m(\omega^2 - \omega_0^2 - i\omega\gamma)} \quad 97$$

Let's go back to the whole metallic sphere, whose dipolar moment is expressed as its volume times the total charge times the displacement of the electron cloud:

$$\vec{\mu} = \frac{4\pi}{3} r^3 en \vec{\delta} \quad 98$$

We can thus write

$$\vec{\mu} = \frac{4\pi}{3} r^3 \frac{ne^2 \vec{E}_0}{m(\omega^2 - \omega_0^2 - i\omega\gamma)} \quad 99$$

By combining Equations 88 and 99 and the relation between ω_p and ω_0 , we have

$$\vec{\mu} = 4\pi\epsilon_0 r^3 \frac{\omega_0^2}{\omega^2 - \omega_0^2 - i\omega\gamma} \vec{E}_0 \quad 100$$

And if we call α the polarizability defined as

$$\alpha = 4\pi r^3 \frac{\omega_0^2}{\omega^2 - \omega_0^2 - i\omega\gamma} \quad 101$$

We can write

$$\vec{\mu} = \alpha \epsilon_0 \vec{E}_0 \quad 102$$

We will now link polarizability to the permittivity of the metal ϵ_{metal} and of the envrioning material ϵ_{env} (by admitting that ϵ_0 can simply be replaced by ϵ_{env}).

Let's define \vec{P} the volumic dipolar moment for the metallic sphere, which is the dipolar moment for only one electron (which is equal to $e \cdot \vec{\delta}$) times the electron volumic concentration. We have

$$\vec{P} = -ne\vec{\delta} \quad 103$$

By considering the total electric field from the ions and electrons in equation 93, we can write

$$\vec{P} = -3\epsilon_{\text{env}} \vec{E}_M \quad 104$$

We can thus define the total field \vec{E}_t at any point M:

$$\vec{E}_t = \vec{E}_0 + \vec{E}_M = \vec{E}_0 - \frac{\vec{P}}{3\epsilon_{\text{env}}} \quad 105$$

By writing the second newton's law for an electron of velocity \vec{v} submitted to Laplace force with total field, and friction force, we have

$$-e\vec{E}_t + m\gamma \vec{v} = -i\omega m \vec{v} \quad 106$$

which gives

$$\vec{v} = \frac{e\vec{E}_t}{i\omega m + \gamma m} \quad 107$$

The expression of polarization current density being the total charge (which is equal to the charge of an electron times it's volumic concentration) times the velocity of charges, we have

$$\vec{J}_P = en\vec{v} = \frac{e^2 n \vec{E}_t}{i\omega m + \gamma m} = \sigma \vec{E}_t \quad 108$$

with the conductivity σ equal to

$$\sigma = \frac{e^2 n}{i\omega m + \gamma m} \quad 109$$

Furthermore, similarly to [Equation 86](#), we have

$$\vec{P} = \epsilon_{\text{env}} \chi_{\text{metal}} \vec{E}_0 \quad 110$$

where χ_{metal} stands for metal susceptilibility $\chi_{\text{metal}} = (\epsilon_{\text{metal}}/\epsilon_{\text{env}}) - 1$. By combining equations 105 and 110 we can write

$$\vec{E}_t = \frac{3\epsilon_{\text{env}}}{2\epsilon_{\text{env}} + \epsilon_{\text{metal}}} \vec{E}_0 \quad 111$$

By combining Equations 97 and 108 and the relation between polarization current density \vec{J}_P and polarization being $\vec{J}_P = \frac{d\vec{P}}{dt}$, we can write

$$\vec{E}_t = 1 - \frac{\omega_0^2}{\omega^2 - \omega_0^2 - i\omega\gamma} \vec{E}_0 \quad 112$$

Which gives, when combined to 111:

$$\frac{\epsilon_{metal} - \epsilon_{env}}{2\epsilon_{env} + \epsilon_{metal}} = \frac{\omega_0^2}{\omega^2 - \omega_0^2 - i\omega\gamma} \quad 113$$

And we recognize the partial expression of polarizability as given equation 101, which allows us to relate polarizability to permittivities:

$$\alpha = 4\pi r^3 \frac{\epsilon_{metal} - \epsilon_{env}}{2\epsilon_{env} + \epsilon_{metal}} \quad 114$$

We thus have resonance when polarizability tends to the infinity, so when $|2\epsilon_{env} + \epsilon_{metal}|$ is minimal. We usually consider that the environment medium's permittivity is real and metal's one is imaginary, so since permittivities depend on frequency, the resonance occurs when $f(\omega) = (\text{Re}(\epsilon_{metal}(\omega)) + 2\epsilon_{env}(\omega))^2 + \text{Im}(\epsilon_{metal}(\omega))^2$ is minimal.

Annex 5. FDTD Equations

For more information, the reader can refer to [144].

We consider a linear isotropic and non magnetic propagation medium.

Maxwell-Faraday-Lenz equation gives us

$$\text{rot}\vec{E} = -\mu_0\mu \frac{\partial\vec{H}}{\partial t} \quad 115$$

Where \vec{E} is the electric field in V/m,

\vec{H} the magnetic field in A/m,

and μ and μ_0 respectively magnetic permeabilities of the considered propagation medium and of vacuum in $\text{kg.m.A}^{-2}\text{s}^{-2}$.

Ampere law's gives us

$$\text{rot}\vec{H} = \vec{J} + \frac{\partial\vec{D}}{\partial t} \quad 116$$

With \vec{J} being the charge current in A.m^{-2} and

\vec{D} the electric induction in $\text{A.m}^{-2}\text{s}$. We have $\vec{D} = \epsilon_0\epsilon_r\vec{E}$, where ϵ_0 and ϵ_r are respectively permittivity of vacuum and of the considered propagation medium in $\text{kg.m.A}^{-2}\text{s}^{-2}$.

For a charge current being equal to zero, we can write a set of equations that are projections of equations 115 and 116 on x,y, and z axis.

$$\frac{\partial\vec{E}_x}{\partial t} = -\frac{1}{\epsilon} \left(\frac{\partial\vec{H}_z}{\partial y} - \frac{\partial\vec{H}_y}{\partial z} \right) \quad 117$$

$$\frac{\partial \vec{E}_y}{\partial t} = -\frac{1}{\varepsilon} \left(\frac{\partial \vec{H}_x}{\partial z} - \frac{\partial \vec{H}_z}{\partial x} \right) \quad 118$$

$$\frac{\partial \vec{E}_z}{\partial t} = -\frac{1}{\varepsilon} \left(\frac{\partial \vec{H}_y}{\partial x} - \frac{\partial \vec{H}_x}{\partial y} \right) \quad 119$$

$$\frac{\partial \vec{H}_x}{\partial t} = \frac{1}{\mu} \left(\frac{\partial \vec{E}_z}{\partial y} - \frac{\partial \vec{E}_y}{\partial z} \right) \quad 120$$

$$\frac{\partial \vec{H}_y}{\partial t} = \frac{1}{\mu} \left(\frac{\partial \vec{E}_x}{\partial z} - \frac{\partial \vec{E}_z}{\partial x} \right) \quad 121$$

$$\frac{\partial \vec{H}_z}{\partial t} = \frac{1}{\mu} \left(\frac{\partial \vec{E}_y}{\partial x} - \frac{\partial \vec{E}_x}{\partial y} \right) \quad 122$$

FDTD consists in solving this partial differential equations system implying a discretization of time and space, using the expression of a derivative

$$f'(x) = \lim_{h \rightarrow 0} \frac{f(x+h) - f(x)}{2h} \quad 123$$

Calculation space is meshed in order to get a space h between all possible points, that is the smallest as possible. Let's consider a square mesh as shown below.

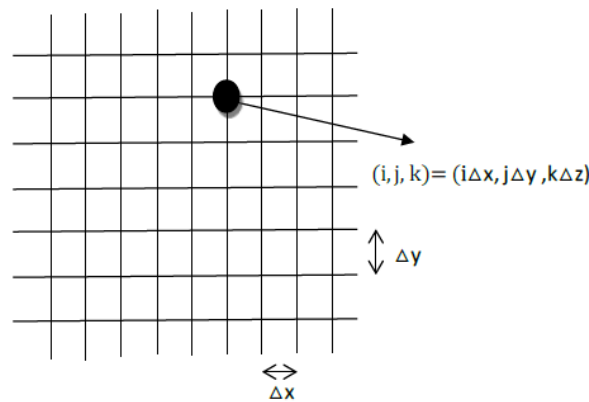


Figure 105. Scheme of a square mesh as the one used for FDTD calculation

The spatial partial derivatives at a certain time t are described using those equations:

$$\frac{\partial f^t(i, j, k)}{\partial x} = \frac{f^t(i + \frac{\Delta x}{2}, j, k) - f^t(i - \frac{\Delta x}{2}, j, k)}{\Delta x} \quad 124$$

$$\frac{\partial f^t(i, j, k)}{\partial y} = \frac{f^t(i, j + \frac{\Delta y}{2}, k) - f^t(i, j - \frac{\Delta y}{2}, k)}{\Delta y} \quad 125$$

$$\frac{\partial f^t(i,j,k)}{\partial z} = \frac{f^t(i,j,k + \frac{\Delta z}{2}) - f^t(i,j,k - \frac{\Delta z}{2})}{\Delta z} \quad 126$$

And for temporal derivative :

$$\frac{\partial f^{t+1/2}(i,j,k)}{\partial t} = \frac{f^{t+1/2}(i,j,k) - f^t(i,j,k)}{\Delta t} \quad 127$$

The elements of electric field $\vec{E}(t_i)$ are calculated for t such as $t = n.\Delta t$, and $\vec{H}(t_i)$ for $t=(n+1/2)\Delta t$, where n is an integer. We thus have six equations that are obtained by recurrence.

$$H_{x(i,j,k)}^{t+1/2} = H_{x(i,j,k)}^{t-1/2} + \frac{\Delta t}{\mu \Delta z} \left(E_{y(i,j,k+\frac{\Delta z}{2})}^t - E_{y(i,j,k-\frac{\Delta z}{2})}^t \right) - \frac{\Delta t}{\mu \Delta y} \left(E_{z(i,j+\frac{\Delta y}{2},k)}^t - E_{z(i,j-\frac{\Delta y}{2},k)}^t \right) \quad 128$$

$$H_{y(i,j,k)}^{t+1/2} = H_{y(i,j,k)}^{t-1/2} + \frac{\Delta t}{\mu \Delta x} \left(E_{z(i+\frac{\Delta x}{2},j,k)}^t - E_{z(i-\frac{\Delta x}{2},j,k)}^t \right) - \frac{\Delta t}{\mu \Delta z} \left(E_{x(i,j,k+\frac{\Delta z}{2})}^t - E_{x(i,j,k-\frac{\Delta z}{2})}^t \right) \quad 129$$

$$H_{z(i,j,k)}^{t+1/2} = H_{z(i,j,k)}^{t-1/2} + \frac{\Delta t}{\mu \Delta y} \left(E_{x(i,j+\frac{\Delta y}{2},k)}^t - E_{x(i,j-\frac{\Delta y}{2},k)}^t \right) - \frac{\Delta t}{\mu \Delta x} \left(E_{y(i+\frac{\Delta x}{2},j,k)}^t - E_{y(i-\frac{\Delta x}{2},j,k)}^t \right) \quad 130$$

$$E_{x(i,j,k)}^{t+1} = E_{x(i,j,k)}^t + \frac{\Delta t}{\varepsilon \Delta y} \left(H_{z(i,j+\frac{\Delta y}{2},k)}^{t+1/2} - H_{z(i,j-\frac{\Delta y}{2},k)}^{t+1/2} \right) - \frac{\Delta t}{\varepsilon \Delta z} \left(H_{y(i,j,k+\frac{\Delta z}{2})}^{t+1/2} - H_{y(i,j,k-\frac{\Delta z}{2})}^{t+1/2} \right) \quad 131$$

$$E_{y(i,j,k)}^{t+1} = E_{y(i,j,k)}^t + \frac{\Delta t}{\varepsilon \Delta z} \left(H_{x(i,j,k+\frac{\Delta z}{2})}^{t+1/2} - H_{x(i,j,k-\frac{\Delta z}{2})}^{t+1/2} \right) - \frac{\Delta t}{\varepsilon \Delta x} \left(H_{z(i+\frac{\Delta x}{2},j,k)}^{t+1/2} - H_{z(i-\frac{\Delta x}{2},j,k)}^{t+1/2} \right) \quad 132$$

$$E_{z(i,j,k)}^{t+1} = E_{z(i,j,k)}^t + \frac{\Delta t}{\varepsilon \Delta x} \left(H_{y(i+\frac{\Delta x}{2},j,k)}^{t+1/2} - H_{y(i-\frac{\Delta x}{2},j,k)}^{t+1/2} \right) - \frac{\Delta t}{\varepsilon \Delta y} \left(H_{x(i,j+\frac{\Delta y}{2},k)}^{t+1/2} - H_{x(i,j-\frac{\Delta y}{2},k)}^{t+1/2} \right) \quad 133$$

Annex 6. Statistical analysis - T-table [304]

As mentioned, the t-test is a statistical test used to compare two Gaussian distribution between them and decide whether they do belong to different distributions (which is equivalent to confirm the null hypothesis). A t-value is calculated starting from the two data we wish to compare.

t Table

df	t _{.50}	t _{.75}	t _{.80}	t _{.85}	t _{.90}	t _{.95}	t _{.975}	t _{.99}	t _{.995}	t _{.999}	t _{.9995}
1	0.000	1.000	1.376	1.963	3.078	6.314	12.71	31.82	63.66	318.31	636.62
2	0.000	0.816	1.061	1.386	1.886	2.920	4.303	6.965	9.925	22.327	31.599
3	0.000	0.765	0.978	1.250	1.638	2.353	3.182	4.541	5.841	10.215	12.924
4	0.000	0.741	0.941	1.190	1.533	2.132	2.776	3.747	4.604	7.173	8.610
5	0.000	0.727	0.920	1.156	1.476	2.015	2.571	3.365	4.032	5.893	6.869
6	0.000	0.718	0.906	1.134	1.440	1.943	2.447	3.143	3.707	5.208	5.959
7	0.000	0.711	0.896	1.119	1.415	1.895	2.365	2.998	3.499	4.785	5.408
8	0.000	0.706	0.889	1.108	1.397	1.860	2.306	2.896	3.355	4.501	5.041
9	0.000	0.703	0.883	1.100	1.383	1.833	2.262	2.821	3.250	4.297	4.781
10	0.000	0.700	0.879	1.093	1.372	1.812	2.228	2.764	3.169	4.144	4.587
11	0.000	0.697	0.876	1.088	1.363	1.796	2.201	2.718	3.106	4.025	4.437
12	0.000	0.695	0.873	1.083	1.356	1.782	2.179	2.681	3.055	3.930	4.318
13	0.000	0.694	0.870	1.079	1.350	1.771	2.160	2.650	3.012	3.852	4.221
14	0.000	0.692	0.868	1.076	1.345	1.761	2.145	2.624	2.977	3.787	4.140
15	0.000	0.691	0.866	1.074	1.341	1.753	2.131	2.602	2.947	3.733	4.073
16	0.000	0.690	0.865	1.071	1.337	1.746	2.120	2.583	2.921	3.686	4.015
17	0.000	0.689	0.863	1.069	1.333	1.740	2.110	2.567	2.898	3.646	3.965
18	0.000	0.688	0.862	1.067	1.330	1.734	2.101	2.552	2.878	3.610	3.922
19	0.000	0.688	0.861	1.066	1.328	1.729	2.093	2.539	2.861	3.579	3.883
20	0.000	0.687	0.860	1.064	1.325	1.725	2.086	2.528	2.845	3.552	3.850
21	0.000	0.686	0.859	1.063	1.323	1.721	2.080	2.518	2.831	3.527	3.819
22	0.000	0.686	0.858	1.061	1.321	1.717	2.074	2.508	2.819	3.505	3.792
23	0.000	0.685	0.858	1.060	1.319	1.714	2.069	2.500	2.807	3.485	3.768
24	0.000	0.685	0.857	1.059	1.318	1.711	2.064	2.492	2.797	3.467	3.745
25	0.000	0.684	0.856	1.058	1.316	1.708	2.060	2.485	2.787	3.450	3.725
26	0.000	0.684	0.856	1.058	1.315	1.706	2.056	2.479	2.779	3.435	3.707
27	0.000	0.684	0.855	1.057	1.314	1.703	2.052	2.473	2.771	3.421	3.690
28	0.000	0.683	0.855	1.056	1.313	1.701	2.048	2.467	2.763	3.408	3.674
29	0.000	0.683	0.854	1.055	1.311	1.699	2.045	2.462	2.756	3.396	3.659
30	0.000	0.683	0.854	1.055	1.310	1.697	2.042	2.457	2.750	3.385	3.646
40	0.000	0.681	0.851	1.050	1.303	1.684	2.021	2.423	2.704	3.307	3.551
60	0.000	0.679	0.848	1.045	1.296	1.671	2.000	2.390	2.660	3.232	3.460
80	0.000	0.678	0.846	1.043	1.292	1.664	1.990	2.374	2.639	3.195	3.416
100	0.000	0.677	0.845	1.042	1.290	1.660	1.984	2.364	2.626	3.174	3.390

The t-table gathers the values under which the t-value, as express in section I.3.b of the Chapter 2 must be in order to confirm the null hypothesis with a certitude corresponding to the index under the t at the top column (0.5, 0.75 ...). The left column corresponds to the number of degree of liberty, or in our case, the number of sample in the compared batches.

If the compared batches have different number of samples, an effective degree can be calculated as followed:

$$ddl_{eff} = \frac{s^4}{\frac{\left(\frac{\Sigma_i}{N_i}\right)^2}{N_i - 1} + \frac{\left(\frac{\Sigma_j}{N_j}\right)^2}{N_j - 1}} \quad 134$$

Annex 7. Tables of values for perovskite solar cell fabrication optimization.

	Jsc (mA/cm ²)	Voc	FF	PCE
Best device	15.9	0.59	36	3.4
Average	12.9	0.46	32	2.0
Standard deviation	2.3	0.11	3	1.0

Table 10. I-V curve for ¹Ti spun at 4000rpm. PSK=¹MAPbI₃. HTL=Poly-TPD. 3 devices.

	Jsc (mA/cm ²)	Voc (V)	FF (%)	PCE (%)
Best device	22.8	0.86	57	11.1
Average	20.6	0.67	46	6.9
Standard deviation	2.6	0.14	3	3.3

Table 11. I-V curve for ¹Ti spun at 2000rpm. PSK=¹MAPbI₃. HTL= Poly-TPD. 4 devices.

	Jsc (mA/cm ²)	Voc (V)	FF (%)	PCE (%)
Best device	12.1	0.77	42	3.9
Average	11.1	0.76	39	3.3
Standard deviation	0.9	0.0	3	0.6

Table 12. I-V curve for ³Ti spun at 5000rpm. PSK=MAPbI_{3-x}Cl_x. HTL=¹Spiro. 2 devices.

	Jsc (mA/cm ²)	Voc (V)	FF (%)	PCE (%)
Best device	26.2	0.72	46	8.6
Average	20.9	0.68	42	6.1
Standard deviation	3.4	0.13	6	2.2

Table 13. I-V curve for ³Ti spun at 2000rpm. PSK= MAPbI_{3-x}Cl_x. HTL=¹Spiro. 7 devices.

	Jsc (mA/cm ²)	Voc (V)	FF (%)	PCE (%)
Best device	25.6	0.85	52	11.4
Average	21.8	0.83	47	8.7
Standard deviation	2.5	0.1	5	2.3

Table 14. I-V curve for ³Ti spun at 3000rpm. PSK=MAPbI_{3-x}Cl_x. HTL=¹Spiro. 4 devices.

	Jsc (mA/cm ²)	Voc (V)	FF (%)	PCE (%)
Best device	20.1	0.82	47	7.7
Average	13.3	0.65	39	4.3
Standard deviation	6.7	0.16	8	3.3

Table 15. I-V curve for ¹Ti spun at 2000rpm. PSK= MAPbI_{3-x}Cl_x. HTL=¹Spiro. 2 devices.

	Jsc (mA/cm ²)	Voc (V)	FF (%)	PCE (%)
Best device	15.7	0.92	50	7.2
Average	14.9	0.87	45	5.9
Standard deviation	0.75	0.04	3	0.9

Table 16. I-V curve for ¹MAPbI₃ Ti = ³Ti Spiro = ²Spiro 7 devices.

	Jsc (mA/cm ²)	Voc (V)	FF (%)	PCE (%)
Best device	16.3	1.09	64	11.3
Average	15.7	1.06	60	10.1
Standard deviation	0.47	0.04	3	1.058

Table 17. I-V curve for FA_{0.83}CS_{0.17}Pb(I_{0.6}Br_{0.4})₃. No ETL. Spiro = ²Spiro 6 devices.

	Jsc (mA/cm ²)	Voc (V)	FF (%)	PCE (%)
Best device	21.8	0.68	45	6.7
Average	20.0	0.66	40	5.4
Standard deviation	1.5	0.01	5	1.2

Table 18. I-V curve for ¹Spiro Ti= ³Ti PSK = ¹MAPbI₃, 3 devices.

	Jsc (mA/cm ²)	Voc (V)	FF (%)	PCE(%)
Best device	5.7	0.39	27	0.6
Average	4.0	0.41	26	0.4
Standard deviation	1.6	0.01	1	0.2

Table 19. I-V curve for Poly-TPD. Ti= ³Ti PSK = ¹MAPbI₃, 2 devices.

	Jsc (mA/cm ²)	Voc (V)	FF (%)	PCE (%)
Best device	12.7	0.94	55	6.6
Average	12.3	0.9	42	4.7
Standard deviation	0.5	0.04	9	1.2

Table 20. I-V curve for ¹Spiro. Ti= ³Ti PSK = ²MAPbI₃, 7 devices.

	Jsc (mA/cm ²)	Voc (V)	FF (%)	PCE (%)
Best device	16.2	1.0	49	8.3
Average	15.7	1.0	47	7.6
Standard deviation	1.2	0.01	2	1.0

Table 21. I-V curve for ²Spiro. Ti= ³Ti PSK = ²MAPbI₃, 4 devices.

Annex 8. Chemicals providers

Spiro-oMeTAD was purchased from **Solaronix**.

Dimethylsulfoxide (DMSO), Titanium(diisopropoxide) bis(2,4-pentanedionate) (75% in isopropanol) was purchased from **Merck**.

Acetone was purchased from **Fischer**.

Er(NO₃)₃·5H₂O (99.99%) was purchased from **Alfa Aesar**.

Silver Nitrate Ag NO₃ was purchased from **Strem**.

Poly(N,N'-bis-4-butylphenyl-N,N'-bisphenyl)benzidine was purchased from **American Dye Source**.

Methylamine solution (40 wt % in water), hydroiodic acid (57 wt % in water), hydrobromic acid (47 wt% in water), hydrochloric acid (37 wt % in water), nitric acid (69 wt % in water), octadecene, oleic acid, ytterbium chloride hexahydrate, methanol, yttrium chloride hexahydrate, gadolinium chloride hydrate, erbium chloride hexahydrate, lead iodide, lead bromide, anhydrous chlorobenzene, sodium hydroxide, ammonium fluoride, anhydrous acetonitrile, hexadecyltrimethylammonium bromide (CTAB), gold (III) chloride trihydrate HAuCl₄, sodium borohydride NaBH₄, ascorbic acid, sodium oleate NaOL, 80% tetrakis (hydroxymethyl) phosphonium chloride, tert-butylpyridine (TBP), anhydrous dichlorobenzene, bis(trifluoromethane)sulfonimide lithium salt (Li-TFSI), anhydrous ethanol, isopropanol (IPA), diethanolamine, formamide acetate, titanium isopropoxide, cesium iodide, ether, Yb(NO₃)₃·5H₂O (99.999%), Y(NO₃)₃·4H₂O (99.99%), K(NO₃) (99.99%), HF (>40% in water) and anhydrous KF (99.99%) were purchased from **Sigma Aldrich**.

Annex 9. Gold growth on UCNPs

Li et al. combine UCNPs synthesis followed by gold shell growth. The protocol of the synthesis 2 of $\text{NaYF}_4:30\%\text{Gd}^{3+}:2\%\text{Er}^{3+}:18\text{Yb}^{3+}$ solvothermal (oleic acid ligands), given in Chapter 3, can be thus followed by a gold shell growth [217]. Since no optimal size had been obtained with this type of particles, we decided to run a test on $\text{KY}_3\text{F}_{10}:5\%\text{Er}^{3+}:20\%\text{Yb}^{3+}$ instead. We mixed growth solution with the UCNPs. The article's protocol suggest to first attach the gold nanoseeds on the surface of the UCNPs and then further mix it with the growth solution, but the SEM images of this experiment suggest that the attachment of gold seeds to UCNPs is in competition with the formation of bigger gold NRs, in which case it would be more profitable to simply mix NRs and UCNPs. The surface chemistry of the two types of UCNPs could explain this difference: in one case (sodium matrix), the particles are covered by oleic acid ligands, whereas in the second case, they are not.

Growth solution

A solution was prepared by dissolving 5 mg of potassium carbonate in 20 mL DI water and stirring for 15min. $400\mu\text{L}$ of 1 wt. % HAuCl_4 was then added. The solution turned colorless after approximately 10 min. The resulting solution was aged by storing it in the refrigerator for at least 1 day. 0.5 mL of UC solution (4mg/mL in IPA) was added to 5mL of the aged gold solution under stirring.

The result was not very conclusive, as we can see by comparing obtained result with the one from the literature in [Figure 106\(a\) and \(b\)](#). We can clearly see that in our case, gold seeds and UCNPs are totally agglomerated, and that the attachment of gold was not as restricted to localized spots.

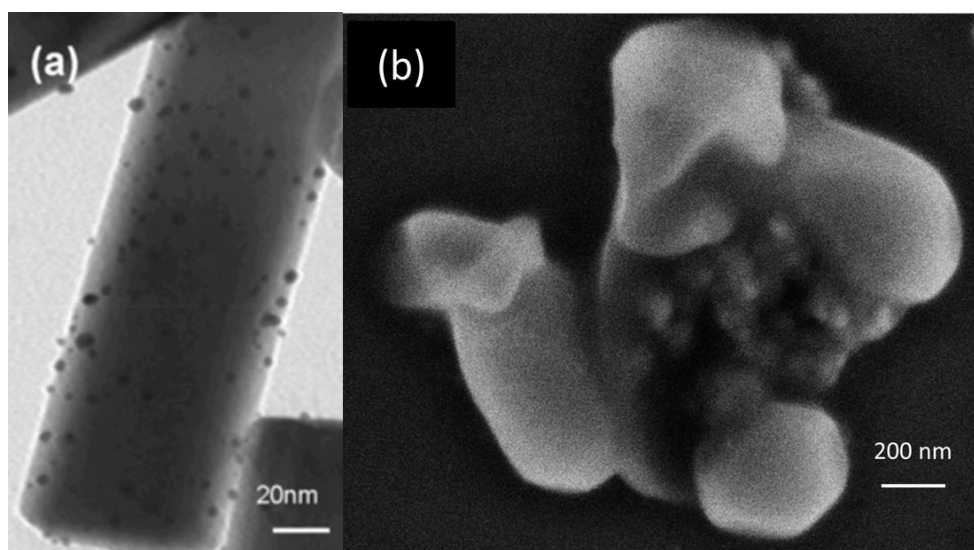
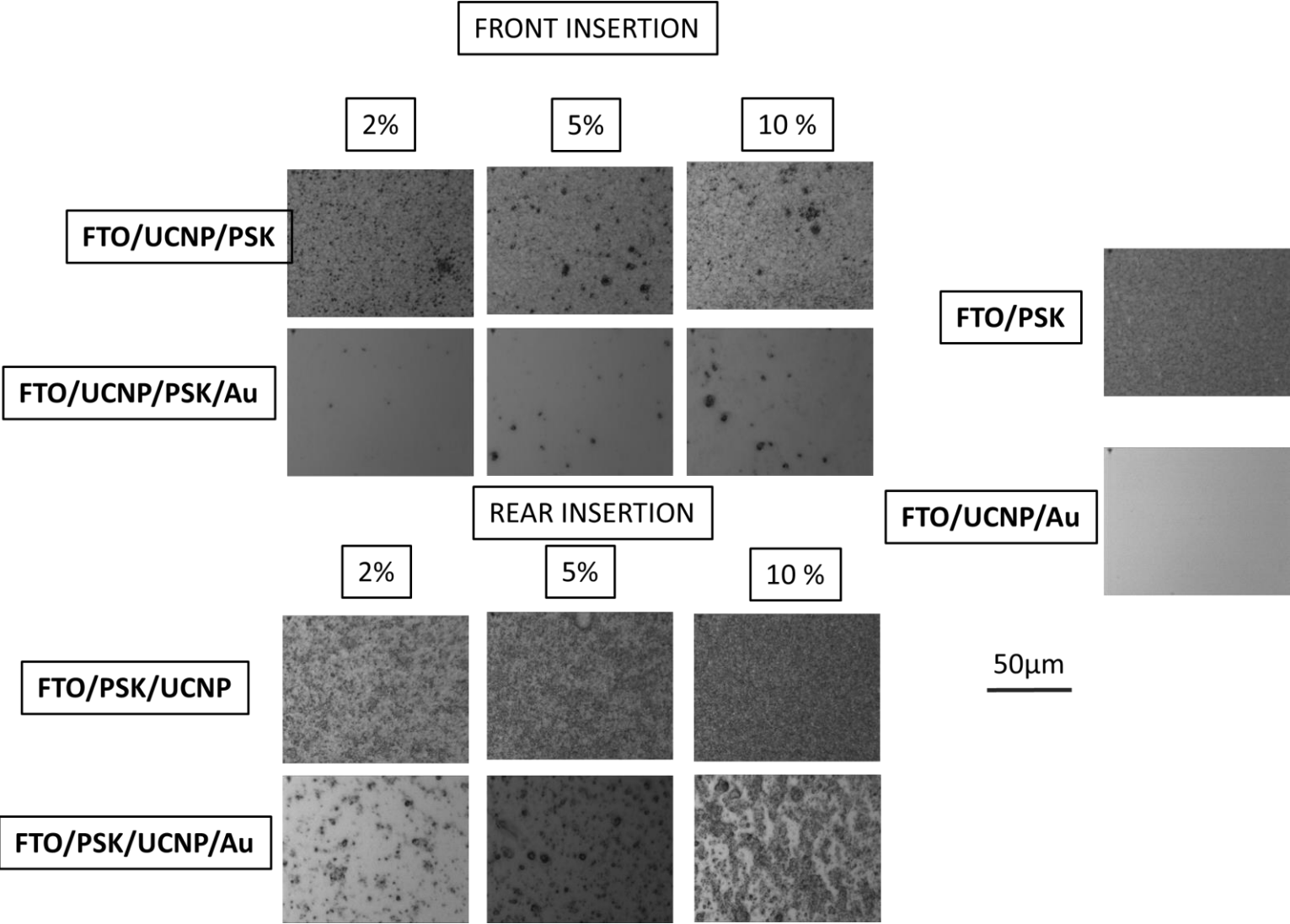


Figure 106. Comparison of SEM pictures of gold attached to UCNPs (a)from the literature [217] (b)experimental test run at the laboratory. The brighter particles seem to correspond to UCNPs, whereas the darker central agglomerate would be the gold nanoseeds cluster.

Annex 10. Influence of concentration in UCNPs on the morphology of the solar cell

Microscrope magnification : x 1000.



Annex 11. Doped KY₃F₁₀:YF₃, KY₃F₁₀ and NaYF₄ insertion in perovskite devices

A.KY₃F₁₀:YF₃ – in collaboration with Zhelu Hu

Those solar cells are ETL-free devices. The Spiro recipe is ²Spiro. The perovskite is FA_{0.83}CS_{0.17}Pb(I_{0.6}Br_{0.4})₃.

a. IV-Curve

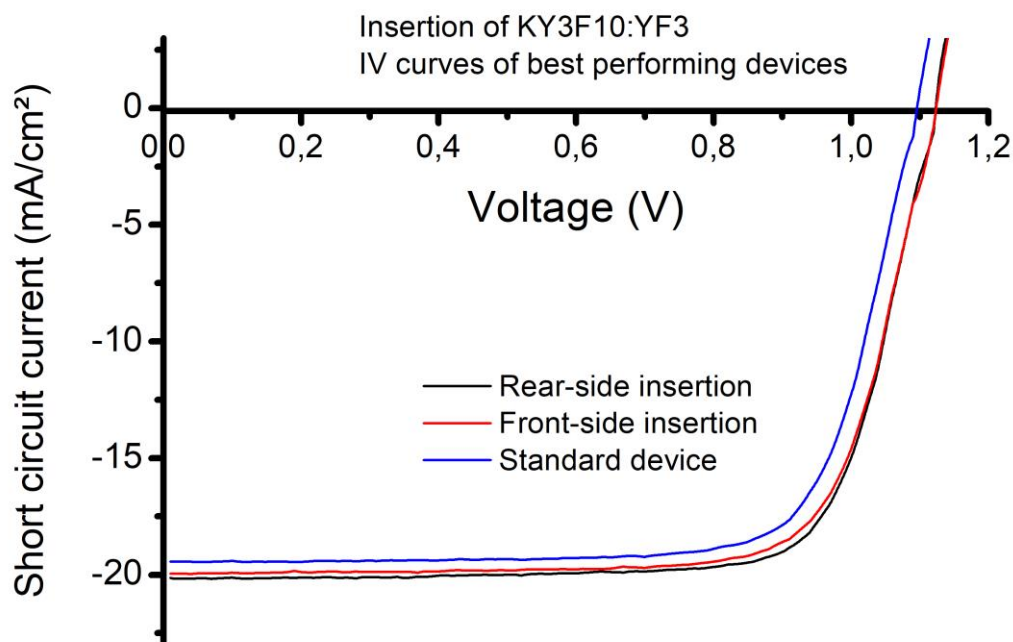


Figure 107. IV curve for the best performing devices with KY₃F₁₀:YF₃ in front- and rear-side insertion (5 wt %)

	J_{sc} (mA/cm ²)	V_{oc} (V)	FF (%)	PCE (%)
Control device	17.4	1.04	72.5	13.1
Front-side insertion	18.1	1.04	71.7	13.5
Rear-side insertion	18.4	1.06	71.3	13.9

Table 22. Summary of the photovoltaic parameters from the best-performing perovskite solar cells with and without co-doped KY₃F₁₀:YF₃ inserted in front-side insertion or rear-side insertion together with the control device (without NP insertion). The UCNP concentration applied was 5 wt%.

b. Concentration and configuration optimization

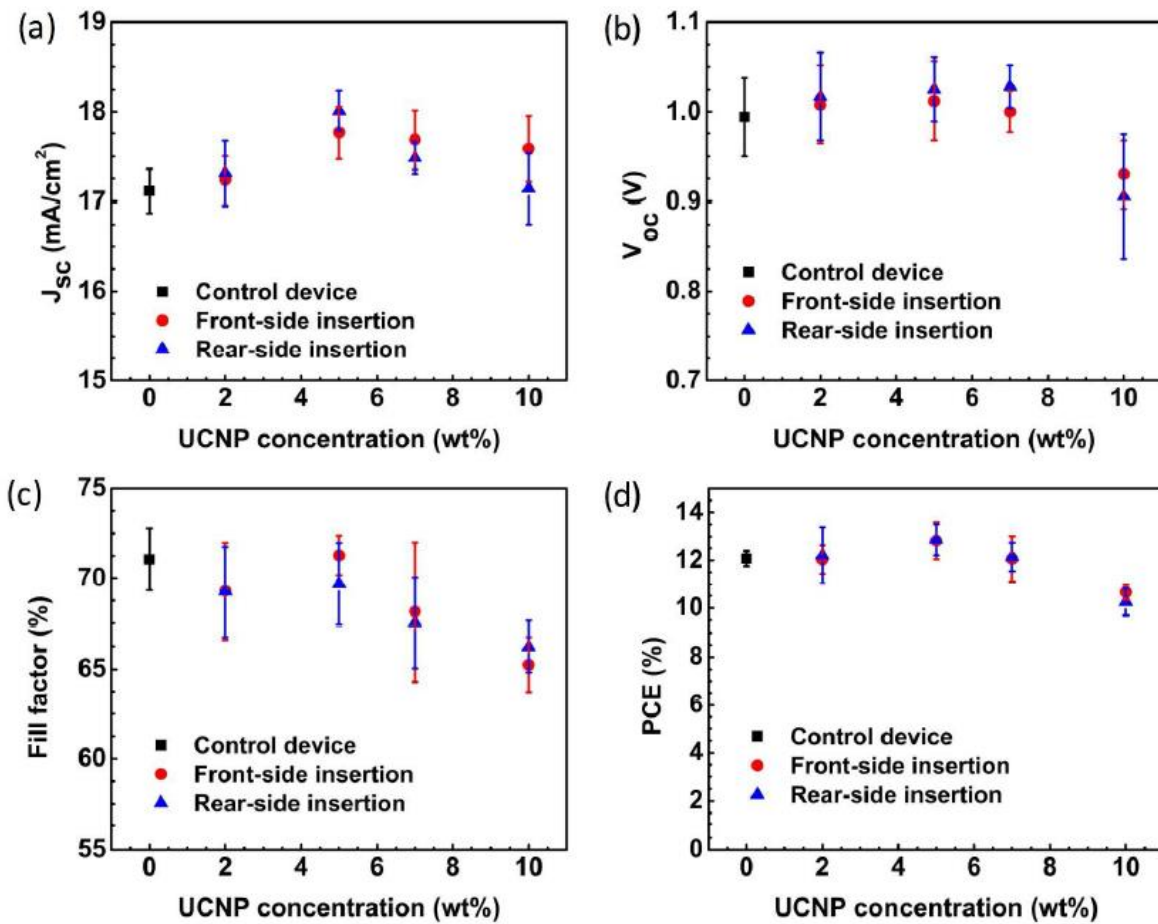


Figure 108. J_{sc} , V_{oc} , FF and PCE for KY₃F₁₀:YF₃ insertion in perovskite (FA_{0.83}CS_{0.17}Pb(I_{0.6}Br_{0.4})₃) ETL free solar cells for different concentrations and in two configuration (front: on the perovskite layer, rear: on the perovskite layer).

The t-value for the compared PCEs between the standard conditions and the ones with 5 wt % in the front-side is 2.86, which means the distributions have a probability of 0.95 to effectively belong to two different distributions (degrees of freedom = 4).

This probability is worth 0.99 for the case of 5 wt % rear-side insertion.

c.EQE

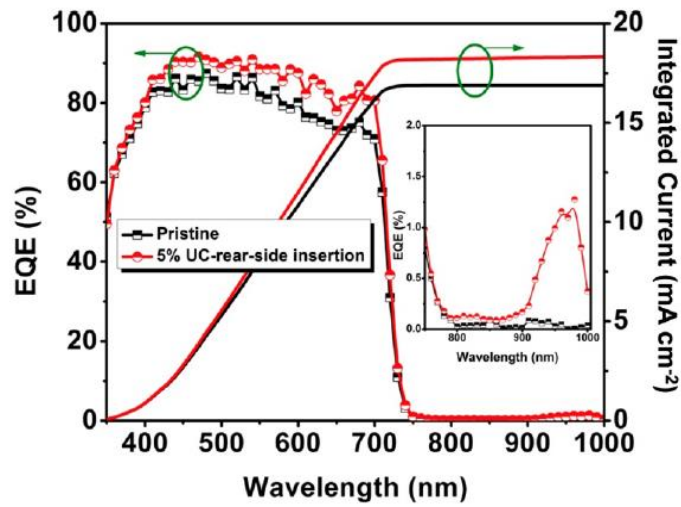


Figure 109. EQE spectra of two planar ETL-free $\text{FA}_{0.83}\text{Cs}_{0.17}\text{Pb}(\text{I}_{0.6}\text{Br}_{0.4})_3$ perovskite solar cells with and without (“pristine”) co-doped $\text{KY}_3\text{F}_{10}:\text{YF}_3$ 5 wt % inserted at the interface between the perovskite layer and the HTL polymer layer. The inset figure exhibits the zoom-in view of the spectrum range between 750 nm and 1000 nm. In collaboration with Zhelu Hu.

B.KY₃F₁₀

Those solar cells are ETL-free devices. The Spiro recipe is ²Spiro. The perovskite is $\text{FA}_{0.83}\text{Cs}_{0.17}\text{Pb}(\text{I}_{0.6}\text{Br}_{0.4})_3$.

a.IV-Curve

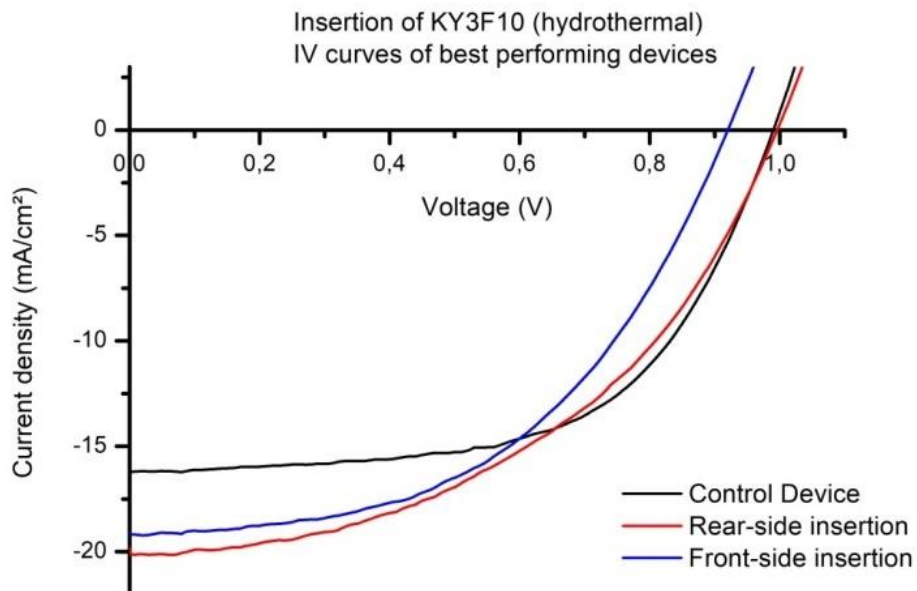


Figure 110. IV curve for the best performing devices with KY_3F_{10} in front- and rear-side insertion (5wt%)

	Jsc (mA/cm ²)	Voc (V)	FF (%)	PCE (%)
Control Device	16.1	1.0	58	9.3
Front-side Insertion	19.2	0.93	49	8.7
Rear-side insertion	19.8	1.0	49	9.7

Table 23. Summary of the photovoltaic parameters from the best-performing perovskite solar cells with and without co-doped KY₃F₁₀ NPs inserted in front-side insertion or rear-side insertion together with the control device (without NP insertion). The UCNP concentration applied was 5 wt%.

b. Concentration and configuration optimization

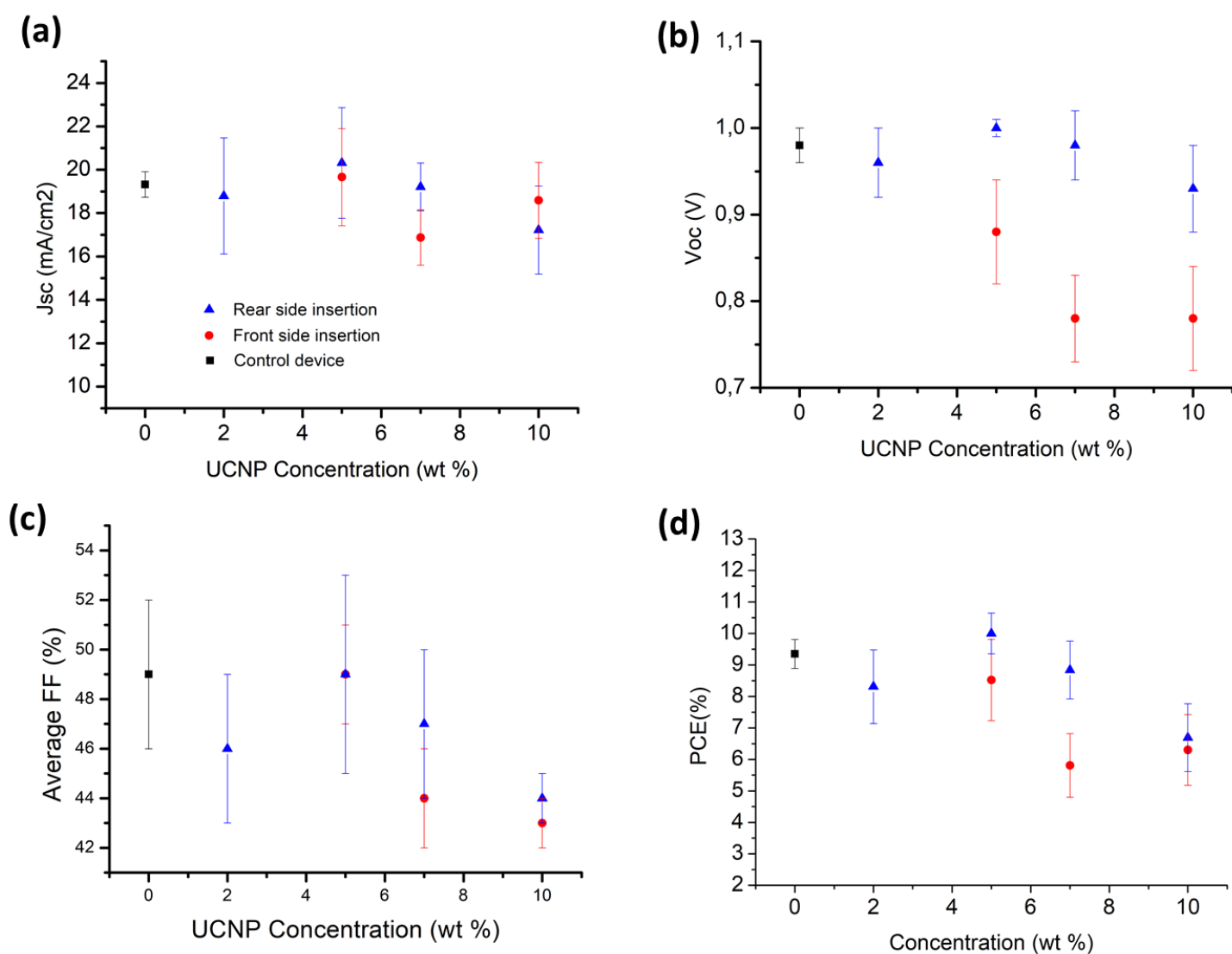


Figure 111. Jsc, Voc, FF and PCE for KY₃F₁₀ insertion in perovskite (FA_{0.83}CS_{0.17}Pb(I_{0.6}Br_{0.4})₃) ETL free solar cells for different concentrations and in two configuration (front: on the perovskite layer, rear: on the perovskite layer).

The t-value for the compared PCEs between the standard conditions and the ones with 5 wt % in the rear-side is 2.86, which means the distributions have a probability of 0.05 to effectively belong to two different distributions (degrees of freedom = 3). This low value does not allow us to conclude on the improvement of the devices by inserting KY_3F_{10} .

C. $NaYF_4$ hydrothermal (synthesis D)

Those solar cells are ETL-free devices. The Spiro recipe is 2 Spiro. The perovskite is $FA_{0.83}Cs_{0.17}Pb(I_{0.6}Br_{0.4})_3$.

a. IV-Curve

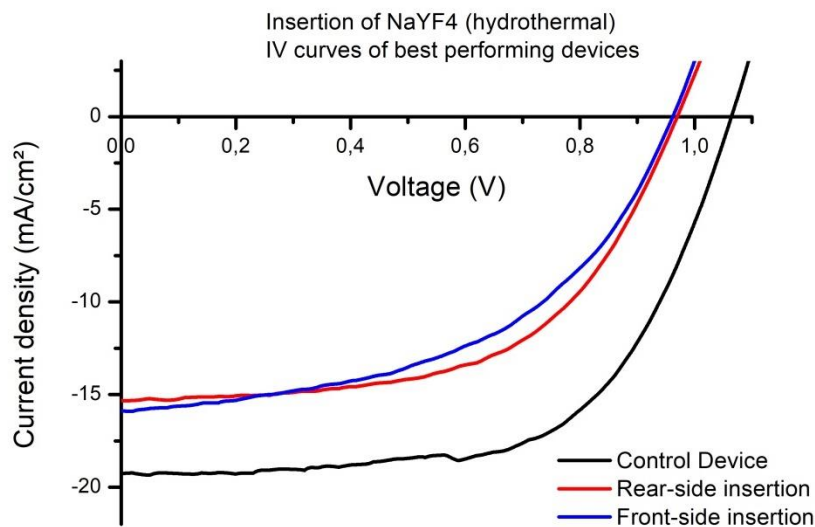


Figure 112. IV curve for the best performing devices with $NaYF_4$ (hydrothermal) in front- and rear-side insertion (5 wt %)

	Jsc (mA/cm ²)	Voc (V)	FF (%)	PCE (%)
Control Device	19.2	1.07	62	12.7
Front-side Insertion	15.9	0.98	53	8.3
Rear-side insertion	15.3	0.97	57	8.5

Table 24. Summary of the photovoltaic parameters from the best-performing perovskite solar cells with and without co-doped $NaYF_4$ inserted in front-side insertion or rear-side insertion together with the control device (without NP insertion). The UCNP concentration applied was 5 wt%.

D. NRs and KY₃F₁₀

Those solar cells include a TiO₂ layer whose recipe is not given in the main text (18mL IPA, 0.25g of diethanolamine, 0.675 mL of TTIP and 17.5 μ L DI water are stirred for 30 min. Deposition occurs at 4000 rpm for 25s. Annealing is done at 120 °C for 15 min and 450°C for an hour).The perovskite is also not mentioned in the main text, its formula is CsFA₇₉MA₁₆PbI_{2.5}Br_{0.5}. It is prepared by mixing in 1mL of DMF/DMSO 4:1 volumic ratio those products: 171 mg FAI, 517 mg of PbI₂, 23.2 mg of MABr, 73.4 mg of PbBr₂ and 39 μ L of Csl solution (390 mg/mL DMSO). The perovskite is spin coated at 1000 rpm for 10s and 5000 rpm for 45s. At 35th second 100 μ L of CBZ is released. Annealing occurs at 100°C for one hour. The Spiro recipe is ¹Spiro.

	Jsc (mA/cm ²)	Voc (V)	FF (%)	PCE (%)
Best device	24.0	1.0	51	12.5
Average	20.3	1.0	54	10.9
Standard deviation	2.0	0.02	3	0.98

Table 25. I-V curve for doped KY₃F₁₀ 2 %. 7 devices.

	Jsc (mA/cm ²)	Voc (V)	FF (%)	PCE (%)
Best device	23.1	1.0	55	13.0
Average	20.9	0.99	52	10.9
Standard deviation	2.2	0.03	3	2.1

Table 26. I-V curve for doped KY₃F₁₀ (hydrothermal) 2 % and NRs on top. 2 devices.

	Jsc (mA/cm ²)	Voc (V)	FF (%)	PCE (%)
Best device	25.1	1.0	56	14.1
Average	22.4	1.0	54	11.9
Standard deviation	2.0	0.03	2	1.6

Table 27. I-V curve for mixed KY₃F₁₀/aqueous solution NRs 1:5 volumic ratio. 3 devices.

Annex 12 – LBIC/fluorescence mapping for $KY_3F_{10}:YF_3$

A. Standard Measure

LBIC-fluorescence measurement was conducted on devices in which $KY_3F_{10}:YF_3$ 5 wt % were integrated. The laser spot is around $75\ \mu\text{m}$ and the laser power 10 mW which gives a power density around $200\ \text{W}/\text{cm}^2/\text{nm}$.

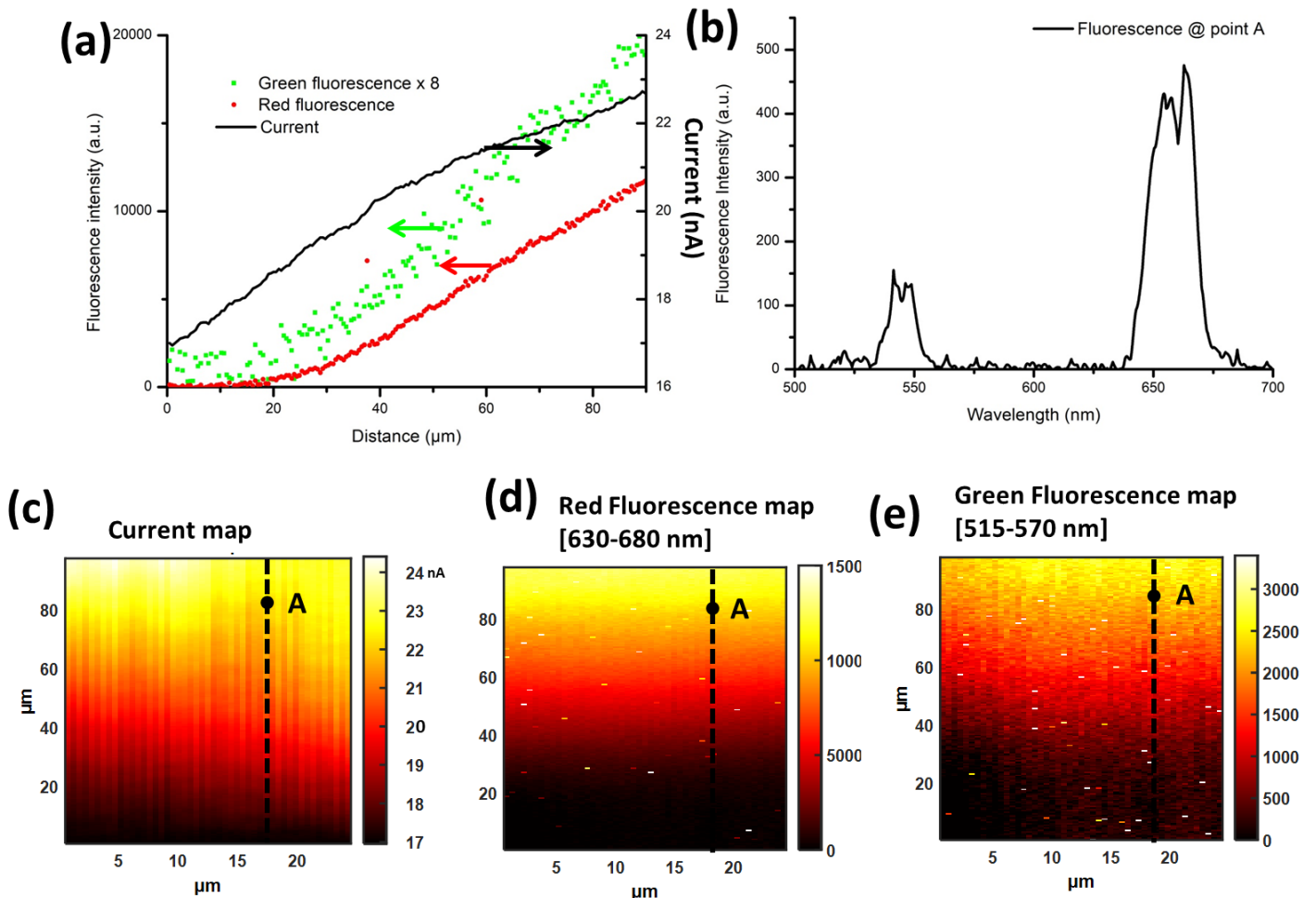


Figure 113. (a) J_{sc} and fluorescence line profile of the dashed line shown in (c), (d) and (e). (b) The upconversion fluorescence spectrum recorded during the LBIC mapping at the point A (labelled in (c)). (c) Short-circuit current J_{sc} mapping under the excitation of a 975 nm NIR laser. (d) and (e) The red and green fluorescence mapping recorded simultaneously during LBIC mapping. Each pixel represents the fluorescence signal integrated between 630 nm and 680 nm for red fluorescence (d) and between 517 nm and 560 nm for green fluorescence (e).

B. Using another microscope magnification

The LBIC/fluorescence experiment showed in Annex 12.A. and whose set up is exposed [Figure 91](#) was repeated with a more powerful microscope objective (x100), in order to decrease the size of the laser spot down to a diameter of 15 μm . The laser intensity was 1.5 mW which gives a power density around 1000 $\text{W}/\text{cm}^2/\text{nm}$.

The result of the LBIC and fluorescence mapping is shown [Figure 114](#).

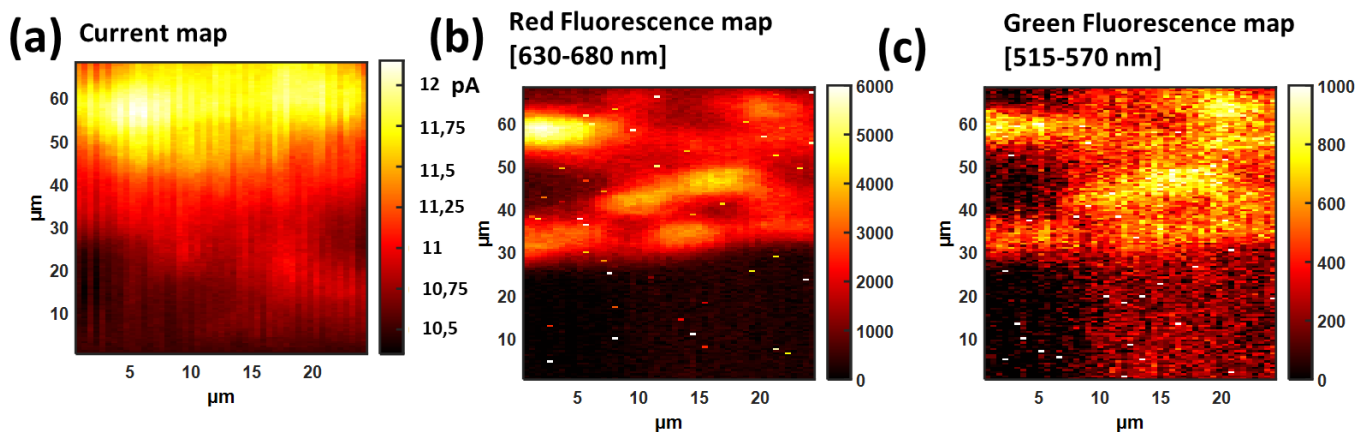


Figure 114. LBIC/Fluorescence measurement of 5 wt % $\text{KY}_3\text{F}_{10}:\text{YF}_3$ solar device. (a) current map (b) Red fluorescence map (c) green fluorescence map

The smaller size of the spot allows us to see fluorescence inhomogeneities on the device. The clearer spots suggest the existence of UCNP aggregates, as in [Figure 91\(c\)](#) whom we cannot really see in the case of a less powerful microscope objective.

We can also note that the dark current was much higher than in the previous LBIC/fluorescence experiment. This can be explained by the lower quality of this device (that gave a PCE of around 3%). Due to a lower excitation density and thus a lower PL intensity, the difference of current between the part of the device with UCNP and the part without is also smaller: it was 3 times higher in the case of the more powerful microscope objective, and it is here only 1.1 times higher.

The decrease of current is not as abrupt as the PL one, as we can see by comparing [Figure 114 \(a\) and \(b\)](#). This could be explained by phenomenon such as drift or hysteresis, that contributes to the current once the PL does not contribute anymore to current generation.

References

- [1] I. Panidi, "Master Thesis Efficient hole transport materials for organo-metal halide perovskite solar cells June 2015 Supervisor : Zhuoying Chen Efficient hole transport materials for organo-metal halide," no. June, 2015.
- [2] A. Miyata *et al.*, "Direct measurement of the exciton binding energy and effective masses for charge carriers in organic-inorganic tri-halide perovskites," *Nat. Phys.*, vol. 11, no. 7, pp. 582–587, 2015.
- [3] E. Edri, S. Kirmayer, S. Mukhopadhyay, K. Gartsman, G. Hodes, and D. Cahen, "Elucidating the charge carrier separation and working mechanism of CH₃NH₃PbI₃-xCl_x perovskite solar cells," *Nat. Commun.*, vol. 5, pp. 1–8, 2014.
- [4] J. Nelson, *The Physics of solar cells*. 2003.
- [5] W. S. Yang, B. Park, E. H. Jung, and N. J. Jeon, "Iodide management in formamidinium-lead-halide – based perovskite layers for efficient solar cells," *Science (80-.)*, vol. 356, no. 6345, pp. 1376–1379, 2017.
- [6] Q. Wang *et al.*, "Qualifying composition dependent p and n self-doping in CH₃NH₃PbI₃ Qualifying composition dependent p and n self-doping in CH₃NH₃PbI₃," vol. 163508, no. 2014, pp. 0–5, 2014.
- [7] P. Liao, X. Zhao, G. Li, Y. Shen, and M. Wang, "A New Method for Fitting Current–Voltage Curves of Planar Heterojunction Perovskite Solar Cells," *Nano-Micro Lett.*, vol. 10, no. 1, p. 5, 2018.
- [8] "<https://www.elprocus.com/pin-diode-basics-working-applications/>." .
- [9] Squirmymcphoe, "https://en.wikipedia.org/wiki/Theory_of_solar_cells#." .
- [10] W. Shockley..., "Detailed balance limit of efficiency of p-n junction solar cells," *J. Appl. Phys.*, vol. 510, no. 1961, 1961.
- [11] "https://en.wikipedia.org/wiki/Shockley%E2%80%93Queisser_limit#/media/File:ShockleyQueisserBreakdown2.svg." .
- [12] W.-J. Yin, J.-H. Yang, J. Kang, Y. Yan, and S.-H. Wei, "Halide perovskite materials for solar cells: a theoretical review," *J. Mater. Chem. A*, vol. 3, no. 17, pp. 8926–8942, 2015.
- [13] Z. C. Zhelu Hu, Hengyang Xiang, Mathilde Schoenauer Sebag, Laurent Billot, Lionel Aigouy, "Compact Layer Free Mixed-Cation Lead Mixed-Halide Perovskite Solar Cells," *Chem. Commun.*, 2018.
- [14] J. I. Pankove and D. A. Kiewit, "Optical Processes in Semiconductors," *J. Electrochem. Soc.*, vol. 119, no. 5, p. 156C, 1972.
- [15] W. E. I. Sha *et al.*, "The efficiency limit of CH₃NH₃PbI₃ perovskite solar cells The efficiency limit of CH₃NH₃PbI₃ perovskite solar cells," vol. 221104, 2015.
- [16] Y. F. Makableh, R. Vasani, J. C. Sarker, A. I. Nusir, S. Seal, and M. O. Manasreh, "Enhancement of GaAs solar cell performance by using a ZnO sol-gel anti-reflection coating," *Sol. Energy Mater. Sol. Cells*, vol. 123, pp. 178–182, 2014.
- [17] R. Bisconti and H. A. Ossenbrink, "Optical modelling of silicon cells in spherical shape," *Sol. Energy Mater. Sol. Cells*, vol. 48, no. 1–4, pp. 1–6, 1997.
- [18] S. B. Rim, S. Zhao, S. R. Scully, M. D. McGehee, and P. Peumans, "An effective light trapping configuration for thin-film solar cells," *Appl. Phys. Lett.*, vol. 91, no. 24, 2007.
- [19] J. Gilot, I. Barbu, M. M. Wienk, and R. A. J. Janssen, "The use of ZnO as optical spacer in polymer solar cells: Theoretical and experimental study," *Appl. Phys. Lett.*, vol. 91, no. 11, 2007.
- [20] A. K. K. Kyaw *et al.*, "Improved light harvesting and improved efficiency by insertion of an optical spacer (ZnO) in solution-processed small-molecule solar cells," *Nano Lett.*, vol. 13, no. 8, pp. 3796–3801, 2013.
- [21] H. L. Yip, S. K. Hau, N. S. Baek, H. Ma, and A. K. Y. Jen, "Polymer solar cells that use self-assembled-monolayer-modified ZnO/metals as cathodes," *Adv. Mater.*, vol. 20, no. 12, pp.

- 2376–2382, 2008.
- [22] J. Y. Kim *et al.*, “New architecture for high-efficiency polymer photovoltaic cells using solution-based titanium oxide as an optical spacer,” *Adv. Mater.*, vol. 18, no. 5, pp. 572–576, 2006.
- [23] P. Bermel, C. Luo, L. Zeng, L. C. Kimerling, and J. D. Joannopoulos, “Improving thin-film crystalline silicon solar cell efficiencies with photonic crystals,” *Opt. Express*, vol. 15, no. 25, p. 16986, 2007.
- [24] A. S. Bhalla, R. Guo, and R. Roy, “The perovskite structure – a review of its role in ceramic science and technology,” *Mater. Res. Innov.*, vol. 4, no. 1, pp. 3–26, 2000.
- [25] I. Chung, B. Lee, J. He, R. P. H. Chang, and M. G. Kanatzidis, “All-solid-state dye-sensitized solar cells with high efficiency,” *Nature*, vol. 9, no. 7399, pp. 486–489, 2010.
- [26] R. Aso, D. Kan, Y. Shimakawa, and H. Kurata, “Atomic level observation of octahedral distortions at the perovskite oxide heterointerface,” *Sci. Rep.*, vol. 3, 2013.
- [27] H. L. Feng *et al.*, “High-temperature ferrimagnetism driven by lattice distortion in double perovskite Ca₂FeOsO₆,” *J. Am. Chem. Soc.*, vol. 136, no. 9, pp. 3326–3329, 2014.
- [28] S. D. Stranks and H. J. Snaith, “Metal-halide perovskites for photovoltaic and light-emitting devices,” *Nature Nanotechnology*, vol. 10, no. 5, pp. 391–402, 2015.
- [29] S. Cho, M. Humar, N. Martino, and S. H. Yun, “Laser Particle Stimulated Emission Microscopy,” *Phys. Rev. Lett.*, vol. 117, no. 19, 2016.
- [30] P. J. Dereń, A. Bednarkiewicz, P. Goldner, and O. Guillot-Nol, “Laser action in LaAlO₃:Nd³⁺ single crystal,” *J. Appl. Phys.*, vol. 103, no. 4, 2008.
- [31] Y. Wang, Y. Shi, G. Xin, J. Lian, and J. Shi, “Two-Dimensional van der Waals Epitaxy Kinetics in a Three-Dimensional Perovskite Halide,” *Cryst. Growth Des.*, vol. 15, no. 10, pp. 4741–4749, 2015.
- [32] A. R. B. M. Yusoff and M. K. Nazeeruddin, “Organohalide Lead Perovskites for Photovoltaic Applications,” *J. Phys. Chem. Lett.*, vol. 7, no. 5, pp. 851–866, 2016.
- [33] A. Kojima, K. Teshima, Y. Shirai, and T. Miyasaka, “Organometal halide perovskites as visible-light sensitizers for photovoltaic cells,” *J. Am. Chem. Soc.*, vol. 131, no. 17, pp. 6050–6051, 2009.
- [34] H. Kim *et al.*, “All-Solid-State Submicron Thin Film,” *Sci. Rep.*, pp. 1–7, 2012.
- [35] N. Pellet *et al.*, “Mixed-organic-cation perovskite photovoltaics for enhanced solar-light harvesting,” *Angew. Chemie - Int. Ed.*, vol. 53, no. 12, pp. 3151–3157, 2014.
- [36] N. J. Jeon *et al.*, “Compositional engineering of perovskite materials for high-performance solar cells,” *Nature*, vol. 517, no. 7535, pp. 476–480, 2015.
- [37] T. M. Koh *et al.*, “Formamidinium-containing metal-halide: An alternative material for near-IR absorption perovskite solar cells,” *J. Phys. Chem. C*, vol. 118, no. 30, pp. 16458–16462, 2014.
- [38] D. P. McMeekin *et al.*, “A mixed-cation lead mixed-halide perovskite absorber for tandem solar cells,” *Science (80-.)*, vol. 351, no. 6269, pp. 151–155, 2016.
- [39] C. Yi *et al.*, “Entropic stabilization of mixed A-cation ABX₃ metal halide perovskites for high performance perovskite solar cells,” *Energy Environ. Sci.*, vol. 9, pp. 656–662, 2016.
- [40] Z. Li, M. Yang, J. S. Park, S. H. Wei, J. J. Berry, and K. Zhu, “Stabilizing Perovskite Structures by Tuning Tolerance Factor: Formation of Formamidinium and Cesium Lead Iodide Solid-State Alloys,” *Chem. Mater.*, vol. 28, no. 1, pp. 284–292, 2016.
- [41] J.-P. Correa-Baena *et al.*, “Promises and challenges of perovskite solar cells,” *Science (80-.)*, vol. 358, no. 6364, pp. 739–744, 2017.
- [42] E. T. Hoke, D. J. Slotcavage, E. R. Dohner, A. R. Bowring, H. I. Karunadasa, and M. D. McGehee, “Reversible photo-induced trap formation in mixed-halide hybrid perovskites for photovoltaics,” *Chem. Sci.*, vol. 6, no. 1, pp. 613–617, 2015.
- [43] C. Wehrenfennig, M. Liu, H. J. Snaith, M. B. Johnston, and L. M. Herz, “Homogeneous emission line broadening in the organo lead halide perovskite CH₃NH₃PbI₃-xCl_x,” *J. Phys. Chem. Lett.*, vol. 5, no. 8, pp. 1300–1306, 2014.
- [44] S. Sun *et al.*, “The origin of high efficiency in low-temperature solution-processable bilayer organometal halide hybrid solar cells,” *Energy Environ. Sci.*, vol. 7, no. 1, pp. 399–407, 2014.

- [45] M. A. Green, A. Ho-Baillie, and H. J. Snaith, "The emergence of perovskite solar cells," *Nat. Photonics*, vol. 8, no. 7, pp. 506–514, 2014.
- [46] L. Yalçın and R. Öztürk, "Performance comparison of c-Si, mc-Si and a-Si thin film PV by PVsyst simulation," *J. Optoelectron. Adv. Mater.*, vol. 15, no. 3–4, pp. 326–334, 2013.
- [47] G. Peng, X. Xu, and G. Xu, "Hybrid Organic-Inorganic Perovskites Open a New Era for Low-Cost, High Efficiency Solar Cells," *J. Nanomater.*, vol. 2015, no. d, p. ID 241853, 2015.
- [48] J. Kim, S.-H. Lee, J. H. Lee, and K.-H. Hong, "The Role of Intrinsic Defects in Methylammonium Lead Iodide Perovskite," *J. Phys. Chem. Lett.*, vol. 5, no. 8, pp. 1312–1317, 2014.
- [49] W.-J. Yin, T. Shi, and Y. Yan, "Unusual defect physics in CH₃NH₃PbI₃ perovskite solar cell absorber," *Appl. Phys. Lett.*, vol. 104, no. 6, p. 063903/1-063903/4, 2014.
- [50] S. Colella *et al.*, "MAPbI_{3-x}Cl_x Mixed Halide Perovskite for Hybrid Solar Cells: The Role of Chloride as Dopant on the Transport and Structural Properties," *Chem. Mater.*, vol. 25, no. 22, pp. 4613–4618, 2013.
- [51] M. Saliba *et al.*, "Incorporation of rubidium cations into perovskite solar cells improves photovoltaic performance," *Science (80-.)*, vol. 354, no. 6309, pp. 206–209, 2016.
- [52] D. W. Dequillettes *et al.*, "Photoluminescence Lifetimes Exceeding 8 μ s and Quantum Yields Exceeding 30% in Hybrid Perovskite Thin Films by Ligand Passivation," *ACS Energy Lett.*, vol. 1, no. 2, pp. 438–444, 2016.
- [53] W. Tress, "Perovskite Solar Cells on the Way to Their Radiative Efficiency Limit – Insights Into a Success Story of High Open-Circuit Voltage and Low Recombination," *Adv. Energy Mater.*, vol. 7, no. 14, 2017.
- [54] K. Domanski *et al.*, "Not All That Glitters Is Gold: Metal-Migration-Induced Degradation in Perovskite Solar Cells," *ACS Nano*, vol. 10, no. 6, pp. 6306–6314, 2016.
- [55] A. Abate *et al.*, "Silolothiophene-linked triphenylamines as stable hole transporting materials for high efficiency perovskite solar cells," *Energy Environ. Sci.*, vol. 8, no. 10, pp. 2946–2953, 2015.
- [56] T. Leijtens, G. E. Eperon, S. Pathak, A. Abate, M. M. Lee, and H. J. Snaith, "Overcoming ultraviolet light instability of sensitized TiO₂ with meso-superstructured organometal tri-halide perovskite solar cells," *Nat. Commun.*, vol. 4, 2013.
- [57] S. S. Shin *et al.*, "Colloidally prepared La-doped BaSnO₃ electrodes for efficient, photostable perovskite solar cells," *Science (80-.)*, vol. 356, no. 6334, pp. 167–171, 2017.
- [58] B. Roose *et al.*, "Mesoporous SnO₂ electron selective contact enables UV-stable perovskite solar cells," *Nano Energy*, vol. 30, pp. 517–522, 2016.
- [59] D. Wang, M. Wright, N. K. Elumalai, and A. Uddin, "Stability of perovskite solar cells," *Solar Energy Materials and Solar Cells*, vol. 147, pp. 255–275, 2016.
- [60] K. A. Bush *et al.*, "23.6%-efficient monolithic perovskite/silicon tandem solar cells with improved stability," *Nat. Energy*, vol. 2, no. 4, 2017.
- [61] F. Bella *et al.*, "Improving efficiency and stability of perovskite solar cells with photocurable fluoropolymers," *Science (80-.)*, vol. 354, pp. 203–206, 2016.
- [62] W. Tress, N. Marinova, T. Moehl, S. M. Zakeeruddin, M. K. Nazeeruddin, and M. Gratzel, "Understanding the rate-dependent J–V hysteresis, slow time component, and aging in CH₃NH₃PbI₃ perovskite solar cells: the role of a compensated electric field," *Energy Environ. Sci.*, vol. 8, pp. 995–1004, 2015.
- [63] K. Domanski *et al.*, "Migration of cations induces reversible performance losses over day/night cycling in perovskite solar cells," *Energy Environ. Sci.*, vol. 10, no. 2, pp. 604–613, 2017.
- [64] M. Bag *et al.*, "Kinetics of Ion Transport in Perovskite Active Layers and Its Implications for Active Layer Stability," *J. Am. Chem. Soc.*, vol. 137, no. 40, pp. 13130–13137, 2015.
- [65] Z. Li *et al.*, "Extrinsic ion migration in perovskite solar cells," *Energy Environ. Sci.*, vol. 10, no. 5, pp. 1234–1242, 2017.
- [66] V. V. Ev, G. M. Zverev, and A. M. Onishchenko, "Nonresonance excitation energy transfer between impurity rare-earth ions," vol. 29, no. 1, 1969.
- [67] G. B. Haxel, J. B. Hedrick, and G. J. Orris, "Rare Earth Elements — Critical Resources for High

- Technology," *United States Geol. Surv. Fact Sheet*, vol. 87, p. 4, 2002.
- [68] J. F. Philipps, T. Töpfer, H. Ebendorff-Heidepriem, D. Ehrhart, and R. Sauerbrey, "Energy transfer and upconversion in erbium-ytterbium-doped fluoride phosphate glasses," *Appl. Phys. B Lasers Opt.*, vol. 74, no. 3, pp. 233–236, 2002.
- [69] F. Song, G. Zhang, M. Shang, H. Tan, J. Yang, and F. Meng, "Three-photon phenomena in the upconversion luminescence of erbium-ytterbium-codoped phosphate glass," *Appl. Phys. Lett.*, vol. 79, no. 12, pp. 1748–1750, 2001.
- [70] K. Zhong, H. Wu, and J. Su, "Enhanced upconversion luminescence of erbium-nitrogen-doped zinc oxide nano-wires by implantation of ytterbium ions," *Spectrosc. Lett.*, vol. 47, no. 1, pp. 52–56, 2014.
- [71] A. F. Da Silva *et al.*, "Intense red upconversion fluorescence emission in NIR-excited erbium-ytterbium doped laponite-derived phosphor," *Opt. Commun.*, vol. 284, no. 19, pp. 4501–4503, 2011.
- [72] G. Yi, Y. Peng, and Z. Gao, "Strong red-emitting near-infrared-to-visible upconversion fluorescent nanoparticles," *Chem. Mater.*, vol. 23, no. 11, pp. 2729–2734, 2011.
- [73] H. Zellmer, P. Riedel, and A. Tünnermann, "Visible upconversion lasers in praseodymium-ytterbium-doped fibers," vol. 421, pp. 417–421, 1999.
- [74] J. De Wild, A. Meijerink, J. K. Rath, W. G. J. H. M. Van Sark, and R. E. I. Schropp, "Towards upconversion for amorphous silicon solar cells," *Sol. Energy Mater. Sol. Cells*, vol. 94, no. 11, pp. 1919–1922, 2010.
- [75] J. Denis, M. Genotelle, and F. Pel, "Tm-Yb-Tm energy transfers and effect of temperature on the fluorescence intensities in oxyfluoride tellurite compounds."
- [76] G. J. Daniels *et al.*, "Resonance energy transfer : The unified theory revisited Resonance energy transfer : The unified theory revisited," vol. 2264, no. 2003, 2016.
- [77] M. M. H. V. Werts, J. W. Hofstraat, F. a. J. Geurts, and J. W. Verhoeven, "Fluorescein and eosin as sensitizing chromophores in near-infrared luminescent ytterbium(III), neodymium(III) and erbium(III) chelates," *Chem. Phys. Lett.*, vol. 276, no. 3–4, pp. 196–201, 1997.
- [78] B. M. van der Ende, L. Aarts, and A. Meijerink, "Lanthanide ions as spectral converters for solar cells," *Phys. Chem. Chem. Phys.*, vol. 11, no. 47, p. 11081, 2009.
- [79] J. F. Suyver *et al.*, "Novel materials doped with trivalent lanthanides and transition metal ions showing near-infrared to visible photon upconversion," *Opt. Mater. (Amst.)*, vol. 27, no. 6, pp. 1111–1130, 2005.
- [80] D. M. Wu, A. García-Etxarri, A. Salleo, and J. A. Dionne, "Plasmon-enhanced upconversion," *J. Phys. Chem. Lett.*, 2014.
- [81] F. Auzel, "Upconversion and Anti-Stokes Processes with f and d Ions in Solids," *Chem. Rev.*, vol. 104, no. 1, pp. 139–173, 2004.
- [82] A. Einstein, "The Quantum Theory of Radiation," *Nature*, vol. 138, no. 3490, pp. 483–484, 1936.
- [83] S. Fischer, H. Steinkemper, P. Löper, M. Hermle, and J. C. Goldschmidt, "Modeling upconversion of erbium doped microcrystals based on experimentally determined Einstein coefficients," *J. Appl. Phys.*, vol. 111, no. 1, pp. 1–29, 2012.
- [84] B. DiBartolo, *Radiationless Processes*. 1979.
- [85] D. L. Dexter, "A theory of sensitized luminescence in solids," *J. Chem. Phys.*, vol. 21, no. 5, pp. 836–850, 1953.
- [86] F. Auzel, "L'auto-extinction de Nd³⁺: Son mecanisme fondamental et un critere predictif simple pour les materiaux minilaser," *Mater. Res. Bull.*, vol. 14, no. 2, pp. 223–231, 1979.
- [87] M. Yokota and O. Tanimoto, "Effects of diffusion on energy transfer by resonance," *J. Phys. Soc. Japan*, vol. 22, no. 3, pp. 779–784, 1967.
- [88] R. B. Barthem, R. Buisson, and J. C. Vial, "Coexistence of two excitation transfer mechanisms in LiYF₄: Pr³⁺," *J. Lumin.*, vol. 38, no. 1–6, pp. 190–192, 1987.
- [89] M. Inokuti and F. Hirayama, "Influence of energy transfer by the exchange mechanism on donor luminescence," *J. Chem. Phys.*, vol. 43, no. 6, pp. 1978–1989, 1965.

- [90] N. Yamada, S. Shionoya, and T. Kushida, "Phonon-Assisted Energy Transfer between Trivalent Rare Earth Ions," *J. Phys. Soc. Japan*, vol. 32, no. 6, pp. 1577–1586, 1972.
- [91] F. Auzel, "Multiphonon-assisted anti-Stokes and Stokes fluorescence of triply ionized rare-earth ions," *Phys. Rev. B*, vol. 13, no. 7, pp. 2809–2817, 1976.
- [92] F. A. JF Pouradier, "Calcul des probabilités des transferts d'énergie entre ions de terres rares. I. une méthode de calcul unifiée utilisant des méthodes tensorielles standard," *J. Phys.*, 1978.
- [93] R. Orbach, *Relaxation and energy transfer*. .
- [94] J. D. Axe and P. F. Weller, "Fluorescence and energy transfer in $\gamma\text{2O3:Eu}^{3+}$," *J. Chem. Phys.*, vol. 40, no. 10, pp. 3066–3069, 1964.
- [95] T. Kushida, "Energy transfer and cooperative optical transitions in rare-earth doped inorganic materials. I. Transition probability calculation," *J. Phys. Soc. Japan*, vol. 34, no. 5, pp. 1318–1326, 1973.
- [96] M. J. Weber, "Radiative and multiphonon relaxation of rare-earth ions in Y2O3 ," *Phys. Rev.*, vol. 171, no. 2, pp. 283–291, 1968.
- [97] L. A. Riseberg and H. W. Moos, "Multiphonon orbit-lattice relaxation of excited states of rare-earth ions in crystals," *Phys. Rev.*, vol. 174, no. 2, pp. 429–438, 1968.
- [98] R. B. Anderson, S. J. Smith, P. S. May, and M. T. Berry, "Revisiting the NIR-to-visible upconversion mechanism in $\text{NaYF}_4\text{:Yb}^{3+},\text{Er}^{3+}$," *J. Phys. Chem. Lett.*, vol. 5, no. 1, pp. 36–42, 2014.
- [99] J. F. Suyver, J. Grimm, M. K. van Veen, D. Biner, K. W. Krämer, and H. U. Güdel, "Upconversion spectroscopy and properties of NaYF_4 doped with , and/or," *J. Lumin.*, vol. 117, no. 1, pp. 1–12, 2006.
- [100] V. Giannini, A. I. Fernández-Domínguez, S. C. Heck, and S. A. Maier, "Plasmonic nanoantennas: Fundamentals and their use in controlling the radiative properties of nanoemitters," *Chemical Reviews*, vol. 111, no. 6, pp. 3888–3912, 2011.
- [101] J.-C. Boyer and F. C. J. M. van Veggel, "Absolute quantum yield measurements of colloidal $\text{NaYF}_4\text{:Er}^{3+},\text{Yb}^{3+}$ upconverting nanoparticles," *Nanoscale*, vol. 2, no. 8, p. 1417, 2010.
- [102] S. Singh and J. E. Geusic, "Observation and saturation of a multiphoton process in NdCl_3 ," *Phys. Rev. Lett.*, vol. 17, no. 16, pp. 865–868, 1966.
- [103] M. Pollnau, D. R. Gamelin, S. R. Lüthi, H. U. Güdel, and M. P. Hehlen, "Power dependence of upconversion luminescence in lanthanide and transition-metal-ion systems," *Phys. Rev. B*, vol. 61, no. 5, pp. 3337–3346, 2000.
- [104] G. De *et al.*, "Infrared-to-ultraviolet up-conversion luminescence of $\text{YF}_3\text{:Yb}^{3+},\text{Tm}^{3+}$ microsheets," *J. Lumin.*, vol. 122–123, no. 1–2, pp. 128–130, 2007.
- [105] F. Vetrone, V. Mahalingam, and J. a. Capobianco, "Near-Infrared-to-Blue Upconversion in Colloidal $\text{BaYF}_5\text{:Tm}^{3+},\text{Yb}^{3+}$ Nanocrystals," *Chem. Mater.*, vol. 21, no. 9, pp. 1847–1851, 2009.
- [106] S. Heer, K. Kömpe, H. U. Güdel, and M. Haase, "Highly efficient multicolour upconversion emission in transparent colloids of lanthanide-doped NaYF_4 nanocrystals," *Adv. Mater.*, vol. 16, no. 23–24, pp. 2102–2105, 2004.
- [107] S. F. Wuister, C. de Mello Donegá, and A. Meijerink, "Efficient energy transfer between nanocrystalline YAG:Ce and TRITC ," *Phys. Chem. Chem. Phys.*, vol. 6, no. 8, pp. 1633–1636, 2004.
- [108] S. Fischer, N. J. J. Johnson, J. Pichaandi, J. C. Goldschmidt, and F. C. J. M. Van Veggel, "Upconverting core-shell nanocrystals with high quantum yield under low irradiance: On the role of isotropic and thick shells," *J. Appl. Phys.*, vol. 118, no. 19, 2015.
- [109] S. Schietinger, L. De S. Menezes, B. Lauritzen, and O. Benson, "Observation of size dependence in multicolor upconversion in single $\text{Yb}^{3+},\text{Er}^{3+}$ codoped NaYF_4 nanocrystals," *Nano Lett.*, vol. 9, no. 6, pp. 2477–2481, 2009.
- [110] P. Gibart, F. Auzel, J. C. Guillaume, and K. Zahraman, "Below band-gap IR response of substrate-free GaAs solar cells using two-photon up-conversion," *Japanese J. Appl. Physics, Part 1 Regul. Pap. Short Notes Rev. Pap.*, vol. 35, no. 8, pp. 4401–4402, 1996.
- [111] A. Shalav, B. S. Richards, K. Krame, and H. Gudel, "Improvements of an Up-conversion

- NaYF₄:Er³⁺ Phosphor/Silicon Solar Cell System for an Enhanced Response in the Near-Infrared," *Photovolt. Spec. Conf. 2005. Conf. Rec. Thirty-first IEEE*, no. 3, pp. 114–117, 2005.
- [112] G. Bin Shan and G. P. Demopoulos, "Near-infrared sunlight harvesting in dye-sensitized solar cells via the insertion of an upconverter-TiO₂ nanocomposite layer," *Adv. Mater.*, vol. 22, no. 39, pp. 4373–4377, 2010.
- [113] J. Yu *et al.*, "Enhanced near-infrared to visible upconversion nanoparticles of Ho(3)(+)-Yb(3)(+)-F(-) tri-doped TiO(2) and its application in dye-sensitized solar cells with 37% improvement in power conversion efficiency," *Inorg Chem*, vol. 53, pp. 8045–8053, 2014.
- [114] H. Q. Wang, M. Batentschuk, A. Osvet, L. Pinna, and C. J. Brabec, "Rare-earth ion doped up-conversion materials for photovoltaic applications," *Adv. Mater.*, vol. 23, no. 22–23, pp. 2675–2680, 2011.
- [115] M. He *et al.*, "Communications Photovoltaic Devices Very Important Paper Monodisperse Dual-Functional Upconversion Nanoparticles Enabled Near-Infrared Organolead Halide Perovskite Solar Cells," pp. 4280–4284, 2016.
- [116] A. Otto, "Eine neue Methode der Anregung nichtstrahlender Oberflächenplasmaschwingungen," *Phys. status solidi*, vol. 26, no. 2, pp. K99–K101, 1968.
- [117] M. Faraday, "The Bakerian Lecture: Experimental Relations of Gold (and Other Metals) to Light," *Philos. Trans. R. Soc. London*, vol. 147, no. 0, pp. 145–181, 1857.
- [118] L. Tonks and I. Langmuir, "Oscillations in ionized gases," *Phys. Rev.*, vol. 33, no. 2, pp. 195–210, 1929.
- [119] D. Pines, "Collective energy losses in solids," *Rev. Mod. Phys.*, vol. 28, no. 3, pp. 184–198, 1956.
- [120] D. Bohm and D. Pines, "A collective description of electron interactions. I. magnetic interactions," *Phys. Rev.*, vol. 82, no. 5, pp. 625–634, 1951.
- [121] G. Ruthemann, "Diskrete Energieverluste mittelschneller Elektronen beim Durchgang durch d??ne Folien," *Ann. Phys.*, vol. 437, no. 3–4, pp. 113–134, 1948.
- [122] D. Bohm and E. P. Gross, "Theory of plasma oscillations. A. Origin of medium-like behavior," *Phys. Rev.*, vol. 75, no. 12, pp. 1851–1864, 1949.
- [123] E. A. Stern and R. A. Ferrell, "Surface plasma oscillations of a degenerate electron gas," *Phys. Rev.*, vol. 120, no. 1, pp. 130–136, 1960.
- [124] C. J. Powell and J. B. Swan, "Origin of the characteristic electron energy losses in aluminum," *Phys. Rev.*, vol. 115, no. 4, pp. 869–875, 1959.
- [125] C. J. Powell and J. B. Swan, "Origin of the characteristic electron energy losses in magnesium," *Phys. Rev.*, vol. 116, no. 1, pp. 81–83, 1959.
- [126] R. H. Ritchie, "Plasma Losses by Fast Electrons in Thin Films," *Phys. Rev.*, vol. 106, no. 5, pp. 874–881, 1957.
- [127] C. Sönnichsen, "Plasmon in Metal Nanostructures," 2001.
- [128] M. R. Gartia *et al.*, "Colorimetrics: Colorimetric Plasmon Resonance Imaging Using Nano Lycurgus Cup Arrays (Advanced Optical Materials 1/2013)," *Adv. Opt. Mater.*, vol. 1, no. 1, pp. 1–1, 2013.
- [129] M. José-Yacamán, L. Rendon, J. Arenas, and M. C. Serra Puche, "Maya Blue Paint: An Ancient Nanostructured Material," *Science (80-.)*, vol. 273, no. 5272, pp. 223–225, 1996.
- [130] M. I. Stockman, "Nanoplasmonics: The physics behind the applications," *Phys. Today*, vol. 64, no. 2, pp. 39–44, 2011.
- [131] S. A. Maier, *Plasmonics: Fundamentals and applications*. 2007.
- [132] A. Polman, "Applied physics: Plasmonics applied," *Science*, vol. 322, no. 5903, pp. 868–869, 2008.
- [133] S. I. Bozhevolnyi, *Plasmonic Nano-Guides and Circuits*. 2008.
- [134] P. G. Kik and M. L. Brongersma, "Surface plasmon nanophotonics," *Springer Ser. Opt. Sci.*, vol. 131, pp. 1–9, 2007.
- [135] E. Petryayeva and U. J. Krull, "Localized surface plasmon resonance: Nanostructures, bioassays and biosensing-A review," *Analytica Chimica Acta*, vol. 706, no. 1, pp. 8–24, 2011.

- [136] X. Huang and M. A. El-Sayed, "Gold nanoparticles: Optical properties and implementations in cancer diagnosis and photothermal therapy," *Journal of Advanced Research*, vol. 1, no. 1. pp. 13–28, 2010.
- [137] K. Okamoto, I. Niki, A. Shvartser, Y. Narukawa, T. Mukai, and A. Scherer, "Surface-plasmon-enhanced light emitters based on InGaN quantum wells," *Nat. Mater.*, vol. 3, no. 9, pp. 601–605, 2004.
- [138] R. F. Oulton *et al.*, "Plasmon lasers at deep subwavelength scale," *Nature*, vol. 461, no. 7264, pp. 629–632, 2009.
- [139] M. W. Knight, H. Sobhani, P. Nordlander, and N. J. Halas, "Photodetection with active optical antennas," *Sci. {(New} York, {N.Y.}}*, vol. 332, no. 6030, pp. 702–704, 2011.
- [140] H. Hu, C. Ma, and Z. Liu, "Plasmonic dark field microscopy," *Appl. Phys. Lett.*, vol. 96, no. 11, 2010.
- [141] E. C. Le Ru, P. G. Etchegoin, E. C. Le Ru, and P. G. Etchegoin, "Chapter 2 – Raman spectroscopy and related optical techniques," in *Principles of Surface-Enhanced Raman Spectroscopy*, 2009, pp. 29–120.
- [142] G. McNay, D. Eustace, W. E. Smith, K. Faulds, and D. Graham, "Surface-enhanced Raman scattering (SERS) and surface-enhanced resonance raman scattering (SERRS): A review of applications," *Applied Spectroscopy*, vol. 65, no. 8. pp. 825–837, 2011.
- [143] H. A. Atwater and A. Polman, "Plasmonics for improved photovoltaic devices," *Nature Materials*, vol. 9, no. 3. pp. 205–213, 2010.
- [144] S. Vedraïne, "Intégration de nanostructures plasmoniques au sein de dispositifs photovoltaïques organiques : étude numérique et expérimentale," 2012.
- [145] Michael Quinten, "Optical Properties of Nanoparticle Systems: Mie and beyond - Quinten - Wiley Online Library," *Wiley-VCH Verlag GmbH & Co. KGaA, Weinheim*, 2011. [Online]. Available: <http://onlinelibrary.wiley.com/book/10.1002/9783527633135>.
- [146] L. J. Mendoza Herrera, D. M. Arboleda, D. C. Schinca, and L. B. Scaffardi, "Determination of plasma frequency, damping constant, and size distribution from the complex dielectric function of noble metal nanoparticles," *J. Appl. Phys.*, vol. 116, no. 23, 2014.
- [147] S. Albaladejo *et al.*, "Radiative corrections to the polarizability tensor of an electrically small anisotropic dielectric particle," *Opt. Express*, vol. 18, no. 4, p. 3556, 2010.
- [148] C. F. Bohren and D. R. Huffman, "Absorption and scattering of light by small particles," *Research supported by the University of Arizona and Institute of Occupational and Environmental Health New York WileyInterscience 1983 541 p*, vol. 1, no. 1. p. xiv, 530 , 1983.
- [149] J. W. Strutt and B. Rayleigh, "The Theory of Sound," *Nature*, vol. 1. p. 340, 1877.
- [150] G. Mie, "Beiträge zur Optik trüber Medien, speziell kolloidaler Metallösungen," *Ann. Phys.*, vol. 330, no. 3, pp. 377–445, 1908.
- [151] I. Charamisinau, G. Happawana, G. Evans, A. Rosen, R. a Hsi, and D. Bour, "Semiconductor laser insert with uniform illumination for use in photodynamic therapy.," *Appl. Opt.*, vol. 44, no. 24, pp. 5055–5068, 2005.
- [152] P. K. Jain, K. S. Lee, I. H. El-Sayed, and M. A. El-Sayed, "Calculated absorption and scattering properties of gold nanoparticles of different size, shape, and composition: Applications in biological imaging and biomedicine," *J. Phys. Chem. B*, vol. 110, no. 14, pp. 7238–7248, 2006.
- [153] B. T. Draine and P. J. Flatau, "Discrete-Dipole Approximation For Scattering Calculations," *J. Opt. Soc. Am. A*, vol. 11, no. 4, p. 1491, 1994.
- [154] N. Destouches, "NANOPARTICULES METALLIQUES Propriétés Modes de synthèse Applications."
- [155] R. Gans, "Über die Form ultramikroskopischer Silberteilchen," *Ann. Phys.*, vol. 352, no. 10, pp. 270–284, 1915.
- [156] C. Sönnichsen *et al.*, "Drastic reduction of plasmon damping in gold nanorods," *Phys. Rev. Lett.*, vol. 88, no. 7, pp. 774021–774024, 2002.
- [157] S. Link and M. A. El-Sayed, "Shape and size dependence of radiative, non-radiative and photothermal properties of gold nanocrystals," *Int. Rev. Phys. Chem.*, vol. 19, no. 3, pp. 409–

- 453, 2000.
- [158] S. Link and M. A. El-Sayed, "Spectral Properties and Relaxation Dynamics of Surface Plasmon Electronic Oscillations in Gold and Silver Nanodots and Nanorods," *J. Phys. Chem. B*, vol. 103, no. 40, pp. 8410–8426, 1999.
- [159] U. Kreibig and M. Vollmer, "Optical Properties of Metal Clusters," *J. Am. Chem. Soc.*, vol. 118, no. 25, pp. 6098–6098, 1995.
- [160] J.-M. C. Wenpeng Chen, "investigation of surface plasmon dispersion."
- [161] J. Mertz, "Radiative absorption, fluorescence, and scattering of a Classical Dipole Near a Lossless Interface : a Unified Description," *J. Opt. Soc. Am. B*, vol. 17, no. 11, pp. 1906–1913, 2000.
- [162] S. Hayashi, K. Kozaru, and K. Yamamoto, "Enhancement of photoelectric conversion efficiency by surface plasmon excitation: A test with an organic solar cell," *Solid State Commun.*, vol. 79, no. 9, pp. 763–767, 1991.
- [163] M. Westphalen, U. Kreibig, J. Rostalski, H. Lüth, and D. Meissner, "Metal cluster enhanced organic solar cells," *Sol. Energy Mater. Sol. Cells*, vol. 61, no. 1, pp. 97–105, 2000.
- [164] M. Saliba *et al.*, "Plasmonic-Induced Photon Recycling in Metal Halide Perovskite Solar Cells," *Adv. Funct. Mater.*, vol. 25, no. 31, pp. 5038–5046, 2015.
- [165] Z. Lu *et al.*, "Plasmonic-enhanced perovskite solar cells using alloy popcorn nanoparticles," *RSC Adv.*, vol. 5, no. 15, pp. 11175–11179, 2015.
- [166] D. M. Schaadt, B. Feng, and E. T. Yu, "Enhanced semiconductor optical absorption via surface plasmon excitation in metal nanoparticles," *Appl. Phys. Lett.*, vol. 86, no. 6, pp. 1–3, 2005.
- [167] A. J. Morfa, K. L. Rowlen, T. H. Reilly, M. J. Romero, and J. Van De Lagemaat, "Plasmon-enhanced solar energy conversion in organic bulk heterojunction photovoltaics," *Appl. Phys. Lett.*, vol. 92, no. 1, 2008.
- [168] X. Chen, C. Zhao, L. Rothberg, and M. K. Ng, "Plasmon enhancement of bulk heterojunction organic photovoltaic devices by electrode modification," *Appl. Phys. Lett.*, vol. 93, no. 12, 2008.
- [169] S.-S. Kim, S.-I. Na, J. Jo, D.-Y. Kim, and Y.-C. Nah, "Plasmon enhanced performance of organic solar cells using electrodeposited Ag nanoparticles," *Appl. Phys. Lett.*, vol. 93, no. 7, p. 73307, 2008.
- [170] S. Pillai, K. R. Catchpole, T. Trupke, and M. A. Green, "Surface plasmon enhanced silicon solar cells," in *Journal of Applied Physics*, 2007, vol. 101, no. 9.
- [171] D. Derkacs, S. H. Lim, P. Matheu, W. Mar, and E. T. Yu, "Improved performance of amorphous silicon solar cells via scattering from surface plasmon polaritons in nearby metallic nanoparticles," *Appl. Phys. Lett.*, vol. 89, no. 9, 2006.
- [172] W. Zhang *et al.*, "Enhancement of Perovskite Based Solar Cells Employing Core-shell Metal Nanoparticles," *Nano Lett.*, p. 130815103150002, 2013.
- [173] N. T. Fofang, T. H. Park, O. Neumann, N. A. Mirin, P. Nordlander, and N. J. Halas, "Plexcitonic nanoparticles: Plasmon-Exciton Coupling in Nanoshell-J- Aggregate complexes," *Nano Lett.*, vol. 8, no. 10, pp. 3481–3487, 2008.
- [174] J. Bellessa, C. Bonnand, J. C. Plenet, and J. Mugnier, "Strong coupling between surface plasmons and excitons in an organic semiconductor," *Phys. Rev. Lett.*, vol. 93, no. 3, pp. 36404–1, 2004.
- [175] J.-L. Wu *et al.*, "Surface plasmonic effects of metallic nanoparticles on the performance of polymer bulk heterojunction solar cells," *ACS Nano*, vol. 5, no. 2, pp. 959–967, 2011.
- [176] F. C. Chen, J. L. Wu, C. L. Lee, Y. Hong, C. H. Kuo, and M. H. Huang, "Plasmonic-enhanced polymer photovoltaic devices incorporating solution-processable metal nanoparticles," *Appl. Phys. Lett.*, vol. 95, no. 1, 2009.
- [177] J. B. Khurgin and A. Boltasseva, "Reflecting upon the losses in plasmonics and metamaterials," *MRS Bull.*, vol. 37, no. 8, pp. 768–779, 2012.
- [178] J. M. Gee, "The effect of parasitic absorption losses on light trapping in thin silicon solar cells," in *Conference Record of the Twentieth IEEE Photovoltaic Specialists Conference*, 1988, pp.

- 549–554 vol.1.
- [179] R. Santbergen, T. L. Temple, R. Liang, A. H. M. Smets, R. A. C. M. M. Van Swaaij, and M. Zeman, "Application of plasmonic silver island films in thin-film silicon solar cells," *J. Opt.*, vol. 14, no. 2, 2012.
- [180] E. S. Arinze, B. Qiu, G. Nyirjesy, and S. M. Thon, "Plasmonic Nanoparticle Enhancement of Solution-Processed Solar Cells: Practical Limits and Opportunities," *ACS Photonics*, vol. 3, no. 2, pp. 158–173, 2016.
- [181] P. Du, P. Jing, D. Li, Y. Cao, Z. Liu, and Z. Sun, "Plasmonic Ag@oxide nanoprisms for enhanced performance of organic solar cells," *Small*, vol. 11, no. 20, pp. 2454–2462, 2015.
- [182] M. Xue *et al.*, "Charge-carrier dynamics in hybrid plasmonic organic solar cells with Ag nanoparticles," *Appl. Phys. Lett.*, vol. 98, no. 25, 2011.
- [183] M. M. Mandoc, W. Veurman, L. J. A. Koster, B. De Boer, and P. W. M. Blom, "Origin of the reduced fill factor and photocurrent in MDMO-PPV:PCNEPV all-polymer solar cells," *Adv. Funct. Mater.*, vol. 17, no. 13, pp. 2167–2173, 2007.
- [184] B. P. Rand, P. Peumans, and S. R. Forrest, "Long-range absorption enhancement in organic tandem thin-film solar cells containing silver nanoclusters," *J. Appl. Phys.*, vol. 96, no. 12, pp. 7519–7526, 2004.
- [185] C. Hägglund, M. Zäch, G. Petersson, and B. Kasemo, "Electromagnetic coupling of light into a silicon solar cell by nanodisk plasmons," *Appl. Phys. Lett.*, vol. 92, no. 5, p. 53110, 2008.
- [186] M. Kirkengen, J. Bergli, and Y. M. Galperin, "Direct generation of charge carriers in c-Si solar cells due to embedded nanoparticles," *J. Appl. Phys.*, vol. 102, no. 9, 2007.
- [187] J. H. Lee, J. H. Park, J. S. Kim, D. Y. Lee, and K. Cho, "High efficiency polymer solar cells with wet deposited plasmonic gold nanodots," *Org. Electron. physics, Mater. Appl.*, vol. 10, no. 3, pp. 416–420, 2009.
- [188] J.-H. Oh *et al.*, "Effect of TiO₂ nanopatterns on the performance of hydrogenated amorphous silicon thin-film solar cells," *Thin Solid Films*, vol. 520, no. 19, pp. 6287–6290, 2012.
- [189] S. Chang, Q. Li, X. Xiao, K. Y. Wong, and T. Chen, "Enhancement of low energy sunlight harvesting in dye-sensitized solar cells using plasmonic gold nanorods," *Energy Environ. Sci.*, vol. 5, no. 11, p. 9444, 2012.
- [190] C. Simovski, D. Morits, P. Voroshilov, M. Guzhva, P. Belov, and Y. Kivshar, "Enhanced efficiency of light-trapping nanoantenna arrays for thin-film solar cells," *Opt. Express*, vol. 21, no. S4, p. A714, 2013.
- [191] N. C. Lindquist, W. A. Luhman, S.-H. Oh, and R. J. Holmes, "Plasmonic nanocavity arrays for enhanced efficiency in organic photovoltaic cells," *Appl. Phys. Lett.*, vol. 93, no. 12, p. 123308, 2008.
- [192] R. A. Pala, J. White, E. Barnard, J. Liu, and M. L. Brongersma, "Design of plasmonic thin-film solar cells with broadband absorption enhancements," *Adv. Mater.*, vol. 21, no. 34, pp. 3504–3509, 2009.
- [193] S. Mookkapati, F. J. Beck, A. Polman, and K. R. Catchpole, "Designing periodic arrays of metal nanoparticles for light-trapping applications in solar cells," *Appl. Phys. Lett.*, vol. 95, no. 5, 2009.
- [194] K. R. Catchpole and S. Pillai, "Absorption enhancement due to scattering by dipoles into silicon waveguides," *J. Appl. Phys.*, vol. 100, no. 4, 2006.
- [195] H. R. Stuart and D. G. Hall, "Enhanced dipole-dipole interaction between elementary radiators near a surface," *Phys. Rev. Lett.*, vol. 80, no. 25, pp. 5663–5666, 1998.
- [196] H. R. Stuart and D. G. Hall, "Thermodynamic limit to light trapping in thin planar structures," *J. Opt. Soc. Am. A*, vol. 14, no. 11, p. 3001, 1997.
- [197] R. S. Kim *et al.*, "E-beam deposited Ag-nanoparticles plasmonic organic solar cell and its absorption enhancement analysis using FDTD-based cylindrical nano-particle optical model.," *Opt. Express*, vol. 20, no. 12, pp. 12649–57, 2012.
- [198] K. min Yoon, K. yeon Yang, and H. Lee, "Fabrication of polycrystalline TiO₂ nanopatterns by TiO₂ sol base imprint lithography," *Thin Solid Films*, vol. 518, no. 1, pp. 126–129, 2009.

- [199] I. Diukman, L. Tzabari, N. Berkovitch, N. Tessler, and M. Orenstein, "Controlling absorption enhancement in organic photovoltaic cells by patterning Au nano disks within the active layer.," *Opt. Express*, vol. 19 Suppl 1, no. January, pp. A64–A71, 2011.
- [200] S.-J. Tsai, M. Ballarotto, D. B. Romero, W. N. Herman, H.-C. Kan, and R. J. Phaneuf, "Effect of gold nanopillar arrays on the absorption spectrum of a bulk heterojunction organic solar cell.," *Opt. Express*, vol. 18 Suppl 4, no. November, pp. A528–A535, 2010.
- [201] M. M. Greve and B. Holst, "Optimization of an electron beam lithography instrument for fast, large area writing at 10 kV acceleration voltage," *J. Vac. Sci. Technol. B, Nanotechnol. Microelectron. Mater. Process. Meas. Phenom.*, vol. 31, no. 4, p. 43202, 2013.
- [202] C. Luo, X. Ni, L. Liu, S. I. M. Nomura, and Y. Chen, "Degassing-assisted patterning of cell culture surfaces," *Biotechnol. Bioeng.*, vol. 105, no. 4, pp. 854–859, 2010.
- [203] K. T. Lee *et al.*, "Simultaneous Enhancement of Upconversion and Downshifting Luminescence via Plasmonic Structure," *Nano Lett.*, vol. 15, no. 4, pp. 2491–2497, 2015.
- [204] X. Liu and D. Yuan Lei, "Simultaneous excitation and emission enhancements in upconversion luminescence using plasmonic double-resonant gold nanorods," *Sci. Rep.*, vol. 5, no. September, p. 15235, 2015.
- [205] Q.-C. Sun, J. Casamada-Ribot, V. Singh, H. Mundoor, I. I. Smalyukh, and P. Nagpal, "Effect of plasmon-enhancement on photophysics in upconverting nanoparticles," *Opt. Express*, vol. 22, no. 10, p. 11516, 2014.
- [206] Y. S. Kim, P. T. Leung, and T. F. George, "Classical decay rates for molecules in the presence of a spherical surface: A complete treatment," *Surf. Sci.*, vol. 195, no. 1–2, pp. 1–14, 1988.
- [207] S. Fischer *et al.*, "Plasmon enhanced upconversion luminescence near gold nanoparticles – simulation and analysis of the interactions: Errata," *Opt. Express*, vol. 21, no. 9, p. 10606, 2013.
- [208] R. Esteban, M. Laroche, and J. J. Greffet, "Influence of metallic nanoparticles on upconversion processes," *J. Appl. Phys.*, vol. 105, no. 3, 2009.
- [209] H. Mertens, A. F. Koenderink, and A. Polman, "Plasmon-enhanced luminescence near noble-metal nanospheres: Comparison of exact theory and an improved Gersten and Nitzan model," *Phys. Rev. B - Condens. Matter Mater. Phys.*, vol. 76, no. 11, pp. 1–12, 2007.
- [210] E. D. Palik, "Palik, Handbook of Optical Constants, Vol.2 (AP, 1991)(ISBN 0125444222).pdf," *Proc Natl Acad Sci USA*, vol. 2. p. Vol 2, 1991.
- [211] L. Aigouy, A. Cazé, P. Gredin, M. Mortier, and R. Carminati, "Mapping and quantifying electric and magnetic dipole luminescence at the nanoscale," *Phys. Rev. Lett.*, vol. 113, no. 7, pp. 1–5, 2014.
- [212] J. Zuloaga and P. Nordlander, "On the energy shift between near-field and far-field peak intensities in localized plasmon systems," *Nano Lett.*, vol. 11, no. 3, pp. 1280–1283, 2011.
- [213] F. Moreno, P. Albella, and M. Nieto-Vesperinas, "Analysis of the spectral behavior of localized plasmon resonances in the near- and far-field regimes," *Langmuir*, vol. 29, no. 22, pp. 6715–6721, 2013.
- [214] P. Alonso-González *et al.*, "Experimental verification of the spectral shift between near- and far-field peak intensities of plasmonic infrared nanoantennas," *Phys. Rev. Lett.*, vol. 110, no. 20, 2013.
- [215] Y.-L. Wang *et al.*, "Tailoring Plasmonic Enhanced Upconversion in Single NaYF₄:Yb³⁺/Er³⁺ Nanocrystals," *Sci. Rep.*, vol. 5, no. 1, p. 10196, 2015.
- [216] S. Schietinger, T. Aichele, H. Q. Wang, T. Nann, and O. Benson, "Plasmon-enhanced upconversion in single NaYF₄:Yb³⁺/Er³⁺ codoped nanocrystals," *Nano Lett.*, vol. 10, no. 1, pp. 134–138, 2010.
- [217] Z. Q. Li *et al.*, "Plasmon-enhanced upconversion fluorescence in NaYF₄:Yb/Er/Gd nanorods coated with Au nanoparticles or nanoshells," *J. Appl. Phys.*, vol. 111, no. 1, 2012.
- [218] A. C. Atre, A. García-Etxarri, H. Alaeian, and J. A. Dionne, "Toward high-efficiency solar upconversion with plasmonic nanostructures," *J. Opt.*, vol. 14, no. 2, 2012.
- [219] F. Meng *et al.*, "Integrated plasmonic and upconversion starlike Y₂O₃:Er/Au@TiO₂ composite

- for enhanced photon harvesting in dye-sensitized solar cells," *J. Power Sources*, vol. 316, pp. 207–214, 2016.
- [220] P. Ramasamy and J. Kim, "Combined plasmonic and upconversion rear reflectors for efficient dye-sensitized solar cells," *Chem. Commun.*, vol. 50, no. 7, pp. 879–881, 2014.
- [221] S. C. Taflove, A. Hagness, *Computational Electrodynamics: The Finite-Difference Time-Domain Method, Third Edition*. 2005.
- [222] K. S. Yee, "Numerical Solution of Initial Boundary Value Problems Involving Maxwell's Equations in Isotropic Media," *IEEE Transactions on Antennas and Propagation*, vol. 14, no. 3, pp. 302–307, 1966.
- [223] M. Saliba *et al.*, "Cesium-containing triple cation perovskite solar cells: improved stability, reproducibility and high efficiency," *Energy Environ. Sci.*, vol. 9, no. 6, pp. 1989–1997, 2016.
- [224] M. Saliba *et al.*, "A molecularly engineered hole-transporting material for efficient perovskite solar cells," *Nat. Energy*, vol. 1, no. 2, p. 15017, 2016.
- [225] D. Bryant *et al.*, "Light and oxygen induced degradation limits the operational stability of methylammonium lead triiodide perovskite solar cells," *Energy Environ. Sci.*, vol. 9, no. 5, pp. 1655–1660, 2016.
- [226] Y. Rong, L. Liu, A. Mei, X. Li, and H. Han, "Beyond efficiency: The challenge of stability in mesoscopic perovskite solar cells," *Advanced Energy Materials*, vol. 5, no. 20, 2015.
- [227] P. Docampo, J. M. Ball, M. Darwich, G. E. Eperon, and H. J. Snaith, "Efficient organometal trihalide perovskite planar-heterojunction solar cells on flexible polymer substrates," *Nat. Commun.*, vol. 4, 2013.
- [228] K. Hwang *et al.*, "Toward large scale roll-to-roll production of fully printed perovskite solar cells," *Adv. Mater.*, vol. 27, no. 7, pp. 1241–1247, 2015.
- [229] D. Liu, M. K. Gangishetty, and T. L. Kelly, "Effect of CH₃NH₃PbI₃ thickness on device efficiency in planar heterojunction perovskite solar cells," *J. Mater. Chem. A*, vol. 2, no. 46, pp. 19873–19881, 2014.
- [230] E. H. Anaraki *et al.*, "Highly efficient and stable planar perovskite solar cells by solution-processed tin oxide," *Energy Environ. Sci.*, vol. 9, no. 10, pp. 3128–3134, 2016.
- [231] Q. Wang, Q. Dong, T. Li, A. Gruverman, and J. Huang, "Thin Insulating Tunneling Contacts for Efficient and Water-Resistant Perovskite Solar Cells," *Adv. Mater.*, pp. 6734–6739, 2016.
- [232] A. Kojima, K. Teshima, Y. Shirai, and T. Miyasaka, "Organometal Halide Perovskites as Visible-Light Sensitizers for Photovoltaic Cells Organometal Halide Perovskites as Visible-Light Sensitizers for Photovoltaic," *J. Am. Chem. Soc.*, vol. 131, no. 17, pp. 6050–6051, 2009.
- [233] X. Zheng *et al.*, "Designing nanobowl arrays of mesoporous TiO₂ as an alternative electron transporting layer for carbon cathode-based perovskite solar cells," *Nanoscale*, vol. 8, no. 12, pp. 6393–6402, 2016.
- [234] J. A. Christians, J. S. Manser, and P. V. Kamat, "Best practices in perovskite solar cell efficiency measurements. Avoiding the error of Making Bad Cells Look Good," *Journal of Physical Chemistry Letters*, vol. 6, no. 5, pp. 852–857, 2015.
- [235] B. Peng, G. Jungmann, C. Jäger, D. Haarer, H.-W. Schmidt, and M. Thelakkat, "Systematic investigation of the role of compact {TiO₂} layer in solid state dye-sensitized TiO₂ solar cells," *Coord. Chem. Rev.*, vol. 248, no. 13–14, pp. 1479–1489, 2004.
- [236] Z. Sun, G. Sitbon, T. Pons, A. A. Bakulin, and Z. Chen, "Reduced Carrier Recombination in PbS - CuInS₂ Quantum Dot Solar Cells," *Sci. Rep.*, vol. 5, p. 10626, 2015.
- [237] J. Zhang, "Roles of the n-type oxide layer in hybrid perovskite solar cells THÈSE de DOCTORAT Université Pierre et Marie Curie - Paris VI," no. Ed 388, 2016.
- [238] Y. Zhou *et al.*, "Distribution of bromine in mixed iodide–bromide organolead perovskites and its impact on photovoltaic performance," *J. Mater. Chem. A*, vol. 4, no. 41, pp. 16191–16197, 2016.
- [239] Y. Wu *et al.*, "Highly compact TiO₂ layer for efficient hole-blocking in perovskite solar cells," *Appl. Phys. Express*, vol. 7, no. 5, 2014.
- [240] K. Wojciechowski, M. Saliba, T. Leijtens, A. Abate, and H. J. Snaith, "Sub-150 °C processed

- meso-superstructured perovskite solar cells with enhanced efficiency,” *Energy Environ. Sci.*, vol. 7, no. 3, pp. 1142–1147, 2014.
- [241] L. Huang *et al.*, “Toward Revealing the Critical Role of Perovskite Coverage in Highly Efficient Electron-Transport Layer-Free Perovskite Solar Cells: An Energy Band and Equivalent Circuit Model Perspective,” *ACS Appl. Mater. Interfaces*, vol. 8, no. 15, pp. 9811–9820, Apr. 2016.
- [242] W. Ke *et al.*, “Efficient hole-blocking layer-free planar halide perovskite thin-film solar cells,” *Nat. Commun.*, vol. 6, p. 6700, 2015.
- [243] Q. Zhu *et al.*, “Compact Layer Free Perovskite Solar Cells with a High-Mobility Hole-Transporting Layer,” *ACS Appl. Mater. Interfaces*, vol. 8, no. 4, pp. 2652–2657, 2016.
- [244] D. Liu, J. Yang, and T. L. Kelly, “Compact layer free perovskite solar cells with 13.5% efficiency,” *J. Am. Chem. Soc.*, vol. 136, no. 49, pp. 17116–17122, 2014.
- [245] E. Edri *et al.*, “Why Lead Methylammonium Tri-iodide Perovskite-Based Solar Cells Require a Mesoporous Electron Transporting Scaffold (but Not Necessarily a Hole Conductor),” *Nano Lett.*, vol. 14, no. 2, pp. 1000–1004, 2014.
- [246] Y. Tidhar *et al.*, “Crystallization of Methyl Ammonium Lead Halide Perovskites : Implications for Photovoltaic Applications Crystallization of Methyl Ammonium Lead Halide Perovskites : Implications for Photovoltaic Applications,” pp. 1–18, 2014.
- [247] P. Wang, M. Ulfa, and T. Pauporté, “Effects of Perovskite Monovalent Cation Composition on the High and Low Frequency Impedance Response of Efficient Solar Cells,” *J. Phys. Chem. C*, vol. 122, no. 4, pp. 1973–1981, 2018.
- [248] D. P. McMeekin *et al.*, “A mixed-cation lead mixed-halide perovskite absorber for tandem solar cells,” *Science (80-.)*, vol. 351, no. 6269, pp. 151–155, 2016.
- [249] S. Wozny *et al.*, “Controlled Humidity Study on the Formation of Higher Efficiency Formamidinium Lead Triiodide-Based Solar Cells,” *Chem. Mater.*, vol. 27, no. 13, pp. 4814–4820, 2015.
- [250] C. Roldán-Carmona *et al.*, “Flexible high efficiency perovskite solar cells,” *Energy Environ. Sci.*, vol. 7, no. 3, p. 994, 2014.
- [251] G. E. Eperon, V. M. Burlakov, P. Docampo, A. Goriely, and H. J. Snaith, “Morphological control for high performance, solution-processed planar heterojunction perovskite solar cells,” *Adv. Funct. Mater.*, vol. 24, no. 1, pp. 151–157, 2014.
- [252] S. D. Stranks *et al.*, “Electron-Hole Diffusion Lengths Exceeding 1 Micrometer in an Organometal Trihalide Perovskite Absorber,” *Science (80-.)*, vol. 342, no. 6156, pp. 341–344, 2013.
- [253] V. D’Innocenzo *et al.*, “Excitons versus free charges in organo-lead tri-halide perovskites,” *Nat. Commun.*, vol. 5, pp. 1–6, 2014.
- [254] H. Yu, F. Wang, F. Xie, W. Li, J. Chen, and N. Zhao, “The role of chlorine in the formation process of ‘CH₃NH₃PbI_{3-x}Cl_x’ perovskite,” *Adv. Funct. Mater.*, vol. 24, no. 45, pp. 7102–7108, 2014.
- [255] N. J. Jeon, J. H. Noh, Y. C. Kim, W. S. Yang, S. Ryu, and S. Il Seok, “Solvent engineering for high-performance inorganic-organic hybrid perovskite solar cells,” *Nat. Mater.*, vol. 13, no. 9, pp. 897–903, 2014.
- [256] R. Schölin, M. H. Karlsson, S. K. Eriksson, H. Siegbahn, E. M. J. Johansson, and H. Rensmo, “Energy level shifts in spiro-OMeTAD molecular thin films when adding Li-TFSI,” *J. Phys. Chem. C*, vol. 116, no. 50, pp. 26300–26305, 2012.
- [257] Z. Hawash, L. K. Ono, and Y. Qi, “Photovoltaics: Moisture and Oxygen Enhance Conductivity of LiTFSI-Doped Spiro-MeOTAD Hole Transport Layer in Perovskite Solar Cells (Adv. Mater. Interfaces 13/2016),” *Advanced Materials Interfaces*, vol. 3, no. 13, 2016.
- [258] Z. Wang *et al.*, “Efficient and Air-Stable Mixed-Cation Lead Mixed-Halide Perovskite Solar Cells with n-Doped Organic Electron Extraction Layers,” *Adv. Mater.*, vol. 29, no. 5, 2017.
- [259] V. Džimbeg-malčić, Ž. Barbarić-mikočević, and K. Itrić, “Kubelka-Munk Theory in Describing Optical Properties of Paper (1),” *Tech. Gaz.*, vol. 18, no. 1, pp. 117–124, 2011.
- [260] C. Strohhöfer and A. Polman, “Absorption and emission spectroscopy in Er³⁺–Yb³⁺ doped

- aluminum oxide waveguides," *Opt. Mater. (Amst.)*, vol. 21, no. 4, pp. 705–712, 2003.
- [261] D. O. Faulkner, J. J. Mcdowell, A. J. Price, D. D. Perovic, N. P. Kherani, and G. A. Ozin, "Measurement of absolute photoluminescence quantum yields using integrating spheres - Which way to go?," *Laser Photonics Rev.*, vol. 6, no. 6, pp. 802–806, 2012.
- [262] E. Saïdi *et al.*, "Scanning thermal imaging by near-field fluorescence spectroscopy," *Nanotechnology*, vol. 20, no. 11, 2009.
- [263] Y. Ye *et al.*, "Upconversion luminescence of NaYF₄:Yb,Er nanocrystals with high uniformity," *J. Rare Earths*, vol. 32, no. 9, pp. 802–805, 2014.
- [264] K. Nigoghossian, S. Ouellet, J. Plain, Y. Messaddeq, D. Boudreau, and S. J. L. Ribeiro, "Upconversion nanoparticle-decorated gold nanoshells for near-infrared induced heating and thermometry," *J. Mater. Chem. B*, vol. 5, no. 34, pp. 7109–7117, 2017.
- [265] D. Lu, S. K. Cho, S. Ahn, L. Brun, C. J. Summers, and W. Park, "Plasmon enhancement mechanism for the upconversion processes in NaYF₄:Yb³⁺,Er³⁺nanoparticles: Maxwell versus Förster," *ACS Nano*, vol. 8, no. 8, pp. 7780–7792, 2014.
- [266] J. Zhao *et al.*, "Controlled Synthesis, Formation Mechanism, and Great Enhancement of Red Upconversion Luminescence of NaYF₄:Yb³⁺, Er³⁺ Nanocrystals/Submicroplates at Low Doping Level," *J. Phys. Chem. B*, vol. 112, no. 49, pp. 15666–15672, 2008.
- [267] F. Wang *et al.*, "Simultaneous phase and size control of upconversion nanocrystals through lanthanide doping," *Nature*, vol. 463, no. 7284, pp. 1061–1065, 2010.
- [268] G. Yi *et al.*, "Synthesis, characterization, and biological application of size-controlled nanocrystalline NaYF₄:Yb,Er infrared-to-visible up-conversion phosphors," *Nano Lett.*, vol. 4, no. 11, pp. 2191–2196, 2004.
- [269] A. Thill, Ö. Ö. Ø. Óðóñ, and Ó. Ø. Ò. Ö. Ôòùö, "Agrégação des partículas: structure, dynamique et simulation. Application au cas d'un écoulement stratifié: l'estuaire du Rhône.," 2006.
- [270] I. Z. Dinic *et al.*, "PEG and PVP assisted solvothermal synthesis of NaYF₄:Yb³⁺/Er³⁺up-conversion nanoparticles," *Adv. Powder Technol.*, vol. 27, no. 3, pp. 845–853, 2016.
- [271] J. Labeguerie, P. Gredin, J. Marrot, and A. Kozak, "Sol – gel synthesis of K₃InF₆ and structural characterization of K₂InC₁₀O₁₀H₆F₉, K₃InC₁₂O₁₄H₄F₁₈ and K₃InC₁₂O₁₂F₁₈," *J. Solid State Chem.*, vol. 178, pp. 3197–3205, 2005.
- [272] F. Wang *et al.*, "Simultaneous phase and size control of upconversion nanocrystals through lanthanide doping," *Nature*, vol. 463, no. 7284, pp. 1061–1065, 2010.
- [273] W. Zhang, "Nanomaterial," vol. 811, 2014.
- [274] T. Jun *et al.*, "Effect of Aspect Ratio Distribution on Localized Surface Plasmon Resonance Extinction Spectrum of Gold Nanorods," *Chinese Phys. Lett.*, vol. 25, no. 12, pp. 4459–4462, 2008.
- [275] H. Xiang *et al.*, "Short-Wave Infrared Sensor by the Photothermal Effect of Colloidal Gold Nanorods," *Small*, vol. 1704013, pp. 1–8, 2018.
- [276] X. Ye, C. Zheng, J. Chen, Y. Gao, and C. B. Murray, "Using Binary Surfactant Mixtures to Simultaneously Improve Dimensional Tunability and Monodispersity in the Seeded-Growth of Gold Nanorods Using Binary Surfactant Mixtures to Simultaneously Improve Dimensional Tunability and Monodispersity in the Seeded-G," *Nano Lett.*, vol. 13, pp. 765–771, 2013.
- [277] A. Guerrero-Martínez, J. Pérez-Juste, E. Carbó-Argibay, G. Tardajos, and L. M. Liz-Marzán, "Gemini-surfactant-directed self-assembly of monodisperse gold nanorods into standing superlattices," *Angew. Chemie - Int. Ed.*, vol. 48, no. 50, pp. 9484–9488, 2009.
- [278] X. Kou *et al.*, "One-step synthesis of large-aspect-ratio single-crystalline gold nanorods by using CTPAB and CTBAB surfactants," *Chem. - A Eur. J.*, vol. 13, no. 10, pp. 2929–2936, 2007.
- [279] X. C. Jiang, A. Brioude, and M. P. Pileni, "Gold nanorods: Limitations on their synthesis and optical properties," *Colloids Surfaces A Physicochem. Eng. Asp.*, vol. 277, no. 1–3, pp. 201–206, 2006.
- [280] D. a Zweifel and A. Wei, "Sulfide-Arrested Growth of Gold Nanorods.," *Chem. Mater.*, vol. 17, no. 6, pp. 4256–4261, 2005.

- [281] H.-Y. Wu, H.-C. Chu, T.-J. Kuo, C.-L. Kuo, and M. H. Huang, "Seed-Mediated Synthesis of High Aspect Ratio Gold Nanorods with Nitric Acid," *Chem. Mater.*, vol. 17, no. 25, pp. 6447–6451, 2005.
- [282] N. Taub, O. Krichevski, and G. Markovich, "Growth of Gold Nanorods on Surfaces," *J. Phys. Chem. B*, vol. 107, no. 42, pp. 11579–11582, 2003.
- [283] J. Pérez-Juste, L. M. Liz-Marzán, S. Carnie, D. Y. C. Chan, and P. Mulvaney, "Electric-field-directed growth of gold nanorods in aqueous surfactant solutions," *Adv. Funct. Mater.*, vol. 14, no. 6, pp. 571–579, 2004.
- [284] M. Liu and P. Guyot-Sionnest, "Mechanism of silver(I)-assisted growth of gold nanorods and bipyramids," *J. Phys. Chem. B*, vol. 109, no. 47, pp. 22192–22200, 2005.
- [285] T. K. Sau and C. J. Murphy, "Seeded high yield synthesis of short Au nanorods in aqueous solution," *Langmuir*, vol. 20, no. 15, pp. 6414–6420, 2004.
- [286] A. Gole and C. J. Murphy, "Seed-mediated synthesis of gold nanorods: Role of the size and nature of the seed," *Chem. Mater.*, vol. 16, no. 19, pp. 3633–3640, 2004.
- [287] B. D. Busbee, S. O. Obare, and C. J. Murphy, "An improved synthesis of high-aspect-ratio gold nanorods," *Adv. Mater.*, vol. 15, no. 5, pp. 414–416, 2003.
- [288] B. Nikoobakht and M. A. El-Sayed, "Preparation and growth mechanism of gold nanorods (NRs) using seed-mediated growth method," *Chem. Mater.*, vol. 15, no. 10, pp. 1957–1962, 2003.
- [289] N. R. Jana, N. R. Jana, L. Gearheart, L. Gearheart, C. J. Murphy, and C. J. Murphy, "Wet Chemical Synthesis of High Aspect Ratio Cylindrical Gold Nanorods," *J. Phys. Chem. B*, vol. 105, no. 19, pp. 4065–4067, 2001.
- [290] N. R. Jana, L. Gearheart, and C. J. Murphy, "Seed-mediated growth approach for shape-controlled synthesis of spheroidal and rod-like gold nanoparticles using a surfactant template," *Adv. Mater.*, vol. 13, no. 18, pp. 1389–1393, 2001.
- [291] S.-S. Chang, C.-L. Lee, and C. R. C. Wang, "Gold Nanorods: Electrochemical Synthesis and Optical Properties," *J. Phys. Chem. B*, vol. 101, no. 34, pp. 6661–6664, 1997.
- [292] R. N. Moussawi and D. Patra, "Synthesis of Au Nanorods through Prereduction with Curcumin: Preferential Enhancement of Au Nanorod Formation Prepared from CTAB-Capped over Citrate-Capped Au Seeds," *J. Phys. Chem. C*, vol. 119, no. 33, pp. 19458–19468, 2015.
- [293] A. B. Serrano-Montes *et al.*, "A General Method for Solvent Exchange of Plasmonic Nanoparticles and Self-Assembly into SERS-Active Monolayers," *Langmuir*, vol. 31, no. 33, pp. 9205–9213, 2015.
- [294] A. Wijaya and K. Hamad-Schifferli, "Ligand customization and DNA functionalization of gold nanorods via round-trip phase transfer ligand exchange," *Langmuir*, vol. 24, no. 18, pp. 9966–9969, 2008.
- [295] Y. Niidome, H. Takahashi, S. Urakawa, K. Nishioka, and S. Yamada, "Immobilization of Gold Nanorods on the Glass Substrate by the Electrostatic Interactions for Localized Plasmon Sensing," *Chem. Lett.*, vol. 33, no. 4, pp. 454–455, 2004.
- [296] G. Robert B., "Solvent-tuned structures," *Nat. Mater.*, vol. 6, no. August, pp. 553–555, 2007.
- [297] D. Fava, Z. Nie, M. A. Winnik, and E. Kumacheva, "Evolution of self-assembled structures of polymer-terminated gold nanorods in selective solvents," *Adv. Mater.*, vol. 20, no. 22, pp. 4318–4322, 2008.
- [298] W. Haiss, N. T. K. Thanh, J. Aveyard, and D. G. Fernig, "Determination of size and concentration of gold nanoparticles from UV-Vis spectra," *Anal. Chem.*, vol. 79, no. 11, pp. 4215–4221, 2007.
- [299] B. L. Feng *et al.*, "Super-hydrophobic surfaces: From natural to artificial," *Adv. Mater.*, vol. 14, no. 24, pp. 1857–1860, 2002.
- [300] S. Ryu *et al.*, "Voltage Output of Efficient Perovskite Solar Cells with high Open-Circuit Voltage and Fill Factor," *Energy Environ. Sci.*, vol. 7, pp. 2614–2618, 2014.
- [301] "http://www.ni-cd.net/accusphp/forum/docjoints/ID99_notes-chap2.pdf."
- [302] P. J. S. Smith, "Lecture 19 : Review , PN junctions , Fermi levels , forward bias," no. chapter 6,

pp. 1–16, 2004.

- [303] R. Houdré,
“<https://wiki.epfl.ch/houdre/documents/DispElec/chapitre%2005%20jonction%20pn.pdf>.” .
- [304] “<http://www.sjsu.edu/faculty/gerstman/StatPrimer/t-table.pdf>.” .
- [305] “<http://rredc.nrel.gov/solar/spectra/am1.5/>.” .